LIÈGE université
Sciences Appliquées

Clustering Analysis for the Micromechanics-Based Reduced Homogenization in the Mechanics of Composite Materials

A thesis submitted in partial fulfillment of the requirements
for the degree of Doctor of Philosophy (Phd) in Engineering Science

by

Kevin SPILKER

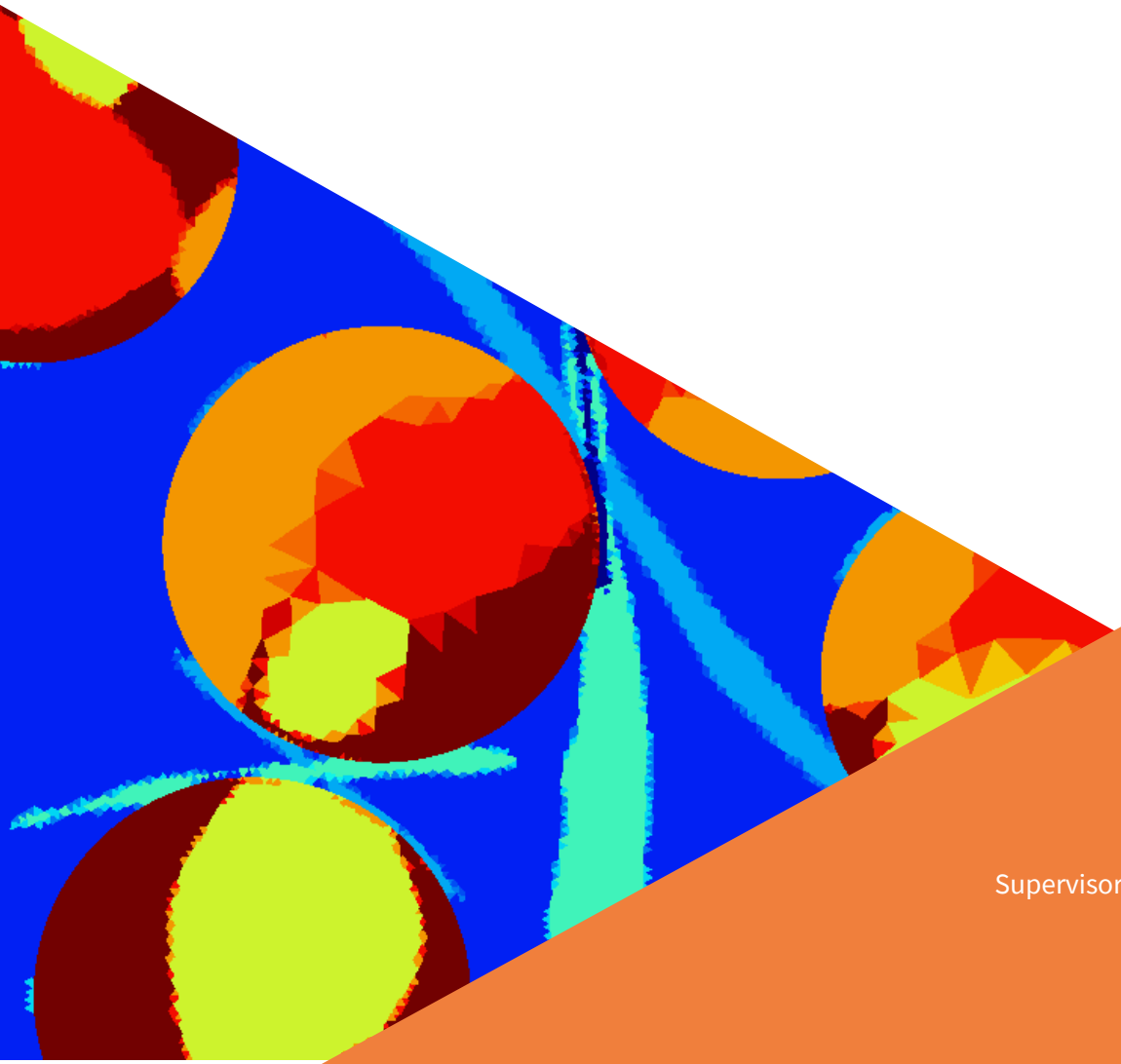

Supervisor: Ludovic NOELS

UNIVERSITY OF LIÈGE

Abstract

Faculty of Applied Sciences
Aerospace and Mechanical Engineering Department

Doctor in Engineering Sciences

Clustering Analyses for the Micromechanics-Based Reduced Homogenization in the Mechanics of Composite Materials

by Kevin SPILKER

The homogenized mechanical response of heterogeneous, elasto-plastic composite materials was investigated by the use of clustering analysis based homogenization (CAH) approaches, relying on two-scale coupling algorithms and on piecewise uniform microscopic fields of internal variables. Clustering algorithms fed by several micromechanical fields can be implemented for the spatial decomposition into the domains with uniform fields of variables. In cases of history-dependent responses of the materials however, the selection of the underlying deformation fields for the clustering procedure is crucial. Not optimized spatial subdomain decompositions of the microscopic domain, meaning that localized effects and evolving deformation patterns are not well represented, can cause overstiff inelastic composite material responses modeled by the CAH approaches. To improve homogenized predictions for the responses of heterogeneous materials, more accurate representations of inelastic localizations were targeted by new spatial decompositions. The numerical estimation of the interaction functions between the subdomains allows the use of the CAH approaches for the numerical modeling of general composite materials with arbitrary microstructures. The CAH methods based on clustering analyses were tested for materials with isotropic and anisotropic microstructures, various material systems with a particular emphasis on the complex case of perfectly plastic material phases, under both proportional and non-proportional loading conditions and histories. The assessment of the predictions by the CAH methods was based on comparisons to reference full-field homogenization results. After the extensive investigation, comparisons could be drawn between the CAH approaches based on different algorithms, and the effect of the underlying spatial decomposition based on elastic and inelastic fields was evaluated. It could be proven that more accurate predictions for the mechanical responses of composite materials can be found when inelastic fields are considered as the foundation of the spatial division into subdomains. Subsequently, a novel approach for the three-scale bridging of woven composite materials based on the CAH approaches was employed. Very good predictions under various complex loading conditions prove the suitability for woven materials, and offer a promising technique for the homogenization of materials with underlying heterogeneous meso and microstructures. Finally, a novel multi-step homogenization scheme as an extension of the transformation field analysis was proposed and employed for the consideration of two scale levels.

Acknowledgments

I would like to take this opportunity to express my gratitude to the people who were involved in my work at the University of Liège over the last four years, that resulted in this doctoral thesis.

At first, I want to thank my promoter and supervisor Prof. Ludovic Noels for giving me the opportunity to work on a highly interesting research topic, his advice and support whenever required through the whole time of my PhD, and his patience that allowed me to adapt to the new challenges and the new working environment.

I want to thank Dr. Ling Wu for many discussions and her advice, helping me to gain a better understanding of the theoretical concepts which I needed for my work. I want to thank Dr. Van-Dung Nguyen for his great patience and help with all the questions and issues related to my implementations into the CM3 library.

I would also like to thank Dr. Laurent Adam for his advice whenever necessary and the many fruitful discussions in the meetings between the CM3 group and e-Xstream (Hexagon). And I thank Mr. Étienne Maillard for his support and organizing the VISCOS project.

I want to thank Prof. Laurent Duchêne, Prof. Ludovic Noels, Dr. Ling Wu, Prof. Pédro Camanho, Prof. Issam Doghri, Dr. Laurent Adam and Mr. Étienne Maillard for their agreement to be part of the jury for my PhD defense and reading my thesis.

I am grateful for the funding by the Walloon Region and Skywin for the research done in the VISCOS project (no.7911-VISCOS), that allowed me to conduct my PhD thesis.

Moreover, I want to thank my friends and PhD fellows, in particular Juan Manuel Calleja Vázquez, Vinayak Gholap, Tianyu Zhang, Ujwal Kishore Jinaga, Nanda Gopala, Soumianarayanan Vijayaraghavan, Eduardo Fernandez and Cedric Laruelle, for all the work related and unrelated discussions and moments. And I want to mention some other friends I made in Liège, in particular Billy-Joe, Jenni, Clara, Gabriel, who I spent time with out of the office environment. All these people helped me to enjoy my daily life in Liège and to remain motivated through the last four years.

Last but not least, I want to thank my parents, Sabine and Ulrich, and my brother Niklas for their patience and support whenever needed during this time.

Contents

List of Abbreviations

ANN	Artificial Neural Network
BC	Boundary Condition(s)
BVP	Boundary Value Problem
CAH	Clustering Analysis Based Homogenization
DMN	Deep Material Network
DNS	Direct Numerical Simulation(s)
DOF	Degree(s) of Freedom
FE	Finite Element
FEA	Finite Element Analysis
FEM	Finite Element Method
FFT	Fast Fourier Transformation
HS	Hashin-Shtrikman
GSM	Generalized Standard Material
LCC	Linear Comparison Composite
MFH	Mean Field Homogenization
MPBC	Mixed Periodic Boundary Condition(s)
MT	Mori-Tanaka
NTFA	Non-uniform Transformation Field Analysis
PBC	Periodic Boundary Condition(s)
PFA	Polarization Field Analysis
POD	Proper Orthogonal Decomposition
RH	Reduced Homogenization
ROM	Reduced Order Model
RVE	Representative volume element
SCCA	Self-consistent Clustering Analysis
TFA	Transformation Field Analysis
UD	Unidirectional

Chapter 1

Introduction

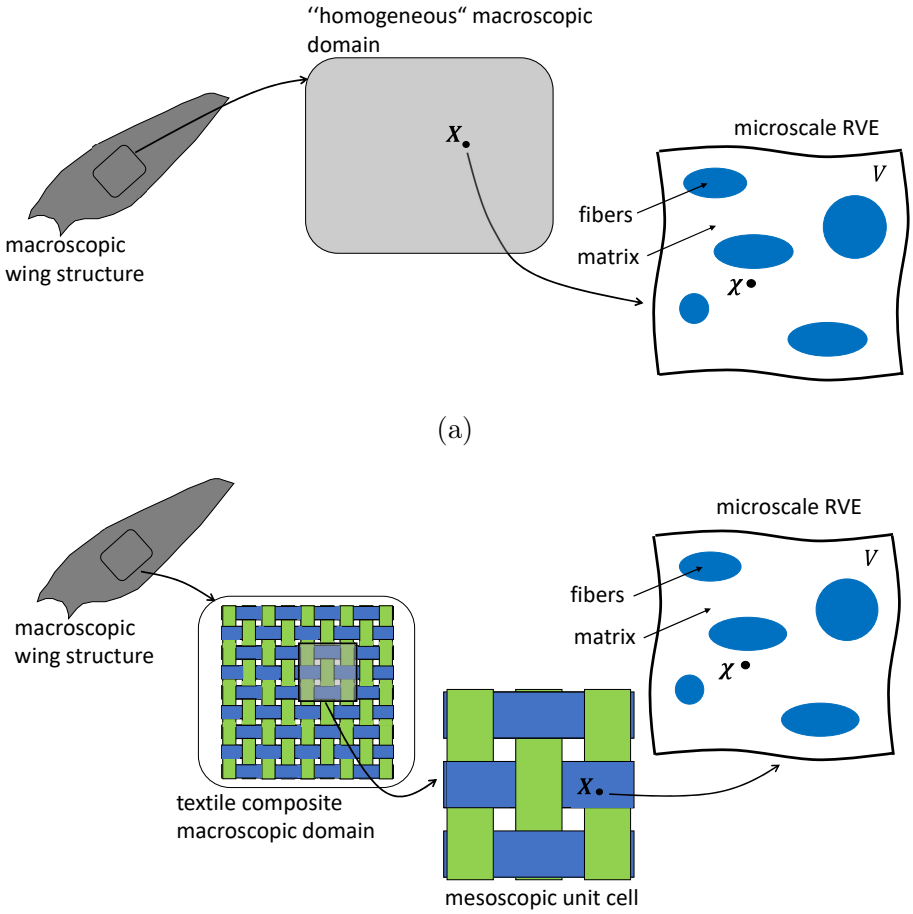

FIGURE 1.1: Schematic representation of a composite wing structure with different kinds of compositions and arrangements of the constituents on the associated scales. The macroscopic domain represents the structural behavior of the wing, built by composite materials on the mesoscale and the microscale. In (a), the macroscopically homogeneous material is built by a composite microstructure consisting of fibers in a matrix material. In (b), the wing structure is built by the weaving process of different yarns on the mesoscale. The yarns have an underlying composite structure on the microscale.

In technologies that rely on the structural use of materials, e.g. aerospace, automotive and wind blade engineering, three factors are all-decisive for the achieved quality: stiffness, strength and weight. While the sufficient stiffness and strength of the used materials ensure the safety of structures and thus of passengers and/or surroundings, the use of light-weight materials boosts the economic value of a certain application. The sought types of materials are multi-phase materials, so called composite materials and schematically depicted in Fig. 1.1. Composite media consist of more than one material phase, engineered in order to exploit the strengths and advantages of the single constituents and achieve optimal performance as a result. Typical composites for industrial applications consist of an inclusion phase, often fibrous, embedded in a matrix material. Fibers are dominantly made of glass, carbon, ceramics, but natural fibers are used as well. The matrix of most industrial applications consists of polymer materials. Composites in civil engineering are typically constructed by steel fibers embedded in concrete. It is mentioned that, besides engineered composite materials, many other types of materials of interest in engineering disciplines have naturally composite microstructures (e.g. biomaterials or geomaterials). Several microstructures consisting of fibrous inclusions in a matrix material investigated in this work are depicted by means of an representative volume element (RVE), which will be explained in more detail in the following, in Fig. 1.2.

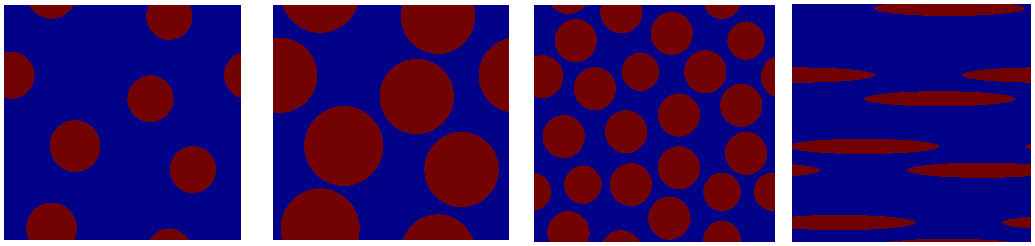

(a) (b) (c) (d)

FIGURE 1.2: Different composite microstructures, represented by RVEs. The microstructures consist of an inclusion phase (red) in a matrix material (blue), both with varying material properties. Investigated in this work are (a-c) isotropic structures with (a,b) different volume fractions and (c) different RVE sizes, and (d) anisotropic structures.

In the aerospace industry, the rising number of passengers and the demand for a reduction of costs has led to an increase of the use of high performance materials over the last years. In nowadays era of sustainable transport technologies relying on higher fuel efficiency or electrification, the use of light-weight composites is becoming even more essential to guarantee physical and economic feasibility. Similarly, longer wind blades allowing for more efficient production of wind energy drive the increasing demand of high-stiffness and low-weight composite materials in the sector of renewable energy production.

Various kinds of composites exist, and continuous research is done on their improvement and the development of novel composite materials and structures. The major drawbacks of the use of composite materials are possibly complex kinds of nonlinear behavior, particularly marked by high localizations of deformation (Fig. 1.3). These complex material nonlinearities can lead to the degradation of the stiffness of the materials and finally to complex and sudden failure modes, requiring for full characterizations of the

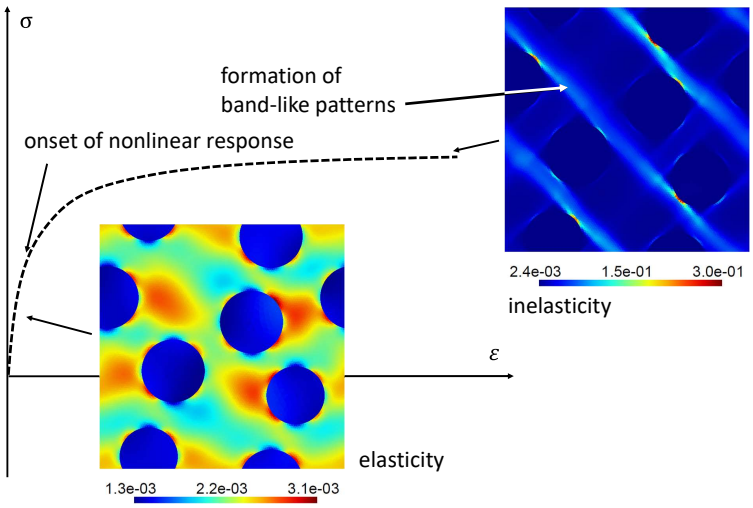

FIGURE 1.3: Schematic display of a highly nonlinear response of a composite material. After a specific yield strength of the material is exceeded by the occurring stresses σ, the formation of inelastic, in particular band-like, deformation patterns starts. The deformation is represented by the equivalent scalar strain ε. The screenshots show equivalent strain distributions in the RVE.

materials performance through extensive testing, before they can finally be introduced in practice. However, the full characterization of these composite materials purely by the use of experiments is not feasible due to several reasons, e.g., composites in high performance applications must resist complex loading conditions and histories, which can be impossible to be implemented in the laboratory. Other examples are the characterization of a materials creep behavior, which may require extremely long observation times. Performing destructive tests for the investigation of a materials fracture or damage behavior, where one manufactured sample is required for one test, may lead to high material expenses. Consequently, the need for numerical tools for the characterization of materials with complex heterogeneous microstructures and under complex loading conditions has seen an increasing demand in many areas of engineering applications.

1.1 Multiscale mechanics in composite media

1.1.1 Homogenization techniques

The typical scale of interest in the computational mechanics of composite materials is the structural, or macroscopic, scale. As already mentioned however, composite materials may have complex structures on lower scales due to varying distributions, sizes and shapes of the material constituents. The precise analysis of the macroscopic mechanical behavior requires the consideration of processes on the lower scales, where constitutive relations of the individual composite constituents are available. Two structural systems are to be distinguished:

- Macroscopic materials that are macroscopically homogeneous, have however an underlying heterogeneous microstructure (Fig. 1.1a). Mechanical processes like plas-

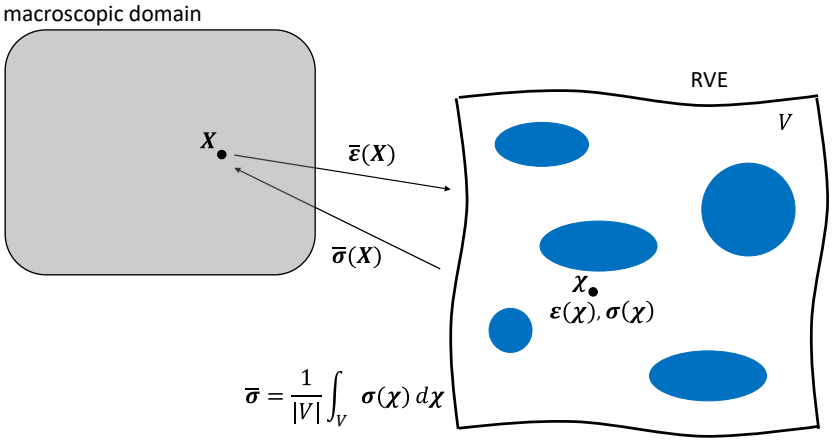

FIGURE 1.4: Schematic demonstration of full-field homogenization approach at a material point $\boldsymbol{X}$ under a strain $\overline{\boldsymbol{\varepsilon}}(\boldsymbol{X})$ in a macroscopic domain, represented by the RVE subjected to a boundary problem expressed through $\overline{\boldsymbol{\varepsilon}}(\boldsymbol{X})$. The overall stress response $\overline{\boldsymbol{\sigma}}(\boldsymbol{X})$ at $\boldsymbol{X}$ follows from computation of the local strain and stress fields $\boldsymbol{\varepsilon}(\boldsymbol{\chi})$ and $\boldsymbol{\sigma}(\boldsymbol{\chi})$ and the averaging of the local reaction stress field over the full RVE domain.

ticity, damage or fracture originate on the microscale and affect the materials macroscopic response.

- Macroscopic materials with composite structures on both meso and microscales (Fig. 1.1b). The mesoscale response is affected by processes like plasticity, damage and fracture, initiating on the microscale. With possibly complex mesoscopic structures and arrangements, the macroscopic response is affected by the processes and structures on both meso and microscales.

Mesoscopic material models for materials with underlying microstructures were introduced for the prediction of damage (Zhuang et al., 2019a,b) and plasticity with damage (Cózar et al., 2022). These mesoscopic constitutive models are constructed by the integration of both micromechanical models as well as phenomenological and mechanism based contributions to predict the onset of microstructural damage or plasticity. A different approach for the modeling of the mesoscopic or macroscopic response of a composite material is based on the simultaneous consideration of two scales. The use of purely micromechanical constitutive relations for plasticity or damage for the determination of the effective behavior of a material allows to predict responses of general and possibly complex material systems under general loading conditions.

Computational analyses linking the materials behavior on the macroscopic or the mesoscopic scale to the processes on the heterogeneous meso or microscale are known as *multiscale simulations* and typically rely on a principle that is known as *mechanical homogenization* (Charalambakis, 2010; Geers, Kouznetsova, and Brekelmans, 2010; Geers et al., 2017; Kanouté, Boso, and Chaboche, 2009; Saeb, Steinmann, and Javili, 2016; Yvonnet, 2019, e.g.). In homogenization based multiscale methods, one material point of the macroscopic (or mesoscopic) domain is considered (Fig. 1.4). The material point in the macroscopic domain contains a selected, but representative, section of the microstructure, required to include all essential structural features. This statistically representative

section is referred to as the *representative volume element* (RVE) and is the key element for the scale bridging of materials. During a multiscale analysis, the deformation state at one point of the macroscopic domain constitutes a boundary value problem (BVP) applied on the RVE. The response computed over the RVE domain is then considered as the local response of the associated material point in the macroscopic domain.

Different estimates for the homogenized mechanical behavior of composite materials exist, with first analytical approaches originating long ago. Classical analytical estimates are certain upper and lower bounds, from which the most stiff and the most compliant possible homogenized responses of a particular composite can be derived. The first introduced bounds for the linear overall properties of heterogeneous two-phase solids are the upper and lower bounds developed by Voigt (1889) and Reuss (1929), assuming iso-strain (Voigt) and iso-stress (Reuss) conditions over both phases without any knowledge of the actual microstructure. The Voigt-Reuss bounds represent the two most distinct cases of microstructural configurations and allow for estimations of the materials overall response solely making use of known phase stiffnesses and volume fractions. The Voigt-Reuss bounds were extended by Hashin and Shtrikman (1962, 1963) towards a variational formulation. The Hashin-Shtrikman bounds, valid for linear and isotropic microstructures, allow for more narrow estimations of the homogenized response. Following, the Hashin-Shtrikman bounds were further extended towards higher order formulations by Kröner (1977) and for the use of anisotropic materials by Willis (1977). Talbot and Willis (1985) introduced the first bounds with the ability to derive overall responses for the case of material phases with nonlinear mechanical behavior by a variational procedure. The variational approach pioneered by Ponte Castañeda (1991) builds the foundation for many subsequent homogenization schemes by introducing a *linear comparison composite* (LCC) with linear properties, being equivalent to the linearized effective properties of the actual nonlinear composite (Ponte Castañeda, 1992, 1996). The LCC approach was extended towards a second-order scheme considering strain and stress field fluctuations in the material phases (Lopez-Pamies and Castañeda, 2004; Lopez-Pamies, Goudarzi, and Danas, 2013; Ponte Castañeda, 2002a, 2002b).

A related but distinct class of (semi-)analytical homogenization schemes is the *mean field homogenization* (MFH). The MFH was initiated on the basic rule of mixtures and assuming a uniform strain or uniform stress throughout all phases of the material. These approaches are known as the Taylor-model and the Sachs-model and correspond to the Voigt-Reuss upper and lower bounds. The work of Eshelby (1957) considering the elastic two-phase problem of a dilute inclusion in an infinite matrix laid the foundation for the following MFH approaches. He pioneered the concept of occurring phase-wise uniform eigenstrains in elastic two-phase materials due to the stiffness mismatch of the inclusion phase and the host phase. The eigenstrains lead to interactions between the phases, depending on the inclusion size and orientation, expressed by the Eshelby tensor. Subsequent MFH schemes rely on per-phase uniform, or average, strain and stress fields, and the relation between the two phases deformation states expressed by so-called strain localization tensors. Different relations for the strain localizations were developed, expressing the phase strains as a function of the composite strain or as a mutual relation between the phases. Most popular MFH formulations are built on the self-consistent scheme (Budiansky, 1965; Hill, 1963, 1965a,b; Kröner, 1958), the *Mori-Tanaka* scheme (Benveniste, 1987; Mori and Tanaka, 1973) or the differential scheme (McLaughlin, 1977; Norris, 1985;

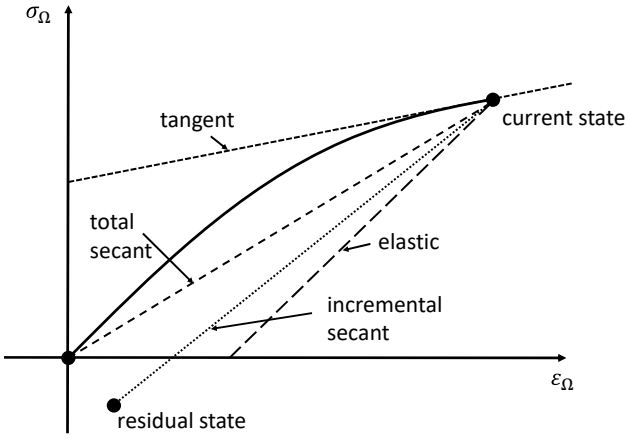

FIGURE 1.5: Schematic display of the nonlinear behavior of a composite material phase denoted by Ω, with indicated references to the materials elastic, tangent and secant stiffnesses used as LCC operators in various MFH schemes. The marked residual state associated to the incremental secant stiffness will be explained in detail in Section 2.

Zimmerman, 1991). Various MFH formalisms exist, depending on the selected LCC operator (see Fig. 1.5). Total secant (Berveiller and Zaoui, 1978; Suquet, 2001), affine (Masson and Zaoui, 1999; Molinari, Canova, and Ahzi, 1987), tangent (Doghri and Ouaar, 2003) and incremental secant (Wu et al., 2013a) MFH schemes were developed for the homogenization of nonlinear composite materials, with extensions towards the integration of second-order statistical moments of the phase strains (Doghri et al., 2011; Wu et al., 2017). Doghri and Friebel (2005) achieved improved MFH predictions when applying isotropization procedures of the phases tangent operators. This isotropization step is waived when using the incremental-secant scheme by Wu et al., 2013a, relying on a naturally isotropic secant operator. An overview of the applicability of various MFH formulations was presented by Chaboche, Kanouté, and Roos (2005). Focusing on the computational capabilities, MFH approaches are able to deliver homogenized composite estimations with very low computational requirements. However, compromises of the validity of MFH approaches with respect to the particular composite structures need to be pointed out. The interaction functions used in MFH schemes are relations depending on a single tensor that contains the geometrical inclusion information. Therefore, composites with fully random isotropic structures can be represented, as well as composites with inclusions that have one preferred orientation. Examples are transverse isotropic inclusions, as unidirectional (UD) fiber composites. Complex composites however, containing more than one structural orientation, can not be reliably covered by MFH approaches. This includes orthotropic structures, for example layered composite laminates with layers that have different preferred orientations or composites with woven structures. In summary it means that MFH approaches, while being computationally very efficient, rely on certain assumptions on the composites microstructural configuration and therefore have obvious limitations when dealing with cases of complex anisotropic microstructures.

Nowadays, thanks to vastly increased computational abilities in recent years, fully

computational multiscale approaches using direct numerical simulations (DNS) for the mesoscale or microscale BVP can be exploited for the homogenization of the mechanics of composite materials. The most widely used solution strategy for DNS is still based on the finite element method (FEM), with the FE^2 formulation (where the "2" denotes a two-scale consideration) introduced by Feyel (1999) and Kouznetsova, Brekelmans, and Baaijens (2001) used for the computational scale-bridging. Alternative fully computational techniques for multiscale problems are based on the Fast Fourier Transformation (FFT), pioneered by Moulinec and Suquet (1998) and Moulinec and Suquet (1994). FFT homogenization approaches make use of the assumption of structural periodicity and the solution of convolution theorems based on the Green's function transformed into the spatial frequency space. Fully computational methods, both based on FE^2 or FFT, allow for a precise spatial discretization, referred to as mesh, of the actual composite microstructure, that respects any structural features and allows for a modeling of structures with unlimited complexity. Mechanical responses are computed locally at each integration point of the mesh (Gauss points) by the associated constitutive relations. The homogenized RVE response, also referred to as full-field solution, follows as the averaged solution of the BVP over the fully discretized RVE integration domain. However, complex heterogeneous microstructures or material behavior may require very fine discretizations or basis functions of higher order, implying extremely high numbers of degrees of freedom (DOF, implied by the number of nodes belonging to the mesh) and immensely large integration domains (given by the number of Gauss points), and therefore the requirement of massive computational power or time to achieve the macroscopic numerical solution. Moreover, strong local distortions of the mesh, occurring under complex loading conditions, can lead to invalid or not converging solutions. For these reasons, even though DNS allow for a very precise approach of structural problems, they may exceed computational capabilities and numerical limitations in cases of complex or highly nonlinear problems.

1.1.2 Reduced homogenization schemes

The objective to reduce the computational efforts of complex multiscale problems, while maintaining the ability to accomplish accurate predictions, has motivated the development of reduced models and *surrogate models*, with computationally much lighter solution stages in comparison to full-field DNS. The estimation of macroscopic responses of materials by taking into account microscopic processes using an underlying reduction scheme will in this work be referred to as *reduced homogenization* (RH). In structural mechanics, the reduced homogenized mechanical response of a material can be achieved through different procedures. While it is mentioned that intersections between the approaches exist, some of the bases to build the surrogate models are named in the following:

1. The approximation of micromechanics-based *analytical scale-couplings* between microscopic and macroscopic mechanical fields through spatial decompositions by means of clustering techniques. This kind of RH approaches will be referred to as *clustering analysis based homogenization* (CAH).

2. Reduced order models, using a complexity-reduction from full-field solutions by a restriction of the space of possible solution fields. Typically, methods like the proper orthogonal decomposition (POD) are used to select the main components of the displacement fields.

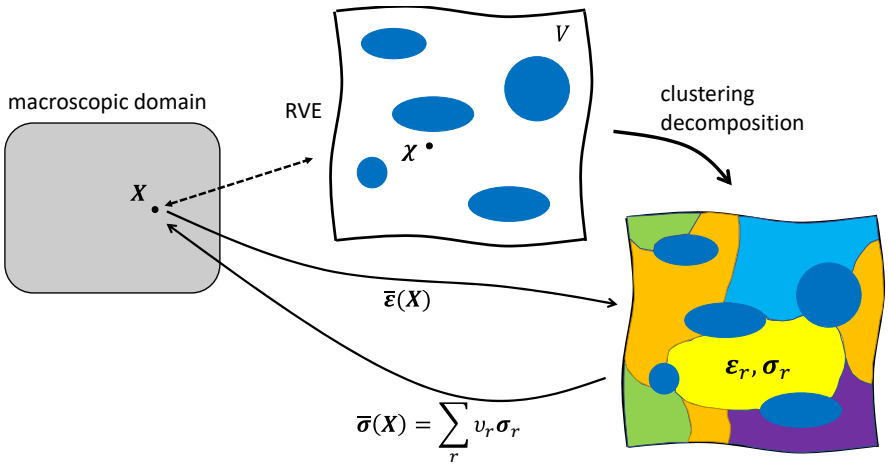

FIGURE 1.6: Schematic multiscaling by CAH: The RVE, representing the macroscopic material point $\boldsymbol{X}$, is decomposed into the subdomains by a clustering technique. During the solution stage of the BVP stated through $\bar{\boldsymbol{\varepsilon}}(\boldsymbol{X})$, the subdomains r have uniform fields of variables. The homogenized stress $\bar{\boldsymbol{\sigma}}(\boldsymbol{X})$ is the result of an averaging over the subdomains.

3. Various kinds of *data-driven* approaches, replacing physics-based constitutive relations by statistical regression algorithms and machine learning procedures to directly predict homogenized behaviors or to estimate potentials that allow deriving the homogenized response.

The first class of RH approaches, the CAH schemes, represent physically-motivated models, built on analytical micromechanical models that rely on spatial concentration functions and influence functions, expressed by spatial convolution theorems. The solution of these convolution theorems as a full-field approach would be much more computationally challenging than DNS using FEM. Therefore, the problems are reduced by a consideration of *piecewise uniform fields*, or average fields, of deformation and internal variables, firstly considered by Dvorak (1990). To be determined are the averaged interactions between the regions with uniform fields, referred to as subdomains. The characteristic of piecewise uniform fields has similarities to MFH approaches, built on the assumption of per-phase uniform fields. However, unlike the MFH, the actual RVE can be decomposed into more than one subdomain per phase. The spatial subdomains are achieved by a decomposition of the original mesh for the actual composite RVE structure, and the interaction functions are estimated through DNS in the so-called offline stage. Therefore, the model reduction is accomplished as a reduction from the degrees of freedom (DOF) of a full-field problem towards the number of DOF represented by the strain tensors of the subdomains. The integration domain is reduced from the number of Gauss points of a full-field problem towards the number of subdomains of the reduced scheme. The CAH reduction technique built on DNS of the actual composite structure in the offline stage allows to neglect any microstructural pre-assumptions. The pioneering approach for the piecewise uniform field homogenization is the *Transformation Field Analysis* (TFA) by Dvorak (1992). The analytical TFA algorithm is based on the separation of elastic and inelastic fields (referred to as eigenfields) and elastic interaction functions inside the heterogeneous medium. Alternative descriptions of the micromechanics in heteroge-

neous composite media make use of the assumption of the (statistical) homogeneity of the medium and the *Lippmann-Schwinger equation* (Kröner, 1978; Lippmann and Schwinger, 1950), considering local polarization stress fields (Eshelby, 1957; Hashin and Shtrikman, 1962, 1963). Polarization stresses are quantified as the deviations between local stress fields and the stress field that would exist in a *homogeneous reference medium*. The first CAH approach based on the Lippmann-Schwinger equation is the self-consistent clustering analysis (SCCA) by Liu, Bessa, and Liu (2016) and Liu, Fleming, and Liu (2018). In the SCCA approach, the reference medium is assumed to be isotropic, and its stiffness can be adapted during inelastic deformation by computing the instantaneous homogenized tangential Lamé parameters. The influence functions for the SCCA algorithm are computed analytically. An approach similar to the SCCA is the Hashin-Shtrikman (HS) type analysis (Cavaliere, Reese, and Wulfinghoff, 2020; Wulfinghoff, Cavaliere, and Reese, 2018), relying on piecewise uniform fields and the integration of an isotropic secant reference stiffness. In this method, the influence functions are determined numerically by pre-simulations. A constant Poisson ratio of the reference medium is assumed in order to achieve a simple scaling of the reference stiffness. Originally implemented for the modeling of nonlinear elastic materials behavior without the evolution of internal state variables, the HS type analysis was later applied to elasto-plastic materials by Castrogiovanni et al. (2021).

The typical issue encountered using the piecewise uniform approximations of analytical micromechanical models is the loss of the precise capture of the physics in the CAH model. Considering analyses of composites with inelastically deforming material phases, the loss of physics is represented by the inability to capture highly localized inelastic processes when using piecewise uniform fields of variables with spatial decompositions much coarser than high fidelity discretizations used for DNS. In the particular case of not sufficiently captured localized inelastic effects, homogenization schemes using piecewise uniform approximations lead to typically overstiff predictions of the response of the composite. In this thesis, we improve the convergence of the TFA with an increasing number of subdomains towards DNS results by using an enhanced inelasticity based subdomain decomposition and corrections estimated from micromechanical inelastic field fluctuations (Spilker et al., 2022). In this way, the CAH model contains more information of the actual physics of the nonlinear problem, leading to more accurate computed responses.

Addressing the issue of overstiff homogenized responses relying on piecewise uniform field approximations, Michel and Suquet (2003) and Michel and Suquet (2004, 2009) introduced the non-uniform TFA (NTFA) and accomplished the goal to achieve better estimates for the composite mechanical response by extending the TFA from the consideration of piecewise uniform fields of internal variables towards an integration of totally non-uniform plastic fields. The non-uniform fields are represented by a number of dominant plastic modes acting as global shape functions, extracted from inelastic offline simulations. The mode activity in the online stage was controlled by and restricted to basic evolution laws. The global NTFA was extended to the computation of evolution equations of internal variables derived from variational principles (Fritzen and Leuschner, 2013), allowing the use of the NTFA for all generalized standard material (GSM) classes, comprising all kinds of material behavior which can be defined through an elastic energy and a dissipation potential. Subsequently, Michel and Suquet (2016) incorporated the use of second-order potentials (Michel and Suquet, 2016) for the NTFA. Based on the NTFA considering a number of global inelastic modes, a strategy was introduced building on

a non-uniform distribution of internal variables over selected subdomains (Sepe, Marfia, and Sacco, 2013). Only elastic offline simulations are required, but evolution equations during the online stage are evaluated at all microscopic integration points resulting in significantly increased computational efforts. A further development incorporates the use of stress instead of inelastic strain shape functions in each subdomain and the solution of weak-form relations for the subdomains, reducing computational requirements for the online stage (Covezzi et al., 2016). A recent extension of this piecewise non-uniform TFA using global inelastic modes combines it with the domain decomposition using a statistical clustering approach based on different deformation conditions (Ri, Hong, and Ri, 2021). The computed overall behavior of the RVE follows purely from the constitutive relations in the subdomains, allowing the computation of the mechanical response for all kinds of heterogeneous material systems.

The second class of RH approaches is based on the application of POD on various snapshots of displacement fields recorded under certain loading conditions applied on the fully discretized composite RVE. The POD procedure extracts the principle components of the entirety of the considered displacement fields, which define the most essential spatial modes of the deformation fields inside the material. Extracting and focusing on the dominant patterns of the displacements fields, the nodes of the mesh are restricted to a reduced space of possible displacements. In this manner, the POD reduces the complexity of the simulations towards a reduced number of allowed displacement modes. However, constitutive equations are still to be solved at all the integration points of the original mesh, meaning that they do not lead to a reduction of the integration domain. This led to the additional development of reduced integration domains (Hernández et al., 2014; Ryckelynck, 2009). Reduced models based on POD and the reduction of the integration domain are called hyper-reduced order models (HPROM).

The third considered class of RH approaches bases on the abundance of available data and the use of high computational capabilities to store and analyse high amounts of these data. The characteristic of numerical solutions based on learning algorithms using various input data instead of physical constitutive laws has established the term of data driven approaches. These approaches include the use of statistical regression to create data-based constitutive relations as well as the application of artificial neural networks (ANNs) and deep learning techniques. Using an available training set of numerical, and possibly experimental, data, the neural network is trained through a forward feeding and backward propagation scheme and adjusting certain fitting parameters. First homogenization of nonlinear elastic materials using ANNs as surrogates for constitutive relations was practised by Le, Yvonnet, and He (2015). Irreversible behaviours could be represented by recurrent neural networks (Gorji et al., 2020; Mozaffar et al., 2019; Wu et al., 2020). Liu and Wu (2019) and Liu, Wu, and Koishi (2019) have developed the so-called deep material network (DMN) approach based on analytical micromechanical models, such as laminate theory, defining mechanistic building blocks which form a binary hierarchical topological structure. Elastic offline simulations define the parameters of the building blocks, so that the DMN can be used to predict nonlinear responses. The good handling of this extrapolation was theoretically explained by Gajek, Schneider, and Böhlke (2020). Nguyen and Noels (2022b) have provided an efficient implementation, Wu, Adam, and Noels (2021) have used complex micromechanical models such as MFH in the mechanistic building blocks for woven composite materials, and Nguyen and Noels (2022a) have replaced the micromechanical models in the building blocks by interactions which obey

the Hill-Mandel condition, i.e. the consistency of the energy variation on both scales.

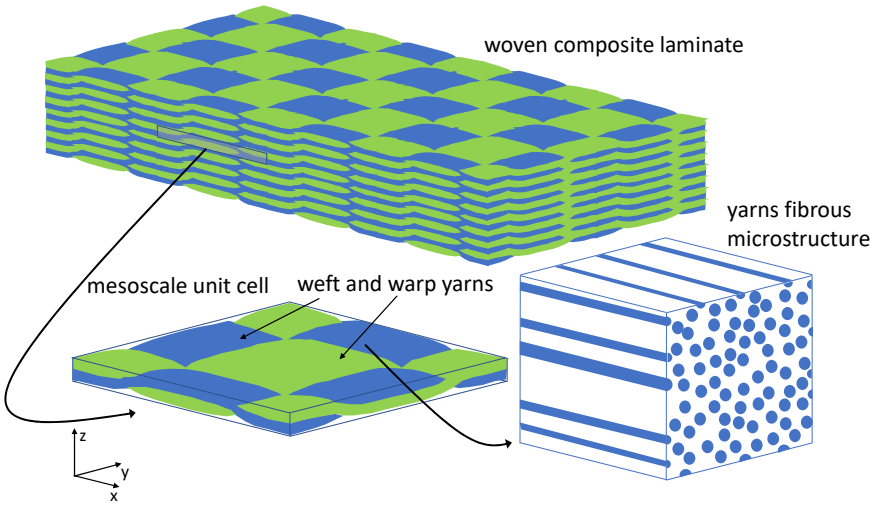

FIGURE 1.7: Schematic demonstration of a woven composite laminate considering the associated scales. A mesoscopic unit cell is extracted from the woven laminate. The yarns of the woven composite have a fibrous microstructure.

1.2 Textile composites

Textile composites are composite structures designed to provide high resistance to complex or multi-axial loading conditions and are therefore used in a broad range of domains, from functional clothing to high performance aerospace applications. In order to resist multi-axial loading conditions, the structures possess complex architectures accomplished by specific manufacturing processes. Many structural textile composite laminates are built by layers, called plies, of particularly arranged high-stiffness yarns embedded in a matrix material. In the context of multiscale materials, the designed textile structure is referred to as the composites mesostructure, with the yarns microstructure constituted by fibers of high stiffness in the same embedding matrix material. The focus of this work is the most classic type of textile composites, manufactured by a weaving process of the yarns. The *woven composites* considered in this work have a mesostructure built by orthogonally arranged, fibrous yarns (Fig. 1.7).

Considering the mechanics of textile or woven composites produced by fiber-based yarns, the evaluation of the structural behavior involves more than one scale. On the one hand, the mesoscale mechanics are characterized by the designed composite architecture of the yarns. The yarns on the other hand, can not be considered homogeneous either. As composite materials on the microscale, the yarns mechanical behavior depends on the microstructure and the material properties associated to fibers and matrix. The fibers in the yarns follow the exact yarn orientations, involving the vertical inclinations due to the woven structure. The fibers have therefore globally non-uniform orientations, implying non-uniform elastic and inelastic responses of the yarns, can however be locally treated as

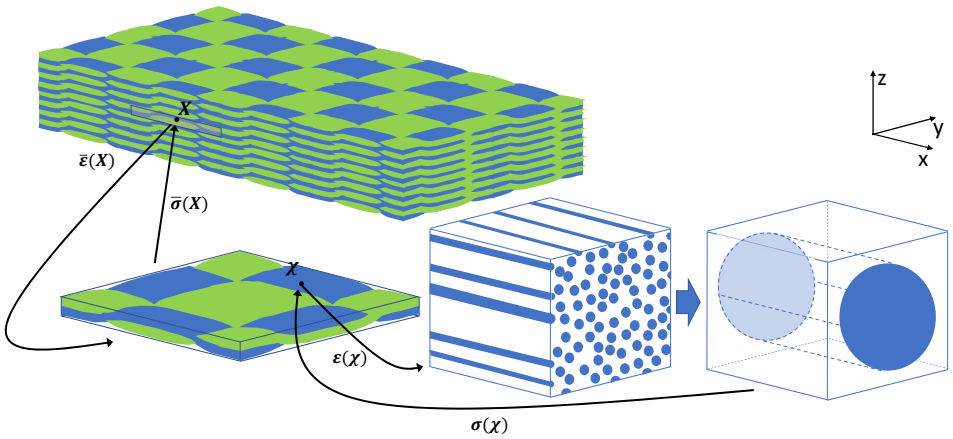

FIGURE 1.8: Schematic demonstration of a mechanical problem of a woven composite considering the associated scales. The deformation state at a certain location inside a structural woven composite $\bar{\boldsymbol{\varepsilon}}(\boldsymbol{X})$ states the boundary problem for the unit cell, representing the mesostructure. The microscopic material points of the yarns in the mesostructural cell are locally considered as a UD fiber composite material. Following from the local deformation at the yarns material points $\boldsymbol{\varepsilon}(\boldsymbol{\chi})$, the MFH is used for the computation of the homogenized response $\boldsymbol{\sigma}(\boldsymbol{\chi})$. The overall stress response of the woven unit cell $\bar{\boldsymbol{\sigma}}(\boldsymbol{X})$ follows from the consideration of the complete local field $\boldsymbol{\chi}$.

UD. In summary, the structural, or macroscopic, behavior of this kind of composite materials is affected by mechanical processes on both mesoscopic and microscopic scales. Consequently, textile composite materials may be classified as *three-scale materials*. Spilker et al. (2022, article submitted) implemented an approach for the microscale-mesoscale-macroscale bridging for woven composites by means of a two-step homogenization using CAH and MFH (Fig. 1.8).

1.3 Objectives of this thesis

In this thesis, the performance of reduced analytical micromechanical models used as CAH schemes is investigated, focusing on the TFA and HS algorithms. These models allow immense potentials for computational savings. The TFA was shown to provide homogenized composite responses in accordance with full-field homogenization techniques when the heterogeneity of the inelastic fields can be sufficiently represented by the spatial subdomain decomposition (Dvorak, Bahei-El-Din, and Wafa, 1994). Furthermore, the TFA with its characteristic to purely rely on the single phase properties, is valid for any microstructural configurations. On the one hand, the HS approach was shown to provide faster convergence towards DNS (Castrogiovanni et al., 2021). On the other hand, relying on an isotropic reference medium, its applicability for generic anisotropic materials is to be investigated. The classical issue of overstiff composite predictions of CAH due to a loss of physics, or more precisely, a loss of the capture of highly localized phenomena, is tackled in this work with the goal to improve the rate of convergence towards the predictions delivered by DNS. The problem of inaccurate results using reasonable numbers of subdomains for the spatial decomposition is approached as following:

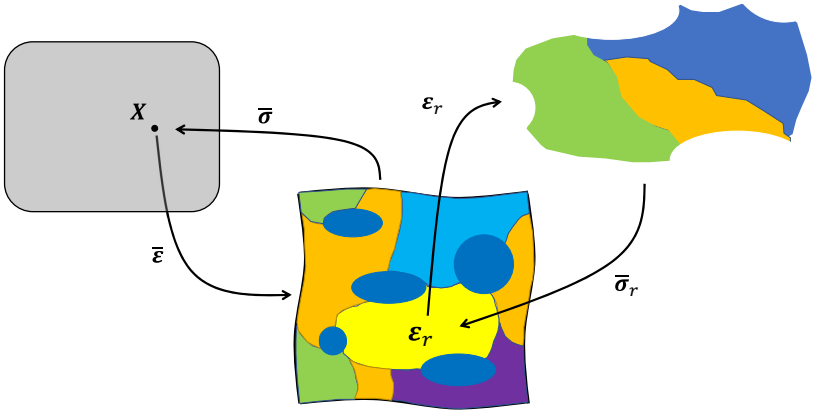

FIGURE 1.9: Multi-step CAH procedure presented for two scale levels: the subdomains of the RVE are again decomposed into sub-subdomains. The strains $\boldsymbol{\varepsilon}_r$ of the RVE subdomains state BVPs for the lower scale level. The solution of the BVP on the lower scale level results in the homogenized stress $\boldsymbol{\sigma}_r = \overline{\boldsymbol{\sigma}}_r$.

- The implementation of enhanced spatial decompositions with respect to classical discretizations that rely on elastic deformation patterns. A number of inelastic deformation conditions is selected, representing typical inelastic deformation patterns in a specific RVE. Based on the computed deformation fields, a k-means clustering technique is used for the partitioning of the RVE into subdomains. Although the spatial decomposition relies on a limited number of simple loading modes, the goal is the extraction of inelastic patterns occurring under various loading conditions and therefore to allow the modeling of more complex and history-dependent loading.

- Further improvements of the capture of localized effects by computing and taking into account fluctuations of the inelastic fields inside the subdomains in the form of a correction factor.

- Modification of the HS approach from a secant towards a tangent formulation in order to allow modeling composite responses under cyclic loading.

- Proposal of a novel multi-step CAH through downscaling and upscaling techniques, allowing for an improved capture localized effects. Implemented is a two-step TFA approach (displayed in Fig. 1.9), where the TFA is used to solve the strain localization on the higher scale level. The strain of one subdomain states a BVP for the underlying subdomains, that is again solved by the TFA algorithm. This procedure can be extended towards the multi-step scaling technique.

The implemented approaches for the enhanced convergence of piecewise uniform field homogenization schemes were tested for various two-dimensional material microstructures and material systems.

With a subdomain decomposition that aims to accurately respect different inelastic patterns in a material, the number of possibly considered inelastic modes cannot be extended infinitely. Consequently, the selection of only a few inelastic modes is of particular interest for composite materials with finite numbers of possible deformation patterns.

One type of materials that accommodate a finite range of possible deformation modes are composite structures with arranged meso- or microstructures, as are textile composites. Following the assumption that the CAH schemes relying on piecewise uniform fields may have a good applicability for woven composite structures, the TFA and HS approaches with underlying inelasticity-based spatial decompositions are used for the reduced scale bridging of the mechanics of woven composite structures. The RH of woven composite structures was treated in previous works, Han et al. (2020) and Wu, Adam, and Noels (2021, e.g.), where Han et al. (2020) investigated the woven composite by the another CAH approach, the SCCA mentioned above. As woven composite materials are considered as three-scale materials, the prediction of the macroscopic response of biaxial woven composites is accomplished by a *two-step homogenization* (Fig. 1.8), exploiting the strengths of two different homogenization techniques for an efficient modeling:

- Physics-based scale-coupling algorithms approximated by piecewise uniform fields allow for the consideration of complex and anisotropic structures. Therefore, it is made use of the CAH approaches based on either the TFA or the HS formulations for the mesoscopic to macroscopic homogenization of the woven RVE.

- The non-uniform anisotropic elastic and inelastic properties of the yarn materials due to locally varying fiber orientations need to be respected by the spatial division into subdomains in order to gather only material points with similar responses in the same subdomain and therefore, guarantee valid effective responses of the particular subdomain. For this sake, an adapted subdomain decomposition designed for the RH of three-scale composite materials, built by a mesostructure containing phases with possibly fully heterogeneous microstructures, is implemented. It allows for piecewise uniform field approximations of composites with heterogeneous and anisotropic meso- and microstructures by respecting locally varying orientations of fibers or inclusions.

- Using the aforementioned new spatial decomposition, the composite yarn material can confidently be treated as a UD fiber composite per subdomain. The MFH, applicable for composites with simple microstructures and low or high inclusion volume fractions, is used for the homogenization of the yarn material and thus, the microscopic to mesoscopic scale bridging. The mesoscopic eigenstrains of the yarns required for the mesoscale to macroscale transition follow from a redefined concept for the computation of the eigenstrains, based on an incremental-secant MFH procedure on the microscale. The integration of the MFH on the microscale allows for the modeling of arbitrary inelastic loading conditions, without the requirement of a predefined unit cell yield criterion (Han et al., 2020).

1.4 Outline

This thesis is organized as follows: In Section 2, the different homogenization techniques considered in this work are presented in detail. This contains the conditions for the scale transition in full-field homogenization techniques as well as different descriptions of the micromechanics in heterogeneous solids and RH approaches that base on the spatial discretization of these micromechanical algorithms, here referred to as CAH. This work focuses on two CAH algorithms, comprising of the TFA and a modified tangent formulation

of the HS type analysis. Furthermore, the MFH approach integrated for the modeling of the woven composite is introduced. Numerical procedures for the iterative solution of the BVPs through the CAH and MFH approaches are presented. In Section 3, all numerical steps to achieve the solution for the mechanical RVE response by using the CAH techniques are presented in detail. The elasticity-based and inelasticity-based reductions from a discretized full-field problem to a reduced problem using the TFA and the HS approaches are described. A new approach is proposed for the incorporation of numerically determined plastic field fluctuations inside the subdomains in order to achieve improved homogenized responses, making use of statistical measures of plastic field inhomogeneities gathered in the offline stage. Subsequently, the CAH results for the responses of a range of RVEs with various microstructures and containing different material systems are presented and compared to the ones following the full-field homogenization using DNS. The tangent HS approach provides generally clearly better predictions than the TFA for the response of isotropic composite RVEs. However it it shown that the method does lead to overcompliant responses of several microstructures with elevated complexity. Furthermore, the modeling capability of strongly anisotropic materials is shown to be limited using the HS approach. In contrast, the TFA is a suitable modeling technique for generic anisotropic microstructures, yet leads to typically overstiff homogenized responses due to overestimated strains accumulations in stiff elastic phases. It is shown that the TFA with a spatial decomposition that bases on inelastic micromechanical patterns achieves clearly improved inelastic responses with respect to an elasticity-based spatial decomposition for all kinds of investigated isotropic and anisotropic microstructures. Section 4 contains the three-scale bridging of the woven composite, involving an adapted clustering that respects inelastic fields and the local yarn orientation as well as the two-step homogenization procedure, comprised by CAH for the mesoscopic homogenization of the woven unit cell the and MFH for the microscopic homogenization of the yarn materials. Two-step homogenization results for various numerical tests with different complex loading conditions performed on the woven unit cell are displayed and compared to full-field homogenization results. The CAH using both the TFA and the HS algorithms, combined with the MFH, allows an accurate representation of the inelastic behavior of the woven unit cell. This is valid for all investigated complex non-proportional loading histories. In Section 5, a new strategy for the CAH of composites is proposed, basing on a multi-step upscaling and downscaling scheme. The multi-step scheme allows for an improved capture of the heterogeneous inelastic fields and at the same time the circumvention of the solution of large systems by a decoupling into sub-systems. The approach was employed for two TFA homogenization steps and details of the implementation of the offline and online stage, as well as first numerical results, are presented. With a homogenization on the lower scale level that appears ineffective at this point, it becomes obvious that further research is required in order to obtain the expected results using the two-step TFA. In Section 6, concluding remarks and potential future extensions of this work are pointed out.

1.5 Contributions

The following novelties were introduced by the work in this thesis:

- A clustering procedure to construct CAH schemes, relying on piecewise uniform field of variables, that allows to take into account actual inelastic patterns evolving in an RVE with its particular microstructure.
- A new correction approach for enhanced predictions by the TFA homogenization scheme by taking into account statistical fluctuations of inelastic fields computed by DNS.
- The modification of the HS homogenization scheme from a secant towards a tangent formulation in order to allow the modeling of cyclic loading conditions.
- A novel microscale-mesoscale-macroscale bridging technique for woven composites using two homogenization steps (Fig. 1.8), allowing the modeling of general inelastic loading conditions.
- A clustering approach for three-scale materials with underlying meso- and microstructures, that takes into account the mesoscale inelastic fields and the heterogeneous microstructural configuration.
- The proposal for a novel multi-step homogenization scheme, implemented for two homogenization steps based on the TFA formulation (Fig. 1.9). This approach is expected to allow improved modeling results while decreasing the computational effort of the clustering-based homogenization methods.

This work has directly resulted in the publication of the following articles in peer reviewed journals as main author:

- K. Spilker, V. D. Nguyen, L. Adam, L. Wu, and L. Noels. "Piecewise-uniform homogenization of heterogeneous composites using a spatial decomposition based on inelastic micromechanics". Composite Structures, June 2022.
- K. Spilker, V. D. Nguyen, L. Wu, and L. Noels. "Three-scale bridging for woven composites using homogenization techniques" (submitted article), 2022.

Moreover, this work has been presented at the following international conferences:

- K. Spilker, L. Noels and L. Wu. "Numerical Evaluation of Interaction Tensors in Heterogeneous Materials". 29th International Workshop on Computational Mechanics of Materials (IWCMM29), September 2019.
- K. Spilker and L. Noels. "Multiscale Modeling of Composites – Piecewise-Uniform Model Order Reduction". 24th International Conference on Composite Structures (ICCS24), June 2021.

Chapter 2

Homogenization of the mechanics in composite media

2.1 Introduction

Almost all existing materials have inhomogeneous compositions at certain length scales, containing alloys, natural materials like bio- or geomaterials, and designed composite materials for industrial purposes. Inhomogeneous compositions imply mismatches of the mechanical properties of the materials constituents. The overall, structural, behavior of the material is then dependent on the properties and volume fractions, shapes, distributions and sizes of the single constituents on the materials microstructure. Consequently, specific multiscale techniques, relying on the use of certain microstructural descriptors, need to be employed for an estimation of the overall behavior. While techniques for the evaluation of the response of a material with linearly-elastic constituents where developed early, the consideration of nonlinear or history-dependent responses of the microstructural constituents underlies a much higher degree of complexity. To obtain nonlinear macroscopic constitutive relations for a material is highly complex because the occurrence of history-dependent phenomena as plasticity or damage on the microscale strongly affect the overall response. In the previous and present centuries, different approaches for the evaluation of the overall response of heterogeneous, nonlinear materials were developed. Several of these nonlinear homogenization techniques, achieving the extraction of overall, or homogenized, responses of heterogeneous composite media under external influences, are presented in this section.

In the following two-scale consideration, it is referred to the upper and lower scales as the macro and microscales, respectively. One point $\boldsymbol{X}$, belonging to a macroscopic material domain, is represented by an associated microstructural domain V, required to contain all essential microscopical features and therefore referred to as the representative volume element (RVE), displayed in Fig. 1.4. The point $\boldsymbol{X}$ is then assumed to be located at the center of the volume V. The total volume of the RVE is given as

$$|V| = \int_V \mathrm{d}\boldsymbol{\chi}\,, \tag{2.1}$$

where $\boldsymbol{\chi} \in V$ denotes the microstructural domain. In a small strain setting, the macroscopic strain $\overline{\boldsymbol{\varepsilon}}(\boldsymbol{X})$ and stress $\overline{\boldsymbol{\sigma}}(\boldsymbol{X})$ are given as the volume averages over the RVE domain as

$$\overline{\boldsymbol{\varepsilon}} = \frac{1}{|V|}\int_V \boldsymbol{\varepsilon}(\boldsymbol{\chi})\mathrm{d}\boldsymbol{\chi} \tag{2.2}$$

and

$$\overline{\boldsymbol{\sigma}} = \frac{1}{|V|}\int_V \boldsymbol{\sigma}(\boldsymbol{\chi})\mathrm{d}\boldsymbol{\chi}\,, \tag{2.3}$$

where the strains are related to the displacements $\boldsymbol{u}(\boldsymbol{\chi})$ as

$$\boldsymbol{\varepsilon}(\boldsymbol{\chi}) = \frac{1}{2}\big(\nabla \otimes \boldsymbol{u}(\boldsymbol{\chi}) + \boldsymbol{u}(\boldsymbol{\chi}) \otimes \nabla\big)\,. \tag{2.4}$$

The local stresses $\boldsymbol{\sigma}(\boldsymbol{\chi}, t)$ at the time t are connected through certain constitutive relations, expressed as

$$\boldsymbol{\sigma}(\boldsymbol{\chi}, t) = f\big(\boldsymbol{\varepsilon}(\boldsymbol{\chi}, t), z(\boldsymbol{\chi}, t'), \forall t' \leq t\big)\,, \tag{2.5}$$

with the internal state variables $z(\boldsymbol{\chi}, t')$, where the dependence on the history is expressed through t' with $t' \leq t$. In the absence of dynamic effects, the local stress field needs to satisfy the force equilibrium

$$\nabla \cdot \boldsymbol{\sigma}(\boldsymbol{\chi}) = f(\boldsymbol{\chi}) \quad \forall \boldsymbol{\chi} \in V \tag{2.6}$$

at any point $\boldsymbol{\chi}$, where the Nabla operator ∇ denotes the spatial gradient and $f(\boldsymbol{\chi})$ the local body forces. On the RVE boundary ∂V, the occurring forces due to the local stress states need to conform with the applied surface traction $\boldsymbol{t}$, expressed as

$$\boldsymbol{n}(\boldsymbol{\chi}) \cdot \boldsymbol{\sigma}(\boldsymbol{\chi}) = \boldsymbol{t}(\boldsymbol{\chi}) \quad \forall \boldsymbol{\chi} \in \partial V\,, \tag{2.7}$$

where $\boldsymbol{n}$ is the outward unit normal on the boundary ∂V.

Assuming a prescribed macroscopic strain $\overline{\boldsymbol{\varepsilon}}$, following the deformation state at the macroscopic material point $\boldsymbol{X}$, the local strain field $\boldsymbol{\varepsilon}(\boldsymbol{\chi})$, the local stress field $\boldsymbol{\sigma}(\boldsymbol{\chi})$ and the macroscopic stress response $\overline{\boldsymbol{\sigma}}$ follow the solution of a boundary value problem (BVP) on the RVE, stated through $\overline{\boldsymbol{\varepsilon}}$. The problem of computational homogenization is schematically presented in Fig. 1.4, where the homogenized stress response under a prescribed macroscopic strain is extracted from the resolution of the BVP over the discretized RVE. Complementary to the averaging theorems for the strain and stress, the volume average of the internal microscopic energy must equal the macroscopic energy in order to guarantee preservation of energy between both scales. The energy consistency between two scales is provided by the Hill-Mandel condition, stated as

$$\overline{\boldsymbol{\sigma}} : \delta\overline{\boldsymbol{\varepsilon}} = \frac{1}{|V|}\int_V (\boldsymbol{\sigma} : \delta\boldsymbol{\varepsilon})\,\mathrm{d}\boldsymbol{\chi}\,. \tag{2.8}$$

In this chapter, different techniques to extract the homogenized response of an RVE are presented. Section 2.2 contains the procedure and conditions of the computational homogenization by full-field DNS. Section 2.3 presents two different micromechanical theories, providing analytical scale-coupling relations for composite media. These relations allow the adoption of CAH schemes by the assumption of piecewise uniform fields. The developed numerical solution procedures of the CAH schemes are presented. In Section 2.4, details on MFH techniques are given, focusing on the Mori-Tanaka formalism. The numerical resolution of the incremental-secant MFH scheme by Wu et al. (2013a) is presented. Section 2.5 presents the different constitutive relations of the composite material phases considered in this work. Section 2.6 contains a brief summary of the presented homogenization approaches for composite media.

2.2 Computational Homogenization

Using Direct Numerical Simulations (DNS) like the FE method, the homogenized strain-stress response of a RVE can be achieved by an integration over the local fields of a constructed microscopic domain. The local fields are results of a BVP, solved numerically over the discretized domain. In mechanical problems, the BVP is typically solved to compute the local displacement field $\boldsymbol{u}(\boldsymbol{\chi})$. In the absence of dynamic effects and body forces, the equilibrium equations

$$\begin{cases} \nabla \cdot \boldsymbol{\sigma} = 0 & \forall \boldsymbol{\chi} \in V \,, \\ \boldsymbol{n} \cdot \boldsymbol{\sigma} = \boldsymbol{t} & \forall \boldsymbol{\chi} \in \partial V \,, \end{cases} \tag{2.9}$$

at all microscopic material points $\boldsymbol{\chi}$, and the Hill-Mandel condition for the transition of scales, are to be satisfied.

Hill-Mandel condition The microscale displacement field is written under the form

$$\boldsymbol{u}(\boldsymbol{\chi}) = \overline{\boldsymbol{\varepsilon}} \cdot (\boldsymbol{\chi} - \boldsymbol{\chi}_{\text{ref}}) + \boldsymbol{u}'(\boldsymbol{\chi}) \tag{2.10}$$

where $\boldsymbol{\chi}_{\text{ref}}$ is a reference point in V and $\boldsymbol{u}'$ is the fluctuation field. Considering the definition of the homogenized strain tensor $\overline{\boldsymbol{\varepsilon}}$ (Eq. (2.2)), the fluctuation field $\boldsymbol{u}'$ should thus satisfy the condition

$$0 = \frac{1}{|V|} \int_V (\nabla \otimes \boldsymbol{u}'(\boldsymbol{\chi}) + \boldsymbol{u}'(\boldsymbol{\chi}) \otimes \nabla) \, \mathrm{d}\boldsymbol{\chi} = \frac{1}{|V|} \int_{\partial V} (\boldsymbol{n} \otimes \boldsymbol{u}' + \boldsymbol{u}' \otimes \boldsymbol{n}) \, \mathrm{d}S \,. \tag{2.11}$$

Besides, substituting Eq. (2.10) in Eq. (2.8), integrating by parts and using the equilibrium condition (2.9) allows the reformulation of the Hill-Mandel condition (2.8) as

$$\overline{\boldsymbol{\sigma}} : \delta\overline{\boldsymbol{\varepsilon}} = \frac{1}{|V|} \int_V \boldsymbol{\sigma} : \delta\boldsymbol{\varepsilon} \, \mathrm{d}\boldsymbol{\chi} = \overline{\boldsymbol{\sigma}} : \delta\overline{\boldsymbol{\varepsilon}} + \frac{1}{|V|} \int_V \boldsymbol{\sigma} : (\delta\boldsymbol{u}' \otimes \nabla) \, \mathrm{d}\boldsymbol{\chi} \,, \tag{2.12}$$

or

$$0 = \int_{\partial V} (\boldsymbol{\sigma} \cdot \boldsymbol{n}) \cdot \delta\boldsymbol{u}' \, \mathrm{d}S = \int_{\partial V} \boldsymbol{t} \cdot \delta\boldsymbol{u}' \, \mathrm{d}S \,. \tag{2.13}$$

Definition of the constrained microscale finite element problem Let $\delta\boldsymbol{u}' \in \mathcal{U}$ be a test function, where $\mathcal{U}$ is an admissible kinematic vector field subset of the minimum kinematic field $\mathcal{U}^{\min}$ satisfying Eq. (2.11), i.e.

$$\mathcal{U}^{\min} = \left\{ \delta\boldsymbol{u}' | \int_{\partial V} (\boldsymbol{n} \otimes \delta\boldsymbol{u}' + \delta\boldsymbol{u}' \otimes \boldsymbol{n}) \, \mathrm{d}S = 0 \right\} . \tag{2.14}$$

Then, the weak form of the microscale equilibrium conditions in Eq. (2.9) reads

$$\int_V \boldsymbol{\sigma} : (\delta\boldsymbol{u}' \otimes \nabla) \, \mathrm{d}\boldsymbol{\chi} = 0 \,, \quad \forall \delta\boldsymbol{u}' \in \mathcal{U} \,. \tag{2.15}$$

If $\mathcal{U} \subset \mathcal{U}^{\min}$, the resolution of this weak form always ensures Eq. (2.12) and the Hill-Mandel condition (2.8) to be satisfied. The variational statement (2.15) of the Hill-

Mandel condition was introduced by Peric et al. (2010) and Schröder, Labusch, and Keip (2016) and is practically implemented by defining specific boundary conditions on the RVE whose constraint is to satisfy Eq. (2.11), as detailed in Nguyen, Wu, and Noels (2017). In this work, we consider the Periodic Boundary Conditions (PBC), for which the admissible kinematic vector field $\mathcal{U}$ is defined by

$$\begin{aligned}\mathcal{U}^{\mathrm{PBC}} &= \big\{\boldsymbol{u}'|\boldsymbol{u}(\boldsymbol{\chi}^+)-\boldsymbol{u}(\boldsymbol{\chi}^-)=\overline{\boldsymbol{\varepsilon}}\cdot(\boldsymbol{\chi}^+-\boldsymbol{\chi}^-)\,,\\ &\qquad \forall\boldsymbol{\chi}^+\in\partial V^+ \text{ and corresponding } \boldsymbol{\chi}^-\in\partial V^-\big\}\subset\mathcal{U}^{\min}\,,\end{aligned} \tag{2.16}$$

where the parallelepiped RVE faces have been separated in opposite surfaces ∂V^- and ∂V^+. Note that the variational statement does not require the PBC to constrain directly the symmetry of the surface traction in order to satisfy the Hill-Mandel condition. This symmetry is a consequence of the microscale problem resolution as shown by considering arbitrary $\delta\boldsymbol{u}'\in\mathcal{U}^{\mathrm{PBC}}$ in Eq. (2.13). The Eq. (2.15) is completed by the PBC (2.16) and the system is solved using the constraint elimination method (Nguyen, Wu, and Noels, 2017). The fourth order macroscale material tensor $\overline{\mathbb{C}}^{\mathrm{alg}}=\partial\overline{\boldsymbol{\sigma}}/\partial\overline{\boldsymbol{\varepsilon}}$ can be extracted from this resolution. It is noted that $\overline{\mathbb{C}}^{\mathrm{alg}}$ is not equal to the volume average of the local stiffness field $\mathbb{C}^{\mathrm{alg}}(\boldsymbol{\chi})$ in the case of non-uniform strain distributions over the RVE.

The base for the computational homogenization of finite domains was set up by the work done by Geers, Kouznetsova, and Brekelmans (2010), Peric et al. (2010), and Saeb, Steinmann, and Javili (2016). The consideration of volume elements with sizes below the statistical representation was treated by Ostoja-Starzewski et al. (2007), where it is shown that the presented formalism for the computational homogenization of statistical volume elements still hold for smaller domains.

2.3 Micromechanics based homogenization

2.3.1 Relations in heterogeneous media

The local strain field $\boldsymbol{\varepsilon}(\boldsymbol{\chi})$ in the domain V under homogeneous loading conditions $\overline{\boldsymbol{\varepsilon}}$ may be computed using the Lippmann-Schwinger equation

$$\boldsymbol{\varepsilon}(\boldsymbol{\chi})=\overline{\boldsymbol{\varepsilon}}+\int_V\Gamma(\boldsymbol{\chi},\boldsymbol{\chi}'):\boldsymbol{\tau}(\boldsymbol{\chi}')\mathrm{d}\boldsymbol{\chi}',\quad \boldsymbol{\chi},\boldsymbol{\chi}'\in V\,, \tag{2.17}$$

with the polarization stress field

$$\boldsymbol{\tau}(\boldsymbol{\chi})=\boldsymbol{\sigma}(\boldsymbol{\chi})-\mathbb{C}:\boldsymbol{\varepsilon}(\boldsymbol{\chi}), \tag{2.18}$$

where $\mathbb{C}$ is the stiffness of a homogeneous reference medium, and the product $\mathbb{C}:\boldsymbol{\varepsilon}(\boldsymbol{\chi})$ represents the stress that would exist locally in the reference medium under the same local strain $\boldsymbol{\varepsilon}(\boldsymbol{\chi})$ (Dvorak, 2013; Kröner, 1977). Polarization stresses in a medium with a reference stiffness following the homogenized secant stiffness are schematically presented in Fig. 2.1 (for the case of a discretization into subdomains that will be introduced in Section 2.3.3).

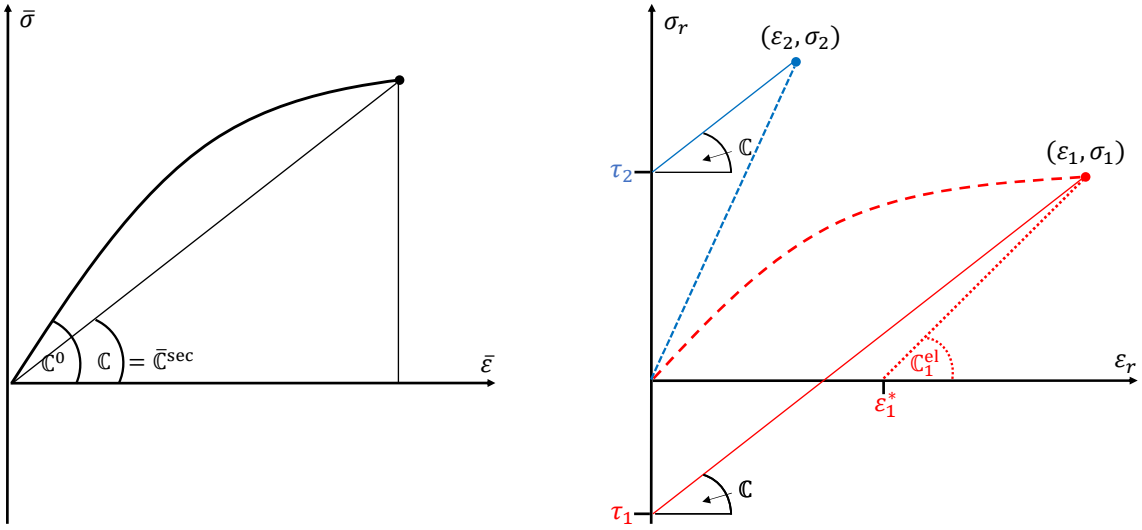

(a) (b)

FIGURE 2.1: Schematic display of the piecewise uniform field consideration with $K = 2$ subdomains, one of them with an elastic response and the other one deforming inelastically. In (a), the homogenized nonlinear $\overline{\boldsymbol{\sigma}} - \overline{\boldsymbol{\varepsilon}}$ response of the composite, with the indicated initial reference stiffness $\mathbb{C}^0 = \overline{\mathbb{C}}^{\text{el}}$ and the current secant reference stiffness $\mathbb{C} = \overline{\mathbb{C}}^{\text{sec}}$. In (b), the $\boldsymbol{\sigma}_r - \boldsymbol{\varepsilon}_r$ responses of both the elastic ($r = 1$, blue) and inelastic ($r = 2$, red) subdomains. Indicated are the eigenstrain $\boldsymbol{\varepsilon}_1^*$ only occurring in the inelastic subdomain, and the polarization stresses of both subdomains $\boldsymbol{\tau}_1$ and $\boldsymbol{\tau}_2$.

The influence of a local polarization stress field on the local strain field is expressed by means of the classical Green's operator

$$\Gamma_{ijkl} = \frac{1}{2}\left[\frac{\partial^2 G_{ik}}{\partial\chi_j \partial\chi_l} + \frac{\partial^2 G_{jk}}{\partial\chi_i \partial\chi_l}\right], \tag{2.19}$$

derived from the Green's function of the homogeneous reference medium $G(\boldsymbol{\chi}, \boldsymbol{\chi}')$, satisfying

$$\mathbb{C}_{ijkl} \frac{\partial^2 G_{kp}}{\partial\chi_l \partial\chi_j}(\boldsymbol{\chi}, \boldsymbol{\chi}') + \delta_{ip}\, \delta(\boldsymbol{\chi} - \boldsymbol{\chi}') = 0\,. \tag{2.20}$$

As the reference medium is homogeneous, the Green's interaction operator Γ is inversely proportional to the stiffness of the medium:

$$\Gamma(\boldsymbol{\chi}, \boldsymbol{\chi}') \propto \mathbb{C}^{-1}\,. \tag{2.21}$$

2.3.2 Transformation Fields

The Transformation Field Analysis (TFA) builds on the separation of elastic fields and so-called transformation fields, comprising eigenstrain fields and eigenstress fields. Local strains are expressed by

$$\boldsymbol{\varepsilon}(\boldsymbol{\chi}) = \boldsymbol{\varepsilon}^{\text{el}}(\boldsymbol{\chi}) + \boldsymbol{\varepsilon}^*(\boldsymbol{\chi})\,, \tag{2.22}$$

where $\boldsymbol{\varepsilon}^{\mathrm{el}}(\boldsymbol{\chi})$ is the local elastic strain field and $\boldsymbol{\varepsilon}^{*}(\boldsymbol{\chi})$ the eigenstrain field. Eigenstrains occurring in nonlinear material phases are schematically displayed in Fig. 2.1b (for the case of a discretization into subdomains that will be introduced in Section 2.3.3). The relation between eigenstrains and eigenstresses is given as

$$\boldsymbol{\varepsilon}^{*}(\boldsymbol{\chi}) = -\mathbb{C}^{\mathrm{el}}(\boldsymbol{\chi})^{-1} : \boldsymbol{\sigma}^{*}(\boldsymbol{\chi})\,, \tag{2.23}$$

with the local elastic stiffness tensor $\mathbb{C}^{\mathrm{el}}(\boldsymbol{\chi})$ and the local elastic compliance being its inverse. The constitutive relation in Eq. (2.5) is alternatively stated under the form

$$\begin{aligned}\boldsymbol{\sigma}(\boldsymbol{\chi}) &= \mathbb{C}^{\mathrm{el}}(\boldsymbol{\chi}) : \big(\boldsymbol{\varepsilon}(\boldsymbol{\chi}) - \boldsymbol{\varepsilon}^{*}(\boldsymbol{\chi})\big) \\ &= \mathbb{C}^{\mathrm{el}}(\boldsymbol{\chi}) : \boldsymbol{\varepsilon}(\boldsymbol{\chi}) + \boldsymbol{\sigma}^{*}(\boldsymbol{\chi})\,,\end{aligned} \tag{2.24}$$

implying that the eigenstrains $\boldsymbol{\varepsilon}^{*}(\boldsymbol{\chi})$ belong to the internal state variables $z(\boldsymbol{\chi})$ in Eq. (2.5).

If the state of the material domain V is elastic, the local strain field $\boldsymbol{\varepsilon}(\boldsymbol{\chi})$ inside the body can be expressed as

$$\boldsymbol{\varepsilon}(\boldsymbol{\chi}) = \mathbb{A}^{\mathrm{el}}(\boldsymbol{\chi}) : \overline{\boldsymbol{\varepsilon}}, \quad \boldsymbol{\chi} \in V \tag{2.25}$$

with the local elastic strain concentration tensor $\mathbb{A}^{\mathrm{el}}(\boldsymbol{\chi})$. The local stress field in Eq. (2.5) is given as

$$\boldsymbol{\sigma}(\boldsymbol{\chi}) = \mathbb{C}^{\mathrm{el}}(\boldsymbol{\chi}) : \boldsymbol{\varepsilon}(\boldsymbol{\chi}), \quad \boldsymbol{\chi} \in V. \tag{2.26}$$

The expression of the overall strain and stress in Eqs. (2.2) and (2.3) can be reformulated to

$$\overline{\boldsymbol{\varepsilon}} = \left[\frac{1}{|V|}\int_{V} \mathbb{A}^{\mathrm{el}}(\boldsymbol{\chi})\,\mathrm{d}\boldsymbol{\chi}\right] : \overline{\boldsymbol{\varepsilon}} \tag{2.27}$$

and

$$\overline{\boldsymbol{\sigma}} = \left[\frac{1}{|V|}\int_{V} \mathbb{C}^{\mathrm{el}}(\boldsymbol{\chi}) : \mathbb{A}^{\mathrm{el}}(\boldsymbol{\chi})\,\mathrm{d}\boldsymbol{\chi}\right] : \overline{\boldsymbol{\varepsilon}}, \tag{2.28}$$

the latter leading to the expression for the overall elastic stiffness

$$\overline{\mathbb{C}}^{\mathrm{el}} = \frac{d\overline{\boldsymbol{\sigma}}}{d\overline{\boldsymbol{\varepsilon}}} = \frac{1}{|V|}\int_{V} \mathbb{C}^{\mathrm{el}}(\boldsymbol{\chi}) : \mathbb{A}^{\mathrm{el}}(\boldsymbol{\chi})\mathrm{d}\boldsymbol{\chi}. \tag{2.29}$$

In the case of a vanishing overall strain $\overline{\boldsymbol{\varepsilon}} = 0$, the local strain field can be expressed as

$$\boldsymbol{\varepsilon}(\boldsymbol{\chi}) = \mathbb{D}(\boldsymbol{\chi}, \boldsymbol{\chi}') : \boldsymbol{\varepsilon}^{*}(\boldsymbol{\chi}') \quad \boldsymbol{\chi}, \boldsymbol{\chi}' \in V\,, \tag{2.30}$$

with the interaction function $\mathbb{D}(\boldsymbol{\chi}, \boldsymbol{\chi}')$, estimating the effect of an eigenstrain field $\boldsymbol{\varepsilon}^{*}(\boldsymbol{\chi}')$ on the strain at $\boldsymbol{\chi}$ (Dvorak, 1992). An existing eigenstrain field in the material domain under a vanishing overall strain $\overline{\boldsymbol{\varepsilon}} = |V|^{-1}\int_{V} \boldsymbol{\varepsilon}(\boldsymbol{\chi})\mathrm{d}\boldsymbol{\chi} = 0$ leads to the expression

$$\int_{V} \boldsymbol{\varepsilon}(\boldsymbol{\chi})\,\mathrm{d}\boldsymbol{\chi} = \int_{V} \mathbb{D}(\boldsymbol{\chi}, \boldsymbol{\chi}') : \boldsymbol{\varepsilon}^{*}(\boldsymbol{\chi}')\,\mathrm{d}\boldsymbol{\chi} = \mathbf{0}, \tag{2.31}$$

implying for arbitrary eigenstrain distributions $\boldsymbol{\varepsilon}^{*}(\boldsymbol{\chi}')$ the condition

$$\int_{V} \mathbb{D}(\boldsymbol{\chi}, \boldsymbol{\chi}')\,\mathrm{d}\boldsymbol{\chi} = \mathbf{0}\,. \tag{2.32}$$

Considering now a general mechanical problem as presented in Eq. (2.22), the resulting local strain field is given as the superposition of the two particular problems presented above

1. the material body with an overall strain $\overline{\boldsymbol{\varepsilon}} \neq 0$ in the absence of an eigenstrain field,
2. the material body under a vanishing overall strain $\overline{\boldsymbol{\varepsilon}} = 0$ and containing an eigenstrain field $\boldsymbol{\varepsilon}^*(\boldsymbol{\chi}) \neq 0$,

expressed by the superposition of the Eqs. (2.25) and (2.30), yielding

$$\boldsymbol{\varepsilon}(\boldsymbol{\chi}) = \mathbb{A}^{\mathrm{el}}(\boldsymbol{\chi}) : \overline{\boldsymbol{\varepsilon}} + \mathbb{D}(\boldsymbol{\chi}, \boldsymbol{\chi}') : \boldsymbol{\varepsilon}^*(\boldsymbol{\chi}'), \quad \boldsymbol{\chi} \in V. \tag{2.33}$$

This equation provides an analytical field relation and a coupling relation between the microscopic and macroscopic scales.

2.3.3 Piecewise uniform fields: Clustering-based homogenization

The scale-coupling formulations presented in Sections 2.3.1 and 2.3.2 can be discretized considering a division of the domain V into subdomains V_r. Average quantities over the subdomains with the volumes

$$|V_r| = \int_{V_r} \mathrm{d}\boldsymbol{\chi} \tag{2.34}$$

are considered instead of local quantities and a uniform distribution of all internal state variables is assumed inside the K subdomains denoted by the index r. The piecewise uniform fields of local variables $\beta(\boldsymbol{\chi})$, where $\beta = \boldsymbol{\varepsilon}, \boldsymbol{\varepsilon}^*, \boldsymbol{\sigma}$, are expressed by

$$\beta(\boldsymbol{\chi}) = \sum_{r=1}^{K} \beta_r \xi_r(\boldsymbol{\chi}) \tag{2.35}$$

with the per-subdomain r constant value β_r and the spatial distribution function

$$\xi_r(\boldsymbol{\chi}) = \begin{cases} 1 & , \text{ if } \boldsymbol{\chi} \in V_r \\ 0 & , \text{ otherwise.} \end{cases} \tag{2.36}$$

It follows

$$\beta_r = \frac{1}{|V_r|} \int_{V_r} \beta(\boldsymbol{\chi}) \mathrm{d}\boldsymbol{\chi}\,, \tag{2.37}$$

meaning that the uniform quantities of a subdomain equal the averaged quantities over the subdomain. The homogenized strain and stress can now be expressed as

$$\overline{\boldsymbol{\varepsilon}} = \sum_{r=1}^{K} v_r \boldsymbol{\varepsilon}_r, \tag{2.38}$$

and

$$\overline{\boldsymbol{\sigma}} = \sum_{r=1}^{K} v_r \boldsymbol{\sigma}_r, \tag{2.39}$$

where $v_r = |V_r|/|V|$ is the volume fraction of the subdomain r. The subdomain stresses $\boldsymbol{\sigma}_r$, assumed uniform per-subdomain, follow from the subdomains particular constitutive relations. The homogenized instantaneous response

$$\delta\overline{\boldsymbol{\sigma}} = \overline{\mathbb{C}}^{\text{alg}} : \delta\overline{\boldsymbol{\varepsilon}} \tag{2.40}$$

is expressed by the tangent stiffness (here referred to as the algorithmic tangent operator), computed as

$$\overline{\mathbb{C}}^{\text{alg}} = \frac{\partial\overline{\boldsymbol{\sigma}}}{\partial\overline{\boldsymbol{\varepsilon}}} = \sum_{r=1}^{K} v_r \frac{\partial\boldsymbol{\sigma}_r}{\partial\boldsymbol{\varepsilon}_r}\frac{\partial\boldsymbol{\varepsilon}_r}{\partial\overline{\boldsymbol{\varepsilon}}}\,, \tag{2.41}$$

where $\partial\boldsymbol{\sigma}_r/\partial\boldsymbol{\varepsilon}_r$ represents the instantaneous response of the subdomain r, and $\partial\boldsymbol{\varepsilon}_r/\partial\overline{\boldsymbol{\varepsilon}}$ are the instantaneous strain localizations of the phases with respect to the overall strain.

2.3.4 Piecewise uniform Transformation Field Analysis (TFA)

Considering Eq. (2.25), the strain field averaged over a certain subdomain V_r in the RVE V under the loading $\overline{\boldsymbol{\varepsilon}}$ in pure elasticity, meaning that no eigenstrain fields $\boldsymbol{\varepsilon}^*(\boldsymbol{\chi})$ exist, is given as

$$\boldsymbol{\varepsilon}_r = \mathbb{A}_r^{\text{el}} : \overline{\boldsymbol{\varepsilon}}\,, \tag{2.42}$$

where the effective strain concentration tensor of the subdomain is calculated as the average over the subdomain following

$$\mathbb{A}_r^{\text{el}} = \frac{1}{|V_r|}\int_{V_r} \mathbb{A}^{\text{el}}(\boldsymbol{\chi})\mathrm{d}\boldsymbol{\chi}\,. \tag{2.43}$$

In the case of a vanishing homogenized strain $\overline{\boldsymbol{\varepsilon}} = 0$ and assuming a uniform eigenstrain field, existing only in one subdomain s,

$$\boldsymbol{\varepsilon}^*(\boldsymbol{\chi}) = \begin{cases} \boldsymbol{\varepsilon}_s^* & \text{, if } \boldsymbol{\chi} \in V_s \\ 0 & \text{, otherwise}\,, \end{cases} \tag{2.44}$$

the local reaction strain field results in

$$\boldsymbol{\varepsilon}(\boldsymbol{\chi}) = \mathbb{D}(\boldsymbol{\chi},\boldsymbol{\chi}') : \boldsymbol{\varepsilon}^*(\boldsymbol{\chi}) = \mathbb{D}_s(\boldsymbol{\chi}) : \boldsymbol{\varepsilon}_s^*\,, \tag{2.45}$$

with no sum on s intended and with $\mathbb{D}_s(\boldsymbol{\chi})$, expressing the local strain reaction due to a uniform eigenstrain field in the subvolume V_s. The effect of the uniform eigenstrain $\boldsymbol{\varepsilon}_s^*$ on the averaged strain over a subdomain V_r is expressed by the interaction tensor $\mathbb{D}_{rs}$, computed as

$$\mathbb{D}_{rs} = \frac{1}{|V_r|}\int_{V_r} \mathbb{D}_s(\boldsymbol{\chi})\mathrm{d}\boldsymbol{\chi}\,. \tag{2.46}$$

If several uniform eigenstrain fields exist in different subdomains s, the local reaction strain field follows as the superposition of the different interaction effects

$$\boldsymbol{\varepsilon}_r = \sum_{s=1}^{K} \mathbb{D}_{rs} : \boldsymbol{\varepsilon}_s^* \,. \tag{2.47}$$

For Eq. (2.38) to remain true for all possible eigenstrain distributions over the subdomains under a homogenized strain $\overline{\boldsymbol{\varepsilon}}$, the condition in Eq. (2.32) in its reduced form

$$\sum_{r=1}^{K} v_r \mathbb{D}_{rs} = \mathbf{0} \tag{2.48}$$

is to be satisfied (Eq. (50.1) in Dvorak (1992)). The reduced general mechanical problem, containing a load $\overline{\boldsymbol{\varepsilon}}$ and the occurrence of transformation fields, results as the superposition of Eqs. (2.42) and (2.47) in

$$\boldsymbol{\varepsilon}_r = \mathbb{A}_r^{\mathrm{el}} : \overline{\boldsymbol{\varepsilon}} + \sum_{s=1}^{K} \mathbb{D}_{rs} : \boldsymbol{\varepsilon}_s^* \,. \tag{2.49}$$

The TFA scale coupling in Eq. (2.49) in its instantaneous form is given as

$$\delta\boldsymbol{\varepsilon}_r = \mathbb{A}_r^{\mathrm{el}} : \delta\overline{\boldsymbol{\varepsilon}} + \sum_{s=1}^{K} \mathbb{D}_{rs} : \delta\boldsymbol{\varepsilon}_s^* \,, \tag{2.50}$$

where the instantaneous eigenstrain $\delta\boldsymbol{\varepsilon}_s^*$ follows as

$$\delta\boldsymbol{\varepsilon}_s^* = -(\mathbb{C}_s^{\mathrm{el}})^{-1} : (\delta\boldsymbol{\sigma}_s - \mathbb{C}_s^{\mathrm{el}} : \delta\boldsymbol{\varepsilon}_s) \tag{2.51}$$

from the subdomains instantaneous response

$$\delta\boldsymbol{\sigma}_s = \mathbb{C}_s^{\mathrm{alg}} : \delta\boldsymbol{\varepsilon}_s \,, \tag{2.52}$$

where $\mathbb{C}_s^{\mathrm{alg}}$ is the algorithmic instantaneous stiffness of the subdomain s. With Eq. (2.52), the Eq. (2.51) is expressed as

$$\delta\boldsymbol{\varepsilon}_s^* = -(\mathbb{C}_s^{\mathrm{el}})^{-1} : (\mathbb{C}_s^{\mathrm{alg}} - \mathbb{C}_s^{\mathrm{el}}) : \delta\boldsymbol{\varepsilon}_s \,. \tag{2.53}$$

Instantaneous strain localizations can be formulated in a similar fashion as the elastic strain localizations in Eq. (2.42) by

$$\delta\boldsymbol{\varepsilon}_r = \mathbb{A}_r^{\mathrm{in,TFA}} : \delta\overline{\boldsymbol{\varepsilon}} \tag{2.54}$$

with the instantaneous strain concentration tensors of the TFA, $\mathbb{A}_r^{\mathrm{in,TFA}}$. A comparison of Eqs. (2.54) and (2.50) leads to the system

$$\begin{aligned} [\mathbb{A}^{\mathrm{el}}] &= [\mathbb{A}^{\mathrm{in,TFA}}] + \{\mathbb{D}_{rs} : (\mathbb{C}_s^{\mathrm{el}})^{-1} : (\mathbb{C}_s^{\mathrm{alg}} - \mathbb{C}_s^{\mathrm{el}})\} : [\mathbb{A}^{\mathrm{in,TFA}}] \\ &= \{\delta_{rs}\mathbb{I} + \mathbb{D}_{rs} : (\mathbb{C}_s^{\mathrm{el}})^{-1} : (\mathbb{C}_s^{\mathrm{alg}} - \mathbb{C}_s^{\mathrm{el}})\} : [\mathbb{A}^{\mathrm{in,TFA}}] \,, \end{aligned} \tag{2.55}$$

where "[ ]" denotes assembled $K \times 1$ vectors and "{ }" denotes square $K \times K$ matrices. The solution of the system results in the instantaneous strain concentration tensors

$$[\mathbb{A}^{\text{in,TFA}}] = \{\delta_{rs}\mathbb{I} + \mathbb{D}_{rs} : (\mathbb{C}_s^{\text{el}})^{-1} : (\mathbb{C}_s^{\text{alg}} - \mathbb{C}_s^{\text{el}})\}^{-1} : [\mathbb{A}^{\text{el}}]\,. \tag{2.56}$$

The homogenized algorithmic stiffness in Eq. (2.41) follows as

$$\overline{\mathbb{C}}^{\text{alg}} = \sum_{r=1}^{K} v_r \frac{\partial \boldsymbol{\sigma}_r}{\partial \boldsymbol{\varepsilon}_r} \frac{\partial \boldsymbol{\varepsilon}_r}{\partial \overline{\boldsymbol{\varepsilon}}} = \sum_{r=1}^{K} v_r \mathbb{C}_r^{\text{alg}} : \mathbb{A}_r^{\text{in,TFA}}\,. \tag{2.57}$$

2.3.5 Numerical Resolution of the TFA

Algorithm 1: Numerical TFA procedure at a glance: Newton-Raphson scheme at one load step for a given overall strain increment $\Delta\overline{\boldsymbol{\varepsilon}}$.

initialize: $\Delta\boldsymbol{\varepsilon}_r = \mathbb{A}_r^{\text{el}} : \Delta\overline{\boldsymbol{\varepsilon}}$ $(r = 1, ..., K)$
iterative procedure:
repeat
  for $r = 1, K$ **do**
    call constitutive relations for subdomain r to compute $\boldsymbol{\sigma}_r$, $\Delta\boldsymbol{\varepsilon}_r^*$ and $\partial\Delta\boldsymbol{\varepsilon}_r^*/\partial\boldsymbol{\varepsilon}_r$, $\mathbb{C}_r^{\text{alg}}$ (details in Section 2.5)
  end
  for $r = 1, K$ **do**
    initialize residual $\boldsymbol{F}_r = \Delta\boldsymbol{\varepsilon}_r - \mathbb{A}_r^{\text{el}} : \Delta\overline{\boldsymbol{\varepsilon}}$
    for $s = 1, K$ **do**
      add eigenstrain interaction contribution to residual: $\boldsymbol{F}_r = \boldsymbol{F}_r - \sum_s \mathbb{D}_{rs} : \Delta\boldsymbol{\varepsilon}_s^*$
      compute Jacobian matrix $\mathbb{J}_{rs} = \delta_{rs}\mathbb{I} - \mathbb{D}_{rs} : (\partial\Delta\boldsymbol{\varepsilon}_s^*/\partial\boldsymbol{\varepsilon}_s)$
    end
  end
  solve $\delta[\boldsymbol{\varepsilon}] = \{\mathbb{J}\}^{-1} : [\boldsymbol{F}]$
  update $[\Delta\boldsymbol{\varepsilon}] = [\Delta\boldsymbol{\varepsilon}] - \delta[\boldsymbol{\varepsilon}]$
until $|[\boldsymbol{F}]| <$ tol;
after convergence:
compute $\overline{\boldsymbol{\sigma}}$ and $\overline{\mathbb{C}}^{\text{alg}}$, following Eq. (2.65) and Eq. (2.70), respectively.

The incremental TFA resolution for the overall RVE response under a prescribed overall strain $\bar{\boldsymbol{\varepsilon}}$, proposed in this work (Spilker et al., 2022), is expressed as

$$\Delta\boldsymbol{\varepsilon}_r - \mathbb{A}_r^{\text{el}} : \Delta\overline{\boldsymbol{\varepsilon}} - \sum_{s=1}^{K} \mathbb{D}_{rs} : \Delta\boldsymbol{\varepsilon}_s^* = 0\,. \tag{2.58}$$

The numerical solution of this system is found using a Newton-Raphson procedure with the subdomain residuals

$$\boldsymbol{F}_r = \Delta\boldsymbol{\varepsilon}_r - \mathbb{A}_r^{\text{el}} : \Delta\overline{\boldsymbol{\varepsilon}} - \sum_{s=1}^{K} \mathbb{D}_{rs} : \Delta\boldsymbol{\varepsilon}_s^*\,, \tag{2.59}$$

iteratively solving the problem $\boldsymbol{F}_r = 0$ by the linearization

$$\boldsymbol{F}_r \rightarrow \boldsymbol{F}_r + \delta \boldsymbol{F}_r = 0. \tag{2.60}$$

Expressed as an assembled system using the $K \times 1$ block column vectors denoted by "[ ]" and the square $K \times K$ block matrices denoted by "{ }", the variational term $\delta[\boldsymbol{F}]$ follows as

$$\delta[\boldsymbol{F}] = \left\{ \frac{\partial \boldsymbol{F}}{\partial \boldsymbol{\varepsilon}} \right\} : \delta[\boldsymbol{\varepsilon}] + \frac{\partial [\boldsymbol{F}]}{\partial \overline{\boldsymbol{\varepsilon}}} : \delta \overline{\boldsymbol{\varepsilon}} = \{\mathbb{J}\} : \delta[\boldsymbol{\varepsilon}] + \frac{\partial [\boldsymbol{F}]}{\partial \overline{\boldsymbol{\varepsilon}}} : \delta \overline{\boldsymbol{\varepsilon}} \,. \tag{2.61}$$

The full Jacobian system $\{\mathbb{J}\}$ consists of the single matrices (no sum on s intended)

$$\mathbb{J}_{rs} = \frac{\partial \boldsymbol{F}_r}{\partial \boldsymbol{\varepsilon}_s} = \delta_{rs} \mathbb{I} - \mathbb{D}_{rs} : \frac{\partial \Delta \boldsymbol{\varepsilon}_s^*}{\partial \boldsymbol{\varepsilon}_s}, \tag{2.62}$$

with the derivatives of the subdomain eigenstrains by the subdomain strains $\partial \Delta \boldsymbol{\varepsilon}_s^* / \partial \boldsymbol{\varepsilon}_s$ following from the nonlinear constitutive relations of the subdomain (Section 2.5). Assuming a constant homogenized strain, implying $\delta \overline{\boldsymbol{\varepsilon}} = 0$, the result

$$\delta[\boldsymbol{\varepsilon}] = -\{\mathbb{J}\}^{-1} : [\boldsymbol{F}] \tag{2.63}$$

is used to correct the strain increments in the subdomains by

$$[\boldsymbol{\varepsilon}] = [\boldsymbol{\varepsilon}] + \delta[\boldsymbol{\varepsilon}] \tag{2.64}$$

per iteration.

Once the computed strain increments of the subdomains have converged, the homogenized stress response is given by

$$\overline{\boldsymbol{\sigma}} = \sum_{r=1}^{K} v_r \boldsymbol{\sigma}_r \,, \tag{2.65}$$

where the stresses $\boldsymbol{\sigma}_r$ follow from the constitutive relations of the subdomain r (Section 2.5). The homogenized instantaneous algorithmic tangent stiffness follows from Eq. (2.57) and is computed as

$$\overline{\mathbb{C}}^{\mathrm{alg}} = \sum_{r=1}^{K} v_r \frac{\partial \Delta \boldsymbol{\sigma}_r}{\partial \boldsymbol{\varepsilon}_r} \frac{\partial \boldsymbol{\varepsilon}_r}{\partial \overline{\boldsymbol{\varepsilon}}} \,, \tag{2.66}$$

where $\partial \Delta \boldsymbol{\sigma}_r / \partial \boldsymbol{\varepsilon}_r$ corresponds to the algorithmic operator of the subdomain $\mathbb{C}_r^{\mathrm{alg}}$, detailed in Section 2.5. The second term

$$\frac{\partial \boldsymbol{\varepsilon}_r}{\partial \overline{\boldsymbol{\varepsilon}}} = \mathbb{A}_r^{\mathrm{in,TFA}} \,, \tag{2.67}$$

representing the subdomains instantaneous strain concentration tensors $\mathbb{A}_r^{\mathrm{in,TFA}}$ (Eq. (2.56)), follows after the solution in Eq. (2.60) with Eq. (2.61) as

$$[\mathbb{A}^{\mathrm{in,TFA}}] = -\{\mathbb{J}\}^{-1} : \frac{\partial [\boldsymbol{F}]}{\partial \Delta \overline{\boldsymbol{\varepsilon}}} = \{\mathbb{J}\}^{-1} : [\mathbb{A}^{\mathrm{el}}] \,, \tag{2.68}$$

such that

$$\mathbb{A}_r^{\mathrm{in,TFA}} = \sum_{s=1}^{K} \{\mathbb{J}\}_{rs}^{-1} : \mathbb{A}_s^{\mathrm{el}} \,. \tag{2.69}$$

The resulting full expression of Eq. (2.66) amounts to

$$\overline{\mathbb{C}}^{\mathrm{alg}} = \sum_{r=1}^{K} v_r \mathbb{C}_r^{\mathrm{alg}} : \mathbb{A}_r^{\mathrm{in,TFA}} = \sum_{r=1}^{K} v_r \mathbb{C}_r^{\mathrm{alg}} : \left[\sum_{s=1}^{K} \{\mathbb{J}\}_{rs}^{-1} : \mathbb{A}_s^{\mathrm{el}} \right] . \tag{2.70}$$

The schematic overview of the numerical TFA procedure is presented in Algorithm 1.

2.3.6 Piecewise uniform Polarization Field Analysis (PFA)

Following Eq. (2.17), and assuming a uniform polarization field, existing only in one subdomain s, expressed as

$$\boldsymbol{\tau}(\boldsymbol{\chi}) = \begin{cases} \boldsymbol{\tau}_s & \text{, if } \boldsymbol{\chi} \in V_s \\ 0 & \text{, otherwise} \end{cases} , \tag{2.71}$$

simultaneously to a vanishing homogenized strain $\overline{\boldsymbol{\varepsilon}}$, the local strain field is given as

$$\boldsymbol{\varepsilon}(\boldsymbol{\chi}) = \int_{V_s} \Gamma(\boldsymbol{\chi}, \boldsymbol{\chi}') \, : \boldsymbol{\tau}(\boldsymbol{\chi}') \mathrm{d}\boldsymbol{\chi}' = \left[\int_{V_s} \Gamma(\boldsymbol{\chi}, \boldsymbol{\chi}') \mathrm{d}\boldsymbol{\chi}' \right] : \boldsymbol{\tau}_s = \Gamma_s(\boldsymbol{\chi}) : \boldsymbol{\tau}_s \,, \tag{2.72}$$

with $\Gamma_s(\boldsymbol{\chi}) = \int_{V_s} \Gamma(\boldsymbol{\chi}, \boldsymbol{\chi}') \mathrm{d}\boldsymbol{\chi}'$, expressing the local strain reaction due to a uniform polarization stress field in a certain subdomain V_s. Considering the averaged reaction over a certain subdomain V_r, the Green's interaction tensors, quantifying the effect of a uniform polarization stress field in the subdomain s on the strain in subdomain r, are defined as

$$\Gamma_{rs} = \frac{1}{|V_r|} \int_{V_r} \Gamma_s(\boldsymbol{\chi}) \mathrm{d}\boldsymbol{\chi} \,. \tag{2.73}$$

The Eq. (2.17) under the assumption of piecewise uniform fields of variables, can be expressed as

$$\boldsymbol{\varepsilon}_r = \overline{\boldsymbol{\varepsilon}} + \sum_{s=1}^{K} \Gamma_{rs} : \boldsymbol{\tau}_s = \overline{\boldsymbol{\varepsilon}} + \sum_{s=1}^{K} \Gamma_{rs} : \left(\boldsymbol{\sigma}_s - \mathbb{C} : \boldsymbol{\varepsilon}_s \right) . \tag{2.74}$$

It is noted that the Green's interaction tensors

$$\Gamma_{rs} \propto (\mathbb{C})^{-1} \tag{2.75}$$

and the stiffness $\mathbb{C}$ are properties of the assumed homogeneous reference medium. As long as the homogenized response of the medium is linear elastic, the interaction tensors and the reference stiffness are constant. During elasticity, the reference medium will have constant elastic stiffness: $\mathbb{C} = \mathbb{C}^0$, where $\mathbb{C}^0$ typically corresponds to the stiffness of the homogenized elastic medium $\overline{\mathbb{C}}^{\mathrm{el}}$. However, if the homogenized response of the medium changes, the properties of the homogeneous reference medium can be chosen to change accordingly. With the adaptive stiffness $\mathbb{C}$, representing the nonlinear homogeneous ref-

erence medium, the Green's interaction function (Eq. (2.75)) changes simultaneously (Wulfinghoff, Cavaliere, and Reese, 2018).

Similarly as seen above for the TFA, the instantaneous strain concentration tensors of the PFA can be expressed as

$$\delta\boldsymbol{\varepsilon}_r = \mathbb{A}_r^{\text{in,PFA}} : \delta\overline{\boldsymbol{\varepsilon}}\,, \tag{2.76}$$

with the subdomains instantaneous strain concentration tensors of the PFA, $\mathbb{A}_r^{\text{in,PFA}}$. The instantaneous form of Eq. (2.74) is given as

$$\delta\boldsymbol{\varepsilon}_r = \delta\overline{\boldsymbol{\varepsilon}} + \sum_{s=1}^{K} \Gamma_{rs} : \left(\delta\boldsymbol{\sigma}_s - \mathbb{C} : \delta\boldsymbol{\varepsilon}_s\right), \tag{2.77}$$

which leads, after a comparison with Eq. (2.76), to the system

$$\begin{aligned}[\mathbb{I}] &= [\mathbb{A}^{\text{in,PFA}}] - \{\Gamma_{rs} : (\mathbb{C}_s^{\text{alg}} - \mathbb{C})\} : [\mathbb{A}^{\text{in,PFA}}] \\ &= \{\delta_{rs}\mathbb{I} - \Gamma_{rs} : (\mathbb{C}_s^{\text{alg}} - \mathbb{C})\} : [\mathbb{A}^{\text{in,PFA}}]\,,\end{aligned} \tag{2.78}$$

and finally to the expression for the instantaneous strain concentration tensors

$$[\mathbb{A}^{\text{in,PFA}}] = \{\delta_{rs}\mathbb{I} - \Gamma_{rs} : (\mathbb{C}_s^{\text{alg}} - \mathbb{C})\}^{-1} : [\mathbb{I}]\,. \tag{2.79}$$

The homogenized algorithmic stiffness in Eq. (2.41) follows as

$$\overline{\mathbb{C}}^{\text{alg}} = \sum_{r=1}^{K} \upsilon_r \frac{\partial\boldsymbol{\sigma}_r}{\partial\boldsymbol{\varepsilon}_r}\frac{\partial\boldsymbol{\varepsilon}_r}{\partial\overline{\boldsymbol{\varepsilon}}} = \sum_{r=1}^{K} \upsilon_r \mathbb{C}_r^{\text{alg}} : \mathbb{A}_r^{\text{in,PFA}}\,. \tag{2.80}$$

It can be accounted in different ways for the nonlinear homogenized response of the actual composite material. The nonlinear behavior of the composite is respected by the consideration of a nonlinear homogeneous reference medium, whose stiffness can be formulated in different ways. In a total formulation, as represented by Eq. (2.74), the reference stiffness would be represented by the homogenized secant stiffness of the medium: $\mathbb{C} = \overline{\mathbb{C}}^{\text{sec}}$. Alternatively, if the homogeneous reference medium is chosen to represent the instantaneous response of the homogenized medium, the incremental formulation for the polarization field analysis,

$$\Delta\boldsymbol{\varepsilon}_r = \Delta\overline{\boldsymbol{\varepsilon}} + \sum_{s=1}^{K} \Gamma_{rs} : \left(\Delta\boldsymbol{\sigma}_s - \mathbb{C} : \Delta\boldsymbol{\varepsilon}_s\right), \tag{2.81}$$

is to be considered, where $\mathbb{C}$ corresponds to the homogenized algorithmic tangent stiffness $\overline{\mathbb{C}}^{\text{alg}}$.

2.3.7 Piecewise uniform Hashin-Shtrikman type formulation

This section introduces simplifications for the PFA (Section 2.3.6), which can be useful to adopt for the homogenization of certain types of composite material systems. The reference stiffness $\mathbb{C}$ is replaced by an isotropic (isotropized) reference stiffness

$$\mathbb{C} = \mathbb{C}^{\text{iso}} = 3\,\kappa\,\mathbb{I}^{\text{vol}} + 2\,G\,\mathbb{I}^{\text{dev}}\,, \tag{2.82}$$

with the bulk modulus κ and the shear modulus G of the reference medium, and where

$$\mathbb{I}^{\mathrm{vol}} = \frac{1}{3}\boldsymbol{I} \otimes \boldsymbol{I}, \tag{2.83}$$

$$\mathbb{I}^{\mathrm{dev}} = \mathbb{I} - \mathbb{I}^{\mathrm{vol}} \tag{2.84}$$

and $\boldsymbol{I}$ and $\mathbb{I}$ are the second and fourth order unity tensors. The isotropic elastic reference stiffness of the material $\mathbb{C}^{\mathrm{iso}}$ in Eq. (2.82) can as well be formulated as a function of the shear modulus G and the Poisson ratio of the reference medium

$$\nu = \frac{3\,\kappa - 2\,G}{2\,(3\,\kappa + G)}\,, \tag{2.85}$$

such that

$$\begin{aligned} \mathbb{C}^{\mathrm{iso}}_{kkkk} &= 2\,G\frac{1-\nu}{1-2\,\nu} \\ \mathbb{C}^{\mathrm{iso}}_{jjkk} &= 2\,G\frac{\nu}{1-2\,\nu} \\ \mathbb{C}^{\mathrm{iso}}_{jkjk} &= G \end{aligned} \tag{2.86}$$

with no sum on k or j intended. The PFA relying on an isotropic reference stiffness is referred to as the Hashin-Shtrikman (HS) type analysis (Wulfinghoff, Cavaliere, and Reese, 2018).

During elasticity, the reference medium is assumed to have the stiffness $\mathbb{C}^{0,\mathrm{iso}}$ with the entries

$$\begin{aligned} \mathbb{C}^{0,\mathrm{iso}}_{kkkk} &= 2\,G^0\frac{1-\nu^0}{1-2\,\nu^0} \\ \mathbb{C}^{0,\mathrm{iso}}_{jjkk} &= 2\,G^0\frac{\nu^0}{1-2\,\nu^0} \\ \mathbb{C}^{0,\mathrm{iso}}_{jkjk} &= G^0\,, \end{aligned} \tag{2.87}$$

with the shear modulus G^0 and the Poisson ratio ν^0 of the elastic reference medium. The Green's interaction tensors in the homogeneous elastic medium are then expressed as

$$\Gamma^0_{rs} \propto (\mathbb{C}^{0,\mathrm{iso}})^{-1}\,. \tag{2.88}$$

Once inelastic effects occur, the instantaneous response of the composite is expressed by the instantaneous isotropic stiffness $\mathbb{C}^{\mathrm{iso}}$. However, with the (non-physical) assumption of a constant Poisson ratio of the reference medium during inelastic deformation $\nu = \nu^0$, as suggested by Wulfinghoff, Cavaliere, and Reese (2018), the instantaneous reference stiffness can be achieved solely by an adaption of the instantaneous reference shear modulus

G as

$$\begin{aligned}\mathbb{C}^{\text{iso}}_{kkkk} &= 2\,G\frac{1-\nu^0}{1-2\,\nu^0}\\ \mathbb{C}^{\text{iso}}_{jjkk} &= 2\,G\frac{\nu^0}{1-2\,\nu^0}\\ \mathbb{C}^{\text{iso}}_{jkjk} &= G\,.\end{aligned} \tag{2.89}$$

With the scaling of the instantaneous reference stiffness by the instantaneous reference shear modulus G as

$$\mathbb{C}^{\text{iso}}(G) = \frac{G}{G^0}\,\mathbb{C}^{0,\text{iso}}\,, \tag{2.90}$$

the instantaneous Green's tensors during inelastic deformation of the material can then be scaled as

$$\Gamma_{rs} = \Gamma^0_{rs} : \mathbb{C}^{0,\text{iso}} : (\mathbb{C}^{\text{iso}})^{-1} = \frac{G^0}{G}\,\Gamma^0_{rs}\,. \tag{2.91}$$

Cavaliere, Reese, and Wulfinghoff (2020) and Wulfinghoff, Cavaliere, and Reese (2018) proposed the total HS formulation

$$\boldsymbol{\varepsilon}_r = \overline{\boldsymbol{\varepsilon}} + \sum_{s=1}^{K} \Gamma_{rs} : \left(\boldsymbol{\sigma}_s - \mathbb{C}^{\text{iso}} : \boldsymbol{\varepsilon}_s\right), \tag{2.92}$$

which, with the reference stiffness and the Green's tensors scaled according to Eqs. (2.90) and (2.91), respectively, can be formulated as

$$\begin{aligned}\boldsymbol{\varepsilon}_r &= \overline{\boldsymbol{\varepsilon}} + \sum_{s=1}^{K} \frac{G^0}{G}\Gamma^0_{rs} : \left(\boldsymbol{\sigma}_s - \frac{G}{G^0}\mathbb{C}^{0,\text{iso}} : \boldsymbol{\varepsilon}_s\right)\\ &= \overline{\boldsymbol{\varepsilon}} + \sum_{s=1}^{K} \Gamma^0_{rs} : \left(\frac{G^0}{G}\boldsymbol{\sigma}_s - \mathbb{C}^{0,\text{iso}} : \boldsymbol{\varepsilon}_s\right).\end{aligned} \tag{2.93}$$

The reference shear modulus is computed as

$$G = \overline{G}^{\mathbf{sec}} = \frac{\overline{\sigma}^{\text{eq}}}{3\,\overline{\varepsilon}^{\text{eq}}}, \tag{2.94}$$

where $\overline{G}^{\mathbf{sec}}$ is the total secant shear modulus of the composite. The equivalent homogenized stress and strain are computed as

$$\overline{\sigma}^{\text{eq}} = \sqrt{\frac{3}{2}\,\text{dev}(\overline{\boldsymbol{\sigma}}) : \text{dev}(\overline{\boldsymbol{\sigma}})} \tag{2.95}$$

and

$$\overline{\varepsilon}^{\text{eq}} = \sqrt{\frac{2}{3}\,\text{dev}(\overline{\boldsymbol{\varepsilon}}) : \text{dev}(\overline{\boldsymbol{\varepsilon}})}\,. \tag{2.96}$$

The use of the total secant shear modulus Eq. (2.94) has two clear disadvantages:

- if the material is being elastically deformed after a previous inelastic loading history, as the case during an unloading stage, the physical instantaneous homogenized stiff-

ness of the composite material equals the elastic stiffness of the composite. However, the isotropic reference stiffness and the Green's tensors do not equal the elastic isotropized stiffness of the material.

- during unloading stages after previous inelastic deformation, the states of a total equivalent strain $\overline{\varepsilon}^{\mathrm{eq}} = 0$ or stress $\overline{\sigma}^{\mathrm{eq}} = 0$ (in an uniaxial stress test, e.g.) can occur in the material. These cases imply singularities of the reference stiffness or of the Green's operators, prohibiting reasonable predictions for the mechanical response of the composite material in the vicinity of these points.

For this sake, an incremental HS formulation expressed as

$$\Delta\boldsymbol{\varepsilon}_r = \Delta\overline{\boldsymbol{\varepsilon}} + \sum_{s=1}^{K} \Gamma_{rs} : \left(\Delta\boldsymbol{\sigma}_s - \mathbb{C}^{\mathrm{iso}} : \Delta\boldsymbol{\varepsilon}_s\right) \tag{2.97}$$

is developed in this work. The reference shear modulus is computed as the incrementally computed secant shear modulus of the material

$$G = \overline{G}^{\mathbf{alg}} = \frac{\Delta\overline{\sigma}^{\mathrm{eq}}}{3\,\Delta\overline{\varepsilon}^{\mathrm{eq}}}\,, \tag{2.98}$$

with the incremental equivalent homogenized stresses and strains computed as in Eqs. (2.95) and (2.96) from $\Delta\overline{\boldsymbol{\varepsilon}}$ and $\Delta\overline{\boldsymbol{\sigma}}$. Since this incremental-secant formulation represents an approximated tangential shear modulus, this incremental shear modulus is denoted as $\overline{G}^{\mathbf{alg}}$. With the scaling of the reference stiffness and the Green's tensors, the incremental HS results in the formulation

$$\Delta\boldsymbol{\varepsilon}_r = \Delta\overline{\boldsymbol{\varepsilon}} + \sum_{s=1}^{K} \Gamma^0_{rs} : \left(\frac{G^0}{G}\Delta\boldsymbol{\sigma}_s - \mathbb{C}^{0,\mathrm{iso}} : \Delta\boldsymbol{\varepsilon}_s\right), \tag{2.99}$$

where the instantaneous shear modulus G is computed as presented in Eq. (2.98). In contrast to the secant formulation in Eq. (2.93), the elastic response of the reference material during instantaneous elastic loading is recovered by the incremental HS algorithm in Eq. (2.99), unaffected by any previous inelastic loading history.

2.3.8 Numerical resolution of the tangent HS type analysis

In the following, a proposed numerical solution procedure of the HS type analysis, formulated based on an isotropic homogenized tangent stiffness of the reference medium, is presented. The subdomain residuals are, according to Eq. (2.99), given as

$$\boldsymbol{F}_r = \Delta\boldsymbol{\varepsilon}_r - \Delta\overline{\boldsymbol{\varepsilon}} - \sum_{s=1}^{K} \Gamma^0_{rs} : \left(\frac{G^0}{G}\Delta\boldsymbol{\sigma}_s - \mathbb{C}^{0,\mathrm{iso}} : \Delta\boldsymbol{\varepsilon}_s\right). \tag{2.100}$$

As for the TFA (Section 2.3.5), the solution follows the linearization of the residuals

$$\boldsymbol{F}_r \to \boldsymbol{F}_r + \delta\boldsymbol{F}_r = 0, \tag{2.101}$$

Algorithm 2: Numerical incremental HS procedure using the tangent shear modulus $\overline{G}^{\mathbf{alg}}$ at a glance: Newton-Raphson scheme at one load step for a given overall strain increment $\Delta\overline{\boldsymbol{\varepsilon}}$.

initialize: $\Delta\boldsymbol{\varepsilon}_r = \Delta\overline{\boldsymbol{\varepsilon}}$ $(r = 1, ..., K)$
iterative procedure:
repeat
  for $r = 1, K$ **do**
    call constitutive relations for subdomain r to compute $\boldsymbol{\sigma}_r$ and $\mathbb{C}_r^{\text{alg}}$ (details in Section 2.5).
  end
  compute $\Delta\overline{\sigma}^{\text{eq}}$, $\Delta\overline{\varepsilon}^{\text{eq}}$ from the incremental stress $\Delta\overline{\boldsymbol{\sigma}}$ and strain $\Delta\overline{\boldsymbol{\varepsilon}}$ as in Eqs. (2.95) and (2.96) and $G = \overline{G}^{\mathbf{alg}}$ following Eq. (2.98)
  for $r = 1, K$ **do**
    initialize residual $\boldsymbol{F}_r = \Delta\boldsymbol{\varepsilon}_r - \Delta\overline{\boldsymbol{\varepsilon}}$
    for $s = 1, K$ **do**
      add polarization influence contribution to residual: $\boldsymbol{F}_r = \boldsymbol{F}_r - \Gamma^0_{rs} : \left[(G^0/G)\,\Delta\boldsymbol{\sigma}_s - \mathbb{C}^{0,\text{iso}} : \Delta\boldsymbol{\varepsilon}_s\right]$
      compute Jacobian matrix $\mathbb{J}_{rs}$ (Eq. (2.103))
    end
  end
  solve $\delta[\boldsymbol{\varepsilon}] = \{\mathbb{J}\}^{-1} : [\boldsymbol{F}]$
  update $[\Delta\boldsymbol{\varepsilon}] = [\Delta\boldsymbol{\varepsilon}] - \delta[\boldsymbol{\varepsilon}]$
until $|[\boldsymbol{F}]| <$ tol;
after convergence:
compute $\overline{\boldsymbol{\sigma}}$ and $\overline{\mathbb{C}}^{\text{alg}}$, following Eq. (2.65) and Eq. (2.114), respectively.

with the variational terms of the subdomains, in the vector notation seen above, expressed as

$$\delta[\boldsymbol{F}] = \{\mathbb{J}\} : \delta[\boldsymbol{\varepsilon}] + \frac{\partial[\boldsymbol{F}]}{\partial\overline{\boldsymbol{\varepsilon}}} : \delta\overline{\boldsymbol{\varepsilon}}\,, \tag{2.102}$$

with the full Jacobian system $\{\mathbb{J}\}$. The overall strain is assumed constant, and thus $\delta\overline{\boldsymbol{\varepsilon}} = 0$. The matrix $\{\mathbb{J}\}$ consists of the single matrices (no sum on s intended)

$$\mathbb{J}_{rs} = \frac{\partial\boldsymbol{F}_r}{\partial\boldsymbol{\varepsilon}_s} = \delta_{rs}\mathbb{I} - \Gamma^0_{rs} : \left(\frac{G^0}{G}\mathbb{C}_s^{\text{alg}} - \mathbb{C}^{0,\text{iso}}\right) + \frac{G^0}{G^2}\left[\sum_{p=1}^{K}\Gamma^0_{rp} : \Delta\boldsymbol{\sigma}_p\right] \otimes \frac{\partial G}{\partial\boldsymbol{\varepsilon}_s}\,, \tag{2.103}$$

with the instantaneous stiffness of the subdomains $\partial\Delta\boldsymbol{\sigma}_s/\partial\boldsymbol{\varepsilon}_s = \mathbb{C}_s^{\text{alg}}$. The derivative $\partial G/\partial\boldsymbol{\varepsilon}_s = \partial\overline{G}^{\mathbf{alg}}/\partial\boldsymbol{\varepsilon}_s$ is, following Eq. (2.98), computed as

$$\frac{\partial\overline{G}^{\mathbf{alg}}}{\partial\boldsymbol{\varepsilon}_s} = \frac{1}{3\,\Delta\overline{\varepsilon}^{\text{eq}}}\frac{\partial\Delta\overline{\sigma}^{\text{eq}}}{\partial\boldsymbol{\varepsilon}_s} - \frac{\Delta\overline{\sigma}^{\text{eq}}}{3\,(\Delta\overline{\varepsilon}^{\text{eq}})^2}\frac{\partial\Delta\overline{\varepsilon}^{\text{eq}}}{\partial\boldsymbol{\varepsilon}_s} \tag{2.104}$$

with

$$\frac{\partial\Delta\overline{\sigma}^{\text{eq}}}{\partial\boldsymbol{\varepsilon}_s} = \frac{3}{2}\upsilon_s\frac{\text{dev}(\Delta\overline{\boldsymbol{\sigma}})}{\Delta\overline{\sigma}^{\text{eq}}} : \mathbb{C}_s^{\text{alg}} \tag{2.105}$$

and

$$\frac{\partial \Delta\overline{\varepsilon}^{\mathrm{eq}}}{\partial \boldsymbol{\varepsilon}_s} = \frac{2}{3}\upsilon_s \frac{\mathrm{dev}(\Delta\overline{\boldsymbol{\varepsilon}})}{\Delta\overline{\varepsilon}^{\mathrm{eq}}}\,. \tag{2.106}$$

After convergence of the strain increments of the subdomains, the homogenized stress response is given by

$$\overline{\boldsymbol{\sigma}} = \sum_{r=1}^{K} \upsilon_r \boldsymbol{\sigma}_r\,. \tag{2.107}$$

The homogenized instantaneous algorithmic tangent stiffness, following from Eq. (2.80), is computed as

$$\overline{\mathbb{C}}^{\mathrm{alg}} = \sum_{r=1}^{K} \upsilon_r \frac{\partial \Delta\boldsymbol{\sigma}_r}{\partial \boldsymbol{\varepsilon}_r} \frac{\partial \boldsymbol{\varepsilon}_r}{\partial \overline{\boldsymbol{\varepsilon}}}\,, \tag{2.108}$$

with subdomains tangent operator $\mathbb{C}_r^{\mathrm{alg}} = \partial\Delta\boldsymbol{\sigma}_r/\partial\boldsymbol{\varepsilon}_r$ and the subdomains instantaneous strain concentration tensors of the HS algorithm

$$\mathbb{A}_r^{\mathrm{in,HS}} = \frac{\partial \boldsymbol{\varepsilon}_r}{\partial \overline{\boldsymbol{\varepsilon}}}\,. \tag{2.109}$$

The instantaneous strain concentration tensors follow after the solution in Eq. (2.101) with Eq. (2.102) and with

$$\frac{\partial \boldsymbol{F}}{\partial \Delta\overline{\boldsymbol{\varepsilon}}} = -\mathbb{I} + \frac{G^0}{G^2} \sum_{s=1}^{K} \Gamma_{rs}^0 : \Delta\boldsymbol{\sigma}_s \otimes \frac{\partial G}{\partial \overline{\boldsymbol{\varepsilon}}}\,, \tag{2.110}$$

as

$$[\mathbb{A}^{\mathrm{in,HS}}] = -\{\mathbb{J}\}^{-1} : \frac{\partial[\boldsymbol{F}]}{\partial \Delta\overline{\boldsymbol{\varepsilon}}} = \{\mathbb{J}\}^{-1} : \left([\mathbb{I}] - \frac{G^0}{G^2}\{\Gamma^0\} : \left[\Delta\boldsymbol{\sigma}_s \otimes \frac{\partial G}{\partial \Delta\overline{\boldsymbol{\varepsilon}}}\right]\right), \tag{2.111}$$

such that

$$\mathbb{A}_r^{\mathrm{in,HS}} = \sum_{s=1}^{K} \{\mathbb{J}\}_{rs}^{-1} : \left[\mathbb{I} - \frac{G^0}{G^2} \sum_{p=1}^{K} \Gamma_{rp}^0 : \Delta\boldsymbol{\sigma}_p \otimes \frac{\partial G}{\partial \Delta\overline{\boldsymbol{\varepsilon}}}\right], \tag{2.112}$$

where

$$\frac{\partial G}{\partial \Delta\overline{\boldsymbol{\varepsilon}}} = \frac{\partial \overline{G}^{\mathbf{alg}}}{\partial \Delta\overline{\boldsymbol{\varepsilon}}} = -\frac{2}{9}\frac{\mathrm{dev}(\Delta\overline{\boldsymbol{\varepsilon}})}{(\Delta\overline{\varepsilon}^{\mathrm{eq}})^3}\,. \tag{2.113}$$

The resulting full expression of Eq. (2.108) amounts to

$$\overline{\mathbb{C}}^{\mathrm{alg}} = \sum_{r=1}^{K} \upsilon_r \mathbb{C}_r^{\mathrm{alg}} : \mathbb{A}_r^{\mathrm{in,HS}}\,. \tag{2.114}$$

An overview of the numerical HS procedure is presented in Algorithm 2.

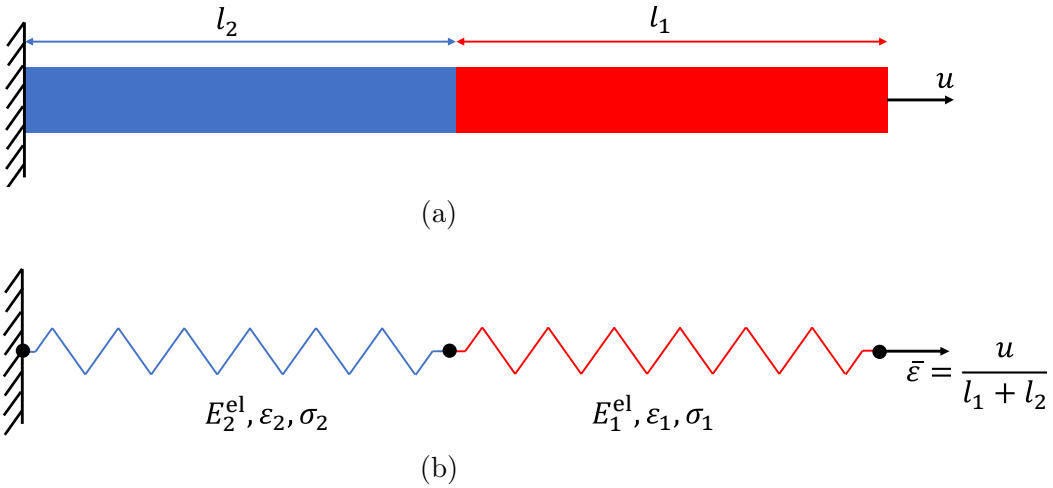

FIGURE 2.2: The (a) structure of a one-dimensional composite bar consisting of two elements referred to as elements 1 and two 2. The BC are indicated, comprised by one fixed end and an applied displacement u on the other end of the bar. In (b), the mechanical representation of the composite bar, consisting of two springs with arbitrary and independent elastic Young's moduli E_1^{el} and E_2^{el}.

2.3.9 Uniaxial nonlinear analysis

In the following simple example, a one-dimensional composite bar, consisting of two subdomains 1 and 2 with different material properties (Fig. 2.2), is numerically investigated by means of the TFA and PFA approaches. This application demonstrates the validity of both micromechanical approaches for the solution of mechanical problems. The bar is divided in two equally spaced elements, such that the volume (length) fractions of the two subdomains are given as $v_1 = v_2 = 1/2$. In the one-dimensional bar, the two couplings

$$\delta\bar{\varepsilon}(t) = v_1\,\delta\varepsilon_1(t) + v_2\,\delta\varepsilon_2(t) \tag{2.115}$$

$$\delta\bar{\sigma}(t) = \delta\sigma_1(t) = \delta\sigma_2(t) \tag{2.116}$$

between the local and global states apply, where

$$\delta\sigma_1(t) = E_1^{\mathrm{alg}}(t)\,\delta\varepsilon_1(t) \tag{2.117a}$$
$$\delta\sigma_2(t) = E_2^{\mathrm{alg}}(t)\,\delta\varepsilon_{\mathrm{II}}(t) \tag{2.117b}$$

with the tangent moduli E_1^{alg} and E_2^{alg}. Using Eqs. (2.115), (2.116) and (2.117), the following can be derived:

$$\delta\varepsilon_1(t) = \frac{E_2^{\mathrm{alg}}(t)}{v_1\,E_2^{\mathrm{alg}}(t) + v_2\,E_1^{\mathrm{alg}}(t)}\,\delta\bar{\varepsilon}(t) \tag{2.118a}$$
$$\delta\varepsilon_2(t) = \frac{E_1^{\mathrm{alg}}(t)}{v_1\,E_2^{\mathrm{alg}}(t) + v_2\,E_1^{\mathrm{alg}}(t)}\,\delta\bar{\varepsilon}(t)\,. \tag{2.118b}$$

Expressing the instantaneous strain distribution by instantaneous strain localization factors of the subdomains, A_1^{in} and A_2^{in}, as

$$\delta\varepsilon_1(t) = A_1^{\text{in}}(t)\,\delta\overline{\varepsilon}(t) \tag{2.119a}$$

$$\delta\varepsilon_2(t) = A_2^{\text{in}}(t)\,\delta\overline{\varepsilon}(t)\,, \tag{2.119b}$$

results in the formulations

$$A_1^{\text{in}}(t) = \frac{E_2^{\text{alg}}(t)}{\upsilon_1\,E_2^{\text{alg}}(t) + \upsilon_2\,E_1(t)} \tag{2.120a}$$

$$A_2^{\text{in}}(t) = \frac{E_1^{\text{alg}}(t)}{\upsilon_1\,E_2^{\text{alg}}(t) + \upsilon_2\,E_1(t)}\,. \tag{2.120b}$$

Transformation Field Analysis The strain localization factors in elasticity are, following Eq. (2.120), as

$$A_1^{\text{el}} = \frac{E_2^{\text{el}}}{\upsilon_1\,E_2^{\text{el}} + \upsilon_2\,E_1^{\text{el}}} \tag{2.121a}$$

$$A_2^{\text{el}} = \frac{E_1^{\text{el}}}{\upsilon_1\,E_2^{\text{el}} + \upsilon_2\,E_1^{\text{el}}}\,. \tag{2.121b}$$

The expressions of the uniaxial eigenstrain-strain interaction factors in the one-dimensional composite bar are given as

$$D_{11} = \frac{\upsilon_2\,E_1^{\text{el}}}{\upsilon_1\,E_2^{\text{el}} + \upsilon_2\,E_1^{\text{el}}} \tag{2.122a}$$

$$D_{21} = -\frac{\upsilon_1\,E_1^{\text{el}}}{\upsilon_1\,E_2^{\text{el}} + \upsilon_2\,E_1^{\text{el}}} \tag{2.122b}$$

$$D_{12} = -\frac{\upsilon_2\,E_2^{\text{el}}}{\upsilon_1\,E_2^{\text{el}} + \upsilon_2\,E_1^{\text{el}}} \tag{2.122c}$$

$$D_{22} = \frac{\upsilon_1\,E_2^{\text{el}}}{\upsilon_1\,E_2^{\text{el}} + \upsilon_2\,E_1^{\text{el}}}\,, \tag{2.122d}$$

with details presented in Appendix A. Following, the matrix $B^{\text{TFA}}(t)$ is considered, representing the relation

$$\begin{bmatrix} A_1^{\text{el}} \\ A_2^{\text{el}} \end{bmatrix} = \begin{Bmatrix} B_{11}^{\text{TFA}} & B_{12}^{\text{TFA}} \\ B_{21}^{\text{TFA}} & B_{22}^{\text{TFA}} \end{Bmatrix} \begin{bmatrix} A_1^{\text{in,TFA}} \\ A_2^{\text{in,TFA}} \end{bmatrix}(t)\,, \tag{2.123}$$

and therefore

$$\begin{bmatrix} A_1^{\text{in,TFA}} \\ A_2^{\text{in,TFA}} \end{bmatrix}(t) = \begin{Bmatrix} B_{11}^{\text{TFA}} & B_{12}^{\text{TFA}} \\ B_{21}^{\text{TFA}} & B_{22}^{\text{TFA}} \end{Bmatrix}^{-1} \begin{bmatrix} A_1^{\text{el}} \\ A_2^{\text{el}} \end{bmatrix}\,, \tag{2.124}$$

where $A_1^{\text{in,TFA}}$ and $A_2^{\text{in,TFA}}$ are the instantaneous strain localization factors of the subdomains, valid for the case of nonlinear behavior of the composite bar. The matrix B^{TFA} is

built with the entries

$$B_{ij}^{\mathrm{TFA}}(t) = \delta_{ij} + \frac{D_{ij}}{E_j^{\mathrm{el}}} \left(E_j^{\mathrm{alg}}(t) - E_j^{\mathrm{el}} \right). \tag{2.125}$$

Polarization Field Analysis The instantaneous polarization stress - strain interaction factors of the homogeneous reference bar (details in Appendix A) are expressed as

$$\Gamma_{11}(t) = -\frac{\upsilon_2}{\overline{E}^{\mathrm{alg}}(t)} \tag{2.126a}$$

$$\Gamma_{21}(t) = -\frac{\upsilon_1}{\overline{E}^{\mathrm{alg}}(t)} \tag{2.126b}$$

$$\Gamma_{12}(t) = -\frac{\upsilon_2}{\overline{E}^{\mathrm{alg}}(t)} \tag{2.126c}$$

$$\Gamma_{22}(t) = -\frac{\upsilon_1}{\overline{E}^{\mathrm{alg}}(t)}\,, \tag{2.126d}$$

with the homogenized instantaneous modulus of the composite bar $\overline{E}^{\mathrm{alg}}$, given by the analytical expression

$$\overline{E}^{\mathrm{alg}}(t) = \upsilon_1\, E_1^{\mathrm{alg}}(t)\, A_1^{\mathrm{in}}(t) + \upsilon_2\, E_2^{\mathrm{alg}}(t)\, A_2^{\mathrm{in}}(t) \tag{2.127}$$

and assumed to be known at any time. The matrix B^{PFA} represents the relation

$$\begin{bmatrix} \mathbb{I} \\ \mathbb{I} \end{bmatrix} = \begin{Bmatrix} B_{11}^{\mathrm{PFA}} & B_{12}^{\mathrm{PFA}} \\ B_{21}^{\mathrm{PFA}} & B_{22}^{\mathrm{PFA}} \end{Bmatrix} \begin{bmatrix} A_1^{\mathrm{in,PFA}} \\ A_2^{\mathrm{in,PFA}} \end{bmatrix} (t)\,, \tag{2.128}$$

and thus

$$\begin{bmatrix} A_1^{\mathrm{in,PFA}} \\ A_2^{\mathrm{in,PFA}} \end{bmatrix} (t) = \begin{Bmatrix} B_{11}^{\mathrm{PFA}} & B_{12}^{\mathrm{PFA}} \\ B_{21}^{\mathrm{PFA}} & B_{22}^{\mathrm{PFA}} \end{Bmatrix}^{-1} \begin{bmatrix} \mathbb{I} \\ \mathbb{I} \end{bmatrix}, \tag{2.129}$$

where $A_1^{\mathrm{in,PFA}}$ and $A_2^{\mathrm{in,PFA}}$ are the instantaneous strain localization factors of the subdomains following the PFA algorithm. The matrix B^{PFA} is built with the entries

$$B_{ij}^{\mathrm{PFA}}(t) = \delta_{ij} - \Gamma_{ij} \left(E_1^{\mathrm{alg}}(t) - \overline{E}^{\mathrm{alg}}(t) \right). \tag{2.130}$$

Bilinear mechanical analysis The subdomain 2 is assumed to deform purely-elastic, meaning that its instantaneous modulus is always

$$E_2^{\mathrm{alg}}(t) = E_2^{\mathrm{el}}\,. \tag{2.131}$$

The response of subdomain 1 is elasto-plastic with a linear hardening after its yield stress σ_1^{Y0} is exceeded, such that its instantaneous tangent modulus is given as

$$E_1^{\mathrm{alg}}(t) = \begin{cases} E_1^{\mathrm{el}}, & \text{if } \sigma_1 < \sigma_1^{\mathrm{Y0}} \\ (H_1\, E_1^{\mathrm{el}})/(H_1 + E_1^{\mathrm{el}}), & \text{if } \sigma_1 \geq \sigma_1^{\mathrm{Y0}}\,. \end{cases} \tag{2.132}$$

with the hardening modulus H_1 during plastic flow. Considered is the case of an ideally-plastic behavior of the subdomain 1, meaning that

$$\sigma_1(t) = \begin{cases} E_1^{\mathrm{el}}\,\varepsilon_1(t), & \text{if}\,\varepsilon_1 < \varepsilon_1^{\mathrm{Y}} \\ \sigma_1^{\mathrm{Y0}}, & \text{if}\,\varepsilon_1 \geq \varepsilon_1^{\mathrm{Y}} \end{cases} \tag{2.133}$$

where $\varepsilon_1^{\mathrm{Y}} = \sigma_1^{\mathrm{Y0}}/E_1^{\mathrm{el}}$ the yield strain. With a vanishing hardening modulus $H_1 = 0$, the instantaneous modulus in Eq. (2.132) results in

$$E_1^{\mathrm{alg}}(t) = \begin{cases} E_1^{\mathrm{el}}, & \text{if}\,\varepsilon_1 < \varepsilon_1^{\mathrm{Y}} \\ 0, & \text{if}\,\varepsilon_1 \geq \varepsilon_1^{\mathrm{Y}}\,. \end{cases} \tag{2.134}$$

For the one-dimensional composite bar with a response characterized by Eqs. (2.131) and (2.134) with $E_1^{\mathrm{el}} = 2000$ MPa, $\sigma_1^{\mathrm{Y0}} = 100$ MPa and $E_2^{\mathrm{el}} = 4000$ MPa under an applied overall strain of $\overline{\varepsilon} = 0.1$, the strain localization over the two elements is computed by Eqs. (2.120), (2.124) and (2.129) for the analytical reference analysis and for the TFA and PFA, respectively. Since the Young's moduli are known from Eqs. (2.131) and (2.134), the instantaneous strain concentration factors for this problem can be characterized a priori for elastic and inelastic deformation. It is presented in Fig. 2.3 that the strain localization in both subdomains computed by the analytical TFA and PFA algorithms is in accordance with the analytical strain localization given by Eq. (2.120). This example verifies the correctness of the TFA and PFA algorithms for the case of piecewise uniform fields of variables.

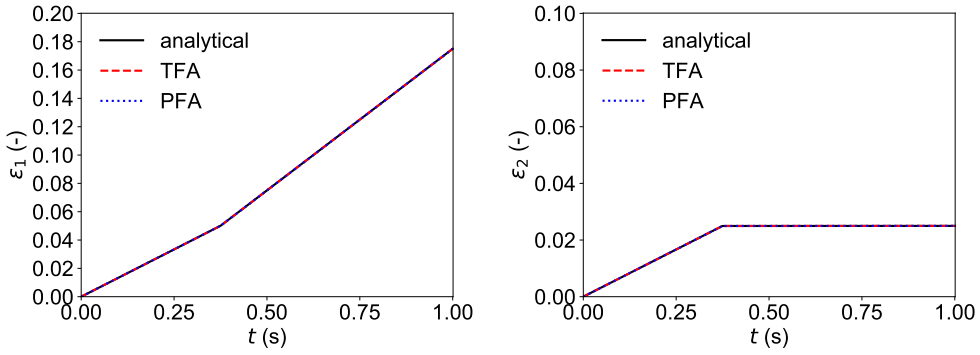

(a) (b)

FIGURE 2.3: Strain localization in both subdomains of the one-dimensional bar following the analytical approach and the analytical TFA and PFA algorithms.

2.4 Mean-Field Homogenization

Mean-Field Homogenization (MFH) approaches are used for the evaluation of the overall response of two-phase media, consisting of one inclusion (subscript II) inside a host phase

(subscript I), with the phase volume ratios v_{I} and v_{II}, where

$$v_{\mathrm{I}} + v_{\mathrm{II}} = 1\,. \tag{2.135}$$

The matrix (host) phase and the inclusion phase are represented by uniform fields of variables with average quantities, meaning that the homogenized strain $\overline{\boldsymbol{\varepsilon}}$ is expressed as

$$\overline{\boldsymbol{\varepsilon}} = v_{\mathrm{I}}\boldsymbol{\varepsilon}_{\mathrm{I}} + v_{\mathrm{II}}\boldsymbol{\varepsilon}_{\mathrm{II}} \tag{2.136}$$

and the homogenized stress as

$$\overline{\boldsymbol{\sigma}} = v_{\mathrm{I}}\boldsymbol{\sigma}_{\mathrm{I}} + v_{\mathrm{II}}\boldsymbol{\sigma}_{\mathrm{II}}\,. \tag{2.137}$$

The homogenized response depends on the structural configuration of the two-phase system, including the geometry and the responses of the single phase. In the case of a host phase with isotropic mechanical properties, the geometrical information of the two-phase medium are expressed by g_{II}, containing the volume fraction, aspect ratio and spatial orientation of the inclusion.

2.4.1 Mori-Tanaka strain localization

The distribution of the strains in Eq. (2.136) using MFH approaches is governed by particular localization rules. Here, the strain localization tensor introduced by Mori and Tanaka (1973) is considered, linking the strain distribution in both phases. The distribution of the occurring strain increments $\Delta\boldsymbol{\varepsilon}_{\mathrm{I}}$ and $\Delta\boldsymbol{\varepsilon}_{\mathrm{II}}$, using the Mori-Tanaka (MT) MFH scheme, is expressed as

$$\Delta\boldsymbol{\varepsilon}_{\mathrm{II}} = \mathbb{B}_{\mathrm{II}} : \Delta\boldsymbol{\varepsilon}_{\mathrm{I}} \tag{2.138}$$

by the MT strain localization tensor

$$\mathbb{B}_{\mathrm{II}} = f(g_{\mathrm{II}}, \mathbb{C}_{\mathrm{I}}^{\mathrm{LCC}}, \mathbb{C}_{\mathrm{II}}^{\mathrm{LCC}})\,, \tag{2.139}$$

where $\mathbb{C}_{\mathrm{I}}^{\mathrm{LCC}}$ and $\mathbb{C}_{\mathrm{II}}^{\mathrm{LCC}}(g_{\mathrm{II}})$ are the so-called linear comparison composite (LCC) operators of the phases. The LCC are stiffness operators represent the linearized nonlinear response of the composites phases. The strain localization tensor $\mathbb{B}_{\mathrm{II}}$ provides the link between the occurring strains in each of the two material phases and is expressed as

$$\mathbb{B}_{\mathrm{II}} = \{\mathbb{I} + \mathbb{S} : [(\mathbb{C}_{\mathrm{I}}^{\mathrm{LCC}})^{-1} : \mathbb{C}_{\mathrm{II}}^{\mathrm{LCC}} - \mathbb{I}]\}^{-1}\,, \tag{2.140}$$

with the fourth order unity tensor $\mathbb{I}$. The Eshelby tensor $\mathbb{S}(g_{\mathrm{II}}, \mathbb{C}_{\mathrm{I}}^{\mathrm{LCC}})$, depending on the inclusion geometry g_{II} and the stiffness operator of the host phase $\mathbb{C}_{\mathrm{I}}^{\mathrm{LCC}}$, expresses the relation of the inclusion strain $\boldsymbol{\varepsilon}_{\mathrm{II}}$ and a misfit strain $\boldsymbol{\varepsilon}_{\mathrm{II}}^{*}$ of the inclusion phase as

$$\boldsymbol{\varepsilon}_{\mathrm{II}} \;= \mathbb{S} : \boldsymbol{\varepsilon}_{\mathrm{II}}^{*} \tag{2.141}$$

under a vanishing overall stress of the composite $\overline{\boldsymbol{\sigma}} = 0$. The misfit strain $\boldsymbol{\varepsilon}_{\mathrm{II}}^{*}$ is the induced strain due to the fitting of the inclusion into the host-phase.

In linear elasticity, the LCC operators of the phases are given as the constant elastic stiffnesses of the phases: $\mathbb{C}_{\mathrm{I}}^{\mathrm{LCC}} = \mathbb{C}_{\mathrm{I}}^{\mathrm{el}}$, $\mathbb{C}_{\mathrm{II}}^{\mathrm{LCC}} = \mathbb{C}_{\mathrm{II}}^{\mathrm{el}}$. The strain localizations in the two

phases during linear elastic deformation is constant and is linked by the expression

$$\boldsymbol{\varepsilon}_{\mathrm{II}} = \mathbb{B}_{\mathrm{II}}^{\mathrm{el}} : \boldsymbol{\varepsilon}_{\mathrm{I}} \,, \tag{2.142}$$

with the constant elastic localization tensor

$$\mathbb{B}_{\mathrm{II}}^{\mathrm{el}} = \{\mathbb{I} + \mathbb{S} : [(\mathbb{C}_{\mathrm{I}}^{\mathrm{el}})^{-1} : \mathbb{C}_{\mathrm{II}}^{\mathrm{el}} - \mathbb{I}]\}^{-1} \,. \tag{2.143}$$

Considering Eq. (2.136), the strain of the host phase can, using Eq. (2.142), be expressed as

$$\boldsymbol{\varepsilon}_{\mathrm{I}} = \{\upsilon_{\mathrm{I}}\mathbb{I} + \upsilon_{\mathrm{II}}\mathbb{B}_{\mathrm{II}}^{\mathrm{el}}\}^{-1} : \overline{\boldsymbol{\varepsilon}} \,. \tag{2.144}$$

If the phases instantaneous responses, expressed by the LCC operators, change due to inelastic effects, the relation between the phase strains gets nonlinear, and therefore, $\mathbb{B}_{\mathrm{II}} \neq \mathbb{B}_{\mathrm{II}}^{\mathrm{el}}$. Different formalisms for the MT strain localization exist, depending on the formulation of the LCC operators. The tangent MFH formulation is a classical incremental strain localization rule for the modeling of nonlinear composite responses, where the LCC operators are given by the phases tangent stiffness operators $\mathbb{C}_{\mathrm{I}}^{\mathrm{LCC}} = \mathbb{C}_{\mathrm{I}}^{\mathrm{alg}}$ and $\mathbb{C}_{\mathrm{II}}^{\mathrm{LCC}} = \mathbb{C}_{\mathrm{II}}^{\mathrm{alg}}$ (Doghri and Ouaar, 2003). Doghri and Friebel (2005) considered an isotropization step of the tangent operators for improved homogenized responses. The relation of the incremental strains in matrix $\Delta\boldsymbol{\varepsilon}_{\mathrm{I}}$ and inclusion $\Delta\boldsymbol{\varepsilon}_{\mathrm{II}}$ is expressed as

$$\Delta\boldsymbol{\varepsilon}_{\mathrm{II}} = \mathbb{B}_{\mathrm{II}}^{\mathrm{tan}} : \Delta\boldsymbol{\varepsilon}_{\mathrm{I}} \,, \tag{2.145}$$

with the tangential strain localization tensor $\mathbb{B}_{\mathrm{II}}^{\mathrm{tan}} = f(g_{\mathrm{II}}, \mathbb{C}_{\mathrm{I}}^{\mathrm{alg}}, \mathbb{C}_{\mathrm{II}}^{\mathrm{alg}})$.

Alternative MFH approaches make use of affine (Molinari, Canova, and Ahzi, 1987) or secant (Berveiller and Zaoui, 1978) formulations for the strain distribution over the two phases. In this work, the incremental-secant MFH formulation is chosen (Wu et al., 2013a), where the strain distribution in the two phases is controlled by incremental-secant stiffness operators of the phases $\mathbb{C}_{\mathrm{I}}^{\mathrm{sec}}$ and $\mathbb{C}_{\mathrm{II}}^{\mathrm{sec}}$, such that $\mathbb{C}_{\mathrm{I}}^{\mathrm{LCC}} = \mathbb{C}_{\mathrm{I}}^{\mathrm{sec}}$ and $\mathbb{C}_{\mathrm{II}}^{\mathrm{LCC}} = \mathbb{C}_{\mathrm{II}}^{\mathrm{sec}}$ (Fig. 2.4). The incremental-secant operators are naturally isotropic tensors, for the case of a pressure-independent plasticity model expressed as

$$\mathbb{C}_{\Omega}^{\mathrm{sec}} = 3\kappa_{\Omega}^{\mathrm{el}}\mathbb{I}^{\mathrm{vol}} + 2G_{\Omega}^{\mathrm{sec}}\mathbb{I}^{\mathrm{dev}} \quad \Omega = \mathrm{I}, \mathrm{II} \,, \tag{2.146}$$

with the elastic bulk modulus $\kappa_{\Omega}^{\mathrm{el}}$ and the secant shear modulus $G_{\Omega}^{\mathrm{sec}}$ of the material phase Ω, deforming inelastically. The implicit isotropy of the incremental-secant stiffness allows to skip an isotropization step of the LCC operator considered by Doghri and Friebel (2005), shown to provide better predictions of the composite. The incremental-secant stiffness tensor $\mathbb{C}_{\Omega}^{\mathrm{sec}}$ follows from the phases constitutive relations, and its computation will be addressed in Section 2.5.3.

2.4.2 Incremental-secant Mori-Tanaka MFH scheme

The incremental-secant procedure is the following: First, the medium is virtually unloaded to a homogenized zero-stress state $\boldsymbol{\sigma}^{\mathrm{res}} = 0$ (Fig. 2.4a). The elastic unloading step is expressed as

$$(\overline{\boldsymbol{\varepsilon}}^{n}, \overline{\boldsymbol{\sigma}}^{n}) \xrightarrow{(\Delta\overline{\boldsymbol{\varepsilon}}^{\mathrm{u}}, \Delta\overline{\boldsymbol{\sigma}}^{\mathrm{u}})} (\overline{\boldsymbol{\varepsilon}}^{\mathrm{res}}, 0) \,, \tag{2.147}$$

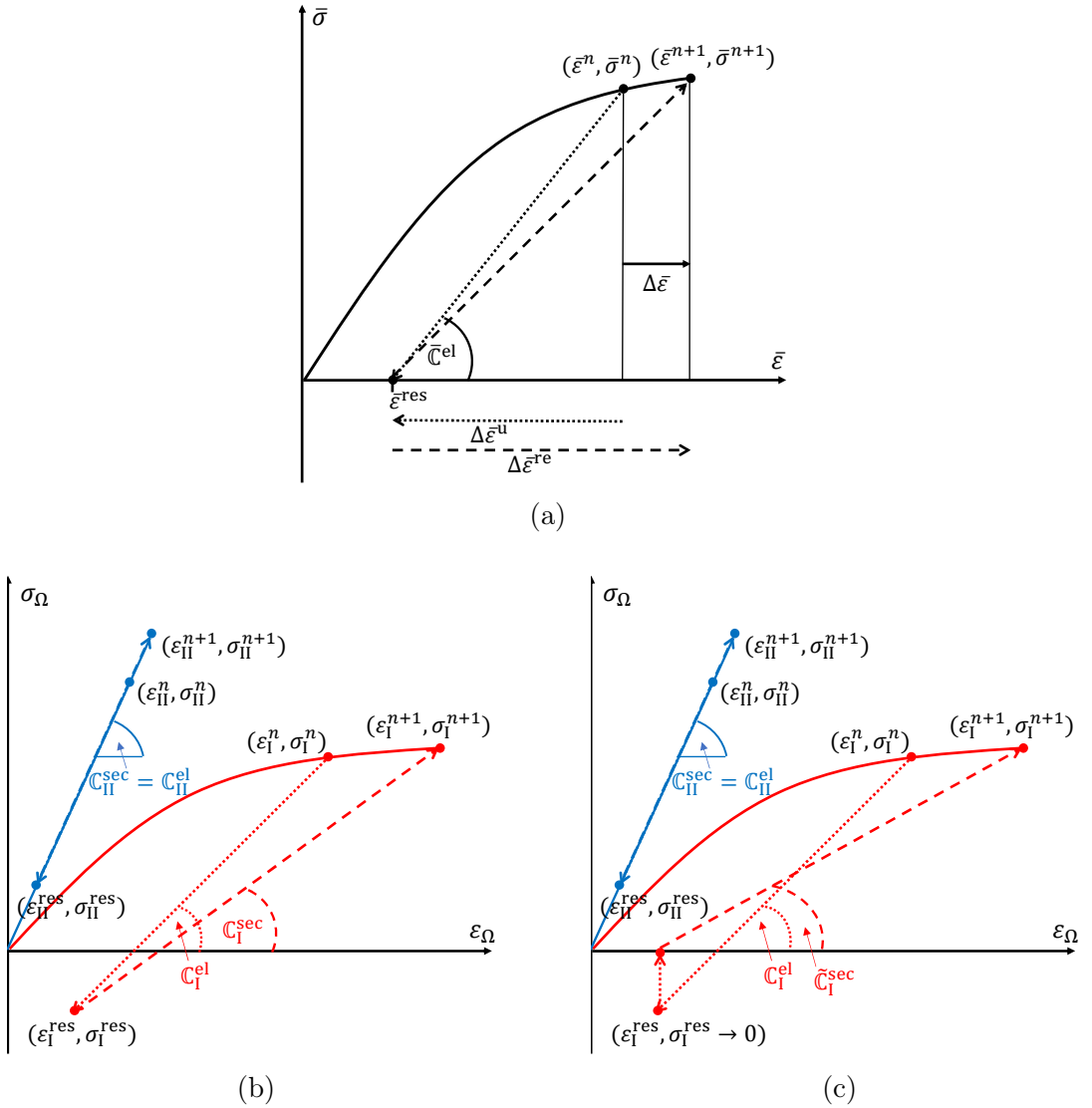

FIGURE 2.4: MFH procedure under an applied strain increment $\Delta\boldsymbol{\varepsilon}$ schematically for a two-phase composite, consisting of an elastic inclusion in an inelastic matrix: The (a) unloading-reloading procedure of the composite towards a zero-stress state (dotted) and to the new homogenized state (dashed), and (b,c) the unloading-reloading step translated to the two separate composite phases. Presented are the (b) residual incremental-secant formalism with the reloading step from the residual state towards the new state and the (c) zero-residual incremental-secant formalism, where the residual state in the inelastic matrix phase is neglected.

where the superscript "n" denotes the previous configuration, $\Delta\overline{\boldsymbol{\varepsilon}}^{\mathrm{u}}$ and $\Delta\overline{\boldsymbol{\sigma}}^{\mathrm{u}}$ are the homogenized strain and stress unloading increments, and $\overline{\boldsymbol{\varepsilon}}^{\mathrm{res}}$ is the composite strain at the virtually unloaded state. As visible in Eq. (2.147), the composite unloading stress increment is given by $\Delta\overline{\boldsymbol{\sigma}}^{\mathrm{u}} = -\overline{\boldsymbol{\sigma}}^{n}$, and since an elastic unloading is considered, the composite unloading strain increment follows as

$$\Delta\overline{\boldsymbol{\varepsilon}}^{\mathrm{u}} = (\overline{\mathbb{C}}^{\mathrm{el}})^{-1} : \Delta\overline{\boldsymbol{\sigma}}^{\mathrm{u}} = -(\overline{\mathbb{C}}^{\mathrm{el}})^{-1} : \overline{\boldsymbol{\sigma}}^{n}\,, \tag{2.148}$$

with the homogenized elastic stiffness $\overline{\mathbb{C}}^{\mathrm{el}}$ (more details given in Appendix B.1), leading to the composite residual strain

$$\overline{\boldsymbol{\varepsilon}}^{\mathrm{res}} = \overline{\boldsymbol{\varepsilon}}^{n} + \Delta\overline{\boldsymbol{\varepsilon}}^{\mathrm{u}} = \overline{\boldsymbol{\varepsilon}}^{n} - (\overline{\mathbb{C}}^{\mathrm{el}})^{-1} : \overline{\boldsymbol{\sigma}}^{n} \,. \tag{2.149}$$

Subsequently, the composite is reloaded towards the new stress state (Fig. 2.4a). The reloading increment towards the new state of the composite at the configuration "$n+1$" is represented by

$$(\overline{\boldsymbol{\varepsilon}}^{\mathrm{res}}, 0) \xrightarrow{(\Delta\overline{\boldsymbol{\varepsilon}}^{\mathrm{re}}, \Delta\overline{\boldsymbol{\sigma}}^{\mathrm{re}})} (\overline{\boldsymbol{\varepsilon}}, \overline{\boldsymbol{\sigma}}) \,, \tag{2.150}$$

where $\Delta\overline{\boldsymbol{\varepsilon}}^{\mathrm{re}}$ is the reloading strain and $\Delta\overline{\boldsymbol{\sigma}}^{\mathrm{re}}$ the reloading stress increment. The homogenized stress in Eq. (2.150), given by Eq. (2.137), follows from the stresses $\boldsymbol{\sigma}_\Omega$ of the material phases $\Omega \in \{\mathrm{I}, \mathrm{II}\}$.

Residual incremental-secant approach As the composite is virtually unloaded, the material phases, denoted by the subscript $\Omega \in \{\mathrm{I}, \mathrm{II}\}$, experience the virtual elastic unloading step

$$(\boldsymbol{\varepsilon}_\Omega^{n}, \boldsymbol{\sigma}_\Omega^{n}) \xrightarrow{(\Delta\boldsymbol{\varepsilon}_\Omega^{\mathrm{u}}, \Delta\boldsymbol{\sigma}_\Omega^{\mathrm{u}})} (\boldsymbol{\varepsilon}_\Omega^{\mathrm{res}}, \boldsymbol{\sigma}_\Omega^{\mathrm{res}}) \,, \tag{2.151}$$

with the unloading strain and stress increments $\Delta\boldsymbol{\varepsilon}_\Omega^{\mathrm{u}}$ and $\Delta\boldsymbol{\sigma}_\Omega^{\mathrm{u}} = \mathbb{C}_\Omega^{\mathrm{el}} : \Delta\boldsymbol{\varepsilon}_\Omega^{\mathrm{u}}$ towards the residual strains and stresses $\boldsymbol{\varepsilon}_\Omega^{\mathrm{res}} = \boldsymbol{\varepsilon}_\Omega^{n} + \Delta\boldsymbol{\varepsilon}_\Omega^{\mathrm{u}}$ and $\boldsymbol{\sigma}_\Omega^{\mathrm{res}} = \boldsymbol{\sigma}_\Omega^{n} + \Delta\boldsymbol{\sigma}_\Omega^{\mathrm{u}}$ (Fig. 2.4b). Unlike in the homogenized consideration of the composite, the residual stress states of the single phases $\boldsymbol{\sigma}_\Omega^{\mathrm{res}}$ do not necessarily equal a zero stress state. The phases unloading strain increments follow from the elastic mean field localization rule in Eq. (2.142) as

$$\Delta\boldsymbol{\varepsilon}_{\mathrm{II}}^{\mathrm{u}} = \mathbb{B}_{\mathrm{II}}^{\mathrm{el}} : \Delta\boldsymbol{\varepsilon}_{\mathrm{I}}^{\mathrm{u}} \,, \tag{2.152}$$

under the conditions $\Delta\overline{\boldsymbol{\varepsilon}}^{\mathrm{u}} = v_{\mathrm{I}}\Delta\boldsymbol{\varepsilon}_{\mathrm{I}}^{\mathrm{u}} + v_{\mathrm{II}}\Delta\boldsymbol{\varepsilon}_{\mathrm{II}}^{\mathrm{u}}$ and $\overline{\boldsymbol{\sigma}}^{\mathrm{res}} = v_{\mathrm{I}}\boldsymbol{\sigma}_{\mathrm{I}}^{\mathrm{res}} + v_{\mathrm{II}}\boldsymbol{\sigma}_{\mathrm{II}}^{\mathrm{res}} = 0$.

The composite constituents are, as the composite is reloaded according to Eq. (2.150), reloaded simultaneously. Subject of the incremental-secant formulation are the strain reloading increments $\Delta\boldsymbol{\varepsilon}_{\mathrm{I}}^{\mathrm{re}}$ and $\Delta\boldsymbol{\varepsilon}_{\mathrm{II}}^{\mathrm{re}}$, describing the loading from a computed residual state towards the new state (Fig. 2.4b), and linked by the incremental-secant strain localization tensor $\mathbb{B}_{\mathrm{II}}^{\mathrm{sec}} = f(g_{\mathrm{II}}, \mathbb{C}_{\mathrm{I}}^{\mathrm{sec}}, \mathbb{C}_{\mathrm{II}}^{\mathrm{sec}})$. The reloading of the phases following the reloading of the composite is expressed as

$$(\boldsymbol{\varepsilon}_\Omega^{\mathrm{res}}, \boldsymbol{\sigma}_\Omega^{\mathrm{res}}) \xrightarrow{(\Delta\boldsymbol{\varepsilon}_\Omega^{\mathrm{re}}, \Delta\boldsymbol{\sigma}_\Omega^{\mathrm{re}})} (\boldsymbol{\varepsilon}_\Omega, \boldsymbol{\sigma}_\Omega) \,. \tag{2.153}$$

Phase strains and stresses at the new configuration "$n+1$" are given as

$$\boldsymbol{\varepsilon}_\Omega = \boldsymbol{\varepsilon}_\Omega^{\mathrm{res}} + \Delta\boldsymbol{\varepsilon}_\Omega^{\mathrm{re}} \tag{2.154a}$$

$$\boldsymbol{\sigma}_\Omega = \boldsymbol{\sigma}_\Omega^{\mathrm{res}} + \Delta\boldsymbol{\sigma}_\Omega^{\mathrm{re}} \,. \tag{2.154b}$$

The relation between the matrix and the inclusion strain reloading increments is expressed following

$$\Delta\boldsymbol{\varepsilon}_{\mathrm{II}}^{\mathrm{re}} = \mathbb{B}_{\mathrm{II}}^{\mathrm{sec}} : \Delta\boldsymbol{\varepsilon}_{\mathrm{I}}^{\mathrm{re}} \,, \tag{2.155}$$

with

$$\mathbb{B}_{\mathrm{II}}^{\mathrm{sec}} = \{\mathbb{I} + \mathbb{S} : [(\mathbb{C}_{\mathrm{I}}^{\mathrm{sec}})^{-1} : \mathbb{C}_{\mathrm{II}}^{\mathrm{sec}} - \mathbb{I}]\}^{-1} \tag{2.156}$$

and the Eshelby tensor $\mathbb{S}(g_{\mathrm{II}}, \mathbb{C}_{\mathrm{I}}^{\mathrm{sec}})$. The homogenization of the reloading strain is expressed as

$$\Delta\overline{\boldsymbol{\varepsilon}}^{\mathrm{re}} = \upsilon_{\mathrm{I}}\Delta\boldsymbol{\varepsilon}_{\mathrm{I}}^{\mathrm{re}} + \upsilon_{\mathrm{II}}\Delta\boldsymbol{\varepsilon}_{\mathrm{II}}^{\mathrm{re}}\,. \tag{2.157}$$

The distribution of the phases reloading strains $\Delta\boldsymbol{\varepsilon}_{\Omega}^{\mathrm{re}}$ follows from the reloading step of the incremental-secant MFH scheme in Eqs. (2.155) and (2.156) based on the incremental-secant phase stiffnesses $\mathbb{C}_{\Omega}^{\mathrm{sec}}$ under the condition in Eq. (2.157). The phases secant operators $\mathbb{C}_{\Omega}^{\mathrm{sec}}$ and reloading stress increments

$$\Delta\boldsymbol{\sigma}_{\Omega}^{\mathrm{re}} = \mathbb{C}_{\Omega}^{\mathrm{sec}} : \Delta\boldsymbol{\varepsilon}_{\Omega}^{\mathrm{re}}\,, \tag{2.158}$$

are computed from the phases constitutive relations (Section 2.5.3). The homogenized algorithmic tangent stiffness $\overline{\mathbb{C}}^{\mathrm{alg}} = \partial\overline{\boldsymbol{\sigma}}/\partial\overline{\boldsymbol{\varepsilon}}$, following from Eq. (2.137), is computed as

$$\overline{\mathbb{C}}^{\mathrm{alg}} = \upsilon_{\mathrm{I}}\frac{\partial\boldsymbol{\sigma}_{\mathrm{I}}}{\partial\boldsymbol{\varepsilon}_{\mathrm{I}}}\frac{\partial\boldsymbol{\varepsilon}_{\mathrm{I}}}{\partial\overline{\boldsymbol{\varepsilon}}} + \upsilon_{\mathrm{II}}\frac{\partial\boldsymbol{\sigma}_{\mathrm{II}}}{\partial\boldsymbol{\varepsilon}_{\mathrm{II}}}\frac{\partial\boldsymbol{\varepsilon}_{\mathrm{II}}}{\partial\overline{\boldsymbol{\varepsilon}}}\,. \tag{2.159}$$

The computation of the derivatives of the phase stresses by the phase strains, $\partial\boldsymbol{\sigma}_{\Omega}/\partial\boldsymbol{\varepsilon}_{\Omega}$, and of the derivatives of the phase strains by the composite strain, $\partial\boldsymbol{\varepsilon}_{\Omega}/\partial\overline{\boldsymbol{\varepsilon}}$, leading to the homogenized tangent stiffness, are outlined in Appendix B.4.

It was acknowledged by Wu et al., 2013a,b, 2017, that the presented incremental-secant MT MFH algorithm may lead to overstiff homogenized predictions of the composite, particularly in cases of elastic inclusions in an elasto-plastic matrix. A variation of the residual incremental-secant approach was implemented by Wu et al. (2013a), that makes use of neglected residual stresses in inelastically deforming material phases. This strategy, referred to as the zero-residual incremental-secant approach, was shown to reliably provide improved results of the incremental-secant MFH.

Zero-residual incremental-secant approach A modification of the incremental-secant approach presented above is the so-called zero-residual incremental-secant scheme (Wu et al., 2013a). In this approach, residual stresses of a phase I (in this work, the zero-residual formalism is adopted for the matrix I only) are neglected, meaning that $\boldsymbol{\sigma}_{\mathrm{I}}^{\mathrm{res}} = 0$ (Fig. 2.4c). Consequently, the reloading step of the matrix phase I with a waived residual stress in Eq. (2.153) is modified to

$$(\boldsymbol{\varepsilon}_{\mathrm{I}}^{\mathrm{res}}, 0) \xrightarrow{(\Delta\boldsymbol{\varepsilon}_{\mathrm{I}}^{\mathrm{re}}, \boldsymbol{\sigma}_{\mathrm{I}})} (\boldsymbol{\varepsilon}_{\mathrm{I}}, \boldsymbol{\sigma}_{\mathrm{I}})\,, \tag{2.160}$$

where the reloading stress increment $\Delta\boldsymbol{\sigma}_{\mathrm{I}}^{\mathrm{re}} = \boldsymbol{\sigma}_{\mathrm{I}}$ in Eq. (2.158) is expressed by the zero-residual incremental-secant operator $\tilde{\mathbb{C}}_{\mathrm{I}}^{\mathrm{sec}}$ as

$$\boldsymbol{\sigma}_{\mathrm{I}} = \tilde{\mathbb{C}}_{\mathrm{I}}^{\mathrm{sec}} : \Delta\boldsymbol{\varepsilon}_{\Omega}^{\mathrm{re}}\,. \tag{2.161}$$

The determination of the zero-residual incremental-secant operator $\tilde{\mathbb{C}}_{\Omega}^{\mathrm{sec}}$ is follows the local constitutive relations of the matrix phase (Section 2.5.3). The strain localization relation between the two phases $\Omega = \mathrm{I}, \mathrm{II}$ changes from the expression in Eq. (2.156) towards

$$\mathbb{B}_{\mathrm{II}}^{\mathrm{sec}} = \{\mathbb{I} + \mathbb{S} : [(\tilde{\mathbb{C}}_{\mathrm{I}}^{\mathrm{sec}})^{-1} : \mathbb{C}_{\mathrm{II}}^{\mathrm{sec}} - \mathbb{I}]\}^{-1}\,, \tag{2.162}$$

resulting in modified phase strain distributions and thus in a modified homogenized response of the composite. The homogenized algorithmic stiffness $\overline{\mathbb{C}}^{\text{alg}}$ (Eq. (2.159)), resulting from the zero-residual incremental-secant formalism, is presented in Appendix B.4.

Algorithm 3: Numerical residual incremental-secant MFH (thus, with considered residual stresses in the matrix phase) procedure at a glance: Newton-Raphson scheme at one load step for a given overall strain increment $\Delta\overline{\boldsymbol{\varepsilon}}$.

compute residual state following Eqs. (2.163), (2.164) and (2.165).
initialize: $\Delta\boldsymbol{\varepsilon}_{\text{II}}^{\text{re}} = \Delta\overline{\boldsymbol{\varepsilon}}^{\text{re}}$
iterative procedure:
repeat
  compute matrix reloading strain increment: $\Delta\boldsymbol{\varepsilon}_{\text{I}}^{\text{re}} = (\Delta\overline{\boldsymbol{\varepsilon}}^{\text{re}} - \upsilon_{\text{II}}\Delta\boldsymbol{\varepsilon}_{\text{II}}^{\text{re}})/\upsilon_{\text{I}}$
  call constitutive relations for both phases $\Omega = \text{I}, \text{II}$ to compute $\boldsymbol{\sigma}_\Omega$ and the secant stiffness tensors $\mathbb{C}_\Omega^{\text{sec}}$ (details in Section 2.5.3)
  evaluate the Eshelby tensor $\mathbb{S}(g_{\text{II}}, \mathbb{C}_{\text{I}}^{\text{sec}})$
  compute stress residual $\boldsymbol{F}$ according Eq. (2.167).
  compute Jacobian matrix $\mathbb{J}$ according Eq. (2.172).
  solve $\delta\boldsymbol{\varepsilon}_{\text{II}} = -\mathbb{J}^{-1} : \boldsymbol{F}$
  update $\Delta\boldsymbol{\varepsilon}_{\text{II}}^{\text{re}} = \Delta\boldsymbol{\varepsilon}_{\text{II}}^{\text{re}} - \delta\boldsymbol{\varepsilon}_{\text{II}}$
until $|\boldsymbol{F}| < \text{tol}$;
after convergence:
compute $\overline{\boldsymbol{\sigma}}$ and $\overline{\mathbb{C}}^{\text{alg}}$, following Eq. (2.137) and Eq. (2.159) with the details given in Appendix B.4, respectively.

2.4.3 Numerical resolution of the incremental-secant MFH scheme

At each load increment $n+1$, the unloading-reloading procedure under the presribed overall strain $\overline{\boldsymbol{\varepsilon}}$ is performed in order to compute the homogenized response. The schematic overview of the numerical incremental-secant scheme (with residual stresses in the matrix) is presented in Algorithm 3. First, the residual state of the composite is determined by the elastic unloading procedure towards $\overline{\boldsymbol{\sigma}}^{\text{res}} = 0$ and

$$\overline{\boldsymbol{\varepsilon}}^{\text{res}} = \overline{\boldsymbol{\varepsilon}}^{n} - \Delta\overline{\boldsymbol{\varepsilon}}^{\text{u}} \tag{2.163a}$$

$$\Delta\overline{\boldsymbol{\varepsilon}}^{\text{u}} = -(\overline{\mathbb{C}}^{\text{el}})^{-1} : \overline{\boldsymbol{\sigma}}^{n}\,. \tag{2.163b}$$

The phase residual states are given by the elastic unloading procedure for the matrix

$$\boldsymbol{\sigma}_{\text{I}}^{\text{res}} = \boldsymbol{\sigma}_{\text{I}}^{n} - \Delta\boldsymbol{\sigma}_{\text{I}}^{\text{u}} \tag{2.164a}$$

$$\Delta\boldsymbol{\sigma}_{\text{I}}^{\text{u}} = \mathbb{C}_{\text{I}}^{\text{el}} : \Delta\boldsymbol{\varepsilon}_{\text{I}}^{\text{u}} \tag{2.164b}$$

$$\boldsymbol{\varepsilon}_{\text{II}}^{\text{res}} = \boldsymbol{\varepsilon}_{\text{I}}^{n} - \Delta\boldsymbol{\varepsilon}_{\text{I}}^{\text{u}} \tag{2.164c}$$

$$\Delta\boldsymbol{\varepsilon}_{\text{I}}^{\text{u}} = \{\upsilon\mathbb{I} + \upsilon\mathbb{B}_{\text{II}}^{\text{el}}\}^{-1} : \Delta\boldsymbol{\varepsilon}^{\text{u}} \tag{2.164d}$$

and for the inclusion

$$\boldsymbol{\sigma}_{\mathrm{II}}^{\mathrm{res}} = \boldsymbol{\sigma}_{\mathrm{II}}^{n} - \Delta\boldsymbol{\sigma}_{\mathrm{II}}^{\mathrm{u}} \tag{2.165a}$$

$$\Delta\boldsymbol{\sigma}_{\mathrm{II}}^{\mathrm{u}} = \mathbb{C}_{\mathrm{II}}^{\mathrm{el}} : \Delta\boldsymbol{\varepsilon}_{\mathrm{II}}^{\mathrm{u}} \tag{2.165b}$$

$$\boldsymbol{\varepsilon}_{\mathrm{II}}^{\mathrm{res}} = \boldsymbol{\varepsilon}_{\mathrm{II}}^{n} - \Delta\boldsymbol{\varepsilon}_{\mathrm{II}}^{\mathrm{u}} \tag{2.165c}$$

$$\Delta\boldsymbol{\varepsilon}_{\mathrm{II}}^{\mathrm{u}} = \mathbb{B}_{\mathrm{II}}^{\mathrm{el}} : \Delta\boldsymbol{\varepsilon}_{\mathrm{I}}^{\mathrm{u}}\,. \tag{2.165d}$$

Subsequently, the reloading procedure is performed by an iterative Newton-Raphson algorithm under the composite reloading strain increment $\Delta\overline{\boldsymbol{\varepsilon}}^{\mathrm{re}}$ in

$$\overline{\boldsymbol{\varepsilon}}^{\mathrm{res}} \xrightarrow{\Delta\overline{\boldsymbol{\varepsilon}}^{\mathrm{re}}} \overline{\boldsymbol{\varepsilon}}^{n+1} \tag{2.166}$$

to compute the phases reloading strain increments $\Delta\boldsymbol{\varepsilon}_{\Omega}^{\mathrm{re}}$. The stress residual (details in Appendix B.2) expresses as

$$\boldsymbol{F} = \mathbb{C}_{\mathrm{I}}^{\mathrm{sec}} : \left[\Delta\boldsymbol{\varepsilon}_{\mathrm{II}}^{\mathrm{re}} - \frac{1}{v_{\mathrm{I}}}\mathbb{S}^{-1} : (\Delta\boldsymbol{\varepsilon}_{\mathrm{II}}^{\mathrm{re}} - \Delta\overline{\boldsymbol{\varepsilon}}^{\mathrm{re}})\right] - \mathbb{C}_{\mathrm{II}}^{\mathrm{sec}} : \Delta\boldsymbol{\varepsilon}_{\mathrm{II}}^{\mathrm{re}}\,, \tag{2.167}$$

with the Eshelby tensor $\mathbb{S}(g_{\mathrm{II}}, \mathbb{C}_{\mathrm{I}}^{\mathrm{sec}})$, where the phase secant stiffnesses $\mathbb{C}_{\mathrm{I}}^{\mathrm{sec}}$ and $\mathbb{C}_{\mathrm{II}}^{\mathrm{sec}}$ follow from the materials constitutive relations (Section 2.5.3). If the zero-residual incremental-secant approach is used, the matrix residual stress in Eq. (2.164) changes to

$$\boldsymbol{\sigma}_{\mathrm{I}}^{\mathrm{res}} = 0 \tag{2.168}$$

and the zero-residual incremental-secant operator $\tilde{\mathbb{C}}_{\mathrm{I}}^{\mathrm{sec}}$ is computed. The Eshelby tensor is expressed as $\mathbb{S}(g_{\mathrm{II}}, \tilde{\mathbb{C}}_{\mathrm{I}}^{\mathrm{sec}})$ and the stress residual (details in Appendix B.2) for the iterative solution is modified from Eq. (2.167) to

$$\boldsymbol{F} = \tilde{\mathbb{C}}_{\mathrm{I}}^{\mathrm{sec}} : \left[\Delta\boldsymbol{\varepsilon}_{\mathrm{II}}^{\mathrm{re}} - \frac{1}{v_{\mathrm{I}}}\mathbb{S}^{-1} : (\Delta\boldsymbol{\varepsilon}_{\mathrm{II}}^{\mathrm{re}} - \Delta\overline{\boldsymbol{\varepsilon}}^{\mathrm{re}})\right] - \mathbb{C}_{\mathrm{II}}^{\mathrm{sec}} : \Delta\boldsymbol{\varepsilon}_{\mathrm{II}}^{\mathrm{re}}\,. \tag{2.169}$$

Similarly as for the TFA (Section 2.3.5), the MFH solution follows the linearization of the stress residual

$$\boldsymbol{F} \to \boldsymbol{F} + \delta\boldsymbol{F} = 0, \tag{2.170}$$

with the variational term expressed as

$$\delta\boldsymbol{F} = \mathbb{J} : \delta\boldsymbol{\varepsilon}_{\mathrm{II}} + \frac{\partial\boldsymbol{F}}{\partial\overline{\boldsymbol{\varepsilon}}} : \delta\overline{\boldsymbol{\varepsilon}}\,, \tag{2.171}$$

where $\mathbb{J}$ is the Jacobian matrix. The overall strain is assumed constant, and thus $\delta\overline{\boldsymbol{\varepsilon}} = 0$. The Jacobian is computed as

$$\mathbb{J} = \frac{d\boldsymbol{F}}{d\boldsymbol{\varepsilon}_{\mathrm{II}}} = \frac{\partial\boldsymbol{F}}{\partial\boldsymbol{\varepsilon}_{\mathrm{II}}} + \frac{\partial\boldsymbol{F}}{\partial\boldsymbol{\varepsilon}_{\mathrm{I}}}\frac{\partial\boldsymbol{\varepsilon}_{\mathrm{I}}}{\partial\boldsymbol{\varepsilon}_{\mathrm{II}}}\,, \tag{2.172}$$

with the detailed expression given in Appendix B.3, leading to the correction

$$\delta\boldsymbol{\varepsilon}_{\mathrm{II}} = -\mathbb{J} : \boldsymbol{F} \tag{2.173}$$

for the inclusion (reloading) strain increment

$$\Delta\boldsymbol{\varepsilon}_{\mathrm{II}}^{\mathrm{re}} = \Delta\boldsymbol{\varepsilon}_{\mathrm{II}}^{\mathrm{re}} + \delta\boldsymbol{\varepsilon}_{\mathrm{II}}\,. \tag{2.174}$$

2.5 Local constitutive relations

2.5.1 Anisotropic linear elasticity

Linear elastic material behavior is assumed in the following. The fourth-order elastic stiffness tensor $\mathbb{C}^{\mathrm{el}}$ in the stress-strain relation

$$\boldsymbol{\sigma} = \mathbb{C}^{\mathrm{el}} : \boldsymbol{\varepsilon}\,, \tag{2.175}$$

representing a generic anisotropic elastic material, can, due to the symmetries of the second-order strain and stress tensors, be expressed as a 6×6 matrix C^{el}, called the Voigt-representation. The stress-strain relation is then given as

$$\boldsymbol{\sigma}^{\mathrm{V}} = C^{\mathrm{el}} \cdot \boldsymbol{\varepsilon}^{\mathrm{V}}\,, \tag{2.176}$$

where $\boldsymbol{\sigma}^{\mathrm{V}} = (\boldsymbol{\sigma}_{11}\,, \boldsymbol{\sigma}_{22}\,, \boldsymbol{\sigma}_{33}\,, \boldsymbol{\sigma}_{23}\,, \boldsymbol{\sigma}_{13}\,, \boldsymbol{\sigma}_{12})$ and $\boldsymbol{\varepsilon}^{\mathrm{V}} = (\boldsymbol{\varepsilon}_{11}\,, \boldsymbol{\varepsilon}_{22}\,, \boldsymbol{\varepsilon}_{33}\,, 2\boldsymbol{\varepsilon}_{23}\,, 2\boldsymbol{\varepsilon}_{13}\,, 2\boldsymbol{\varepsilon}_{12})$ are the stress and strain vectors. With the stresses $\boldsymbol{\sigma}$ deriving from a strain energy density function U as

$$\boldsymbol{\sigma}_{ij} = \frac{\partial U}{\partial \boldsymbol{\varepsilon}_{ij}}\,, \tag{2.177}$$

and therefore

$$\mathbb{C}^{\mathrm{el}}_{ijkl} = \frac{\partial^2 U}{\partial \boldsymbol{\varepsilon}_{ij}\partial \boldsymbol{\varepsilon}_{kl}} = \frac{\partial^2 U}{\partial \boldsymbol{\varepsilon}_{kl}\partial \boldsymbol{\varepsilon}_{ij}} = \mathbb{C}^{\mathrm{el}}_{klij} \tag{2.178}$$

the 36 material parameters reduce to 21 independent elastic parameters. The resulting fully anisotropic elastic stiffness tensor $\mathbb{C}^{\mathrm{el}}$ in Voigt-notation, C^{el}, is expressed as

$$C^{\mathrm{el}} = \begin{Bmatrix} C^{\mathrm{el}}_{11} & C^{\mathrm{el}}_{12} & C^{\mathrm{el}}_{13} & C^{\mathrm{el}}_{14} & C^{\mathrm{el}}_{15} & C^{\mathrm{el}}_{16} \\ C^{\mathrm{el}}_{12} & C^{\mathrm{el}}_{22} & C^{\mathrm{el}}_{23} & C^{\mathrm{el}}_{24} & C^{\mathrm{el}}_{25} & C^{\mathrm{el}}_{26} \\ C^{\mathrm{el}}_{13} & C^{\mathrm{el}}_{23} & C^{\mathrm{el}}_{33} & C^{\mathrm{el}}_{34} & C^{\mathrm{el}}_{35} & C^{\mathrm{el}}_{36} \\ C^{\mathrm{el}}_{14} & C^{\mathrm{el}}_{24} & C^{\mathrm{el}}_{34} & C^{\mathrm{el}}_{44} & C^{\mathrm{el}}_{45} & C^{\mathrm{el}}_{46} \\ C^{\mathrm{el}}_{15} & C^{\mathrm{el}}_{25} & C^{\mathrm{el}}_{35} & C^{\mathrm{el}}_{45} & C^{\mathrm{el}}_{55} & C^{\mathrm{el}}_{56} \\ C^{\mathrm{el}}_{16} & C^{\mathrm{el}}_{26} & C^{\mathrm{el}}_{36} & C^{\mathrm{el}}_{46} & C^{\mathrm{el}}_{56} & C^{\mathrm{el}}_{66} \end{Bmatrix}\,. \tag{2.179}$$

In many materials however, the elastic responses in the different spatial orientations are not fully independent.

Orthotropic materials Orthotropic materials have three underlying orthogonal planes of symmetry, resulting in a reduction from 21 to nine independent elastic parameters. The

elastic stiffness is represented by

$$C^{\mathrm{el}} = \begin{Bmatrix} C_{11}^{\mathrm{el}} & C_{12}^{\mathrm{el}} & C_{13}^{\mathrm{el}} & 0 & 0 & 0 \\ C_{12}^{\mathrm{el}} & C_{22}^{\mathrm{el}} & C_{23}^{\mathrm{el}} & 0 & 0 & 0 \\ C_{13}^{\mathrm{el}} & C_{23}^{\mathrm{el}} & C_{33}^{\mathrm{el}} & 0 & 0 & 0 \\ 0 & 0 & 0 & C_{44}^{\mathrm{el}} & 0 & 0 \\ 0 & 0 & 0 & 0 & C_{55}^{\mathrm{el}} & 0 \\ 0 & 0 & 0 & 0 & 0 & C_{66}^{\mathrm{el}} \end{Bmatrix} . \tag{2.180}$$

Transverse-isotropic materials If additionally to the orthotropy, the material has one preferred orientation, meaning that its response in one orientation is different from the response in the other two orientations, it is referred to as transverse-isotropic or polar-anisotropic (used in Section 3.5.5 and for the fibers of the yarns in Section 4). Fibrous materials do typically possess one preferred orientation. The transverse-isotropic stiffness tensor can be represented by five independent elastic parameters as

$$C^{\mathrm{el}} = \begin{Bmatrix} C_{11}^{\mathrm{el}} & C_{12}^{\mathrm{el}} & C_{13}^{\mathrm{el}} & 0 & 0 & 0 \\ C_{12}^{\mathrm{el}} & C_{11}^{\mathrm{el}} & C_{13}^{\mathrm{el}} & 0 & 0 & 0 \\ C_{13}^{\mathrm{el}} & C_{13}^{\mathrm{el}} & C_{33}^{\mathrm{el}} & 0 & 0 & 0 \\ 0 & 0 & 0 & C_{44}^{\mathrm{el}} & 0 & 0 \\ 0 & 0 & 0 & 0 & C_{44}^{\mathrm{el}} & 0 \\ 0 & 0 & 0 & 0 & 0 & (C_{11}^{\mathrm{el}} - C_{12}^{\mathrm{el}})/2 \end{Bmatrix} . \tag{2.181}$$

Isotropic materials Materials that have the same elastic stress-strain response in all spatial orientations are referred to as elastically isotropic. Their stiffness tensor is fully characterized by two elastic material parameters, expressed as

$$C^{\mathrm{el}} = \begin{Bmatrix} C_{11}^{\mathrm{el}} & C_{12}^{\mathrm{el}} & C_{12}^{\mathrm{el}} & 0 & 0 & 0 \\ C_{12}^{\mathrm{el}} & C_{11}^{\mathrm{el}} & C_{12}^{\mathrm{el}} & 0 & 0 & 0 \\ C_{12}^{\mathrm{el}} & C_{12}^{\mathrm{el}} & C_{11}^{\mathrm{el}} & 0 & 0 & 0 \\ 0 & 0 & 0 & (C_{11}^{\mathrm{el}} - C_{12}^{\mathrm{el}})/2 & 0 & 0 \\ 0 & 0 & 0 & 0 & (C_{11}^{\mathrm{el}} - C_{12}^{\mathrm{el}})/2 & 0 \\ 0 & 0 & 0 & 0 & 0 & (C_{11}^{\mathrm{el}} - C_{12}^{\mathrm{el}})/2 \end{Bmatrix} . \tag{2.182}$$

The isotropic elastic stiffness operator $\mathbb{C}^{\mathrm{el}}$ (or C^{el} in the Voigt-notation) can be represented by, e.g., the elastic bulk and shear moduli κ^{el} and G^{el}, as will be used for the nonlinear material models considered in this work, described subsequently in Sections 2.5.2 and 2.5.3.

2.5.2 Nonlinear material behavior: J_2-plasticity model

In this work, local inelastic stress responses and the local tangent stiffnesses follow from the classical J_2-plasticity model. Isotropic elasticity is assumed for the nonlinear material phases. The isotropic elastic stiffness of the nonlinear material phase can be expressed as

$$\mathbb{C}^{\mathrm{el}} = 3\kappa^{\mathrm{el}}\mathbb{I}^{\mathrm{vol}} + 2G^{\mathrm{el}}\mathbb{I}^{\mathrm{dev}} , \tag{2.183}$$

with the materials elastic bulk modulus κ^{el} and shear modulus G^{el}. In this section, the material point denoted by $\boldsymbol{\chi}$ and the subscript r referring to the subdomain V_r are omitted

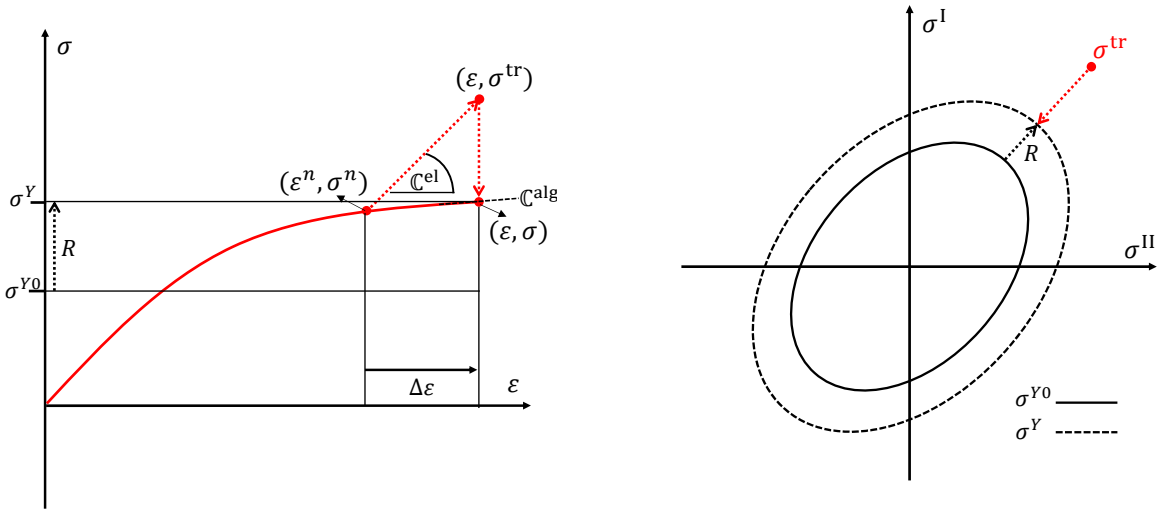

(a) (b)

FIGURE 2.5: Return mapping algorithm and isotropic hardening demonstration (a) in the stress-strain plot for the uniaxial case, showing the correction from the trial stress state towards the new stress state and (b) in the plane of the principal stresses for the biaxial stress state, demonstrating the mapping from the trial stress state on to the current yield surface.

in the equations. The yield function for isotropic hardening

$$f^{\mathrm{Y}}(\boldsymbol{\sigma}, p) = \sigma^{\mathrm{eq}} - \sigma^{\mathrm{Y}}(p) \leq 0 \tag{2.184}$$

is to be fulfilled in order to satisfy the von Mises law, where p is the accumulated equivalent plastic strain. In the yield function $f^{\mathrm{Y}}(\boldsymbol{\sigma}, p)$, the current yield stress reads

$$\sigma^{\mathrm{Y}} = \sigma^{\mathrm{Y0}} + R(p), \tag{2.185}$$

with the initial yield stress σ^{Y0} and the hardening stress $R(p)$ following from the expression of the governing hardening law and the equivalent accumulated plastic strain p. A schematic demonstration of the increasing yield stress due to isotropic hardening is presented in Fig. 2.5. The equivalent accumulated plastic strain p, as the time integral of its rate $\dot{p}$, follows from the purely deviatoric plastic strain rate tensor $\dot{\boldsymbol{\varepsilon}}^{\mathrm{p}}$ as

$$\dot{p} = \sqrt{\frac{2}{3}\dot{\boldsymbol{\varepsilon}}^{\mathrm{p}} : \dot{\boldsymbol{\varepsilon}}^{\mathrm{p}}}\,, \tag{2.186}$$

such that

$$\dot{\boldsymbol{\varepsilon}}^{\mathrm{p}} = \dot{p}\,\boldsymbol{N}\,, \tag{2.187}$$

where

$$\boldsymbol{N} = \frac{\partial f^{\mathrm{Y}}}{\partial \boldsymbol{\sigma}} = \frac{3}{2}\frac{\mathrm{dev}(\boldsymbol{\sigma})}{\sigma^{\mathrm{eq}}} \tag{2.188}$$

is the plastic flow direction and $\mathrm{dev}(\boldsymbol{\sigma})$ is the deviatoric stress. The equivalent stress is computed as

$$\sigma^{\mathrm{eq}} = \sqrt{\frac{3}{2}\,\mathrm{dev}(\boldsymbol{\sigma}) : \mathrm{dev}(\boldsymbol{\sigma})}\,. \tag{2.189}$$

This convention for the equivalent stresses representing a stress tensor is the one used in the following. The purely deviatoric incremental plastic strain, as the time integral of $\dot{\boldsymbol{\varepsilon}}_{\mathrm{I}}^{\mathrm{p}}$ over the time increment is expressed as

$$\Delta\boldsymbol{\varepsilon}^{\mathrm{p}} = \Delta p \boldsymbol{N}\,, \tag{2.190}$$

The second part is the current equivalent von Mises stress, computed following Eq. (2.189). The resolution of the incremental problem at one current load increment follows a predictor-corrector scheme, starting from the assumption of no occurring plastic flow, and hence the incremental ("predicted") elastic trial stress state

$$\boldsymbol{\sigma}^{\mathrm{tr}} = \boldsymbol{\sigma}_n + \mathbb{C}^{\mathrm{el}} : \Delta\boldsymbol{\varepsilon}, \tag{2.191}$$

where $\boldsymbol{\sigma}_n$ is the stress solved at the former load increment, and the corresponding yield function

$$f^{\mathrm{Y}}(\boldsymbol{\sigma}, \boldsymbol{\varepsilon}^{\mathrm{p}}) = \sigma^{\mathrm{tr,eq}} - \sigma^{\mathrm{Y}}\,. \tag{2.192}$$

It can be shown that $\boldsymbol{N} = \boldsymbol{N}^{\mathrm{tr}}$, where

$$\boldsymbol{N}^{\mathrm{tr}} = \frac{3}{2}\frac{\mathrm{dev}(\boldsymbol{\sigma}^{\mathrm{tr}})}{\sigma^{\mathrm{tr,eq}}}\,. \tag{2.193}$$

In case of $f^{\mathrm{Y}} > 0$, the scheme yields, by solving the above equations in order to satisfy the condition (2.184), the resulting plastic strain increment given by Eq. (2.190), with the plastic flow direction following Eq. (2.193). The plastic flow maps the trial stress state in Eq. (2.191) on to the corresponding yield surface (Fig. 2.5), finally providing the ("corrected") stress state as

$$\boldsymbol{\sigma} = \boldsymbol{\sigma}^{\mathrm{tr}} - \mathbb{C}^{\mathrm{el}} : \Delta\boldsymbol{\varepsilon}^{\mathrm{p}}. \tag{2.194}$$

For isotropic elasticity, Eq. (2.194) can be expressed as

$$\boldsymbol{\sigma} = \boldsymbol{\sigma}^{\mathrm{tr}} - 2G^{\mathrm{el}}\Delta\boldsymbol{\varepsilon}^{\mathrm{p}}, \tag{2.195}$$

with the elastic shear modulus of the material G^{el}. The derivative of the plastic strain increment in Eq. (2.190) reads

$$\frac{\partial\Delta\boldsymbol{\varepsilon}^{\mathrm{p}}}{\partial\boldsymbol{\varepsilon}} = \frac{2G^{\mathrm{el}}}{h}\boldsymbol{N}\otimes\boldsymbol{N} + 2G^{\mathrm{el}}\frac{\Delta p}{\sigma^{\mathrm{tr,eq}}}\left(\frac{3}{2}\mathbb{I}^{\mathrm{dev}} - \boldsymbol{N}\otimes\boldsymbol{N}\right), \tag{2.196}$$

and the consistent tangent stiffness reads

$$\begin{aligned}\mathbb{C}^{\mathrm{alg}} = \frac{\partial\Delta\boldsymbol{\sigma}}{\partial\boldsymbol{\varepsilon}} &= \mathbb{C}^{\mathrm{el}} - 2G^{\mathrm{el}}\frac{\partial\Delta\boldsymbol{\varepsilon}^{\mathrm{p}}}{\partial\boldsymbol{\varepsilon}} \\ &= \mathbb{C}^{\mathrm{el}} - \frac{(2G^{\mathrm{el}})^2}{h}\boldsymbol{N}\otimes\boldsymbol{N} - (2G^{\mathrm{el}})^2\frac{\Delta p}{\sigma^{\mathrm{tr,eq}}}\left(\frac{3}{2}\mathbb{I}^{\mathrm{dev}} - \boldsymbol{N}\otimes\boldsymbol{N}\right)\end{aligned}, \tag{2.197}$$

where

$$h = 3G^{\mathrm{el}} + \partial R/\partial p. \tag{2.198}$$

Details of the computations in Eqs. (2.196) and (2.197) are given in Appendix C.1.

2.5.3 Incremental-secant formulation of the J_2-plasticity model

The stress-strain response during the incremental-secant reloading procedure Eq. (2.158), given by

$$\boldsymbol{\varepsilon} = \boldsymbol{\varepsilon}^{\mathrm{res}} + \Delta\boldsymbol{\varepsilon}^{\mathrm{re}} \tag{2.199a}$$
$$\boldsymbol{\sigma} = \boldsymbol{\sigma}^{\mathrm{res}} + \Delta\boldsymbol{\sigma}^{\mathrm{re}}\,, \tag{2.199b}$$

is governed by the J_2-plasticity model. In the following, the common convention for the equivalent strains is used for the strain tensors:

$$\varepsilon^{\mathrm{eq}} = \sqrt{\frac{2}{3}\,\mathrm{dev}(\boldsymbol{\varepsilon}) : \mathrm{dev}(\boldsymbol{\varepsilon})}\,. \tag{2.200}$$

The radial return mapping algorithm as described in Section 2.5.2 corrects the elastic trial stress state back towards the current yield surface. During the incremental-secant reloading increment, the stress state correction provided by the purely deviatoric plastic strain increment

$$\Delta\boldsymbol{\varepsilon}^{\mathrm{p}} = \Delta p \boldsymbol{N}^{\mathrm{sec}}\,, \tag{2.201}$$

points back from the elastic trial reloading stress $\Delta\boldsymbol{\sigma}^{\mathrm{re,tr}} = \mathbb{C}^{\mathrm{el}} : \Delta\boldsymbol{\varepsilon}^{\mathrm{re}}$ towards the actual reloading stress $\Delta\boldsymbol{\sigma}^{\mathrm{re}}$. Therefore, the flow direction is given as

$$\boldsymbol{N}^{\mathrm{sec}} = \frac{3}{2}\frac{\mathrm{dev}(\Delta\boldsymbol{\sigma}^{\mathrm{re}})}{\Delta\sigma^{\mathrm{re,eq}}} = \frac{3}{2}\frac{\mathrm{dev}(\Delta\boldsymbol{\sigma}^{\mathrm{re,tr}})}{\Delta\sigma^{\mathrm{re,tr,eq}}}\,, \tag{2.202}$$

and the stress state (Eq. (2.199b)) follows as

$$\Delta\boldsymbol{\sigma}^{\mathrm{re}} = \Delta\boldsymbol{\sigma}^{\mathrm{re,tr}} - 2G^{\mathrm{el}}\,\Delta\boldsymbol{\varepsilon}^{\mathrm{p}}\,. \tag{2.203}$$

Following the elastic isotropy in Eq. (2.183), the incremental-secant stiffness can be expressed as an isotropic tensor

$$\mathbb{C}^{\mathrm{sec}} = 3\kappa^{\mathrm{el}}\mathbb{I}^{\mathrm{vol}} + 2G^{\mathrm{sec}}\mathbb{I}^{\mathrm{dev}}\,, \tag{2.204}$$

where the incremental shear modulus is given as

$$G^{\mathrm{sec}} = \frac{\Delta\sigma^{\mathrm{re,eq}}}{3\,\Delta\varepsilon^{\mathrm{re,eq}}} = G^{\mathrm{el}} - \frac{3(G^{\mathrm{el}})^2\Delta p}{\Delta\sigma^{\mathrm{re,tr,eq}}}\,. \tag{2.205}$$

Under the reloading increment, the occuring plastic flow (Eq. (2.201)) differs from the one in the tangent formulation Section 2.5.2, implying that the algorithmic tangent stiffness

$$\mathbb{C}^{\mathrm{alg}} = \frac{\partial\Delta\boldsymbol{\sigma}}{\partial\boldsymbol{\varepsilon}} = \mathbb{C}^{\mathrm{el}} - 2G^{\mathrm{el}}\frac{\partial\Delta\boldsymbol{\varepsilon}^{\mathrm{p}}}{\partial\boldsymbol{\varepsilon}} \tag{2.206}$$

changes. The full expression for $\mathbb{C}^{\mathrm{alg}}$ following the incremental-secant formulation is presented in Appendix C.

If however, the zero-residual incremental-secant approach is adopted for the matrix phase, the reloading step in Eq. (2.199) changes to

$$\boldsymbol{\varepsilon} = \boldsymbol{\varepsilon}^{\mathrm{res}} + \Delta\boldsymbol{\varepsilon}^{\mathrm{re}} \tag{2.207a}$$

$$\Delta\boldsymbol{\sigma}^{\mathrm{re}} = \boldsymbol{\sigma}\,. \tag{2.207b}$$

Accordingly, the plastic flow direction during the reloading increment, pointing back from the elastic trial stress state $\boldsymbol{\sigma}^{\mathrm{tr}}$ towards the new stress state $\boldsymbol{\sigma}$, changes to the one given by the tangent formulation in Section 2.5.2,

$$\boldsymbol{N} = \frac{3}{2}\frac{\mathrm{dev}(\boldsymbol{\sigma}^{\mathrm{tr}})}{\sigma^{\mathrm{tr,eq}}}\,. \tag{2.208}$$

The zero-residual incremental-secant shear modulus

$$\tilde{G}^{\mathrm{sec}} = \frac{\sigma^{\mathrm{eq}}}{3\,\Delta\varepsilon^{\mathrm{re,eq}}} = G^{\mathrm{el}} - \frac{3(G^{\mathrm{el}})^2\Delta p}{\sigma^{\mathrm{tr,eq}}} \tag{2.209}$$

leads to the expression of the zero-residual incremental stiffness tensor

$$\tilde{\mathbb{C}}^{\mathrm{sec}} = 3\kappa^{\mathrm{el}}\mathbb{I}^{\mathrm{vol}} + 2\tilde{G}^{\mathrm{sec}}\mathbb{I}^{\mathrm{dev}}\,. \tag{2.210}$$

The algorithmic tangent stiffness of the nonlinear material, following the zero-residual incremental-secant formalism, is the one in Eq. (2.197).

2.6 Summary

Different homogenization approaches were presented, starting from the computational, or full-field, homogenization that bases on the extraction of homogenized properties from computed microscopic fields of variables. Following, clustering based homogenization (CAH) approaches are presented, basing on piecewise uniform fields of variables instead of the computed fields on the microscale. In order to replace the microscopic full-field solution, certain concentration and influence functions need to be defined between the subdomains. The definition of these concentration and influence functions distinguish the different homogenization approaches. For the Mori-Tanaka MFH approach, influence tensors between both material phases are computed based on the Eshelby tensor of the inclusion and certain linearized stiffness operators of the phases. Methods like the TFA and PFA generalize the MFH approach in the sense that they allow the consideration of an arbitrary number of subdomains with uniform fields of variables. The concentration and influence functions considered for these methods create couplings between the subdomain variables and between the subdomains and the overall loading. The validity of both approaches has been demonstrated by means of a simple example with piecewise uniform stress and strain fields. The HS algorithm, based on the assumption of an isotropic reference medium, was presented as a simplified PFA. In this context, a tangent formalism was suggested in order to account for cyclic loading cases. The numerical solution procedures for the TFA, the HS type analysis, and the incremental-secant MFH formalism, relying on iterative Newton-Raphson schemes, are developed.

Chapter 3

Clustering analyses of composite RVEs

3.1 Introduction

This chapter details the TFA (Section 2.3.4) and HS (Section 2.3.7) approaches developed in this thesis, both relying on piecewise uniform fields of variables, used as CAH techniques suitable for the purpose of multiscale modeling of random-structured inelastic composite materials during various loading conditions. The TFA and the HS scale coupling relations can be used in combination with any inelastic local constitutive relations for the subdomains. The main difference between the two methods is that the HS homogenization approach relies on the integration of a homogeneous and isotropic reference medium, while for the TFA, solely the responses of the single subdomains are considered for the estimation of the homogenized response.

It is well known that homogenization approaches based on piecewise uniform fields of internal variables lead to typically overstiff predicted homogenized responses of nonlinear composite materials (Spilker et al., 2022). The main reason for the too stiff computed responses is the insufficient ability to capture highly localized nonlinear effects. In this work, elasto-plastic materials are considered with hardening properties and under loading conditions that lead to complex and very localized accumulations of plasticity. In order to improve the accuracy of the methods, the following ingredients are considered

- In order for the spatial division into subdomains to be well-representative of the inelastic micromechanical deformation patterns inside the material, this subdivision is based on plastic strain tensor distributions obtained by selected offline loading conditions;
- In order to remain general for different microstructures, the local interaction functions are evaluated numerically;
- In order to account for plastic field fluctuations inside each subdomain and to allow for an additional acceleration of the convergence towards full-field results, a sensible correction approach for the use of piecewise uniform field TFA is constructed from the inelastic field fluctuations within each subdomain observed during the offline stage.

This chapter is structured as follows: Section 3.2 presents the clustering techniques for the spatial decompositions based on elastic and on plastic deformation fields. The Sections 3.3 and 3.4 outline all the details on the construction of the two adopted CAH schemes, including the determination of the averaged concentration and interaction tensors and the determination of a correction for the TFA that bases on plastic field fluc-

tuations, referred to as *plastic fluctuation correction* (PFC). The modified TFA solution scheme under consideration of the PFC is given. In Section 3.5, the numerical results of the extensive testing of the CAH schemes for various material systems are presented. The reduced homogenized responses computed by the use of the TFA and the HS approaches are compared to the reference results following high-fidelity full-field simulations. The results following the CAH models are investigated, and while the CAH models are generally able to represent the full-field solutions fairly accurate, reasons for poor representations of the elastic and/or inelastic behaviors of particular material systems are discussed. Finally, in Section 3.6 conclusions are drawn regarding the suitability of the CAH approaches for generic microstructures, the accuracy of the two CAH models and the effectivity of the plasticity based in comparison to not optimized spatial subdomain decompositions.

3.2 Spatial division based on local deformation fields

In order to use the TFA as a reduced technique for the mechanical homogenization, the microscopic points of the RVE are divided into several subdomains and over the subdomains averaged quantities

$$\beta_r = \frac{1}{|V_r|} \int_{V_r} \beta(\boldsymbol{\chi}) \mathrm{d}\boldsymbol{\chi} \tag{3.1}$$

are considered. For the case of more than one material phase, each phase is subdivided separately. A more refined discretization than simply using one subdomain per material phase is achieved by selecting a local variable $\beta(\boldsymbol{\chi})$ and analyzing its distribution in the corresponding phase. The microscopic points are then divided based on the local similarity of the selected quantity. Thereby the subdivisions are not necessarily coherent in space. In the following, RVE decompositions based on elastic and inelastic strain distributions are presented. A k-means clustering approach as proposed by Liu, Bessa, and Liu (2016) is used to divide all microscopic points in the full-field domain into partitions based on the similarity of their elastic or inelastic strain tensors (MacQueen, 1967). In order to achieve accurate mechanical local fields for the spatial partitioning, certain discrete numerical full field simulations are performed in the offline stage. The number and type of the full field pre-simulations depend on the chosen variable to be characterized. In the following, all N_r local data points constituting the subdomain volume V_r are denoted by the index i, expressed as

$$\boldsymbol{\chi}_i \in V_r, \quad i = 1, ..., N_r \,. \tag{3.2}$$

After the spatial decomposition, interaction tensors between the subdomains are determined. The division of all local material points into the subdomains is performed phase-wise, and in the following, the material phases are denoted by the index Ω.

3.2.1 Elasticity based clustering

The local elastic strain concentration tensors $\mathbb{A}^{\mathrm{el}}(\boldsymbol{\chi})$ in an RVE link the strain at any material point $\boldsymbol{\chi}$ in the microscopic domain inside the RVE, considered in elasticity and without any eigenfields, to the overall strain of the RVE following from Eq. (2.25) as

$$\boldsymbol{\varepsilon}(\boldsymbol{\chi}) = \mathbb{A}^{\mathrm{el}}(\boldsymbol{\chi}) : \overline{\boldsymbol{\varepsilon}} \,. \tag{3.3}$$

The local strain concentration tensors in the RVE are fully characterized by the computation of local strain fields $\boldsymbol{\varepsilon}(\boldsymbol{\chi})$ under certain different loading cases applied by prescribed strain boundary conditions $\overline{\boldsymbol{\varepsilon}}$ on the elastic RVE (Section 2.2). For the estimation of all local strain concentration tensors in a 3D heterogeneous structure, the six different orthogonal boundary modes

$$\overline{\boldsymbol{\varepsilon}}^{(1)} = E^{\mathrm{BC}} \vec{e}_x \otimes \vec{e}_x \,, \tag{3.4a}$$

$$\overline{\boldsymbol{\varepsilon}}^{(2)} = E^{\mathrm{BC}} \vec{e}_y \otimes \vec{e}_y \,, \tag{3.4b}$$

$$\overline{\boldsymbol{\varepsilon}}^{(3)} = E^{\mathrm{BC}} \vec{e}_z \otimes \vec{e}_z \,, \tag{3.4c}$$

$$\overline{\boldsymbol{\varepsilon}}^{(4)} = \frac{1}{2} E^{\mathrm{BC}} (\vec{e}_x \otimes \vec{e}_y + \vec{e}_y \otimes \vec{e}_x) \,, \tag{3.4d}$$

$$\overline{\boldsymbol{\varepsilon}}^{(5)} = \frac{1}{2} E^{\mathrm{BC}} (\vec{e}_x \otimes \vec{e}_z + \vec{e}_z \otimes \vec{e}_x) \,, \tag{3.4e}$$

$$\overline{\boldsymbol{\varepsilon}}^{(6)} = \frac{1}{2} E^{\mathrm{BC}} (\vec{e}_y \otimes \vec{e}_z + \vec{e}_z \otimes \vec{e}_y) \tag{3.4f}$$

are applied on the RVE, with a strain magnitude E^{BC} and the canonical unit vectors in a 3D space $\vec{e}_x$, $\vec{e}_y$ and $\vec{e}_z$. For 2D analyses, the boundary modes $\overline{\boldsymbol{\varepsilon}}^{(1)}$, $\overline{\boldsymbol{\varepsilon}}^{(2)}$ and $\overline{\boldsymbol{\varepsilon}}^{(4)}$ are applied. Writing Eq. (3.3) in Voigt-notation, the local elastic strain concentration tensors $\mathbb{A}^{\mathrm{el}}(\boldsymbol{\chi})$ are fully characterized by a comparison of the resulting local strain field $\boldsymbol{\varepsilon}(\boldsymbol{\chi})$ to the prescribed overall strain $\overline{\boldsymbol{\varepsilon}}$. After the determination of the full strain concentration tensor field, a k-means clustering technique (MacQueen, 1967) is applied on the local elastic strain concentration tensors. The k-means clustering approach divides the data points it is applied on, into a number K of partitions by solving an optimization problem minimizing the in-partition variances. Here, it is used as a multi-dimensional clustering approach, grouping all the fourth order strain concentration tensors at the microscopic points $\boldsymbol{\chi}$ inside one material phase V_Ω into a number of K_Ω partitions. During the clustering procedure, all tensor entries are taken into account, meaning that the dimensionality amounts to the number of (independent) components of a fourth-order tensor. The goal is the minimization of the function

$$H[\mathbb{A}^{\mathrm{el}}(\boldsymbol{\chi})] = \sum_{r=1}^{K_\Omega} \sum_{i=1}^{N_r} ||\mathbb{A}^{\mathrm{el}}(\boldsymbol{\chi}_i) - \mathbb{A}^{\mathrm{el}}_r||^2, \quad \boldsymbol{\chi} \in V_\Omega, \quad \boldsymbol{\chi}_i \in V_r \subset V_\Omega, \quad r \in 1, ..., K_\Omega \,, \tag{3.5}$$

where

$$||\mathbb{Z}|| = \sqrt{\mathbb{Z} :: \mathbb{Z}} \,, \tag{3.6}$$

indicated by minimal variances of the strain concentration tensors $\mathbb{A}^{\mathrm{el}}(\boldsymbol{\chi}_i)$ in one subdomain r to the corresponding subdomain average strain concentration tensor of the subdomain

$$\mathbb{A}^{\mathrm{el}}_r = \frac{1}{|V_r|} \int_{V_r} \mathbb{A}^{\mathrm{el}}(\boldsymbol{\chi}) \mathrm{d}\boldsymbol{\chi} \,. \tag{3.7}$$

The optimization problem is solved by an iterative process finally achieving the optimal decomposition of all data points into the K_Ω sets. This optimal decomposition of one material phase Ω is accomplished as follows:

1. First an arbitrary number of clusters K_Ω is chosen and strain concentration tensors at random data points are defined as the $r = 1, ..., K_\Omega$ initial cluster mean values

$\mathbb{A}_r^{\mathrm{el}}$.

2. Iterative clustering procedure starts

   2.1. Variances of all local strain concentration tensors from the different cluster means

   $$||\mathbb{A}^{\mathrm{el}}(\boldsymbol{\chi}) - \mathbb{A}_s^{\mathrm{el}}||^2, \quad \boldsymbol{\chi} \in V_\Omega, \quad s \in 1, ..., K_\Omega \tag{3.8}$$

   are calculated. All corresponding local data points i are assigned to a set r, so that the variance between the local strain concentration tensor $\mathbb{A}^{\mathrm{el}}(\boldsymbol{\chi}_i)$ and the assigned cluster mean $\mathbb{A}_r^{\mathrm{el}}$ is minimal:

   $$||\mathbb{A}^{\mathrm{el}}(\boldsymbol{\chi}_i) - \mathbb{A}_r^{\mathrm{el}}||^2 \leq ||\mathbb{A}^{\mathrm{el}}(\boldsymbol{\chi}_i) - \mathbb{A}_s^{\mathrm{el}}||^2, \quad \begin{array}{l} \boldsymbol{\chi}_i \in V_r \subset V_\Omega, \\ \forall s,\ r \in 1, ..., K_\Omega,\ s \neq r\,. \end{array} \tag{3.9}$$

   2.2. Following, all strain concentration tensors assigned to the cluster are used to determine the updated cluster means $\mathbb{A}_r^{\mathrm{el}}$ using Eq. (3.7).

3. The iterative procedure ends when convergence of the procedure is reached, indicated by a stationary assignment of the local data points to the sets. The cluster means after convergence of the k-means clustering procedure act as the strain concentration tensors of the subdomains in the online stage.

The elasticity-based spatial division and the computation of the strain concentration tensors are as well summarized in Algorithm 4.

3.2.2 Inelasticity based clustering

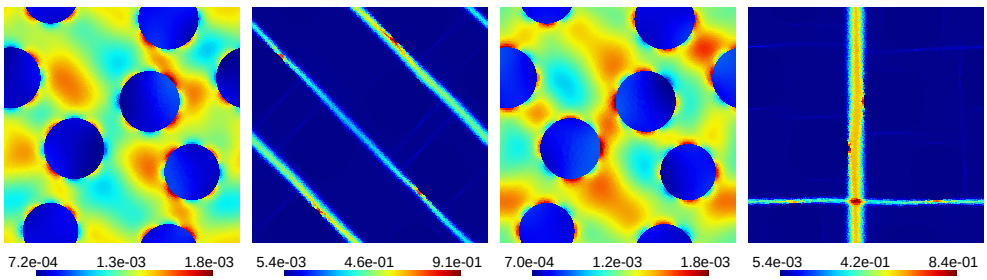

FIGURE 3.1: Computed equivalent strain fields in a composite RVE with $v_{\mathrm{II}} = 30$ % of circular stiff elastic inclusions embedded in an elasto-plastic matrix following the application of the boundary condition states (a,b) biaxial (as in Eq. (3.10a)) and (c,d) pure shear deformation (as in Eq. (3.10b)) during (a,c) purely elastic deformation and (b,d) after severe plastic deformation has occurred.

Inelastic deformation due to plastic flow, initiated when the initial yield limit of a material is exceeded, carries the major part of the total deformation under inelastic loading conditions. Inelastic deformation patterns in the material can deviate strongly from the spatial elastic deformation distributions (see Fig. 3.1), implying that subdivisions based

Algorithm 4: Overview of the spatial division based on elastic or inelastic strain distributions and the computation of the subdomains strain concentration tensors.

```
select elastic material properties for all phases Ω of the RVE domain
for i = 1, ..., 6 do
    perform DNS:
    apply ε̄^(i) (Eq. (3.4)) on RVE domain V
    compute ε(χ)
    compute i-th column of 𝔸^el(χ) (Eq. (3.3)) written in Voigt notation
end
if inelasticity based decomposition then
    set the actual, potentially inelastic, material properties for all phases Ω of the
     RVE domain
    for l = 1, 2 do
        perform DNS:
        apply ε̄^in(l) (Eq. (3.10))
        compute ε^p(l)(χ) and store temporarily
        compute ε_Ω^p(l) and p_Ω^(l) (Eqs. (3.13) and (3.12))
        normalize: ε^p(l)(χ) → φ^(l)(χ) (Eq. (3.14))
        transform: φ^(l)(χ) → q^(l)(χ) (Eq. (3.15))
    end
    assemble q(χ) (Eq. (3.16))
    perform spatial division based on q(χ) (Section 3.2.2)
end
else
    perform spatial division based on 𝔸^el(χ) (Section 3.2.1)
end
for r=1,...,K do
    compute 𝔸_r^el by averaging over V_r (Eq. (3.7))
end
```

on the distribution of elastic strains do not necessarily represent the actual deformation patterns during inelastic deformation. In particular the highly localized plasticity leading to shear band formation in the RVE can not be identified during elastic deformation states of the RVE. Consequently, in order to achieve an improved spatial division into subdomains that represents the physics of a material under inelastic deformation states, micromechanical deformation patterns occurring during inelastic deformation are captured by means of the conduction of simulations containing inelastic deformation in the material. The deformation modes applied on the RVE were selected with the goal to allow an identification of different important deformation patterns inside the RVE, with an emphasis on the formation of the shear band patterns. For the investigated cases of 2D structures in this work, the following biaxial and pure shear deformation boundary modes

$$\overline{\boldsymbol{\varepsilon}}^{\mathrm{in}^{(1)}} = E^{\mathrm{BC,in}}(\vec{e}_x \otimes \vec{e}_x - \vec{e}_y \otimes \vec{e}_y) \tag{3.10a}$$

$$\overline{\boldsymbol{\varepsilon}}^{\mathrm{in}^{(2)}} = E^{\mathrm{BC,in}}(\vec{e}_x \otimes \vec{e}_y + \vec{e}_y \otimes \vec{e}_x) \tag{3.10b}$$

with the overall deformation factor $E^{\mathrm{BC,in}}$ were selected, both resulting in distinct isochoric deformation states and pure shearing in different orientations inside the material. The resulting inelastic deformation patterns are presented in Fig. 3.1.

Note that the consideration of local equivalent plastic strains

$$p(\boldsymbol{\chi}) = \sqrt{\frac{2}{3}\boldsymbol{\varepsilon}^{\mathrm{p}}(\boldsymbol{\chi}) : \boldsymbol{\varepsilon}^{\mathrm{p}}(\boldsymbol{\chi})}\,, \tag{3.11}$$

expressed as scalar values representing the local plastic strain tensors $\boldsymbol{\varepsilon}^{\mathrm{p}}(\boldsymbol{\chi})$, do not contain sufficient information of the actual inelastic field to provide a spatial decomposition that accounts for the physics of an inelastic RVE problem. The highly heterogeneous character of the local plastic strain field $\boldsymbol{\varepsilon}^{\mathrm{p}}(\boldsymbol{\chi})$ comprises local isochoric deformation states represented by different signs of the plastic strain tensor entries. Equivalent plastic strains $p(\boldsymbol{\chi})$ however, do possess of a positive sign, irrespective of the signs of the single plastic strain tensor entries. Therefore, a clustering based on local equivalent plastic strain fields does not allow the account for the actual heterogeneity of the inelastic deformation states, implying that the consideration of all entries of the local plastic strain tensor field $\boldsymbol{\varepsilon}^{\mathrm{p}}(\boldsymbol{\chi})$ is inevitable for a representation of the inelastic deformation states by the subdomains.

After the choice of n_{p} (here $n_{\mathrm{p}} = 2$) different overall strain modes, the distinct simulations $l = 1, ..., n_{\mathrm{p}}$ with the corresponding boundary conditions $\overline{\boldsymbol{\varepsilon}}^{\mathrm{in}^{(l)}}$ (Eq. (3.10)) are performed and the local plastic strain fields $\boldsymbol{\varepsilon}^{\mathrm{p}^{(l)}}(\boldsymbol{\chi})$ computed. It is reiterated that the goal of the inelasticity based spatial decomposition is to account for the dominant inelastic deformation patterns emerging under different loading conditions on the RVE. However, different deformation states of the RVE may lead to different degrees of plastification in the material. If one applied loading case results in a higher degree of plasticity than a second applied loading case, meaning that the magnitude of the local plastic strain tensor field under the first loading case clearly exceeds the one occurring under the second loading case, the use of the k-means clustering would account more for the inelastic patterns under the first loading case than for the inelastic patterns under the second loading case. Therefore, in order to achieve a spatial decomposition that accounts to the same degree for the inelastic patterns emerging under all of the applied loading modes $l = 1, ..., n_{\mathrm{p}}$, the local plastic strain tensor fields $\boldsymbol{\varepsilon}^{\mathrm{p}^{(l)}}(\boldsymbol{\chi})$ are to be normalized by a sensibly chosen quantity that represents the magnitude of plasticity. Since the material phases Ω of the RVE are clustered separately, a reasonable choice for the normalization of the plastic strain fields under the loading mode l inside a specific material phase Ω, expressed as $\boldsymbol{\varepsilon}^{\mathrm{p}^{(l)}}(\boldsymbol{\chi}),\ \forall \boldsymbol{\chi} \in V_\Omega$, is the per-phase equivalent average plastic strain

$$p_\Omega^{(l)} = \sqrt{\frac{2}{3}\boldsymbol{\varepsilon}_\Omega^{\mathrm{p}^{(l)}} : \boldsymbol{\varepsilon}_\Omega^{\mathrm{p}^{(l)}}}\,, \tag{3.12}$$

following from the plastic strain averaged over the corresponding material phase V_Ω

$$\boldsymbol{\varepsilon}_\Omega^{\mathrm{p}^{(l)}} = \frac{1}{|V_\Omega|}\int_{V_\Omega} \boldsymbol{\varepsilon}^{\mathrm{p}^{(l)}}(\boldsymbol{\chi})\mathrm{d}\boldsymbol{\chi}\,. \tag{3.13}$$

In summary, for a capture of the inelastic deformation patterns and localizations under different inelastic loading conditions $l = 1, ..., n_{\mathrm{p}}$, the computed plastic strain fields $\boldsymbol{\varepsilon}^{\mathrm{p}^{(l)}}(\boldsymbol{\chi})$

are normalized as

$$\boldsymbol{\phi}^{(l)}(\boldsymbol{\chi}) = \boldsymbol{\varepsilon}^{\mathrm{p}^{(l)}}(\boldsymbol{\chi})/p_{\Omega}^{(l)}, \quad \forall \boldsymbol{\chi} \in V_{\Omega}\,. \tag{3.14}$$

The Voigt notation is used for the transformation

$$\boldsymbol{\phi}^{(l)}(\boldsymbol{\chi}) \rightarrow \boldsymbol{q}^{(l)}(\boldsymbol{\chi}) \tag{3.15}$$

to obtain the local 6×1 vectors $\boldsymbol{q}^{(l)}(\boldsymbol{\chi})$[1]. Following, the normalized plastic strain fields are arranged in local $1 \times 6\,n_{\mathrm{P}}$ vectors

$$\boldsymbol{q}(\boldsymbol{\chi}) = \left(\boldsymbol{q}^{(1)^T}(\boldsymbol{\chi})\,, \ldots\,, \boldsymbol{q}^{(n_{\mathrm{P}})^T}(\boldsymbol{\chi})\right)^{\mathrm{T}}, \tag{3.16}$$

representing the entirety of the local inelastic fields. A k-means clustering procedure similar to the one described above for the fourth-order elastic strain concentration tensors (Section 3.2.1) is performed, dividing all discrete material points in the considered RVE phase Ω into a number of K_{Ω} partitions r containing N_r data points based on the similarities of the local vectors $\boldsymbol{q}(\boldsymbol{\chi})$. The optimal decomposition is achieved by a minimization of the function

$$J[\boldsymbol{q}(\boldsymbol{\chi})] = \sum_{r=1}^{K_{\Omega}} \sum_{i=1}^{N_r} |\boldsymbol{q}(\boldsymbol{\chi}_i) - \boldsymbol{q}_r|^2, \quad \boldsymbol{\chi} \in V_{\Omega}, \quad \boldsymbol{\chi}_i \in V_r \subset V_{\Omega}, \quad r \in 1, ..., K_{\Omega}\,, \tag{3.17}$$

where

$$|\boldsymbol{z}| = \sqrt{\boldsymbol{z} \cdot \boldsymbol{z}}\,, \tag{3.18}$$

with the local vectors $\boldsymbol{q}(\boldsymbol{\chi}_i)$ inside the set r and the determined respective subdomain means

$$\boldsymbol{q}_r = \left(\boldsymbol{q}_r^{(1)} \ldots \boldsymbol{q}_r^{(n_{\mathrm{P}})}\right)^{\mathrm{T}} = \frac{1}{|V_r|} \int_{V_r} \boldsymbol{q}(\boldsymbol{\chi}) \mathrm{d}\boldsymbol{\chi}\,. \tag{3.19}$$

After the division of all local points inside the microscopic RVE domain into subdomains based on inelastic fields, the strain concentration tensors $\mathbb{A}_r^{\mathrm{el}}$ of the subdomains r are determined using Eq. (3.7) following the application of the elastic loading modes (detailed in Section 3.2.1) given by Eq. (3.4).

The inelasticity-based spatial division and the computation of the strain concentration tensors are as well summarized in Algorithm 4. The computation of the interaction tensors for the TFA $\mathbb{D}_{rs}$ and for the HS type analysis Γ_{rs} follow in the Sections 3.3.1 and 3.4.3.

3.3 Transformation Field Analysis

The implementation of the TFA based on piecewise uniform fields (Section 2.3.4) of variables is presented for the modeling of nonlinear composite materials. Elasto-plastic constitutive relations are considered for the subdomains (Section 2.5.2). Therefore, the eigenstrains $\boldsymbol{\varepsilon}^*(\boldsymbol{\chi})$ introduced in Section 2.3.2 equal plastic strains $\boldsymbol{\varepsilon}^{\mathrm{p}}(\boldsymbol{\chi})$. The reduced incremental TFA scale coupling relation (Eq. (2.49)) is recalled:

$$\Delta\boldsymbol{\varepsilon}_r = \mathbb{A}_r^{\mathrm{el}} : \Delta\overline{\boldsymbol{\varepsilon}} + \sum_{s=1}^{K} \mathbb{D}_{rs} : \Delta\boldsymbol{\varepsilon}_s^*\,, \tag{3.20}$$

[1] Even for 2D cases, the 6 components of the plastic strain tensor are considered.

where

$$\Delta\boldsymbol{\varepsilon}_s^* = \Delta\boldsymbol{\varepsilon}_s^{\mathrm{p}}. \tag{3.21}$$

The spatial decomposition into subdomains r based on elastic and inelastic strains, and the computation of the subdomains average elastic strain concentration tensors $\mathbb{A}_r^{\mathrm{el}}$ were presented in Section 3.2. The computation of the eigenstrain-strain interaction tensors $\mathbb{D}_{rs}$ between two subdomains r and s, for construction of the CAH scheme in Eq. (3.20), follows in Section 3.3.1. The numerical solution of the TFA CAH scheme was outlined in Section 2.3.5.

3.3.1 Eigenstrain - strain interaction tensors

Algorithm 5: Overview of the computation of the eigenstrain-strain interaction tensors.

```
select elastic material properties for all phases Ω of the RVE domain
for i = 1, ..., 6 do
    for s = 1, ..., K do
        perform DNS:
        apply ε*^(i) (Eq. (3.24)) in the whole subdomain V_s
        compute ε(χ)
        compute i-th column of D_s(χ) (Eq. (3.23)) written in Voigt notation
        for r = 1, ..., K do
            compute i-th column of D_rs in Voigt notation by averaging over V_r
              (Eq. (3.26))
        end
    end
end
```

The TFA homogenization method relies on so-called interaction tensors, describing the elastic influences of eigenstrains at the "radiating" material points on the deformation field inside the RVE. The TFA relation under a vanishing overall strain is expressed following Eq. (2.30). Considering a uniform eigenstrain in one certain subdomain s as

$$\boldsymbol{\varepsilon}^*(\boldsymbol{\chi}') = \boldsymbol{\varepsilon}_s^*, \quad \boldsymbol{\chi}' \in V_s, \tag{3.22}$$

local strains are given as

$$\boldsymbol{\varepsilon}(\boldsymbol{\chi}) = \mathbb{D}_s(\boldsymbol{\chi}) : \boldsymbol{\varepsilon}_s^*, \tag{3.23}$$

with the local interaction function $\mathbb{D}_s(\boldsymbol{\chi})$ estimating the total effect of a uniform eigenstrain in an entire subdomain s on the strain at $\boldsymbol{\chi}$ (no sum over s intended).

The eigenstrain-strain interaction tensors $\mathbb{D}_s(\boldsymbol{\chi})$ are determined by applying a vanishing overall strain, i.e. $\overline{\boldsymbol{\varepsilon}} = 0$, imposed by boundary conditions on the RVE in elasticity. Simultaneously, six orthogonal uniform eigenstrain modes are applied in each "radiating" subdomain s one at a time. The eigenstrain modes, with the eigenstrain factor E^*, in 3D

analyses are

$$\boldsymbol{\varepsilon}_s^{*(1)} = E^* \vec{e}_x \otimes \vec{e}_x \tag{3.24a}$$

$$\boldsymbol{\varepsilon}_s^{*(2)} = E^* \vec{e}_y \otimes \vec{e}_y \tag{3.24b}$$

$$\boldsymbol{\varepsilon}_s^{*(3)} = E^* \vec{e}_z \otimes \vec{e}_z \tag{3.24c}$$

$$\boldsymbol{\varepsilon}_s^{*(4)} = \frac{1}{2} E^* (\vec{e}_x \otimes \vec{e}_y + \vec{e}_y \otimes \vec{e}_x) \tag{3.24d}$$

$$\boldsymbol{\varepsilon}_s^{*(5)} = \frac{1}{2} E^* (\vec{e}_x \otimes \vec{e}_z + \vec{e}_z \otimes \vec{e}_x) \tag{3.24e}$$

$$\boldsymbol{\varepsilon}_s^{*(6)} = \frac{1}{2} E^* (\vec{e}_y \otimes \vec{e}_z + \vec{e}_z \otimes \vec{e}_y), \tag{3.24f}$$

while in 2D analyses, solely the modes $\boldsymbol{\varepsilon}_s^{*(1)}$, $\boldsymbol{\varepsilon}_s^{*(2)}$ and $\boldsymbol{\varepsilon}_s^{*(4)}$ are applied. The reaction strain field $\boldsymbol{\varepsilon}(\boldsymbol{\chi})$ emerging from the vanishing overall strain and each applied eigenstrain mode is computed. Local interaction tensors are fully characterized considering Eq. (3.23) in Voigt-notation and a comparison to the imposed eigenstrains in Eq. (3.24). Averaging the resulting strain field $\boldsymbol{\varepsilon}(\boldsymbol{\chi})$ over a certain subdomain V_r to achieve the subdomain strain

$$\boldsymbol{\varepsilon}_r = \frac{1}{|V_r|} \int_{V_r} \boldsymbol{\varepsilon}(\boldsymbol{\chi}) \, \mathrm{d}\boldsymbol{\chi} = \left[\frac{1}{|V_r|} \int_{V_r} \mathbb{D}_s(\boldsymbol{\chi}) \, \mathrm{d}\boldsymbol{\chi} \right] : \boldsymbol{\varepsilon}_s^* \tag{3.25}$$

leads to the characterization of the interaction tensors

$$\mathbb{D}_{rs} = \frac{1}{|V_r|} \int_{V_r} \mathbb{D}_s(\boldsymbol{\chi}) \, \mathrm{d}\boldsymbol{\chi} \tag{3.26}$$

between subdomains, such that

$$\boldsymbol{\varepsilon}_r = \mathbb{D}_{rs} : \boldsymbol{\varepsilon}_s^* \quad \forall r, s \in 1, ..., K \, . \tag{3.27}$$

In summary, the local fourth-order interaction tensors $\mathbb{D}_{rs}$ represent elastic influence factors of a uniform eigenstrain in the subdomain s on the average strain in the subdomain r. The determination of the interaction tensors $\mathbb{D}_{rs}$ is summarized in the Algorithm 5.

3.3.2 Account for plastic fluctuations

While the TFA used as a full-field modeling method as in Eq. (2.33) would lead to correct predictions of the materials behavior (Dvorak, Bahei-El-Din, and Wafa, 1994), it was recognized that, using the approximation of averages over subdomains, the tangent behavior of the material during inelastic deformation may be strongly overestimated. This overstiff modeled behavior is a consequence of underestimated occurring plastic strain in plastically highly compliant material phases. Considering the numerical TFA approach, too low plastic strains imply underestimated interaction effects between the phases and therefore inaccurate strain distributions over the phases, in particular underestimated strains in plastic phases and therefore overestimated strain accumulations in stiff phases. Overestimated strain accumulations in stiff phases lead effectively to an overstiff behavior of the overall composite material.

Chaboche et al. (2001) proposed an approach to artificially increase plastic strains in plastic subdomains by a consideration of a type of subdomains instantaneous strain concentration tensors. However, this approach has the following limitations: the used subdomains instantaneous strain concentration tensors are computed as the asymptotic strain concentration tensors, dependent solely on the known subdomains asymptotic tangent stiffness (not equivalent to the subdomain tangent stiffness in Eq. (2.197)). Firstly, the asymptotic tangent stiffness cannot be used for a nonlinear hardening behavior, where the subdomains tangent stiffness is not constant. Secondly, the subdomains instantaneous strain concentration tensors can generally not be computed just from the local tangent stiffness. For an accurate estimation of the instantaneous strain concentration tensor, the overall tangent stiffness needs to be known as well (Aboudi, Arnold, and Bednarcyk, 2013; Dvorak, 1992).

In the following, it is accounted for a physical explanation of the overstiff material behavior during inelastic deformation. The instantaneous spatial strain distribution in a material domain is constant as long as the material is deforming purely linear-elastic. This holds even if the material has experienced previous inelastic deformation. The stable strain distribution under elastic loads implies that it can be correctly recovered by means of the constant, once for all numerically determined, elastic strain concentration tensors. The constant strain distribution, however, does not hold for inelastic behavior of the material phases. Plastic strain is a direct consequence of the amount of local deformations during inelastic material behavior (Section 2.5.2). It means that high fluctuations in the localization of deformation are directly correlated to high plastic field fluctuations. Thus, plastic field fluctuations can be regarded as a marker for the heterogeneity of the local deformation field. In subdomains with deformations considered as uniform, the microscopic yield starting points, and therefore the heterogeneity of the local onsets of nonlinear behavior, are not well-represented. It implies that a certain degree of considered uniform, although actually heterogeneous, deformation $\boldsymbol{\varepsilon}_r$ of the subdomain leads to effectively underestimated plastic yielding and thus plastic strains. This underestimation worsens if the deformation accumulates in very localized zones, unable to be covered by the subdomains. Therefore, the more heterogeneous the actual deformation field in a subdomain, the higher becomes the underestimation of the plastic strain due to the considered uniform deformation. The use of the TFA method using a finer decomposition into subdomains is motivated by a more accurate representation of the highly heterogeneous plastic field, resulting in a less stiff overall behavior of the material. If the inelastic field fluctuations are fully taken into account and the tangent behavior of the material can be estimated correctly (see the non-uniform TFA, Michel and Suquet (2003)).

Algorithm 6: Overview of the calculation of the PFC factors.

Plastic strain fields $\boldsymbol{\varepsilon}^{\mathrm{p}^{(l)}}(\boldsymbol{\chi}),\ l = 1, 2$ are stored according to Algorithm 4.
for *r=1,...,K* **do**
  for $l = 1, 2$ **do**
    compute $p^{(l)}(\boldsymbol{\chi})$ (Eq. (3.31))
    compute $p_r^{(l)}$ and $\hat{p}_r^{(l)}$ (Eqs. (3.33) and (3.34))
    compute $\alpha_r^{(l)}$ (Eq. (3.35))
  end
end

In order to use the uniform TFA method and account for the problem of underestimated inelastic and interaction effects in the subdomains due to the not well-captured deformation field heterogeneities, an artificial increase for the subdomains eigenstrain as in

$$\Delta\boldsymbol{\varepsilon}_r^{*\mathrm{corr}} = \Delta p_r^{\mathrm{corr}} \boldsymbol{N}_r^{\mathrm{corr}} = f_r^{\mathrm{PFC}}\big(\boldsymbol{\varepsilon}_r^{\mathrm{p}}(\boldsymbol{\chi})\big)\, \Delta\boldsymbol{\varepsilon}_r^{*} \tag{3.28}$$

is sought, with a plastic fluctuation correction (PFC) function f_r^{PFC} that depends on the magnitude of the fluctuations of the in-subdomain plastic field $\boldsymbol{\varepsilon}_r^{\mathrm{p}}(\boldsymbol{\chi})$. Since in case of a perfectly fine subdivision, and therefore no plastic fluctuations, the TFA leads to correct results, f_r^{PFC} must satisfy

$$\Delta\boldsymbol{\varepsilon}_r^{*\mathrm{corr}} \to \Delta\boldsymbol{\varepsilon}_r^{*}, \quad \text{if}\, \boldsymbol{\varepsilon}_r^{\mathrm{p}}(\boldsymbol{\chi}) \to \boldsymbol{\varepsilon}_r^{\mathrm{p}}\,, \quad \boldsymbol{\chi} \in V_r\,. \tag{3.29}$$

The Eq. (3.29) means that the artificial correction needs to vanish if the local plastic strain field $\boldsymbol{\varepsilon}_r^{\mathrm{p}}(\boldsymbol{\chi})$ is actually uniform, occurring if ,e.g., $K \to \infty$. In this work, a first approach is tested, where f_r^{PFC} is considered as a scalar function $f_r^{\mathrm{PFC}} = \alpha_r$, correcting the subdomains equivalent plastic strain, while the plastic flow direction is not manipulated:

$$\Delta p_r^{\mathrm{corr}} = \alpha_r \Delta p_r\,, \quad \boldsymbol{N}_r^{\mathrm{corr}} = \boldsymbol{N}_r. \tag{3.30}$$

The particular proposed PFC factors in this paper are determined offline as the square root of the ratio between the arithmetic means $p_r^{(l)}$ and the harmonic means $\hat{p}_r^{(l)}$ of the plastic fields inside the subdomains. Therefore, the PFC factors can be determined once for all after the application of the BC in Eq. (3.10) for the inelasticity based spatial decomposition (Section 3.2.2). In the following, the procedure leading to the determination of the PFC correction for the subdomain r is described: After the RVE domain was subdivided into a certain number of subdomains based on the plastic fields $\boldsymbol{\varepsilon}^{\mathrm{p}^{(l)}}(\boldsymbol{\chi})$ under the loading modes $l = 1, ..., n_{\mathrm{p}}$, the computed equivalent plastic strain field

$$p^{(l)}(\boldsymbol{\chi}) = \sqrt{\frac{2}{3}\boldsymbol{\varepsilon}^{\mathrm{p}^{(l)}}(\boldsymbol{\chi}) : \boldsymbol{\varepsilon}^{\mathrm{p}^{(l)}}(\boldsymbol{\chi})} \tag{3.31}$$

is analyzed. Considering the equivalent plastic fields inside the subdomain r under each mode

$$p_r^{(l)}(\boldsymbol{\chi}) = p^{(l)}(\boldsymbol{\chi}), \quad \boldsymbol{\chi} \in V_r, \tag{3.32}$$

the arithmetic mean $p_r^{(l)}$ and the harmonic mean $\hat{p}_r^{(l)}$ are achieved using

$$p_r^{(l)} = \frac{1}{|V_r|}\int_{V_r} p^{(l)}(\boldsymbol{\chi})\mathrm{d}\boldsymbol{\chi} \tag{3.33}$$

and

$$\hat{p}_r^{(l)} = \left[\frac{1}{|V_r|}\int_{V_r} \frac{\mathrm{d}\boldsymbol{\chi}}{p^{(l)}(\boldsymbol{\chi})}\right]^{-1}. \tag{3.34}$$

Consequently, one PFC factor $\alpha_r^{(l)}$ for the subdomain r is determined under each of the n_{p} inelastic offline deformation modes l as a measure of the heterogeneity of the corresponding in-subdomain plastic fields $\boldsymbol{\varepsilon}_r^{\mathrm{p}^{(l)}}(\boldsymbol{\chi})$.

In cases of non-uniform distributions, the harmonic mean is always lower than the arithmetic mean. Since the harmonic mean is close to zero as soon as only a low number

of material points exhibit no or very low plastic strains, a lower limit of plasticity inside the subdomain must be defined in order to achieve reasonable correction factors. Here, the PFC for a subdomain r is solely taken into account if $p_r^{(l)} \geq p_\Omega^{(l)}$, implying a sufficiently high harmonic mean of the plastic field. The formulation of the PFC finally reads

$$\alpha_r^{(l)} = \begin{cases} \sqrt{p_r^{(l)} / \hat{p}_r^{(l)}}\,, & p_r^{(l)} > p_\Omega^{(l)} \\ 1\,, \quad \text{otherwise.} \end{cases} \tag{3.35}$$

The procedure towards the calculation of the correction factors is summarized in Algorithm 6.

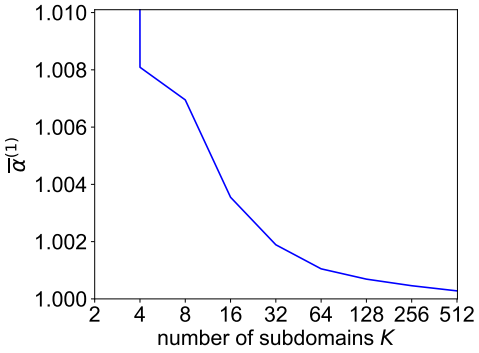

FIGURE 3.2: Exemplary computed total plastic fluctuation correction resulting from the application of the deformation mode $l = 1$ described in Eq. (3.10a) on the composite material with the volume fraction of inclusions $v_{\mathrm{II}} = 30$ % considered in Section 3.5.2.

The expression Eq. (3.35) results in increasing corrections for the subdomains r the more the considered plastic field in the subdomain r varies. An increasing number of subdomains implies decreasing plastic field heterogeneities inside the subdomains and therefore decreasing correction effects as a function of the numbers of subdomains. The evolution of the total corrections

$$\bar{\alpha}^{(l)} = \sum_{r=1}^{K} v_r \alpha_r^{(l)} \tag{3.36}$$

as a function of the used number of subdomains is presented in Fig. 3.2 for the exemplary case of the corrections $\alpha_r^{(1)}$ determined under the deformation mode $l = 1$ (Eq. (3.10a)). An additional restriction for the use of the PFC is mentioned: for reasons of an irregular behavior of the correction factors in the range of very low numbers of subdomains causing unreliable TFA modeling results, the PFC was not integrated for numbers of subdomains $K < 8$. For higher numbers of subdomains beyond the defined cut-off number of subdomains, i.e. for $K \geq 8$, a clear logarithmic decrease of the total correction $\bar{\alpha}^{(1)}$ under an increasing number of subdomains is recognized. The selection of the correction factor α_r out of the pool $\alpha_r^{(1)}, ..., \alpha_r^{(n_\mathrm{P})}$ during the online stage is based on the current loading conditions, i.e. follows the consideration of the dominant component of the current overall

strain increment $\Delta\overline{\boldsymbol{\varepsilon}}$, with, for 2D problems:

$$\alpha_r = \begin{cases} \alpha_r^{(1)}, & \text{if } \Delta\overline{\boldsymbol{\varepsilon}}_{11} > \Delta\overline{\boldsymbol{\varepsilon}}_{12} \text{ or } \Delta\overline{\boldsymbol{\varepsilon}}_{22} > \Delta\overline{\boldsymbol{\varepsilon}}_{12} \\ \alpha_r^{(2)}, & \text{if } \Delta\overline{\boldsymbol{\varepsilon}}_{12} > \Delta\overline{\boldsymbol{\varepsilon}}_{11} \text{ and } \Delta\overline{\boldsymbol{\varepsilon}}_{12} > \Delta\overline{\boldsymbol{\varepsilon}}_{22}. \end{cases} \tag{3.37}$$

With a correction factor selection that depends on the current loading expressed by the homogenized strain increment $\Delta\overline{\boldsymbol{\varepsilon}}$, the correction factors can as well be applied for non-proportional loading histories $\overline{\boldsymbol{\varepsilon}}(t)$ containing different loading stages. If more different offline deformation modes were applied, the correction factor under the current loading could be selected based on minimal deviations between the various offline deformation modes $\overline{\boldsymbol{\varepsilon}}^{\mathrm{in}(l)}$ and the current strain increment, i.e. $\alpha_r = \alpha_r^{(k)}$ if $||\Delta\overline{\boldsymbol{\varepsilon}} - \overline{\boldsymbol{\varepsilon}}^{\mathrm{in}(k)}||^2 \leq ||\Delta\overline{\boldsymbol{\varepsilon}} - \overline{\boldsymbol{\varepsilon}}^{\mathrm{in}(m)}||^2, \quad \forall m,\, k \neq m$ (where, in order to allow this comparison, all strain tensors should be normalized by their own equivalent values). The proposed PFC in Eq. (3.28) with Eq. (3.30) modifies the original TFA constitutive equation Eq. (2.49) in incremental formulation to

$$\Delta\boldsymbol{\varepsilon}_r = \mathbb{A}_r^{\mathrm{el}} : \Delta\overline{\boldsymbol{\varepsilon}} + \sum_{s=1}^{K} \alpha_s \mathbb{D}_{rs} : \Delta\boldsymbol{\varepsilon}_s^*. \tag{3.38}$$

Considering the property given in Eq. (2.48), which arises from the numerical evaluation of the tensors $\mathbb{D}_{rs}$ (Section 3.3.1), the modified condition for the interaction tensors

$$\sum_{r=1}^{K} \alpha_s v_r \mathbb{D}_{rs} = \alpha_s \left(\sum_{r=1}^{K} v_r \mathbb{D}_{rs} \right) = \mathbf{0}, \quad \forall s \in 1, ..., K \tag{3.39}$$

is automatically satisfied.

3.3.3 Numerical Resolution of the TFA with PFC factor

The numerical solution of the TFA was presented in Section 2.3.5. Here, the solution scheme for the TFA is reiterated, however with the integration of the PFC correction factors. The iterative incremental solution of the TFA, with the integration of the PFC factors α_s (Eq. (3.37)), for the overall RVE response under a prescribed overall strain $\bar{\boldsymbol{\varepsilon}}$, is expressed as

$$\Delta\boldsymbol{\varepsilon}_r - \mathbb{A}_r^{\mathrm{el}} : \Delta\overline{\boldsymbol{\varepsilon}} - \sum_{s=1}^{K} \alpha_s \mathbb{D}_{rs} : \Delta\boldsymbol{\varepsilon}_s^* = 0\,, \tag{3.40}$$

where $\alpha_s = 1$ if no PFC is desired. The numerical solution

$$\boldsymbol{F}_r \rightarrow \boldsymbol{F}_r + \delta\boldsymbol{F}_r = 0\,, \tag{3.41}$$

with

$$\delta[\boldsymbol{F}] = \{\mathbb{J}\} : \delta[\boldsymbol{\varepsilon}] + \frac{\partial[\boldsymbol{F}]}{\partial\overline{\boldsymbol{\varepsilon}}} : \delta\overline{\boldsymbol{\varepsilon}}\,, \tag{3.42}$$

where $K \times 1$ block column vectors denoted by "[ ]" and the square $K \times K$ block matrices denoted by "{ }", is now achieved, under a constant homogenized strain per iteration

Algorithm 7: Numerical TFA procedure with PFC at a glance: Newton-Raphson scheme at one load step for a given overall strain increment $\Delta\overline{\boldsymbol{\varepsilon}}$.

initialize: $\Delta\boldsymbol{\varepsilon}_r = \mathbb{A}_r^{\mathrm{el}} : \Delta\overline{\boldsymbol{\varepsilon}}$ $(r = 1, ..., K)$
iterative procedure:
repeat
  for $r = 1, K$ **do**
    call constitutive relations for subdomain r to compute $\boldsymbol{\sigma}_r$, $\Delta\boldsymbol{\varepsilon}_r^*$ and $\partial\Delta\boldsymbol{\varepsilon}_r^*/\partial\boldsymbol{\varepsilon}_r$, $\mathbb{C}_r^{\mathrm{alg}}$ (details in Section 2.5)
  end
  for $r = 1, K$ **do**
    initialize residual $\boldsymbol{F}_r = \Delta\boldsymbol{\varepsilon}_r - \mathbb{A}_r^{\mathrm{el}} : \Delta\overline{\boldsymbol{\varepsilon}}$
    for $s = 1, K$ **do**
      select correction factor α_s according to the criterion in Eq. (3.37)
      add eigenstrain interaction contribution to residual:
      $\boldsymbol{F}_r = \boldsymbol{F}_r - \sum_s \alpha_s \mathbb{D}_{rs} : \Delta\boldsymbol{\varepsilon}_s^*$
      compute Jacobian matrix $\mathbb{J}_{rs} = \delta_{rs}\mathbb{I} - \alpha_s\mathbb{D}_{rs} : (\partial\Delta\boldsymbol{\varepsilon}_s^*/\partial\boldsymbol{\varepsilon}_s)$
    end
  end
  solve $\delta[\boldsymbol{\varepsilon}] = \{\mathbb{J}\}^{-1} : [\boldsymbol{F}]$
  update $[\Delta\boldsymbol{\varepsilon}] = [\Delta\boldsymbol{\varepsilon}] - \delta[\boldsymbol{\varepsilon}]$
until $|[\boldsymbol{F}]| <$ tol;
after convergence:
compute $\overline{\boldsymbol{\sigma}}$ and $\overline{\mathbb{C}}^{\mathrm{alg}}$, following Eq. (2.65) and Eq. (2.70), respectively.

and thus $\delta\overline{\boldsymbol{\varepsilon}} = 0$, by the construction of the subdomain residuals

$$\boldsymbol{F}_r = \Delta\boldsymbol{\varepsilon}_r - \mathbb{A}_r^{\mathrm{el}} : \Delta\overline{\boldsymbol{\varepsilon}} - \sum_{s=1}^{K} \alpha_s \mathbb{D}_{rs} : \Delta\boldsymbol{\varepsilon}_s^* \tag{3.43}$$

and the Jacobian system $\{\mathbb{J}\}$, consisting of the single matrices (no sum on s intended)

$$\mathbb{J}_{rs} = \frac{\partial \boldsymbol{F}_r}{\partial \boldsymbol{\varepsilon}_s} = \delta_{rs}\mathbb{I} - \alpha_s\mathbb{D}_{rs} : \frac{\partial\Delta\boldsymbol{\varepsilon}_s^*}{\partial\boldsymbol{\varepsilon}_s}, . \tag{3.44}$$

3.4 Hashin-Shtrikman type analysis

As an alternative approach to the TFA (Section 3.3), the HS type analysis introduced in Sections 2.3.6 and 2.3.7, is deployed for the CAH of the mechanics of nonlinear composites. The reduced incremental HS scale coupling relation (Eq. (2.97)) is recalled:

$$\Delta\boldsymbol{\varepsilon}_r = \Delta\overline{\boldsymbol{\varepsilon}} + \sum_{s=1}^{K} \Gamma_{rs} : \left(\Delta\boldsymbol{\sigma}_s - \mathbb{C}^{\mathrm{iso}} : \Delta\boldsymbol{\varepsilon}_s\right), \tag{3.45}$$

relying on the isotropic stiffness operator $\mathbb{C}^{\text{iso}}$ of the reference medium and the Green's interaction tensors in the reference medium

$$\Gamma_{rs} = f\big((\mathbb{C}^{\text{iso}})^{-1}\big) \propto (\mathbb{C}^{\text{iso}})^{-1} \,. \tag{3.46}$$

Details on the construction of the CAH model in Eq. (3.45) will be given subsequently. The definition of the nonlinear reference medium with the stiffness $\mathbb{C}^{\text{iso}}$, accounting for nonlinear homogenized responses, and the determination of the Green's tensors Γ_{rs} in the nonlinear medium, will be presented in Section 3.4.1. As for the TFA, both elastic and inelastic decompositions into subdomains, presented in Section 3.2, will be tested.

3.4.1 Definition of the reference medium

For reasons outlined in the Section 2.3.7, the proposed reference medium that has the total secant stiffness of the homogenized composite (Wulfinghoff, Cavaliere, and Reese, 2018), was replaced by a reference medium with an isotropic incremental tangent stiffness, referred to as $\mathbb{C}^{\text{iso}}$. The reference stiffness $\mathbb{C}^{\text{iso}}$ is assumed to depends only on an updated algorithmic shear modulus (see Section 2.3.7 for details), defined as the homogenized incremental shear modulus:

$$G = \overline{G}^{\mathbf{alg}} = \frac{\Delta \overline{\sigma}^{\text{eq}}}{3\,\Delta \overline{\varepsilon}^{\text{eq}}} \,. \tag{3.47}$$

With an isotropic reference stiffness that depends only on an updated algorithmic shear modulus (see Section 2.3.7 for details), expressed as $\mathbb{C}^{\text{iso}}(\overline{G}^{\mathbf{alg}})$, it can be scaled from the isotropic stiffness of the elastic reference medium, $\mathbb{C}^{0,\text{iso}}$, as

$$\mathbb{C}^{\text{iso}}(\overline{G}^{\mathbf{alg}}) = \frac{\overline{G}^{\mathbf{alg}}}{G^0}\,\mathbb{C}^{0,\text{iso}} \,, \tag{3.48}$$

where G^0 is the elastic reference shear modulus. Following Eq. (3.46), the instantaneous Green's tensors during inelastic deformation of the material, Γ_{rs}, can then be scaled as

$$\Gamma_{rs} = \Gamma^0_{rs} : \mathbb{C}^{0,\text{iso}} : (\mathbb{C}^{\text{iso}})^{-1} = \frac{G^0}{\overline{G}^{\mathbf{alg}}}\,\Gamma^0_{rs} \,, \tag{3.49}$$

where

$$\Gamma^0_{rs} = f\big((\mathbb{C}^{0,\text{iso}})^{-1}\big) \propto (\mathbb{C}^{0,\text{iso}})^{-1} \tag{3.50}$$

are the Green's interaction tensors in the elastic reference medium with the stiffness $\mathbb{C}^{0,\text{iso}}$. The scaling of the reference stiffness and the Green's tensors, according to Eqs. (3.48) and (3.49), allows the reformulation of Eq. (3.45) towards

$$\Delta\boldsymbol{\varepsilon}_r = \Delta\overline{\boldsymbol{\varepsilon}} + \sum_{s=1}^{K} \Gamma^0_{rs} : \left(\frac{G^0}{\overline{G}^{\mathbf{alg}}} \Delta\boldsymbol{\sigma}_s - \mathbb{C}^{0,\text{iso}} : \Delta\boldsymbol{\varepsilon}_s \right) , \tag{3.51}$$

with more details given in Section 2.3.7. The numerical solution of the HS type analysis was outlined in Section 2.3.8.

Considering the Eq. (3.51), and with an homogenized algorithmic shear modulus $\overline{G}^{\mathbf{alg}}$ that is computed and updated during the solution stage, the linear elastic reference medium with the isotropic stiffness $\mathbb{C}^{0,\text{iso}}$ and shear modulus G^0 needs to be determined

offline, as well as the Green's interaction tensors Γ^0_{rs} between two subdomains r and s in the elastic isotropic reference medium. The evaluation of these quantities will follow in the Sections 3.4.2 and 3.4.3.

3.4.2 Elastic homogeneous and isotropic reference stiffness

The homogenized elastic stiffness of the material body $\overline{\mathbb{C}}^{\mathrm{el}}$ is, following Eq. (2.29), computed as

$$\overline{\mathbb{C}}^{\mathrm{el}} = \frac{d\overline{\boldsymbol{\sigma}}}{d\overline{\boldsymbol{\varepsilon}}} = \frac{1}{|V|}\int_V \mathbb{C}^{\mathrm{el}}(\boldsymbol{\chi}) : \mathbb{A}^{\mathrm{el}}(\boldsymbol{\chi})\mathrm{d}\boldsymbol{\chi}\,. \tag{3.52}$$

The approach proposed by Moakher and Norris (2006), yielding the closest isotropic stiffness tensor to an anisotropic one based on the minimal Euclidean distance, is used to determine the isotropic elastic reference stiffness

$$\mathbb{C}^{0,\mathrm{iso}} = 3\,\kappa^0\,\mathbb{I}^{\mathrm{vol}} + 2\,G^0\,\mathbb{I}^{\mathrm{dev}}\,, \tag{3.53}$$

where

$$\mathbb{I}^{\mathrm{vol}} = \frac{1}{3}\boldsymbol{I}\otimes\boldsymbol{I}, \tag{3.54}$$

$$\mathbb{I}^{\mathrm{dev}} = \mathbb{I} - \mathbb{I}^{\mathrm{vol}} \tag{3.55}$$

and $\boldsymbol{I}$ and $\mathbb{I}$ are the second and fourth order unity tensors. The equivalent homogenized bulk modulus κ^0 and shear modulus G^0 are determined as

$$\kappa^0 = \frac{1}{3}\,\mathrm{Tr}(\overline{\mathbb{C}}^{\mathrm{el}} : \mathbb{I}^{\mathrm{vol}}) \tag{3.56}$$

and

$$G^0 = \frac{1}{10}\,\mathrm{Tr}(\overline{\mathbb{C}}^{\mathrm{el}} : \mathbb{I}^{\mathrm{dev}})\,, \tag{3.57}$$

where the trace of a fourth order tensor is computed as

$$\mathrm{Tr}(\mathbb{Z}) = \mathbb{Z}_{ijij} \tag{3.58}$$

using the Einstein convention.

3.4.3 Green's interaction tensors

Following Section 3.4.1, the influence function $\Gamma^0(\boldsymbol{\chi},\boldsymbol{\chi}')$ is computed inside the homogeneous medium with the isotropic stiffness $\mathbb{C}^{0,\mathrm{iso}}$. In a domain with the homogeneous stiffness $\mathbb{C}^{0,\mathrm{iso}}$, the polarization stress field $\boldsymbol{\tau}(\boldsymbol{\chi})$ in Eq. (2.18) equals the externally applied eigenstress field $\boldsymbol{\sigma}^*(\boldsymbol{\chi})$. With a vanishing overall strain $\overline{\boldsymbol{\varepsilon}} = 0$, and a uniform eigenstress $\boldsymbol{\sigma}^*_s$ inside one subdomain s, the average strain in a subdomain r is, following Eq. (2.74), given as

$$\boldsymbol{\varepsilon}_r = \Gamma^0_{rs} : \boldsymbol{\sigma}^*_s. \tag{3.59}$$

The influence tensors $\Gamma^0_{rs} = f\big((\mathbb{C}^{0,\mathrm{iso}})^{-1}\big)$ can be fully characterized by applying the uniform eigenstress modes

$$\boldsymbol{\sigma}^*(\boldsymbol{\chi}') = \boldsymbol{\sigma}^*_s,\ \boldsymbol{\chi}' \in V_s\,, \quad s = 1,\ldots K \tag{3.60}$$

Algorithm 8: Overview of the computation of the elastic Greens polarization stress-strain interaction tensors, computed as the elastic eigenstress-strain interaction tensors in the elastic homogeneous medium.

```
select linear elastic material properties for all phases Ω of the RVE domain
for i = 1, ..., 6 do
    apply ε̄^(i) (Eq. (3.4)) on RVE domain V
    compute ε(χ)
    compute i-th column of 𝔸^el(χ) (Eq. (3.3)) written in Voigt notation
end
compute ℂ̄^el (Eq. (3.52))
determine ℂ^0,iso from ℂ̄^el (Eq. (3.53))
generate a copy of the RVE domain with a homogeneous linear elastic behavior
  with ℂ^el(χ) = ℂ^0,iso
for i = 1, ..., 6 do
    for s = 1, ..., K do
        perform DNS:
        apply σ*^(i) (Eq. (3.61)) in the whole subdomain V_s
        compute ε(χ)
        compute i-th column of Γ^0_s(χ) written in Voigt notation
        for r = 1, ..., K do
            compute i-th column of Γ^0_rs in Voigt notation by averaging over V_r
        end
    end
end
```

in each subdomain V_s one at a time, simultaneously to the fixed zero overall strain $\overline{\boldsymbol{\varepsilon}} = 0$, and computing the average strain in the subdomain V_r. The eigenstrain modes in 3D analyses are

$$\boldsymbol{\sigma}_s^{*(1)} = S^* \vec{e}_x \otimes \vec{e}_x \tag{3.61a}$$

$$\boldsymbol{\sigma}_s^{*(2)} = S^* \vec{e}_y \otimes \vec{e}_y \tag{3.61b}$$

$$\boldsymbol{\sigma}_s^{*(3)} = S^* \vec{e}_z \otimes \vec{e}_z \tag{3.61c}$$

$$\boldsymbol{\sigma}_s^{*(4)} = \frac{1}{2} S^* (\vec{e}_x \otimes \vec{e}_y + \vec{e}_y \otimes \vec{e}_x) \tag{3.61d}$$

$$\boldsymbol{\sigma}_s^{*(5)} = \frac{1}{2} S^* (\vec{e}_x \otimes \vec{e}_z + \vec{e}_z \otimes \vec{e}_x) \tag{3.61e}$$

$$\boldsymbol{\sigma}_s^{*(6)} = \frac{1}{2} S^* (\vec{e}_y \otimes \vec{e}_z + \vec{e}_z \otimes \vec{e}_y), \tag{3.61f}$$

with the eigenstress factor S^*. In 2D analyses, the modes $\boldsymbol{\sigma}_s^{*(1)}$, $\boldsymbol{\sigma}_s^{*(2)}$ and $\boldsymbol{\sigma}_s^{*(4)}$ are applied.

3.4.4 Quantification of the computational reduction

The computational effort for the solution of a numerical problem in the computational solid mechanics at one load step has two main contributions:

1. The computation of local fields of variables. Constitutive equations need to be evaluated at every integration point, implying a linear increase in the computational time for this task under an increase of the number of integration points.

2. The solution of the system of equations. The size of the system of equations is #DOF × #DOF, meaning a quadratic increase of the solution effort under an increasing number of the DOF.

In a DNS using FE, the Gauss integration points build the integration domain of the problem. The number of DOF follows from the number of nodes, depending on the mesh size for the problem. Both the size of the integration domain and the number of nodes depend on the required mesh size and the polynomial order for the basis functions. In this work, the typical mesh for 2D problems consists of an approximate number of $30,000$ triangular elements with quadratic basis functions, corresponding to approximately 90.000 integration points, $60,000$ nodes and thus $\#\text{DOF}^{\text{DNS}} = 120.000$, corresponding to a stiffness matrix of the size $\#\text{DOF}^{\text{DNS}} \times \#\text{DOF}^{\text{DNS}}$. However it is noted that the stiffness matrix of a FE solution is sparse, and the computational effort for the solution can be significantly reduced using sparsification algorithms.

The typical number of subdomains for the TFA homogenization lies in the order of magnitude of $K \approx 10^2$. Using the HS approach, numbers of subdomains in the order of magnitude $K \approx 10$ may be sufficient in some cases. The detailed CAH results in dependence of the numbers of subdomains will be presented in Section 3.5. The number of integration points equals K, the number of subdomains with uniform fields of variables. The number of DOF are given by $K \times$ the number of independent strain tensor entries. In 2D, the number of DOF amounts to $\#\text{DOF}^{\text{TFA}} = 3K$ and the numerical system to be solved has the size $\#\text{DOF}^{\text{TFA}} \times \#\text{DOF}^{\text{TFA}} = 9 \cdot K \times K$. The entries $\mathbb{J}_{rs}$ of the matrix system $\{\mathbb{J}\}$ to be numerically inverted are all non-zero, meaning that $\{\mathbb{J}\}$ cannot be significantly sparsified. The comparison of the computational times was performed for one numerical test, with the results presented in Table 3.4 in Section 3.5.2.

3.5 Numerical Applications

In this section, numerical applications of the TFA and HS schemes developed in this work are presented. Details of the offline and online stages, and the numerical results of applying the methods to different periodic two-phase structures with varying inclusion phase volume fractions, elastic and inelastic material properties and degrees of anisotropy, displayed in Fig. 3.3, are presented. The analyzed material systems are

- A linear-elastic circular inclusion phase with isotropic elasticity in an elasto-plastic matrix phase in Section 3.5.2. Different volume fractions of the inclusion phase $v_{\text{II}} = 20$ %, 30 % and 50 % in one small and one larger RVE were considered. The associated microstructures are presented in Figs. 3.3a, 3.3b, 3.3d and 3.3e, respectively. Triangular meshes with second-order elements were used for the mesh. The respective numbers of elements of the created meshes for these four RVEs are 26508, 27656, 40278, 40460.

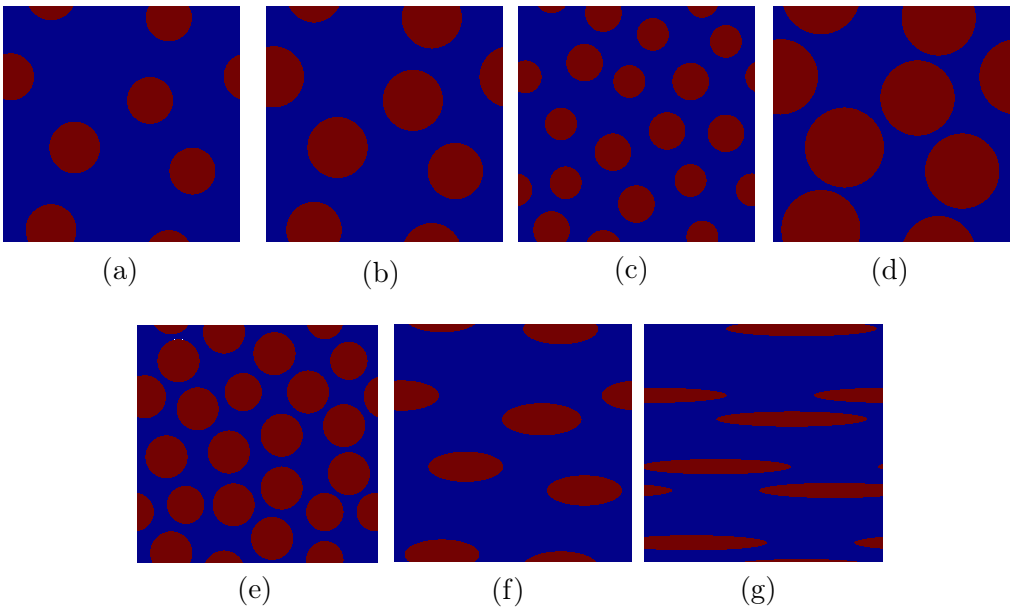

FIGURE 3.3: RVEs with different investigated microstructures: (a-e) Isotropic structures with the volume fractions of inclusions v_{II} = of (a) 20 %, (b,c) 30 %, (d,e) 50 %, and (f,g) anisotropic microstructures with the inclusions aspect ratios (f) 2.5 and (g) 10.

- Circular inclusions with higher and with lower elastic stiffness than the matrix phase and elasto-plastic behavior of both inclusion and matrix phases in Section 3.5.3. For this material system, the volume fraction of inclusions $v_{\mathrm{II}} = 30$ % with the associated RVE (Fig. 3.3b) and mesh were considered.

- Circular elastic inclusions with rubber-like mechanical properties, characterized by a vanishing shear resistance in Section 3.5.4. For this material system, a larger RVE with $v_{\mathrm{II}} = 30$ %, displayed in Fig. 3.3c, was used. The created mesh consisted of 30946 triangular second-order elements.

- A linear-elastic inclusion phase with transverse-isotropic elasticity in an elasto-plastic matrix phase for the case of elongated inclusions in Section 3.5.5. One volume fraction of inclusions $v_{\mathrm{II}} = 20$ % was considered, with two different degrees of anisotropy, represented by the aspect ratios 2.5 and 10 between the radii of the elliptic inclusions in the two spatial orientations. The two associated microstructures are displayed in Figs. 3.3f and 3.3g. The created meshes consisted of 30018 and 34326 triangular second-order elements, respectively.

The material properties of the phases are denoted by the indices Ω = I, II, where the index I denotes the matrix and the index II the inclusion phase. The created meshes mentioned above were used for the FE DNS of the offline stage (Sections 3.2, 3.3.1 and 3.4.3) and for the computation of the reference full-field homogenization results using FE DNS.

Different numerical tests were performed, described by the following boundary conditions:

- prescribed overall axial loading-unloading cycle up to 6% strain in x-axis orientation with free motion of one edge with its normal in y-orientation, corresponding to overall plane-strain uniaxial tension boundary conditions

$$\begin{aligned} &\overline{\varepsilon}_{xx} = 0 \rightarrow 0.06 \rightarrow 0 \\ &\overline{\sigma}_{yy} = 0,\, \overline{\varepsilon}_{zz} = 0\,; \end{aligned} \tag{3.62}$$

- prescribed overall pure shear strain loading-unloading cycle up to 4%

$$\overline{\boldsymbol{\varepsilon}} = \begin{pmatrix} 0 & 0 \\ 0 & 0 \end{pmatrix} \rightarrow \begin{pmatrix} 0 & 0.04 \\ 0.04 & 0 \end{pmatrix} \rightarrow \begin{pmatrix} 0 & 0 \\ 0 & 0 \end{pmatrix}\,; \tag{3.63}$$

- non-proportional prescribed loading consisting of four different stages of biaxial isochoric and shear loading and unloading stages, represented by the overall strain evolution $\overline{\boldsymbol{\varepsilon}}(t)$, $t = [0, T]$, $T = 1.0$, with $\overline{\varepsilon}_{zz} = 0$:

$$\begin{aligned} \overline{\boldsymbol{\varepsilon}}(0) = \begin{pmatrix} 0 & 0 \\ 0 & 0 \end{pmatrix} \rightarrow \overline{\boldsymbol{\varepsilon}}(T/4) = \begin{pmatrix} 0.06 & 0 \\ 0 & -0.06 \end{pmatrix} \rightarrow \overline{\boldsymbol{\varepsilon}}(T/2) = \begin{pmatrix} 0.06 & 0.04 \\ 0.04 & -0.06 \end{pmatrix} \\ \rightarrow \overline{\boldsymbol{\varepsilon}}(3T/4) = \begin{pmatrix} 0 & 0.04 \\ 0.04 & 0 \end{pmatrix} \rightarrow \overline{\boldsymbol{\varepsilon}}(T) = \begin{pmatrix} 0 & 0 \\ 0 & 0 \end{pmatrix}\,. \end{aligned} \tag{3.64}$$

The resulting homogenized axial stress-strain responses under the uniaxial tension and shear stress-strain responses under the pure shearing conditions computed by the TFA and HS algorithms based on the underlying foundations for the subdomain decomposition are presented. Displayed are computed homogenized, and for several material systems the phases, stress-strain responses by the TFA, HS type analysis and the FE, and a convergence analysis based on the peak stresses computed by the TFA and HS tending towards the peak stresses computed by the FE method when increasing the number of subdomains. The deviations of the homogenized axial and shear peak stresses $\max(\overline{\boldsymbol{\sigma}})^{\mathrm{CAH}}_{xx}$, $\max(\overline{\boldsymbol{\sigma}})^{\mathrm{CAH}}_{xy}$ by the reduced CAH schemes to the corresponding peak stresses $\max(\overline{\boldsymbol{\sigma}})^{\mathrm{FE}}_{xx}$, $\max(\overline{\boldsymbol{\sigma}})^{\mathrm{FE}}_{xy}$ computed by the FE method under uniaxial tension and pure shearing, respectively, lead to the error estimations of the reduced schemes

$$e_{xx} = \left[\frac{\max(\overline{\boldsymbol{\sigma}}_{xx})^{\mathrm{CAH}} - \max(\overline{\boldsymbol{\sigma}}_{xx})^{\mathrm{FE}}}{\max(\overline{\boldsymbol{\sigma}}_{xx})^{\mathrm{FE}}}\right] \times 100\%\,, \tag{3.65a}$$

$$e_{xy} = \left[\frac{\max(\overline{\boldsymbol{\sigma}}_{xy})^{\mathrm{CAH}} - \max(\overline{\boldsymbol{\sigma}}_{xy})^{\mathrm{FE}}}{\max(\overline{\boldsymbol{\sigma}}_{xy})^{\mathrm{FE}}}\right] \times 100\%\,, \tag{3.65b}$$

where the superscript CAH represents either the TFA or HS homogenization methods. In the following, the CAH schemes with one subdomain per material phase, equivalent to incremental MFH approaches (without an isotropization step), are referred to as TFA 2 and HS 2. The CAH schemes with an underlying subdomain decomposition based on elasticity are referred to by the addition -E. The new approach using a plasticity based foundation for the spatial decomposition is referred to by the addition -P. The use of the plastic fluctuation correction (PFC) for the TFA-P during the online stage (as described in Sections 3.3.2 and 3.3.3) is referred to as TFA-PFC.

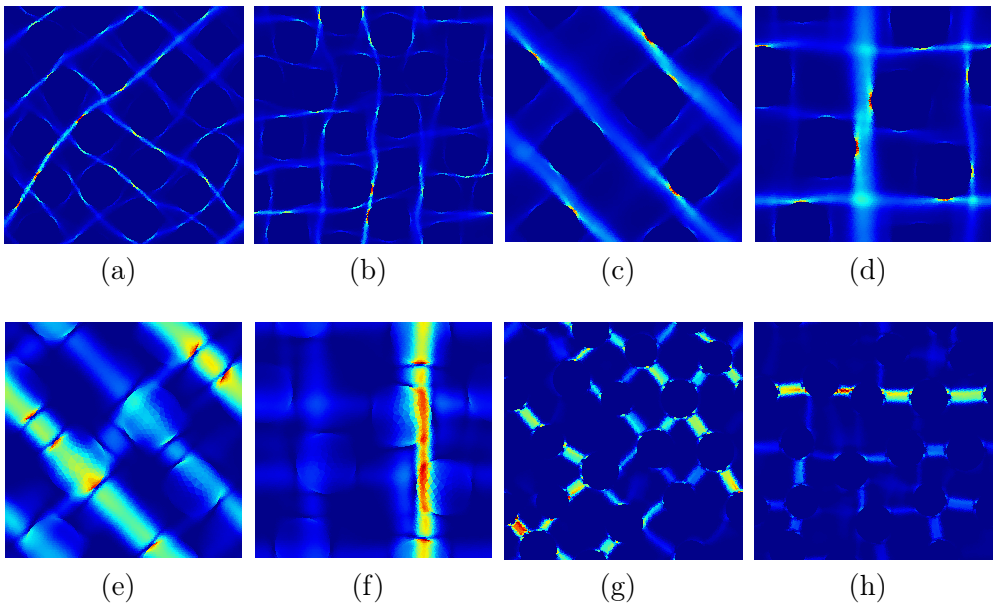

FIGURE 3.4: Equivalent plastic strain fields in different isotropic microstructures with an elasto-plastic matrix under the (a,c,e,g) biaxial isochoric and (b,d,f,h) pure shear offline deformation modes: (a,b) the larger RVE with $v_{\mathrm{II}} = 50\%$ of elastic inclusions, the RVE with $v_{\mathrm{II}} = 30\%$ of (c,d) stiff and (e,f) compliant elasto-plastic inclusions, and (g,h) rubber-like elastic inclusions.

3.5.1 Offline stage

Cluster decompositions are consequences of the two different clustering techniques described in Section 3.2.1 based on elastic and in Section 3.2.2 based on plastic strain distributions. Practical information for the conduction of the offline stage simulations under inelastic conditions are presented. While the elastic phase properties used during the offline stage must be equal to the ones considered in the online stage, the inelastic properties are allowed to differ. The purpose of the choice of the inelastic phase properties during the offline stage is the ability to identify the inelastic deformation patterns in order to achieve well-represented inelastic fields by the spatial division. In the following, the superscript "off" for the material properties denotes that these values are used in the offline stage and are not necessarily the same as the material properties considered in the online stage. In case of elastic inclusions in an elasto-plastic matrix phase, the low yield strength $\sigma_{\mathrm{I}}^{\mathrm{Y0,off}} = 10$ MPa and the inelastic behavior given by the power-law hardening relation

$$R = H_{\mathrm{I}}^{\mathrm{off}}\, p^{m_{\mathrm{I}}^{\mathrm{off}}} \tag{3.66}$$

with the hardening modulus $H_{\mathrm{I}}^{\mathrm{off}} = 50$ MPa and hardening exponent $m_{\mathrm{I}}^{\mathrm{off}} = 0.05$ are used in the offline stage, causing high plastic localizations, which enables the identification of localized deformations. A convergence study was performed in order to specify the overall deformation factor $E^{\mathrm{BC,in}}$ that determines the degree of the RVE deformation (Appendix D). It was found that, using the aforementioned inelastic material properties, the final plastic field patterns are established under an overall deformation of 2 %. Therefore, the overall deformation factor $E^{\mathrm{BC,in}} = 2$ % was chosen for the offline deformation modes.

In the case of elasto-plasticity in both phases, low yield strengths values $\sigma_{\mathrm{I}}^{\mathrm{Y0,off}} = \sigma_{\mathrm{II}}^{\mathrm{Y0}} =$ 10 MPa are used and the inelastic behavior in each phase is expressed by the power-law relation

$$R = H_{\Omega}^{\mathrm{off}}\, p^{m_{\Omega}^{\mathrm{off}}}, \quad \Omega = \mathrm{I,II} \tag{3.67}$$

with $m_{\Omega}^{\mathrm{off}} = 0.05$. In case of an inclusion phase that is stiffer than the matrix phase, the hardening moduli are $H_{\mathrm{I}}^{\mathrm{off}} = 50$ MPa and $H_{\mathrm{II}}^{\mathrm{off}} = 100$ MPa. In the reversed case of a more compliant inclusion phase, the hardening moduli $H_{\mathrm{II}}^{\mathrm{off}} = 50$ MPa and $H_{\mathrm{I}}^{\mathrm{off}} = 100$ MPa are reversed.

Examples of plastic strain fields evolved in different microstructures are presented in Figs. 3.1b, 3.1d and 3.4. Resulting subdomain decompositions of various RVEs with different volume fractions of the inclusion phase $\upsilon_{\mathrm{II}} = 20$ %, 30 % and 50 % are presented in Fig. 3.5, where the inclusion phase is occupied by only one subdomain. The inclusion represented by one subdomain is used for TFA in cases of elastic inclusions, because no eigenstrain field is to be captured in the inclusion phase. Using the HS however, polarization stress fields exist in inelastic and elastic phases, and thus the inclusion phase may be decomposed into subdomains as well. An example of the spatial division of the matrix and inclusion phase is presented in Fig. 3.6. In the case of the inelasticity based clustering, since no inelastic strains occur in the elastic inclusion phase, the RVE was divided based on total strain fields.

3.5.2 Isotropic microstructures with stiff elastic inclusions

Considered is an isotropic microstructure, which consists of a matrix material with circular inclusions covering a volume fraction of successively $\upsilon_{\mathrm{II}} = 20$ %, 30 % and 50 % (see Fig. 3.5). The elastic properties of the two phases are given in terms of the following bulk and shear moduli

- matrix: bulk modulus $\kappa_{\mathrm{I}} = 10$ GPa and shear modulus $\mu_{\mathrm{I}} = 3$ GPa;
- inclusion phase: bulk modulus $\kappa_{\mathrm{II}} = r_{\mathrm{II}}\kappa_{\mathrm{I}}$ and shear modulus $\mu_{\mathrm{II}} = r_{\mathrm{II}}\mu_{\mathrm{I}}$, with successive values of r_{II} =2, 10 and 100.

Spatial division The offline stage simulations were performed using a mesh consisting of 26508 and 27656 quadratic triangular elements for respectively $\upsilon_{\mathrm{II}} = 20$ % and υ_{II} =30 %. For the RVE with the volume fraction of inclusions υ_{II} =50 %, the effect of a mesh refinement is studied by considering two meshes of 40278 and 158420 triangular quadratic elements. Considered is a material system consisting of an elasto-plastic matrix material reinforced by stiff linear-elastic inclusions. The material properties used for the inelastic conditions in the offline stage for this material system are given in Section 3.5.1, and resulting strain fields after inelastic deformation for υ_{II} =30 % are presented in Figs. 3.1b and 3.1b. Under both deformation modes, the inelastic deformation is carried by a low number of plastic shear bands, traversing the material through the inter-inclusion spaces. While under the biaxial isochoric deformation mode, the plastic shear bands crossing the material are diagonally oriented, the pure shear deformation mode causes plastic shear bands in axial orientations. Solely the thickness of the band-like structures changes in dependence of the inclusion phase volume fraction: In case of the lower volume fraction and higher inter-inclusion spaces, the plastic bands are wider, while in case of the high volume fraction and therefore narrow inter-inclusion spaces, the plastic bands

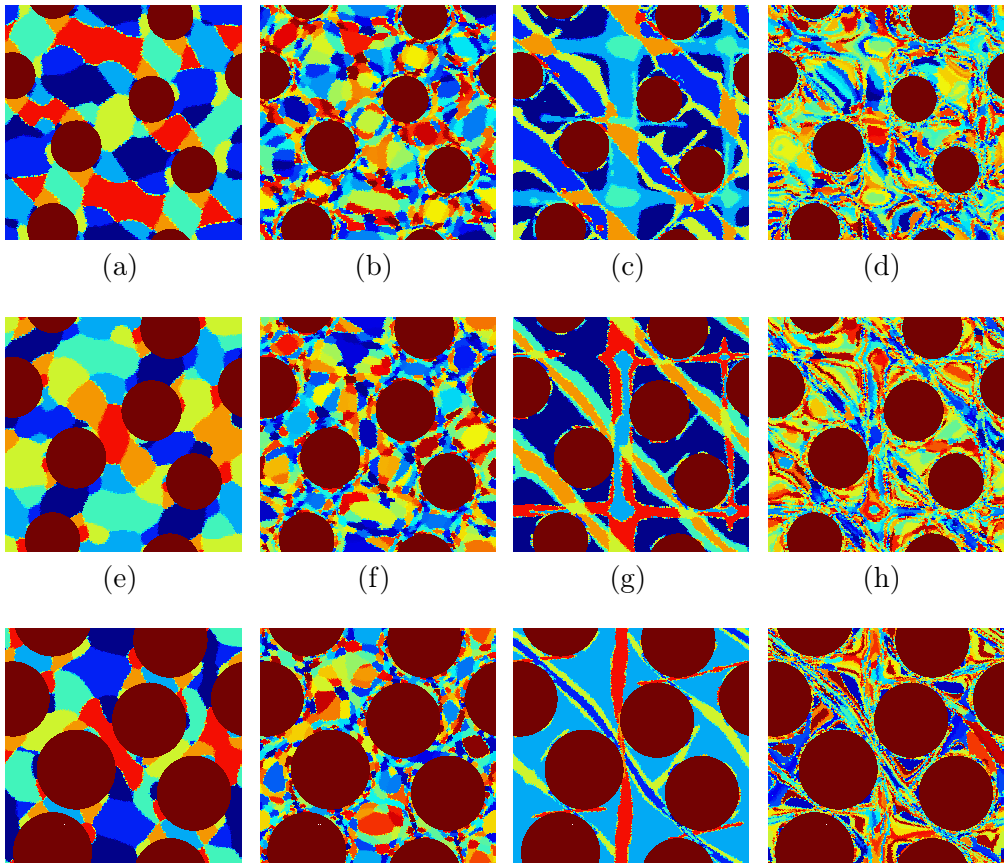

FIGURE 3.5: Microstructure of the composite materials with (a-d) $v_{\mathrm{II}} = 20$ % , (e-h) $v_{\mathrm{II}} = 30$ % and (i-l) $v_{\mathrm{II}} = 50$ % circular stiff elastic inclusions in an elasto-plastic matrix (case of 40278 elements), and spatial decompositions based on elastic deformation into (a, e, i) 8 subdomains and (c, g, k) 128 subdomains and based on inelastic deformation into (b, f, j) 8 subdomains and (d, h, l) 128 subdomains. The depicted spatial decompositions, with the inclusion phase represented by only one subdomains, were used for the TFA computations. For $v_{\mathrm{II}} = 20$ %, the same displayed spatial decomposition was used for the HS approach. For $v_{\mathrm{II}} = 30$ % and $v_{\mathrm{II}} = 50$ %, the numbers of the subdomains constituting the inclusion phase for the HS approach were increased to 2 and 4, respectively (Fig. 3.6).

are narrower. The full-field RVE domain was successively divided in the offline stage into $K = 2, 16, 32, 64, 128, 256, 512$ subdomains, of which one subdomain is sufficient to represent the elastic inclusion phase. The spatial subdivisions of the RVE into $K = 8$ and $K = 128$ subdomains based on elastic and based on plastic deformation are displayed in Fig. 3.5 (for the case of v_{II} =50 %, only the decomposition for the mesh of 40278 triangular quadratic elements is shown). The consideration of plastic strain distributions allows a spatial subdivision representing the inelastic band-like deformation patterns and their intersections. The Fig. 3.7 shows the spatial distribution of the PFC factors (Section 3.3.2), representing the degree of the plastic heterogeneity in the subdomains, after the inelasticity based clustering of the RVE domain with v_{II} =30 % into 8 and 128 subdomains (see Figs. 3.5g and 3.5h). The highest values (red color) of the PFC are located in regions

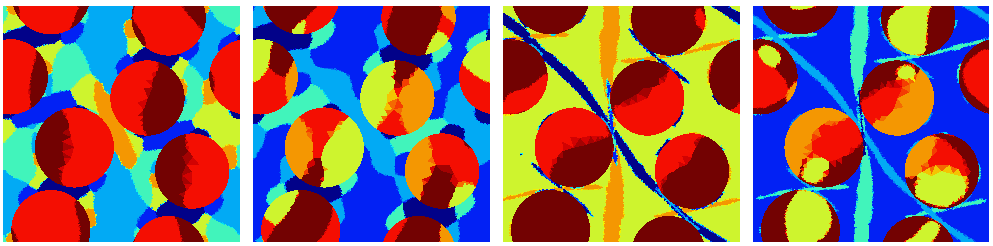

(a) (b) (c) (d)

FIGURE 3.6: Microstructure of the composite materials with $v_{\mathrm{II}} = 50$ % circular stiff elastic inclusions in an elasto-plastic matrix (case of 40278 elements). The spatial decompositions for the case of a clustering of the elastic inclusion phase, based on (a,b) elastic deformations and (c,d) total deformation after inelastic loading into 8 subdomains, with distributions of the number of subdomains in matrix and inclusion phases of (a,c) 6-2 and (b,d) 4-4.

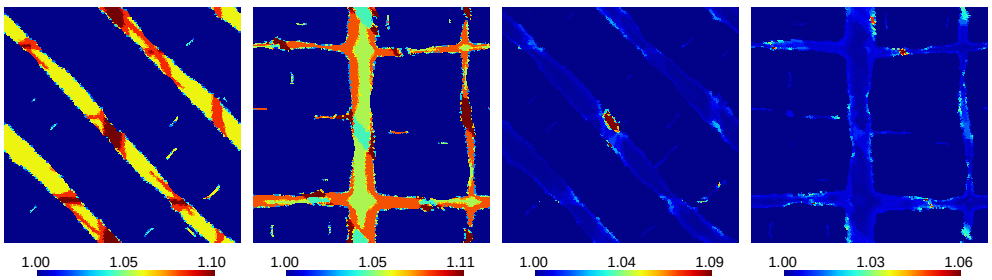

(a) (b) (c) (d)

FIGURE 3.7: Spatial distribution of the plastic fluctuation corrections (PFC) $\alpha_r^{(1)}$ (a, c) and $\alpha_r^{(2)}$ (b, d) for the microstructure with $v_{\mathrm{II}} = 30$ % elastic inclusions for the cases of 8 (a, b) and 128 (c, d) subdomains.

with high plastic strain concentrations, being not sufficiently captured by the clustering, what leads to high local plastic field fluctuations inside the subdomains. This occurs for example in regions where the plastic deformation patterns under the different offline deformation cases intersect (see the dark red regions in Figs. 3.7a and 3.7b). In these regions, the clustering needs to account for the inelastic fields under both deformation modes, leading to a less accurate coverage of the single inelastic fields. Furthermore, the decrease of the PFC factor values with an increasing number of subdomains (see Eq. (3.29)) is clearly visible.

Effect of the inclusion volume fraction The matrix material behaves perfectly plastic with the yield strength $\sigma_{\mathrm{I}}^{\mathrm{Y0}} = 100$ MPa, while the inclusions deform linearly-elastic. The elastic stiffness contrast between both phases is taken as $r_{\mathrm{II}} = 2$. For both tested loading cases of uniaxial tension and pure shear deformation, the stress-strain responses of the composite material are displayed in Figs. (3.8) - (3.11) for the three tested volume fractions, and the peak stress errors at maximum loading are reported in Table 3.1.

TABLE 3.1: Peak stress errors (computed as in Eq. (3.65)) using the different CAH approaches for the composite material with different volume fractions v_{II} of circular stiff elastic inclusions embedded in a perfectly plastic matrix (Fig. 3.5). Negative error values mean overcompliant composite predictions.

v_{II} =20%	TFA-E 512	TFA-P 512	TFA-PFC 512	HS-E 128	HS-P 128
e_{xx} (%)	9	5	4	2	0
e_{xy} (%)	8	2	2	1	0
v_{II} =30%	TFA-E 512	TFA-P 512	TFA-PFC 512	HS-E 128	HS-P 128
e_{xx} (%)	19	8	7	3	0
e_{xy} (%)	15	5	4	2	0
v_{II} =50%	TFA-E 512	TFA-P 512 (coarse/fine)	TFA-PFC 512 (coarse/fine)	HS-E 128	HS-P 128
e_{xx} (%)	51	42/36	36/30	2	-2
e_{xy} (%)	41	27/19	17/11	0	-5

For low and moderate volume fractions, it is visible in Figs. 3.8a and 3.8c and in Figs. 3.9a and 3.9c that the TFA-P allows a better convergence towards the reference result than the TFA-E throughout the whole range of the numbers of subdomains, and continues to converge in the region of high numbers of subdomains $K \geq 256$, where the TFA-E results do not significantly improve anymore. Consequently, the peak stress errors can be strongly reduced using the TFA-P in comparison with the TFA-E, while the TFA-PFC provides an additional improvement that decreases with increasing numbers of subdomains. The stress-strain responses computed by the TFA-P and TFA-PFC with 512 subdomains cover the reference stress-strain responses computed by the full-field homogenization closely and with significantly higher accuracy than the TFA-E (Figs. 3.8b and 3.8d and Figs. 3.9b and 3.9d).

The average responses of the phases under the uniaxial tension test, resulting from the CAH and full-field homogenization, are displayed in Fig. 3.10. It is visible that the HS approach allows the accurate modeling of perfect plasticity of the matrix (Fig. 3.10a) and no occurring strains in the inclusion phase (Fig. 3.10b) during inelastic behavior of the matrix. Comparing the TFA approaches, it is recognized that the TFA-P leads to a clear improvement of the phase strains predictions with respect to the TFA-E. Particularly the strain, and therefore stress, of the inclusion phase (Fig. 3.10b) are clearly reduced using the TFA-P, resulting in the more compliant predictions of the composite.

Considering the higher inclusion volume fraction in Figs. 3.11a and 3.11c, the TFA-E achieves better results than the TFA-P in the range of low numbers of subdomains. However, the convergence rate of the TFA-E method starts to decrease earlier then the convergence rate of the TFA-P, leading to better TFA-P results in the range of high numbers of subdomains. Nonetheless, clearly stiffer stress-strain responses than for the lower volume fractions are achieved using the TFA-E and TFA-P approaches with up to 512 subdomains (Figs. 3.11b and 3.11d). Furthermore it is visible that the TFA-P prediction does not continue to converge towards the reference results in the range $256 \leq K \leq 512$ when the spatial division is based on offline simulations using the coarse mesh. The fading convergence implies that the k-means clustering was not able to define a meaningful subdomain refinement for $K > 256$. For this reason, the previously mentioned

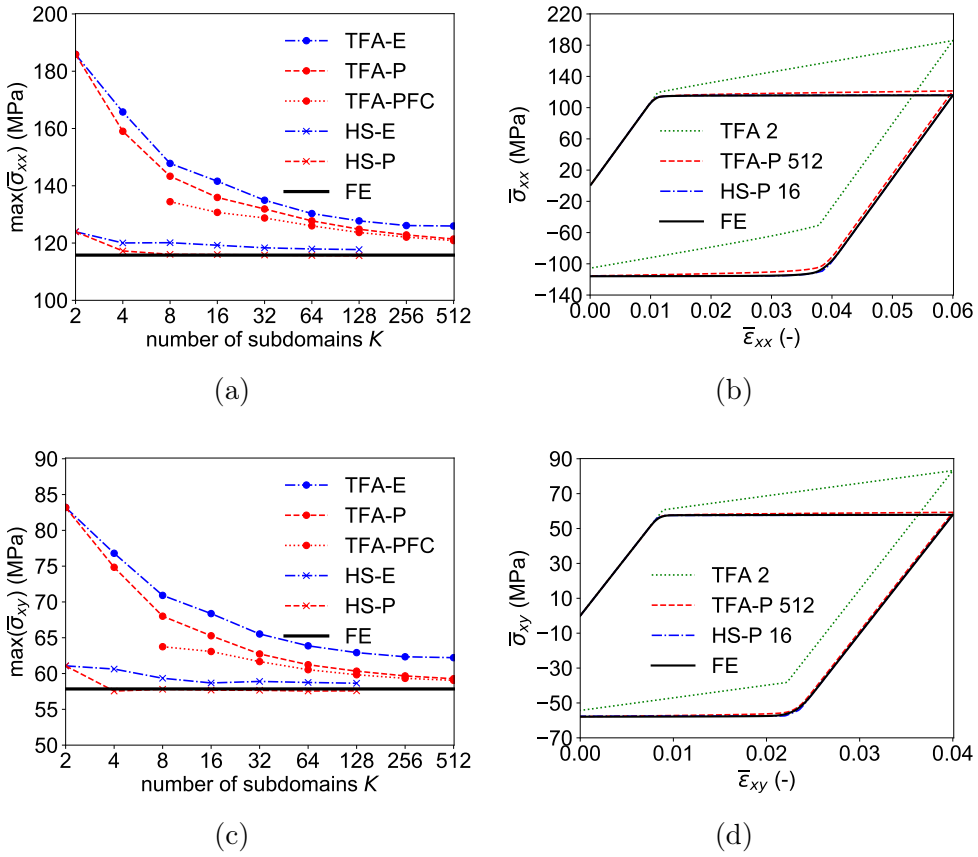

FIGURE 3.8: Normal stress response under uniaxial tension (Eq. (3.62)) and shear stress response under pure shear deformation (Eq. (3.63)) of a composite material with $v_{\mathrm{II}} = 20$ % of circular stiff elastic inclusions embedded in a perfectly plastic matrix in comparison to the full-field FE result. Displayed are (a, c) the convergence of the peak stress depending on the number of subdomains (Fig. 3.5) and (b, d) stress-strain curves computed by the different CAH approaches.

refined mesh, with half dimensions for the triangular quadratic elements, was tested in the offline stage for comparison. It is recognized that the use of a finer mesh allows further improvements of accuracy and a proceeding convergence towards the full-field results (denoted as TFA-P fine in Figs. 3.11a and 3.11c). The TFA-PFC provides a slight improvement for the uniaxial tension test and a significant error reduction for the pure shear test (Table 3.1).

For all tested inclusion volume fractions $v_{\mathrm{II}} = 20\%, 30\%, 50\%$, the HS approach provides very high accuracies of the homogenized behavior in the range of low numbers of subdomains, with the HS-P showing a faster rate of convergence than the HS-E in the range $K \leq 8$. Very good predictions are achieved with only one subdomains per material phase. The HS-P yields nearly exact results with only four subdomains in case of the lowest inclusion volume fraction $v_{\mathrm{II}} = 20\%$, with eight subdomains for $v_{\mathrm{II}} = 30\%$, and with 16 subdomains for the highest volume fraction $v_{\mathrm{II}} = 50\%$. However, the HS-P results in too compliant predictions of the composite, that keep decreasing under increasing numbers of subdomains (see Figs. 3.11a and 3.11c). Therefore it is concluded that the HS approach does not show a convergence towards the full-field prediction.

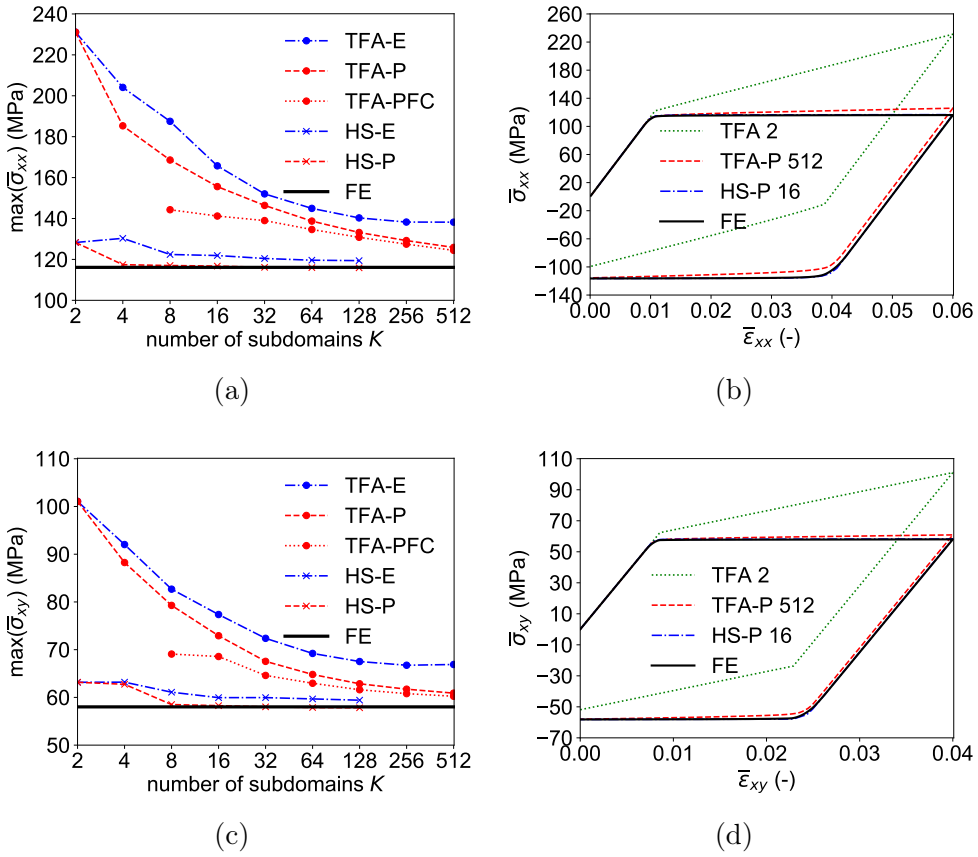

FIGURE 3.9: Normal stress response under uniaxial tension (Eq. (3.62)) and shear stress response under pure shear deformation (Eq. (3.63)) of a composite material with $v_{\mathrm{II}} = 30$ % of circular stiff elastic inclusions embedded in a perfectly plastic matrix in comparison to the full-field FE result. Displayed are (a, c) the convergence of the peak stress depending on the number of subdomains (Fig. 3.5(e-h)) and (b, d) stress-strain curves computed by the different CAH approaches.

TABLE 3.2: Peak stress errors (computed as in Eq. (3.65)) using the different CAH approaches for the composite material with $v_{\mathrm{II}} = 30$ % (Fig. 3.5(e-h)) consisting of circular stiff elastic inclusions embedded in a perfectly plastic matrix for different phases Young's moduli ratios r_{II}. Negative error values mean overcompliant composite predictions.

$r_{\mathrm{II}} = 2$	TFA-E 512	TFA-P 512	TFA-PFC 512	HS-E 128	HS-P 128
e_{xx} (%)	19	8	7	3	0
e_{xy} (%)	15	5	4	2	0
$r_{\mathrm{II}} = 10$	TFA-E 512	TFA-P 512	TFA-PFC 512	HS-E 128	HS-P 128
e_{xx} (%)	23	11	9	4	-2
e_{xy} (%)	18	6	5	4	-2
$r_{\mathrm{II}} = 100$	TFA-E 512	TFA-P 512	TFA-PFC 512	HS-E 128	HS-P 128
e_{xx} (%)	24	11	9	4	-2
e_{xy} (%)	19	6	4	4	-2

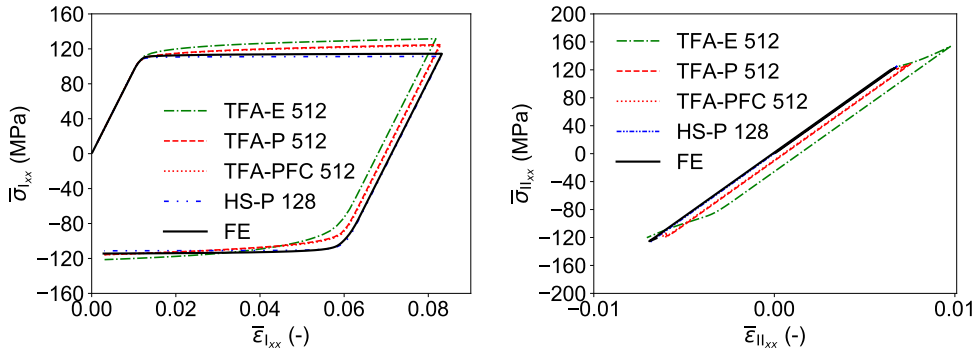

(a) (b)

FIGURE 3.10: Responses of the (a) matrix and (b) inclusion phases under uniaxial tension (Eq. (3.62)) of a composite material with $v_{\mathrm{II}} = 30$ % of circular stiff elastic inclusions embedded in a perfectly plastic matrix in comparison to the full-field FE result. The responses of the composite phases are the average responses of all the subdomains constituting the corresponding phase.

Effect of the elastic stiffness contrast between the phases The RVE with the inclusion volume fraction $v_{\mathrm{II}} = 30\%$ is considered, now with an increased elastic stiffness of the inclusion phase. The elastic properties of the matrix remain the same as before and it follows a perfectly plastic behavior. While in the examples above, the ratio of the Young's moduli of the inclusion phase and the matrix phase was $r_{\mathrm{II}} = 2$, this ratio is increased to $r_{\mathrm{II}} = 10$ and $r_{\mathrm{II}} = 100$. Since it was recognized that the TFA yields overstiff results due to overestimated deformations of stiff elastic phases, the investigation of high elastic stiffness contrasts is an important test of the capabilities of the TFA and HS CAH approaches for general composite materials. With the same RVE and material system of elastic inclusions in an elasto-plastic matrix as in the first example of this section and consequently the same inelastic patterns, the subdomain decompositions are nearly identical to the ones in Fig. 3.5(e-h), and therefore not displayed. Throughout the whole range of numbers of subdomains, the TFA-P leads to improved results compared to the TFA-E, with the TFA-PFC allowing for further improvements of accuracy in both the uniaxial tension and pure shear tests in the region of low and intermediate numbers of subdomains $8 \leq K \leq 128$. (Figs. 3.12 and 3.13). A comparison of the initial case $r_{\mathrm{II}} = 2$ and the two cases $r_{\mathrm{II}} = 10$ and $r_{\mathrm{II}} = 100$ shows a decreasing TFA-E accuracy with increasing stiffness of the inclusion phase. In opposition to that, the TFA-P is only weakly affected by the increasing inclusion stiffness and provides accurate results with 512 subdomains (Table 3.2). The TFA-PFC nearly recovers the reference results with hardly rising errors due to the increasing inclusion phase stiffness.

Similarly, the accuracies of the modeled responses by the HS method appear unaffected by the increasing contrast of the elastic properties. With the HS-P, allowing for a faster convergence and more accurate results than the HS-E, nearly exact captures of the full-field results are achieved using only eight subdomains for both cases of $r_{\mathrm{II}} = 10$ and $r_{\mathrm{II}} = 100$. The predictions are however too compliant and slightly decreasing under increasing numbers of subdomains.

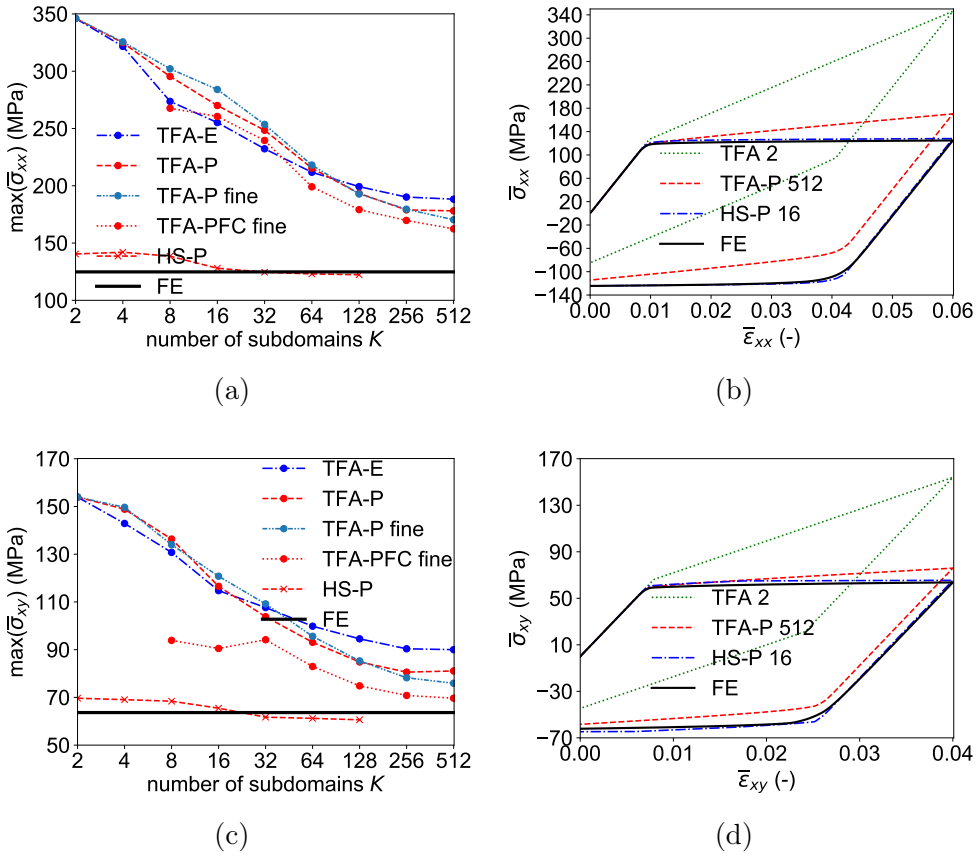

FIGURE 3.11: Normal stress response under uniaxial tension (Eq. (3.62)) and shear stress response under pure shear deformation (Eq. (3.63)) of a composite material with $v_{\mathrm{II}} = 50$ % of circular stiff elastic inclusions embedded in a perfectly plastic matrix in comparison to the full-field FE result. Displayed are (a, c) the convergence of the peak stress depending on the number of subdomains (Fig. 3.5(i-l)) and (b, d) stress-strain curves computed by the different CAH approaches.

TABLE 3.3: Peak stress errors (computed as in Eq. (3.65)) using the different CAH approaches for the larger composite RVE with $v_{\mathrm{II}} = 50$ % (Fig. 3.14) consisting of circular stiff elastic inclusions embedded in a perfectly plastic matrix. Negative error values mean overcompliant composite predictions.

small RVE	TFA-E 512	TFA-P 512	TFA-PFC 512	HS-E 128	HS-P 128
e_{xx} (%)	51	42	36	2	-2
e_{xy} (%)	41	27	17	0	-5
large RVE	TFA-E 512	TFA-P 512	TFA-PFC 512	HS-E 128	HS-P 128
e_{xx} (%)	57	37	30	3	-2
e_{xy} (%)	37	16	10	-3	-6

Effect of the RVE size In the examples above, relatively small extracts of microstructures were considered as RVEs. In this section, the TFA is applied for the case of a real representative portion of an isotropic microstructure with an inclusions volume fraction $v_{\mathrm{II}} = 50\%$, expected to contain higher varieties of deformation states within the RVE.

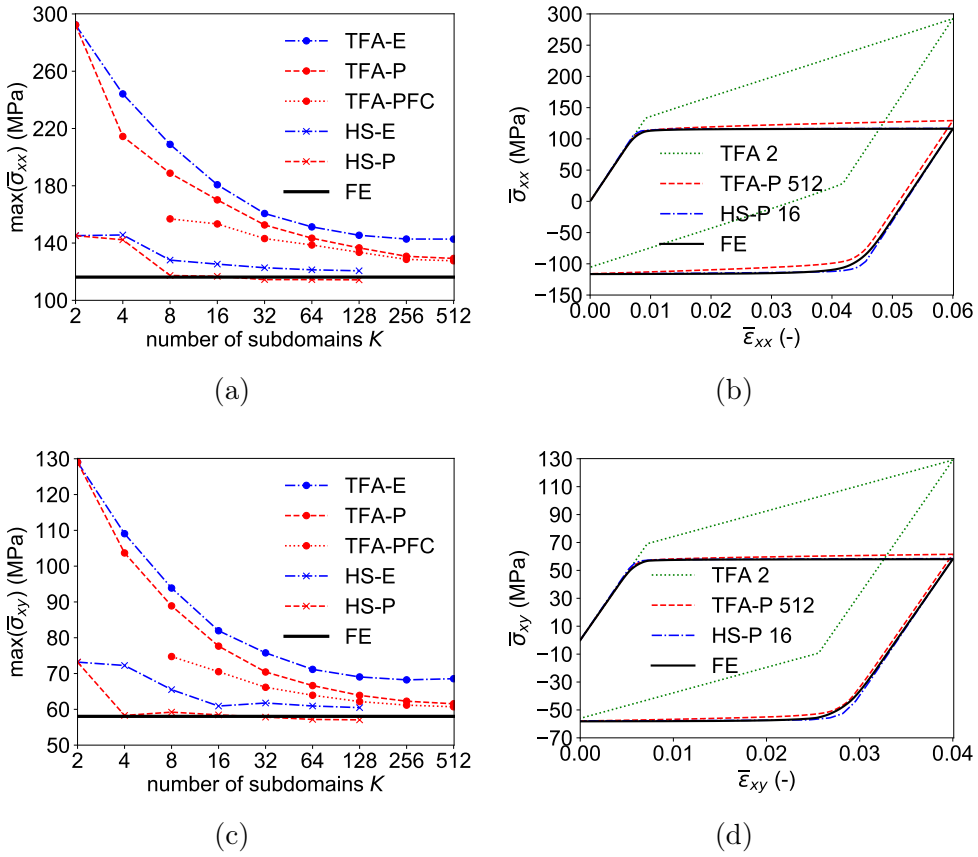

FIGURE 3.12: Normal stress response under uniaxial tension (Eq. (3.62)) and shear stress response under pure shear deformation (Eq. (3.63)) of a composite material with $v_{\mathrm{II}} = 30$ % (Fig. 3.5(e-h)) consisting of circular stiff elastic inclusions embedded in a perfectly plastic matrix with a ratio of the Young's moduli $r_{\mathrm{II}} = 10$ in comparison to the full-field FE result. Displayed are (a,c) the convergence of the peak stress depending on the number of subdomains and (b,d) stress-strain curves computed by the different CAH approaches.

By this application it is investigated if equal degrees of accuracy as for smaller RVEs are achieved for a real RVE using the same range of numbers of subdomains. The elastic (the phase contrast $r_{\mathrm{II}} = 2$ is considered for this application) and inelastic phase properties are the same as above. The offline stage simulations were performed with a mesh consisting of 40460 triangular quadratic elements, which corresponds to the coarser mesh size for the small RVE with $v_{\mathrm{II}} = 50\%$. The inelastic deformation again localizes in plastic shear band deformation patterns, oriented diagonally resulting from biaxial isochoric and oriented axially resulting from the pure shear deformation mode (Fig. 3.4 (a,b)). In comparison to the examples above, the number of band-like structures is increased, with some of them still traversing the whole material domain in the presence of a much higher number of obstacles. Following, the RVE domain was divided into $K = 2$, 16, 32, 64, 128, 256, 512 subdomains. The microstructure and the spatial divisions resulting from elastic and inelastic deformation into 8 and 128 subdomains are displayed in Fig. 3.14.

The results of convergence analyses are presented in Fig. 3.15. The TFA-E and the TFA-P have an equal rate of convergence towards the full-field result in the range $K \leq$

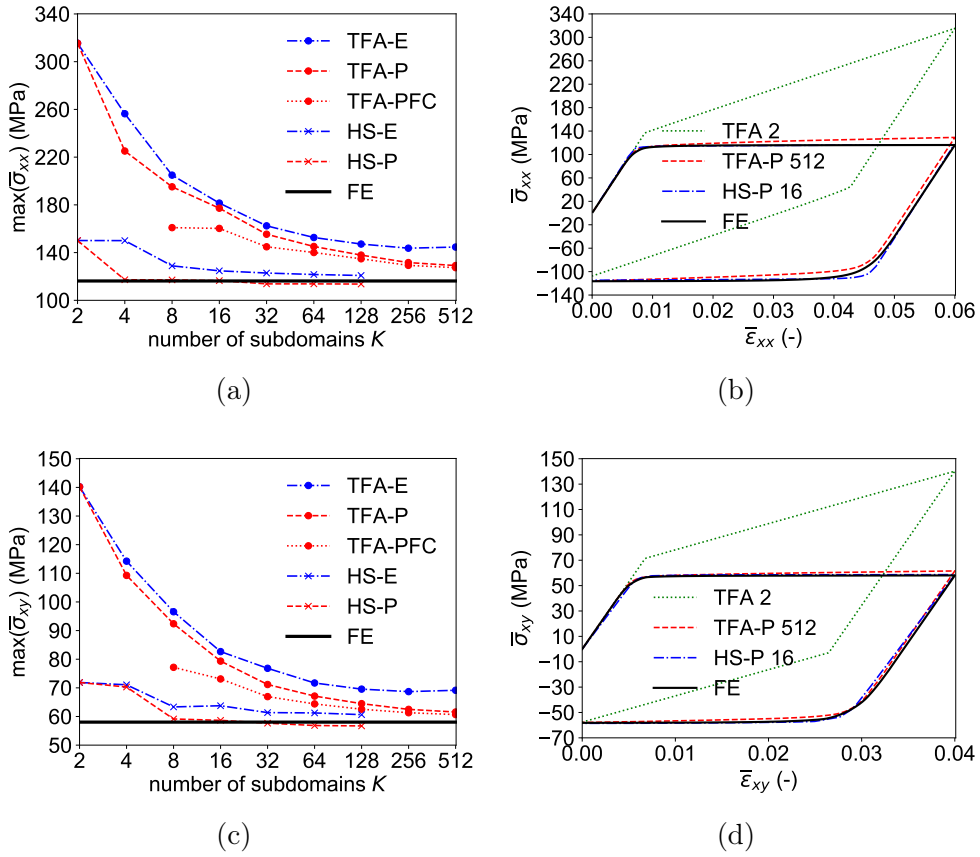

FIGURE 3.13: Normal stress response under uniaxial tension (Eq. (3.62)) and shear stress response under pure shear deformation (Eq. (3.63)) of a composite material with $v_{\mathrm{II}} = 30$ % (Fig. 3.5(e-h)) consisting of circular stiff elastic inclusions embedded in a perfectly plastic matrix with a ratio of the Young's moduli $r_{\mathrm{II}} = 100$ in comparison to the full-field FE result. Displayed are (a,c) the convergence of the peak stress depending on the number of subdomains and (b,d) stress-strain curves computed by the different CAH approaches.

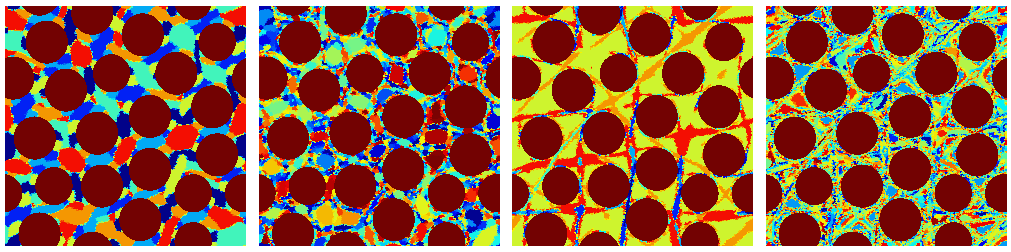

FIGURE 3.14: Microstructure and spatial decompositions of the larger composite RVE with $v_{\mathrm{II}} = 50$ % of circular stiff elastic inclusions in an elasto-plastic matrix based on elastic deformation into (a) 8 subdomains and (b) 128 subdomains and based on inelastic deformation into (c) 8 subdomains and (d) 128 subdomains.

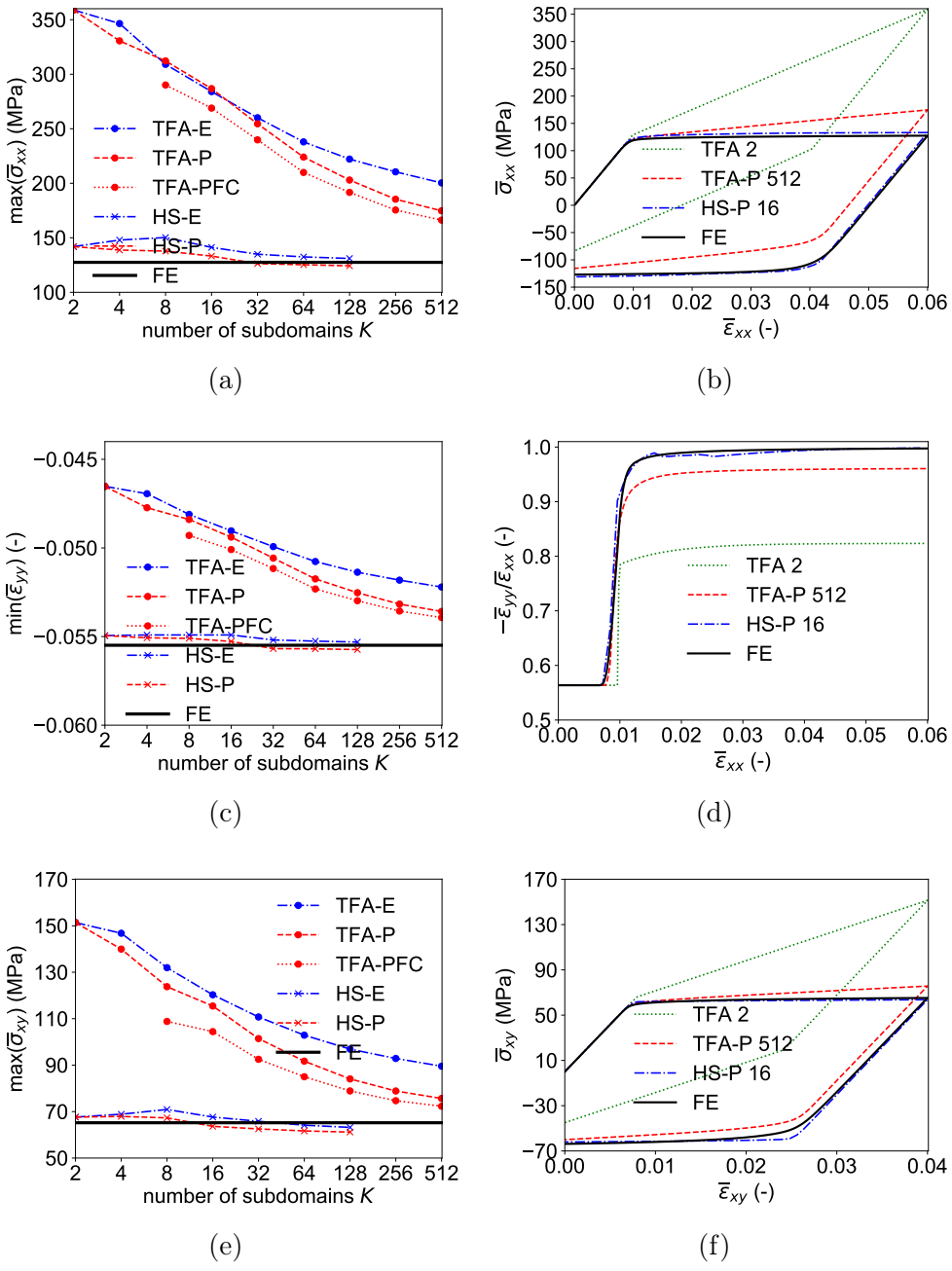

FIGURE 3.15: Normal stress response under uniaxial tension (Eq. (3.62)) and shear stress response under pure shear deformation (Eq. (3.63)) of the larger composite RVE with $v_{\mathrm{II}} = 50$ % (Fig. 3.14) consisting of circular stiff elastic inclusions embedded in a perfectly plastic matrix in comparison to the full-field FE result. Displayed are (a,c,e) the convergence of the (a,e) peak stress and (c) transverse strains depending on the number of subdomains and (b,d,f) the curves of the (b,f) stress-strain relation and the (d) transverse to longitudinal strain ratio computed by the different CAH approaches.

32 in the uniaxial tension test. After this point, the TFA-P shows a faster decrease in error than the TFA-E and therefore allows improved stress-strain predictions (Figs. 3.15a and 3.15b). The error by the TFA-P with 512 subdomains is still considerably high but

significantly lower than the one by the TFA-E, and the TFA-PFC provides complementary improvements (Table 3.3). It is important to recognize that the PFC has more effect on the TFA results for this larger RVE than for the smaller RVE with $v_{\mathrm{II}} = 50\%$ (compare Tabs. 3.1 and 3.3). Both the HS-E and HS-P deliver very accurate homogenized responses already with one subdomain per phase, with the HS-P providing a better convergence towards the full-field result in the range of low numbers of subdomains. However, the homogenized predictions by the HS-P keep decreasing towards too compliant responses under increasing numbers of subdomains. Furthermore, the convergence of the transverse strain $\overline{\boldsymbol{\varepsilon}}_{yy}$ and the evolution of the homogenized ratio of the transverse strain to the longitudinal strain during the uniaxial tension test were investigated and are presented in Figs. 3.15c and 3.15d. Similarly to the stress response, the TFA-P and TFA-PFC allow a better convergence of $\overline{\boldsymbol{\varepsilon}}_{yy}$ than the TFA-E towards the FE result. The TFA-PFC allows for slightly better estimations of the instantaneous Poisson ratio than the TFA-P. The HS-E and HS-P approaches provide almost exact predictions of the transversal deformation. Considering the pure shear test, the convergence achieved by the TFA-P is clearly better than that achieved by the TFA-E throughout the whole range of subdomains. For a number of subdomains $K = 512$, the TFA-P provides a clearly higher accuracy for the stress-strain response predictions, with an error that is less than half compared to the one achieved using the TFA-E (Figs. 3.15e and 3.15f). The TFA-PFC results in even less stiff responses and achieves an acceptable modeling accuracy. Compared to the results achieved for the small RVE using an equal offline stage mesh size (see errors for the case $v_{\mathrm{II}} = 50\%$ with the coarse mesh in Table 3.1), the computation errors are lower. Therefore it is concluded, that the TFA-PFC method is more accurate for larger RVEs. The HS-E and HS-P methods provide, as for the uniaxial tension test, very accurate homogenized responses already with one subdomain only per phase.

TABLE 3.4: CPU time speed-ups for the non-proportional loading program in Eq. (3.64) using the different numbers of subdomains K for the TFA-P and HS-P methods.

K	2	4	8	16	32	64	128	256	512
TFA speed-up	3.2e6	1.9e6	9.2e5	2.8e5	6.8e4	1.3e4	2.5e3	460	70
HS speed-up	9.2e5	3.9e5	1.1e5	5.8e4	1.0e4	2.6e3	600	130	24

Non-proportional loading In order to further explore the abilities of the TFA and HS methods, an isochoric non-proportional loading program (3.64) displayed in Fig. 3.16a is applied to the $v_{\mathrm{II}} = 30$ % RVE consisting of circular stiff elastic inclusions embedded in an elasto-plastic matrix (Fig. 3.5(e-h)). The elastic properties of the phases have a contrast $r_{\mathrm{II}} = 2$ for this application. The inelastic behavior of the matrix with the initial yield strength $\sigma_{\mathrm{I}}^{\mathrm{Y0}} = 100$ MPa follows the power-law hardening behavior

$$R = H_{\mathrm{I}}\, p^{m_{\mathrm{I}}} \tag{3.68}$$

with the matrix hardening modulus $H_{\mathrm{I}} = 50$ MPa and exponent $m_{\mathrm{I}} = 0.05$.

Compared are the evolutions of the different stress components predicted by the TFA-P and TFA-PFC with 128 subdomains and the HS-P with 16 subdomains compared to the reference full-field computations (Figs. 3.16c and 3.16d). A high accuracy of the modeled normal stress response during the applied axial deformation by the all three

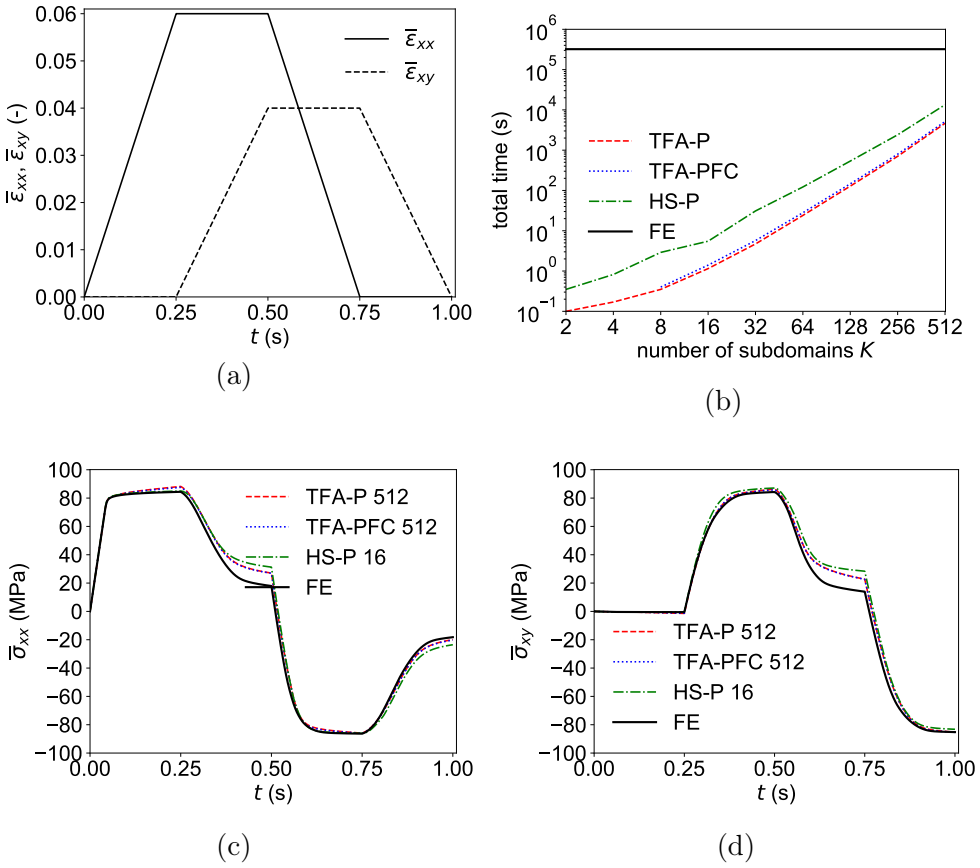

FIGURE 3.16: Non-proportional loading: Evolution of the (a) prescribed overall strain components, (b) the CPU time comparison for different subdomains numbers K and (c, d) the computed homogenized stress components predicted by the TFA-P, TFA-PFC and HS-P approaches compared to the FE full-field for the composite material with $v_{\mathrm{II}} = 30$ % (Fig. 3.5(e-h)) consisting of circular stiff elastic inclusions embedded in an elasto-plastic matrix.

CAH methods in the time interval $t = [0, 0.25]$ is achieved. Following, inaccuracies are found considering the too low axial stress decrease during the shear loading stage from $t = [0.25, 0.5]$. Therefore, the predicted axial stresses have too high initial values at the start of the subsequent axial strain unloading stage from $t = [0.5, 0.75]$ but return back to the reference prediction at the end of this stage. During the final axial unloading stage from $t = [0.75, 1]$, perfect accuracies of TFA-P and TFA-PFC are maintained and therefore, correct final axial stresses are predicted. Similar observations are made for the shear stress evolution. Sole inaccuracies are found during the axial strain unloading stage from $t = [0.5, 0.75]$, where the shear stress decrease is too low, particularly using the HS-P with 16 subdomains. During the remaining deformation evolution, the shear stresses are correctly predicted and therefore, correct final shear stresses are predicted by all considered CAH approaches.

CPU time consumptions for performing the numerical analysis in Eq. (3.64) using the CAH algorithms with the different numbers of subdomains and the FE analysis with the same mesh as used for the offline stage simulations (27656 quadratic triangular elements), are displayed in Fig. 3.16b. The computational speed-ups using the different numbers

of subdomains for this 2D analysis are summarized in Table 3.4, providing an estimation of the possible computational savings allowed by the CAH approaches for 2D analyses. The time efficiency of the TFA is higher than the one provided by the HS scheme. The TFA has a faster convergence of the iterative solution than the HS approach. This can be explained by the characteristics of the two CAH schemes. The TFA solution depends on the responses of the single subdomains only (Section 2.3.5). The HS relies on the computation of shear modulus of the isotropic reference medium at every iteration of every load step (Section 2.3.8). Therefore, the response of the reference medium needs to converge besides the responses of the subdomains, which has an effect on the required time to reach the computational solution. In addition to the time savings provided by the CAH schemes, large CPU load reductions are provided by the use of CAH schemes with respect to performing full-field simulations due to the much smaller numerical solutions (see Section 3.4.4).

3.5.3 Isotropic microstructures with elasto-plastic inclusions

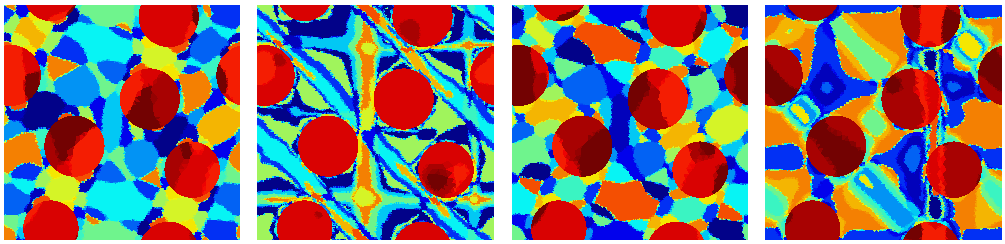

(a) (b) (c) (d)

FIGURE 3.17: Microstructure and spatial decompositions of the elasto-plastic composite material with $v_{\mathrm{II}} = 30$ % of circular (a,b) stiff and (c,d) more compliant elasto-plastic inclusions based on elastic and inelastic strains into 20 subdomains, 16 of them constituting the matrix and 4 the inclusion phase.

Stiff inclusions Considered is an isotropic microstructure, which consists of a matrix material with circular inclusions covering a volume fraction of $v_{\mathrm{II}} = 30$ %. The elastic properties of the two phases are given in terms of the following bulk and shear moduli

- matrix: bulk modulus $\kappa_{\mathrm{I}} = 10$ GPa and shear modulus $\mu_{\mathrm{I}} = 3$ GPa;
- inclusion phase: bulk modulus $\kappa_{\mathrm{II}} = 20$ GPa and shear modulus $\mu_{\mathrm{II}} = 6$ GPa.

Both phases can deform elasto-plastically, with the yield strengths of both phases $\sigma_{\mathrm{I}}^{\mathrm{Y0}} = \sigma_{\mathrm{II}}^{\mathrm{Y0}} = 100$ MPa and a hardening behavior following the power-law relation

$$R = H_{\Omega}\, p^{m_{\Omega}}\,, \quad \Omega = \mathrm{I,II} \tag{3.69}$$

with the hardening moduli $H_{\mathrm{I}} = 50$ MPa and $H_{\mathrm{II}} = 100$ MPa and the two tested combinations of the exponents $m_{\mathrm{I}} = 0.05$, $m_{\mathrm{II}} = 0.4$ and $m_{\mathrm{I}} = 0.4$, $m_{\mathrm{II}} = 0.05$.

During the offline stage, the same mesh as in Section 3.5.2 was used. The material properties used during the inelastic offline stage simulations for a material consisting of

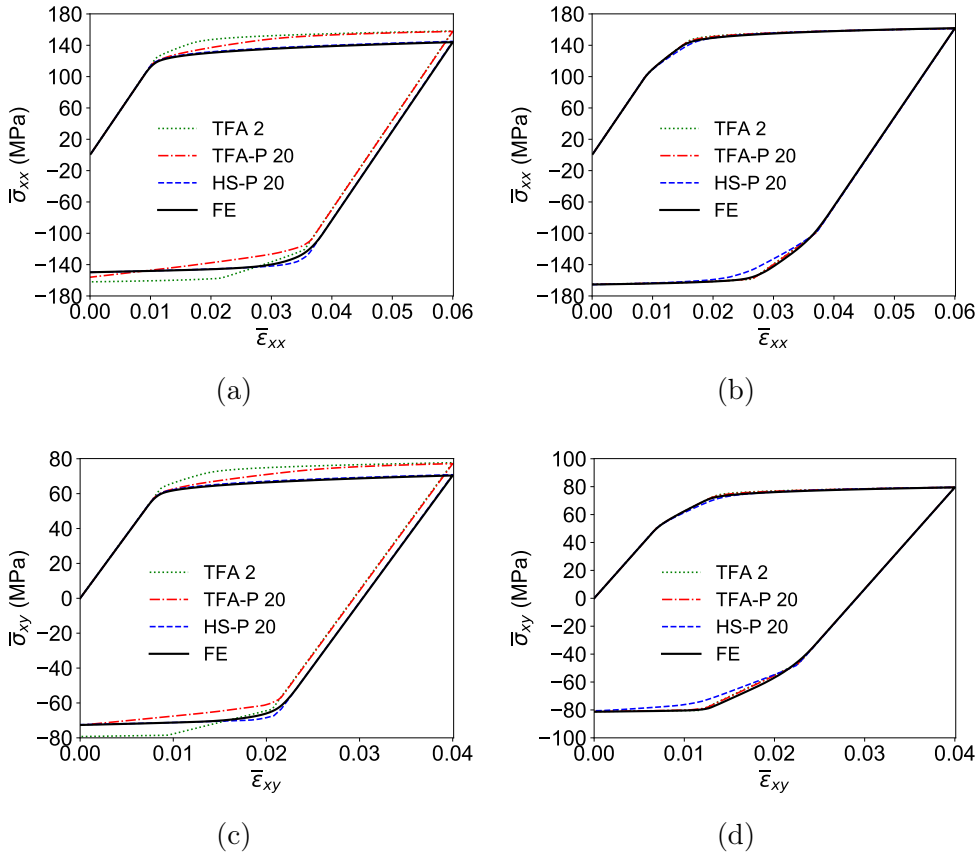

FIGURE 3.18: Normal stress response under uniaxial tension (Eq. (3.62)) and shear stress response under pure shear deformation (Eq. (3.63)) of a composite material consisting of circular stiff elasto-plastic inclusions in an elasto-plastic matrix (Fig. 3.17) and the different hardening exponents of the phases (a,c) $m_{\mathrm{I}} = 0.4$ and $m_{\mathrm{II}} = 0.05$ and (b,d) $m_{\mathrm{I}} = 0.05$ and $m_{\mathrm{II}} = 0.4$ resulting from the use of the different CAH approaches in comparison to the full-field FE results.

stiff elasto-plastic inclusions in an elasto-plastic matrix are given in Section 3.5.1. As previously, diagonal and axially-oriented inelastic bands, crossing the material on inter-inclusion paths, are formed during the biaxial and the pure shear deformation modes, respectively (Figs. 3.4c and 3.4d). The inelastic deformations in the inclusions are not connected to the shear bands. The RVE was divided into $K = 20$ subdomains, where the matrix phase is composed of 16 and the inclusion phase of four subdomains. The spatial RVE decompositions based on elastic and plastic strain distributions are depicted in Figs. 3.17a and 3.17b. The plasticity based spatial subdivision approach allows covering deformation patterns corresponding to the same general shear band orientations and their intersecting regions in the matrix phase as in the considerations of elastic inclusions.

The resulting strain-stress responses are displayed in Fig. 3.18. Very high accuracies are accomplished with the TFA and HS approaches using only one subdomain per material phase (green curves). The full-field solution is nearly perfectly recovered by both CAH methods in the cases of a low hardening exponent in the more compliant matrix phase and a high hardening exponent in the stiffer inclusion phase (Figs. 3.18b and 3.18d). Less accurate results represented by a slightly overstiff behavior compared to the full-field

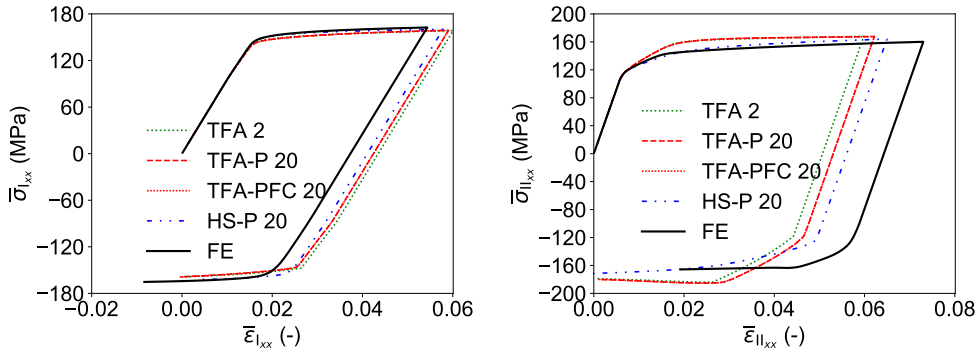

(a) (b)

FIGURE 3.19: Responses of the (a) matrix and (b) inclusion phases under uniaxial tension (Eq. (3.62)) of a composite material consisting of circular stiff elasto-plastic inclusions in an elasto-plastic matrix (Fig. 3.17) with the hardening exponents of the phases $m_{\mathrm{I}} = 0.05$ and $m_{\mathrm{II}} = 0.4$ in comparison to the full-field FE result. The responses of the composite phases are the average responses of all the subdomains constituting the corresponding phase.

solution are predicted using the TFA and HS methods in the case of a high hardening exponent in the matrix phase and a low hardening exponent in the inclusion phase (Figs. 3.18a and 3.18c).

The average responses of the phases with the hardening exponents $m_{\mathrm{I}} = 0.05$, $m_{\mathrm{II}} = 0.4$ under the uniaxial tension test, resulting from the CAH and full-field homogenization, are displayed in Fig. 3.19. It is visible that, although the composite response for this test are nearly perfectly accurate (Fig. 3.18b), the strain concentrations in the single phases deviate from the ones of the full-field computation. Using the TFA, the matrix strains are overestimated and the inclusion strains are underestimated, with a convergence towards the full-field result with higher numbers of subdomains. The HS-P leads to slightly improved strain localizations in the two phases with respect to the TFA methods.

Compliant inclusions Now, the role of the two materials are reversed compared to the case considered in Section 3.5.3, meaning that the stiff material constitutes the matrix phase and the more compliant material the inclusion phase, represented in terms of the elastic properties

- matrix: bulk modulus $\kappa_{\mathrm{I}} = 20$ GPa and shear modulus $\mu_{\mathrm{I}} = 6$ GPa;
- inclusion phase: bulk modulus $\kappa_{\mathrm{II}} = 10$ GPa and shear modulus $\mu_{\mathrm{II}} = 3$ GPa.

Accordingly, the inelastic properties are reversed, implying a power-law hardening behavior (Eq. (3.69)) of the corresponding phases governed by $\sigma_{\mathrm{I}}^{\mathrm{Y0}} = \sigma_{\mathrm{II}}^{\mathrm{Y0}} = 100$ MPa, the hardening moduli $H_{\mathrm{I}} = 100$ MPa and $H_{\mathrm{II}} = 50$ MPa and the two combinations of the exponents $m_{\mathrm{I}} = 0.05$, $m_{\mathrm{II}} = 0.4$ and $m_{\mathrm{I}} = 0.4$, $m_{\mathrm{II}} = 0.05$.

During the inelastic offline stage simulations (performed with the same mesh as in Section 3.5.2 and the inelastic material properties for a material with compliant elasto-plastic inclusions in an elasto-plastic matrix given in Section 3.5.1), the inelastic defor-

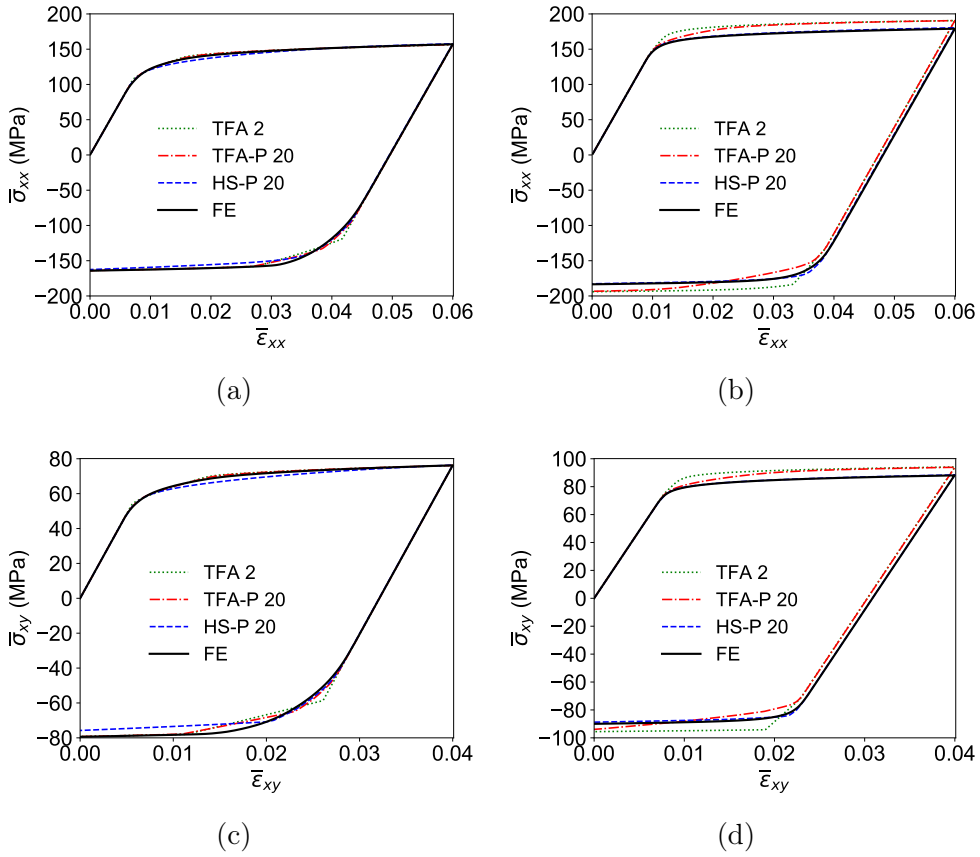

FIGURE 3.20: Normal stress response under uniaxial tension (Eq. (3.62)) and shear stress response under pure shear deformation (Eq. (3.63)) of a composite material consisting of circular more compliant elasto-plastic inclusions in an elasto-plastic matrix (Fig. 3.17) and the different hardening exponents of the phases (a,c) $m_{\mathrm{I}} = 0.4$ and $m_{\mathrm{II}} = 0.05$ and (b,d) $m_{\mathrm{I}} = 0.05$ and $m_{\mathrm{II}} = 0.4$ resulting from the use of the different CAH approaches in comparison to the full-field FE results.

mation localizes in band-like patterns, oriented diagonally caused by biaxial isochoric and axially caused by pure shear overall deformation (Figs. 3.4e and 3.4f). Different from the case of stiff elasto-plastic inclusions (Figs. 3.17a and 3.17b), the inclusions are now integrated in the plastic shear bands. The resulting subdomain decompositions into a total of 20 subdomains based on elasticity and plasticity are presented in Figs. 3.17c and 3.17d, where the matrix phase is constituted by 16 subdomains and the inclusion phase by four subdomains. With inclusions considered being more compliant than the matrix phase, the subdomain patterns using plastic strain distributions do not avoid but connect through the inclusions.

The axial stress response under uniaxial tension and the shear stress response under pure shear conditions are presented in Fig. 3.20. Again, the TFA and HS approaches yield accurate predictions with only one subdomains per material phase. The full-field results are nearly exactly reproduced in the cases of a low hardening exponent in the more compliant phase, here the inclusion phase (Figs. 3.20a and 3.20c). Low errors in comparison with the full-field result only in case of a high hardening exponent in the more compliant phase (Figs. 3.20b and 3.20d).

3.5.4 Isotropic microstructures with rubber-like inclusions

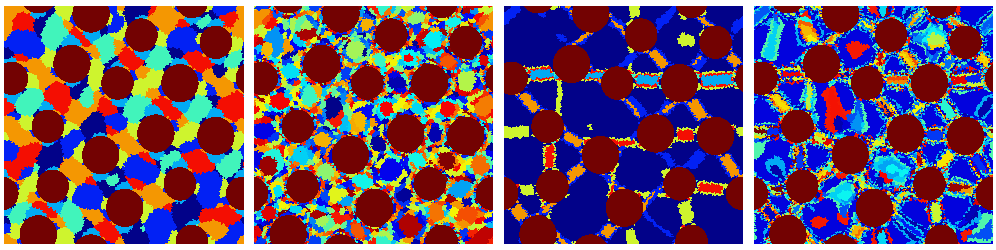

(a) (b) (c) (d)

FIGURE 3.21: Microstructure and spatial decompositions of the composite RVE with $v_{\mathrm{II}} = 30$ % of circular elastic rubber-like inclusions in an elasto-plastic matrix based on elastic deformation into (a) 8 subdomains and (b) 128 subdomains and based on inelastic deformation into (c) 8 subdomains and (d) 128 subdomains.

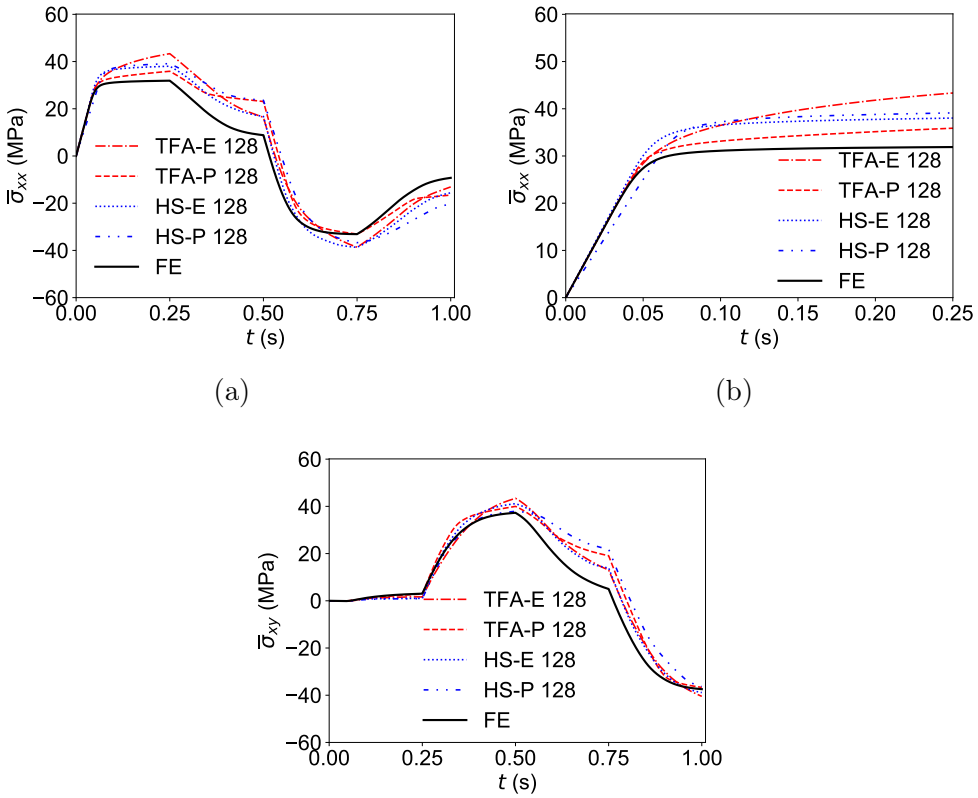

FIGURE 3.22: Non-proportional loading (Eq. (3.64)): the computed homogenized (a,b) normal and (c) shear stress components predicted by the TFA-E, TFA-P, HS-E and HS-P approaches compared to the FE full-field for the composite material with $v_{\mathrm{II}} = 30$ % (Fig. 3.21) consisting of rubber-like elastic inclusions embedded in an elasto-plastic matrix. The plot in (b) is a close-up of the first biaxial loading stage t=[0,0.25].

The isotropic microstructure consists of a matrix material with circular inclusions that have a rubber-like response and cover a volume fraction of $\upsilon_{\mathrm{II}} = 30$ %. The elastic properties of the two phases are given in terms of the following bulk and shear moduli

- matrix: bulk modulus $\kappa_{\mathrm{I}} = 10$ GPa and shear modulus $\mu_{\mathrm{I}} = 3$ GPa;
- inclusion phase: bulk modulus $\kappa_{\mathrm{II}} = 2$ GPa and vanishing shear modulus $\mu_{\mathrm{II}} = 0$.

The inelastic behavior of the matrix with the initial yield strength $\sigma_{\mathrm{I}}^{\mathrm{Y0}} = 100$ MPa follows the power-law hardening behavior

$$R = H_{\mathrm{I}}\, p^{m_{\mathrm{I}}} \tag{3.70}$$

with the matrix hardening modulus $H_{\mathrm{I}} = 50$ MPa and exponent $m_{\mathrm{I}} = 0.05$.

The inelastic patterns show diagonal and axial shear bands resulting from the applied biaxial and pure shear loading, respectively (Figs. 3.4g and 3.4h). The band-like inelastic structures form between the highly compliant inclusions. The spatial decompositions resulting from elastic and inelastic deformation modes are presented in Fig. 3.21.

The composite structure was tested under a non-proportional loading path, with the results being reported in Fig. 3.22. It is visible that using both TFA and HS approaches, the composite response during the axial and shear loading stages could be significantly improved by using inelasticity based spatial decompositions. It is recognized during the first axial loading stage that using the HS-P approach, the elastic response is too compliant, and the yield point is not accurately captured by both HS-E and HS-P (Fig. 3.22b). While fairly good predictions for the loading responses were provided by the TFA-P and HS-P, the unloading responses show far too low stress reductions, and the predictions are worse than using the elasticity based spatial decompositions.

3.5.5 Anisotropic microstructures and material behavior

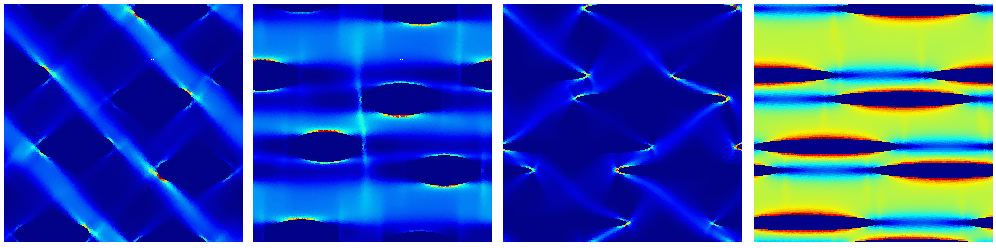

(a) (b) (c) (d)

FIGURE 3.23: Equivalent plastic strain fields in the anisotropic microstructures with (a,b) $r_x/r_y = 2.5$ and (c,d) $r_x/r_y = 10$ under the (a,c) biaxial isochoric and (b,d) pure shear offline deformation modes.

The two anisotropic microstructures consist of a matrix with elliptic, purely-elastic inclusions, covering a volume fraction $\upsilon_{\mathrm{II}} = 20$ %. The degree of anisotropy represented by the ratio of the radii r_x and r_y of the elliptic inclusions differs for the two microstructures: they are successively taken as $r_x/r_y = 2.5$ and $r_x/r_y = 10$, with the elongations along the x-axis orientation. The material system consists of an elasto-J$_2$-plastic matrix material

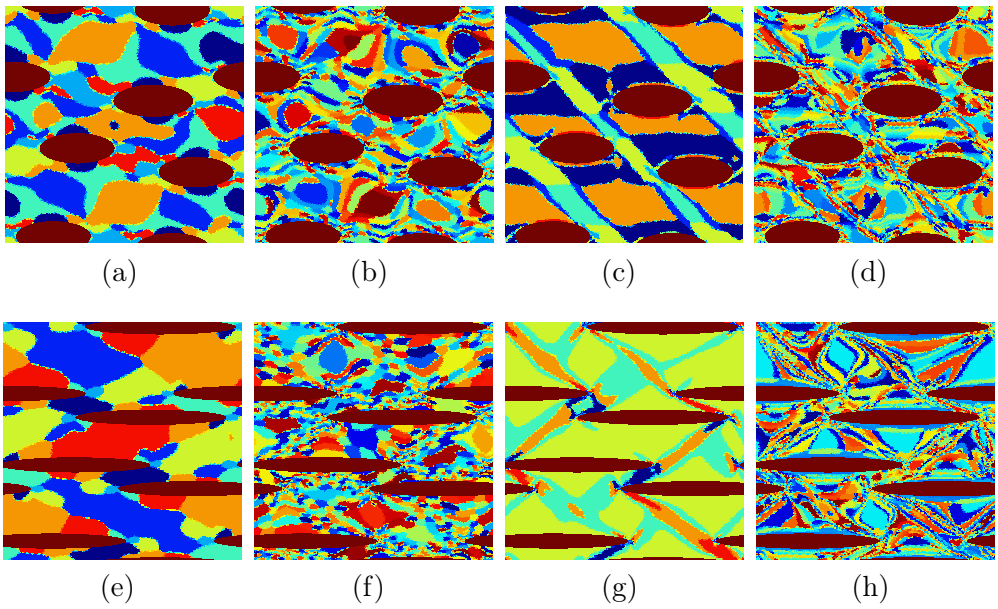

(a) (b) (c) (d)

(e) (f) (g) (h)

FIGURE 3.24: Microstructure and spatial decompositions of the composite material with an anisotropic structure with $v_{\text{II}} = 20\%$ of elliptic stiff and anisotropic elastic inclusions with (a-d) aspect ratio $r_x/r_y = 2.5$ and (e-h) aspect ratio $r_x/r_y = 10$ in an elasto-plastic matrix based on elastic deformation into (a, e) 8 subdomains and (c, g) 128 subdomains and based on inelastic deformation into (b, f) 8 subdomains and (d, h) 128 subdomains.

TABLE 3.5: Peak stress errors (computed as in Eq. (3.65)) using the different CAH approaches for the composite material with an anisotropic microstructure and $v_{\text{II}} = 20\%$ (Fig. 3.24) consisting of elliptic stiff elastic inclusions embedded in a perfectly plastic matrix. Negative error values mean overcompliant composite predictions.

$r_x/r_y = 1$	TFA-E 512	TFA-P 512	TFA-PFC 512	HS-E 128	HS-P 128
e_{xx} (%)	9	5	4	2	0
e_{xy} (%)	8	2	2	1	0
$r_x/r_y = 2.5$	TFA-E 512	TFA-P 512	TFA-PFC 512	HS-E 128	HS-P 128
e_{xx} (%)	11	6	5	2	-2
e_{xy} (%)	4	2	1	0	-1
$r_x/r_y = 10$	TFA-E 512	TFA-P 512	TFA-PFC 512	HS-E 128	HS-P 128
e_{xx} (%)	17	13	10	1	-5
e_{yy} (%)	10	4	3	3	-4
e_{xy} (%)	1	1	1	0	0

with the elastic and inelastic material properties as in Section 3.5.2 and stiff linear-elastic inclusions with the transverse-isotropic (or "polar-anisotropic") properties (Section 2.5.1)

- $E_x = 40$ GPa, $E_y = E_z = 10$ GPa
- $\nu_{xy} = \nu_{xz} = 0.24$, $\nu_{yz} = 0.3333$,
- $G_{xy} = G_{xz} = G^{\text{LT}} = 8$ GPa, $G_{yz} = G^{\text{TT}} = \frac{E_y}{2\,(1+\nu_{yz})} = 3.75$ GPa

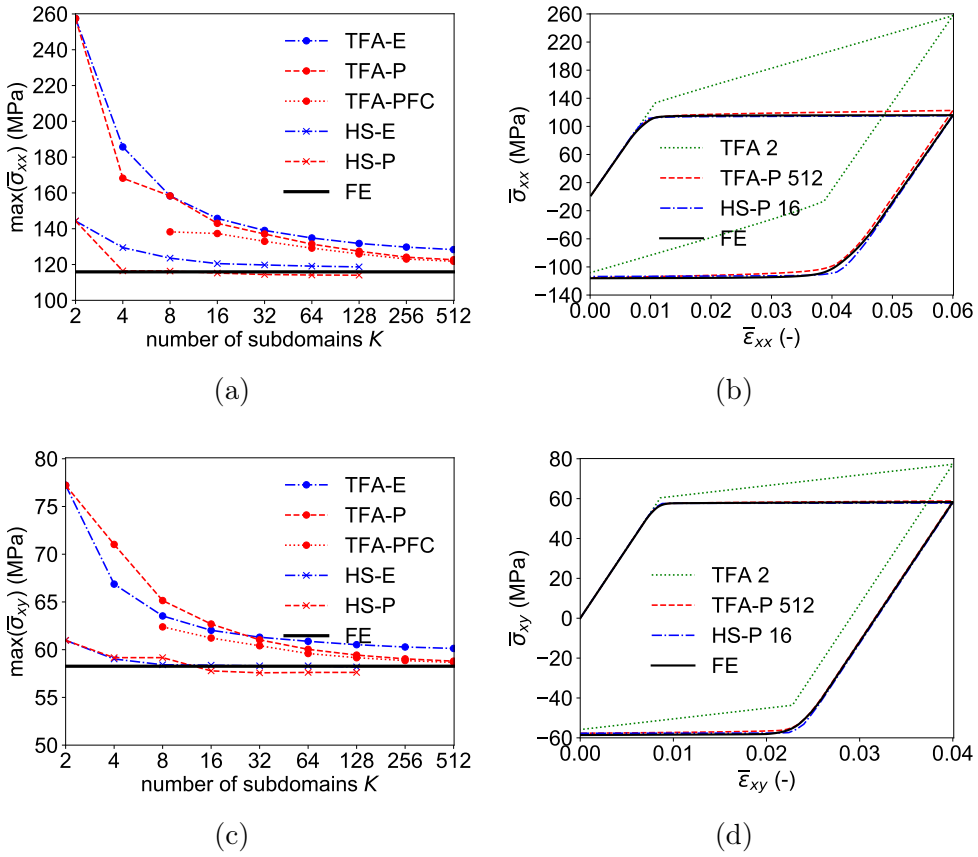

FIGURE 3.25: Normal stress response under uniaxial tension in x-direction (longitudinal loading, Eq. (3.62)) and shear stress response under pure shear deformation (Eq. (3.63)) of a composite material with an anisotropic microstructure of $v_{\mathrm{II}} = 20\%$ (Fig. 3.24(a-d)) elliptic stiff and anisotropic elastic inclusions with an aspect ratio $r_x/r_y = 2.5$ embedded in a perfectly plastic matrix in comparison to the full-field FE result. Displayed are (a, c) the convergence of the peak stress depending on the number of subdomains and (b, d) stress-strain curves computed by the different CAH approaches.

where the inclusion phase subscript "$\Omega = \mathrm{II}$" is omitted for the simplicity of notation. Additionally to the uniaxial tension test in longitudinal fiber direction and the pure shear test, a transverse uniaxial tension test with up to $\overline{\varepsilon}_{yy} = 3\%$ (exchange of xx and yy in Eq. (3.62)) was applied on the RVE with the high inclusion aspect ratio. The computation errors of the tension in y-direction are denoted as e_{yy}.

Spatial division The offline stage simulations were performed using meshes consisting of 30018 and 34326 triangular quadratic elements for the microstructure with the lower degree of anisotropy and the one used for the strong isotropic microstructure, respectively. The inelastic material properties of the elasto-plastic matrix during the offline stage simulations are the ones given in Section 3.5.1 for the material system of elastic inclusions in an elasto-plastic matrix. The inclusions anisotropic elastic behavior is described by the previously introduced elastic properties. In the case of the microstructure with the lower anisotropy $r_x/r_y = 2.5$, the inelastic deformations under the biaxial deformation and pure shearing are carried by a low number of wide shear bands, traversing the material in

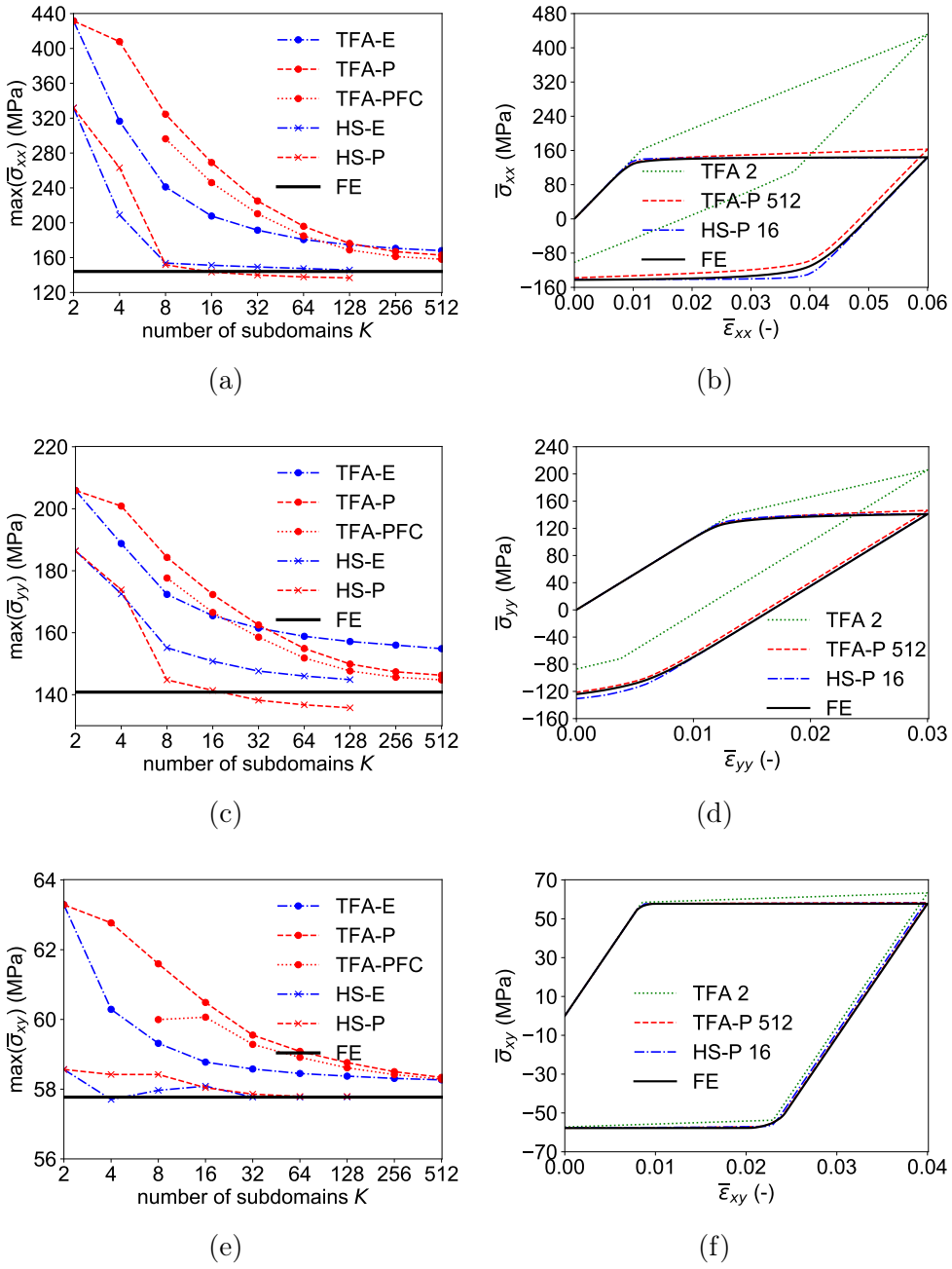

FIGURE 3.26: Normal stress responses under uniaxial tension in x-direction (longitudinal loading, Eq. (3.62)) and in y-direction (transverse loading) and shear stress response under pure shear deformation (Eq. (3.63)) of a composite material with an anisotropic microstructure of $v_{\mathrm{II}} = 20\%$ (Fig. 3.24(e-h)) elliptic stiff and anisotropic elastic inclusions with an aspect ratio $r_x/r_y = 10$ embedded in a perfectly plastic matrix in comparison to the full-field FE result. Displayed are (a, c, e) the convergence of the peak stress depending on the number of subdomains and (b, d, f) stress-strain curves computed by the different CAH approaches.

diagonal and axial directions, as recognized in the spatial decomposition (Figs. 3.23a and 3.23b). In the case of a strong anisotropy expressed by $r_x/r_y = 10$, the inelastic patterns

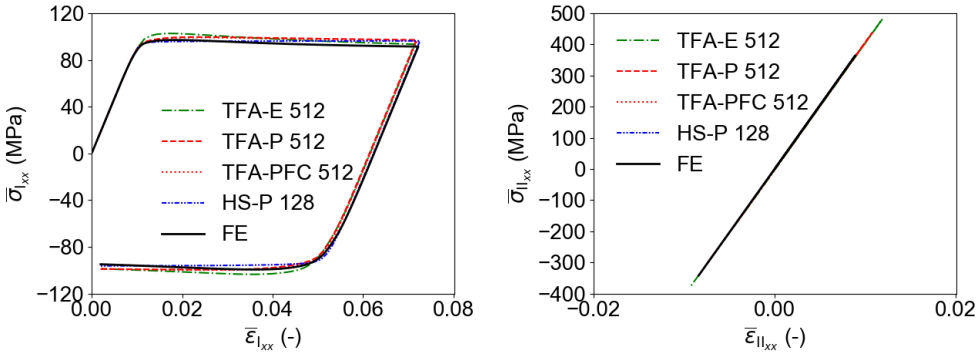

(a) (b)

FIGURE 3.27: Responses of the (a) matrix and (b) inclusion phases under uniaxial tension (Eq. (3.62)) of a composite material with an anisotropic microstructure of $v_{\mathrm{II}} = 20\%$ (Fig. 3.24(e-h)) elliptic stiff and anisotropic elastic inclusions with an aspect ratio $r_x/r_y = 10$ embedded in a perfectly plastic matrix in comparison to the full-field FE result. The responses of the composite phases are the average responses of all the subdomains constituting the corresponding phase.

differ from the previously considered cases (Figs. 3.23c and 3.23d). Under the biaxial isochoric deformation, plastic localizations form around and between the sharp peaks of the inclusions. Under pure shearing, plastic strain localizes in longitudinal direction and particularly along the long inclusion edges, while the regions between the inclusion peaks are almost spared by the occurrence of plasticity. The RVE domains were divided in the offline stage into $K = 2$, 16, 32, 64, 128, 256, 512 subdomains, with one subdomain representing the elastic inclusion phase. The microstructures and the spatial decompositions resulting from elastic and inelastic deformation into 8 and 128 subdomains are presented in Figs. (3.24a) - (3.24d) for the lower anisotropy $r_x/r_y = 2.5$ and in Figs. (3.24e) - (3.24h) for the higher anisotropy $r_x/r_y = 10$.

Nonlinear analyses The matrix material behaves perfectly plastic with the yield strength $\sigma_{\mathrm{I}}^{\mathrm{Y0}} = 100$ MPa, while the inclusions deform linearly-elastic with the transverse-isotropic elastic properties given above. In case of the lower degree of anisotropy, the TFA-P provides a better convergence towards the reference result than the TFA-E throughout the whole range of the numbers of subdomains for the uniaxial tension test and for $K \geq 32$ for the pure shear test. The TFA-PFC yields additional improvements of accuracy in the region of low numbers of subdomains. It is recognized that peak stress errors are low using TFA-E but can still be significantly reduced using the TFA-P and TFA-PFC (Table 3.5 and Figs. 3.25a and 3.25c). Therefore, the stress-strain responses computed by the TFA-P and TFA-PFC with 512 subdomains show negligible deviations from the reference full-field stress-strain responses under uniaxial tension and pure shearing (Figs. 3.25b and 3.25d). The HS-P approach shows a better convergence than the HS-E, reaching nearly exact coverages of the full-field result with only four subdomains.

In case of the strong anisotropic microstructure, the TFA-E provides more accurate results than the TFA-P and TFA-PFC for a wide range of subdomains for both the uniaxial tension and the pure shear tests (Figs. 3.26a, 3.26c and 3.26e). In the uniaxial tests,

the TFA-P and TFA-PFC show a higher convergence rate towards the reference results and allow more accurate predictions for respectively $K \geq 128$ and $K \geq 32$. With 512 subdomains, the peak stress error is slightly in the longitudinal tension and significantly in the transverse tension test reduced using the TFA-P and the TFA-PFC (Table 3.5), visible in the computed stress-strain responses (Figs. 3.26b and 3.26d).

The average responses of the phases under the longitudinal uniaxial tension test (see Fig. 3.26b for the homogenized response), resulting from the CAH and full-field homogenization, are displayed in Fig. 3.27. All TFA and HS approaches allow an accurate modeling of the matrix behavior, with a slight stress reduction during the inelastic deformation (Fig. 3.27a). Unlike the HS-P, the TFA approaches lead to increasing strain, and therefore stress, in the inclusion phase during inelastic deformation of the matrix (Fig. 3.27b), with better predictions provided by the TFA-P and TFA-PFC than the TFA-E. The emerging stresses in the matrix lead to stiffer responses of the composite when using the TFA than using the HS type approach.

Wulfinghoff, Cavaliere, and Reese (2018) recognized overstiff homogenized responses of the HS approach for anisotropic microstructures using a secant scheme (Section 2.3.7). This led to the introduction of a scalar correction factor to decrease the response of the isotropic reference medium. With the tangent HS scheme developed in this work however, no overstiff results are recognized for the anisotropic structure in this section. The HS-E and HS-P provide very high rate of convergence in the range $K \leq 8$ and accurate results with eight subdomains for the uniaxial tension tests. The homogenized predictions keep decreasing however towards too compliant results under increasing numbers of subdomains (Fig. 3.26a). Under transverse loading, the continuous decrease of the homogenized responses is even more significant (Fig. 3.26c). No convergence towards the full-field results can be recognized in this loading case. In the pure shear test, the computation errors are negligible using the HS method with only one subdomain per phase or using the TFA with sufficiently high numbers of subdomains (Figs. 3.26e and 3.26f).

Table 3.6: Material properties of the highly anisotropic microstructure. The material properties were adapted from Wu et al. (2015).

Matrix (M10.1 epoxy)		Fibre (UD300 HS(R) carbon fibre)	
Property	Value	Property	Value
Young's modulus E_{I} [GPa]	3.2	Young's modulus $E_{\mathrm{II}}^{\mathrm{L}}$ [GPa]	230
Poisson ratio ν_{I} [-]	0.3	Young's modulus $E_{\mathrm{II}}^{\mathrm{T}}$ [GPa]	40
Initial yield stress $\sigma_{\mathrm{I}}^{\mathrm{Y0}}$ [MPa]	100	Poisson ratio $\nu_{\mathrm{II}}^{\mathrm{TT}}$ [-]	0.2
Hardening modulus H_{I} [MPa] (offline)	50	Poisson ratio $\nu_{\mathrm{II}}^{\mathrm{LT}}$ [-]	0.256
Hardening exponent m_{I} [-]	0.05	shear modulus $G_{\mathrm{II}}^{\mathrm{LT}}$ [GPa]	24

Highly anisotropic structures Additionally to the anisotropic structures above, both TFA and HS method were applied for uniaxial tension tests of a strongly anisotropic microstructure. The material properties of the transverse-isotropic fibers (Section 2.5.1) and the matrix are given by Table 3.6, and the matrix follows the power law hardening in Eq. (3.68). The matrix embeds an inclusion phase with a very high stiffness contrast and an aspect ratio of $r_x/r_y = 10$, occupying a volume fraction of $v_{\mathrm{II}} = 50$ %. The structure was divided into $K = 16$, 128 subdomains (Fig. 3.28a) and loaded in longitudinal and transverse directions. The resulting responses following the full-field and reduced CAH

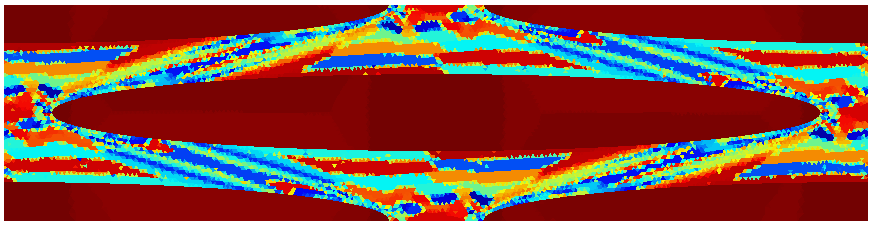

(a)

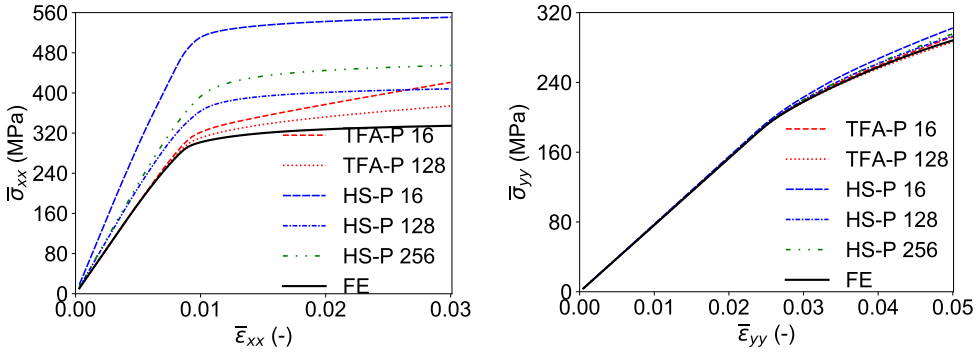

(b) (c)

FIGURE 3.28: Microstructure, cluster division and homogenized stress responses of the highly anisotropic composite material with an inclusion aspect ratio of $r_x/r_y = 10$ and volume fraction of $v_{\mathrm{II}} = 50$ %: in (a) the division into 128 subdomains (four subdomains for the inclusion phase), and the homogenized normal stress responses under uniaxial tension in (b) longitudinal and (c) transverse loading.

TABLE 3.7: Elastic properties computed following Eqs. (3.71), (3.72) and (3.73) using FE DNS and the TFA and HS algorithms with 16 and 128 subdomains for the strongly anisotropic microstructure with $r_x/r_y = 10$.

method →	FE	TFA-P 16	TFA-P 128	HS-P 16	HS-P 128	HS-P 256
$\Delta\overline{\sigma}_{xx}/\Delta\overline{\varepsilon}_{xx}$ (GPa)	35.98	35.98	35.98	59.93	42.68	43.86
$\Delta\overline{\sigma}_{yy}/\Delta\overline{\varepsilon}_{yy}$ (GPa)	7.65	7.65	7.65	7.75	7.69	7.68
$-\Delta\overline{\varepsilon}_{yy}/\Delta\overline{\varepsilon}_{xx}$ (-)	0.439	0.439	0.439	0.498	0.429	0.439

methods are reported in Figs. 3.28b and 3.28c. Furthermore, the homogenized elastic ratios (similar to $\overline{E}_x^{\mathrm{el}}$ and $\overline{E}_y^{\mathrm{el}}$ and the elastic Poisson ratio $\overline{\nu}_{xy}^{\mathrm{el}}$, but here the setting is plane-strain with $\overline{\boldsymbol{\varepsilon}}_{zz} = 0$) were identified as the instantaneous mechanical properties in the elastic regime (thus at low strains, denoted as "at $\overline{\varepsilon}_{xx} = 0$" under uniaxial tension $\overline{\sigma}_{xx}$ and as "at $\overline{\varepsilon}_{yy} = 0$" under uniaxial tension $\overline{\sigma}_{yy}$) as

$$\frac{\Delta\overline{\sigma}_{xx}}{\Delta\overline{\varepsilon}_{xx}} \quad \text{at } \overline{\varepsilon}_{xx} = 0 \text{ and with } \overline{\varepsilon}_{zz} = 0 \tag{3.71}$$

and

$$-\frac{\Delta\overline{\varepsilon}_{yy}}{\Delta\overline{\varepsilon}_{xx}} \quad \text{at } \overline{\varepsilon}_{xx} = 0 \text{ and with } \overline{\varepsilon}_{zz} = 0 \tag{3.72}$$

under uniaxial tension $\overline{\sigma}_{xx}$, and

$$\frac{\Delta\overline{\sigma}_{yy}}{\Delta\overline{\varepsilon}_{yy}} \quad \text{at } \overline{\varepsilon}_{yy} = 0 \text{ and with } \overline{\varepsilon}_{zz} = 0 \tag{3.73}$$

under uniaxial tension $\overline{\sigma}_{yy}$, and are reported in Table 3.7.

The elastic and inelastic responses under transverse tension can be well captured by both TFA and HS approaches, with slightly more accurate results provided by the TFA (Eq. (3.28c)). The achieved modeling quality by the two methods under longitudinal load differs strongly (Eq. (3.28b)). The TFA provides exact estimations of the longitudinal Young's modulus and accurate yield point predictions. The inelastic response is stiff compared to the reference result, and shows a convergence with an increasing number of subdomains. In contrast, the HS method leads to a highly overstiff elastic response, with an estimation of the elastic Young's modulus that has an error of 67% using 16 subdomains and of 19% using 128 subdomains. Besides, the estimation of the yield onset is inaccurate using the HS approach, while the hardening behavior can be well captured. Considering the elastic behavior modeled by the HS method, a clearly improved result is achieved using 128 subdomains with respect to 16 subdomains. Therefore, additionally to the predicted responses by the HS with 16 and 128 subdomains, the result with 256 subdomains (green dashed curve in Figs. 3.28b and 3.28c) was added for an evaluation of the convergence towards the reference result under increasing numbers of subdomains. Recognizing clearly stiffer homogenized elastic, particularly under uniaxial tension in longitudinal fiber orientation, and inelastic responses using 256 subdomains than with 128 subdomains (Table 3.7, Fig. 3.28c), it is concluded that the HS approach does not lead to a convergence towards the reference result under increasing numbers of subdomains for the investigated highly anisotropic microstructure, neither of the elastic response nor of the yield point and the inelastic behavior. The overstiff behavior modeled during elastic deformation may be approached by the introduction of a scalar correction factor, as proposed by Wulfinghoff, Cavaliere, and Reese (2018). Comparing the achieved results in Figs. 3.25, 3.26 and 3.28 however, the inaccuracy of the HS approach depends on various material and structural parameters, e.g. the aspect ratio of the inclusions, the volume fraction of the inclusions, the stiffness contrast between the inclusion and the matrix phase, as well as on the number of subdomains used.

3.5.6 Evaluation of the achieved results

For a two-phase microstructure where both phases deform inelastically, both the TFA and the HS homogenization algorithms provide fairly accurate stress-strain predictions with only one subdomain per phase (see Section 3.5.3). However it is to be mentioned, that although the homogenized composite predictions are well-representative of the homogenized responses computed by full-field solutions, the strain localizations in the single composite phases may deviate from the full-field solution.

The mechanical predictions using the TFA for composite materials consisting of purely elastic inclusions in a perfectly plastic matrix could be significantly improved with an optimized subdomain decomposition which bases on inelastic fields compared to a subdomain decomposition based on elastic fields (see Sections 3.5.2 and 3.5.5). The enhanced representation of the real interaction field by means of an inelasticity based subdomain decomposition results in more accurate strain distributions over the material phases during the

online stage and therefore allows an improved TFA modeling accuracy. The quality of the TFA modeling and the improvement of the enhanced spatial decomposition with respect to the spatial decomposition based on elasticity were verified with regard of the following influences: the volume fractions of the stiff inclusion phases (Fig. 3.29a), the contrast between the phase stiffnesses (Fig. 3.29b) and the degree of microstructural anisotropy (Fig. 3.29c). The TFA-P provides accurate results with errors $< 10\%$ for the cases of low or moderate inclusion volume fractions $v_{\mathrm{II}} = 20\%$ and 30%. High prediction errors with up to 512 subdomains are encountered for a high inclusion phase volume fraction $v_{\mathrm{II}} = 50\%$. However it is important to note that the computation errors appear to decrease under an increasing size of the considered RVE (Tabs. 3.1 and 3.3). It is recognized that the TFA errors are increasing as a function of the inclusion volume fraction. Further it is shown that the subdomain decomposition based on inelastic fields under proportional deformation modes holds for loading-unloading cycles as well as for a non-proportional loading path consisting of four consecutive deformation stages. The proposed fluctuation correction (denoted as TFA-PFC) has a positive impact on the achieved TFA modeling results of elastic inclusions in a perfectly plastic matrix due to the artificially increased interaction effects.

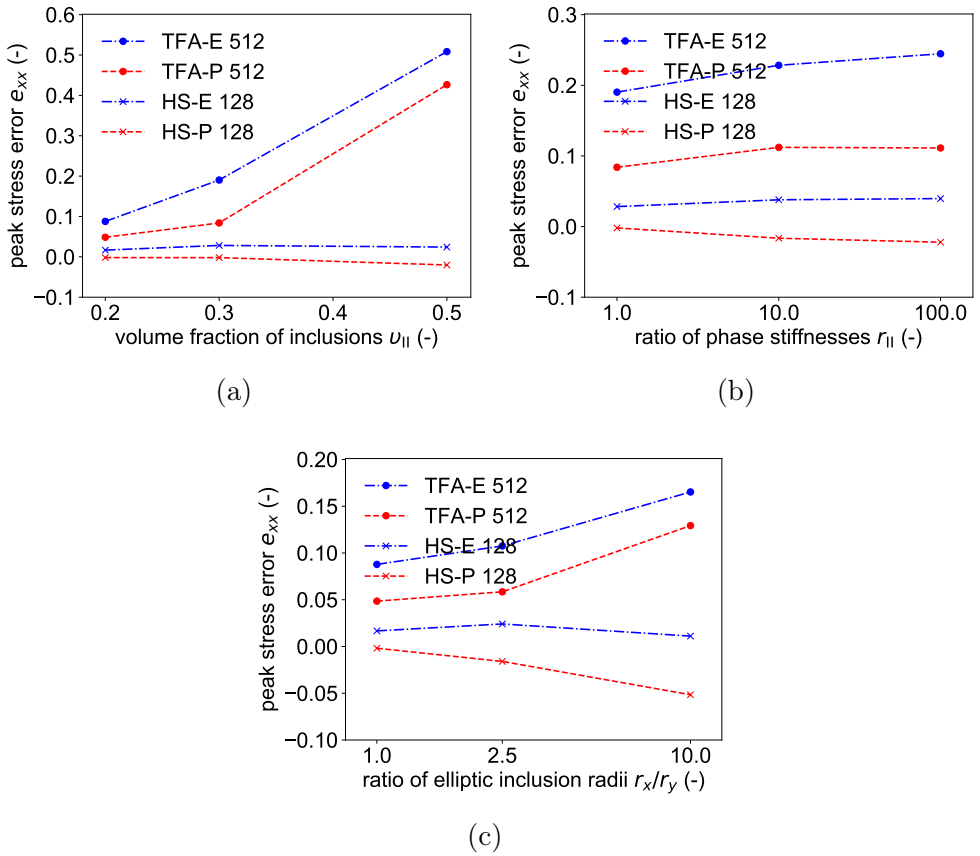

(a) (b)

(c)

FIGURE 3.29: Summary of the prediction quality of the homogenized responses in dependence of the microstructural properties: error quantification as a function of (a) the inclusion volume volume fraction v_{II}, (b) the elastic stiffness contrast between the phases for the isotropic microstructure with $v_{\mathrm{II}} = 30$ %, and (c) the anisotropy of the microstructures with $v_{\mathrm{II}} = 20$ %.

In the following, the prediction errors of the TFA homogenization for cases of elastic inclusions and an elasto-plastic behavior of the matrix phase are treated in more detail. The modeled overstiff behavior is a result of overestimated instantaneous strain concentrations in the stiff phases and underestimated strain concentrations in the inelastically deforming phases during inelastic deformation of the material. This behavior can be clearly recognized in Fig. 3.10, where it is shown that the perfect-plastic behavior can not be fully reflected using the TFA approach. The micromechanical TFA formulated in Eq. (2.33) provides analytical strain distributions, and it was shown that equal results to FE computations are achieved if the spatial configuration of subdomains equals the one of the elements. In an infinitesimally fine discretized domain, the eigenstrain reaction strain field

$$f(\boldsymbol{\chi}) = \mathbb{D}(\boldsymbol{\chi}, \boldsymbol{\chi}') : \boldsymbol{\varepsilon}^*(\boldsymbol{\chi}') \tag{3.74}$$

in Eq. (2.33), averaged over a subdomain V_r, would be expressed as

$$f_r = \int_{V_r} f(\boldsymbol{\chi}) \mathrm{d}\boldsymbol{\chi} = \int_{V_r} \mathbb{D}(\boldsymbol{\chi}, \boldsymbol{\chi}') : \boldsymbol{\varepsilon}^*(\boldsymbol{\chi}') \mathrm{d}\boldsymbol{\chi} \,. \tag{3.75}$$

The overstiff responses encountered when larger domains are considered uniform mean, that the coverage of the eigenstrain reaction field by the consideration of average interaction tensors $\mathbb{D}_{rs}$ (Eq. (3.26)) and piecewise uniform fields $\boldsymbol{\varepsilon}_s^* = \text{const.} \in V_s, \forall V_s$, resulting in the approximation

$$f_r = \sum_{s=1}^{K} \mathbb{D}_{rs} : \boldsymbol{\varepsilon}_s^* \tag{3.76}$$

is insufficient, corresponding to underestimated interaction effects. The consequently overestimated strain and therefore stress accumulations in stiff phases cause, following Eq. (2.65), overestimated composite stress responses. The issue of an overestimated tangent behavior can as well be analysed by a consideration of the composite tangent stiffness, computed as in Eq. (2.70). Following Eq. (2.70), the error in the overall tangent stiffness is explained by inaccurate instantaneous strain concentration tensors $\mathbb{A}_r^{\text{in}}$. As visible in Eq. (2.68) with Eq. (2.62), the $\mathbb{A}_r^{\text{in}}$ are directly dependent of the term $\mathbb{D}_{rs} : \partial \Delta \boldsymbol{\varepsilon}_s^* / \partial \boldsymbol{\varepsilon}_s$. Inaccuracies in the spatial capture of the inelastic interaction field due to an averaging over subdomains (Section 3.3.2), and hence insufficient contributions of the term $\mathbb{D}_{rs} : \partial \Delta \boldsymbol{\varepsilon}_s^* / \partial \boldsymbol{\varepsilon}_s$, are the cause of inaccurate instantaneous strain concentrations during the TFA computation.

The case of a matrix with a perfectly plastic mechanical behavior is a complex one. If the matrix phase behaves perfectly plastic, it carries all deformation in the material and the inclusions undergo no strain. The concentration of the entire overall strain in the matrix phase and zero strain in the inclusions can, using the TFA approach, solely be successfully modeled if the interaction field is fully captured by the spatial decomposition, meaning that the case of elastic inclusions in a perfectly plastic matrix is a highly-complex material system. In composite materials with heterogeneous microstructures, a capture of the full highly-heterogeneous plastic field is impossible using numbers of subdomains that are reasonably low, leading naturally to incorrect strain accumulations in the phases (Fig. 3.10), comprised by overestimated strains in the inclusions and underestimated strains in the matrix, and therefore to an overestimated tangent behavior by the TFA method. According to Fig. 3.10 however, the TFA-P provides clear improvements of the

strain localization with respect to the TFA-E. Originating from the incorrect phase strain distributions, the high errors for the case of a high volume fraction of the inclusion phase are explained as follows: First, the heterogeneity of the plastic field increases in case of higher volume fractions of inclusions, making the efficient representation of the plastic field by an averaging procedure more complex. Second, the inability of the TFA method to avoid occurring strains in stiff inclusions becomes more severe the higher the volume fraction of inclusions. Higher numbers of subdomains may lead to more accurate results, but at the same time, extremely fine meshes are required for the k-means clustering to identify meaningful subdomains when such high numbers of subdomains are used, resulting in more time-expansive offline and online stages.

The HS method provides good accuracies and a fast convergence of the homogenized responses under low numbers of subdomains $K \leq 8$ for cases where the inclusion phase deforms purely elastic and the matrix phase deforms inelastically with low hardening characteristics, or even perfectly-plastic as in most of the presented examples. Very accurate results are achieved with typically only eight subdomains. The high prediction accuracies were verified for low to high volume fractions of inclusions (Fig. 3.29a) and phases stiffness contrasts (Fig. 3.29b) and structural anisotropies (Fig. 3.29c). An issue of the HS approach is however, that after the initial apparent convergence towards the correct results in the range of low numbers of subdomains, the homogenized results keep decreasing under increasing numbers of subdomains, resulting in too compliant inelastic responses in several cases. The overcompliant results are recognized particularly for isotropic structures with high volume fractions of inclusions (see Fig. 3.29a at $\upsilon_{\mathrm{II}} = 50\%$) and for anisotropic structures (Fig. 3.29c).

The HS modeling of anisotropic materials is demonstrated to be critical. While accurate, slightly overcompliant, predictions are achieved if the inclusion volume fraction is low (Figs. 3.25 and 3.26, Table 3.5, Fig. 3.29c), strong anisotropies resulting from high stiffness contrasts and high inclusion volume fractions (microstructure depicted in Fig. 3.28a, phase properties given in Table 3.6) lead to high errors of the elastic and inelastic predictions by the HS approach (Fig. 3.28, Table 3.7). Furthermore, the increase of the numbers of subdomains does not lead to a convergence of the elastic or the inelastic response of the highly anisotropic material. Wulfinghoff, Cavaliere, and Reese (2018) introduced a correction factor in order to artificially decrease the stiffness of the reference medium during the online stage. It is demonstrated in this work however, that a specific correction factor for the HS modeling of anisotropic microstructures is not applicable. The error of the HS predictions was shown to be dependent on various structural and material parameters, e.g. the aspect ratio of the inclusions, the volume fraction of the inclusions, the stiffness contrast between the inclusion and the matrix phase. It means that, for the identification of a valid correction factor for the HS type analysis of a particular anisotropic microstructural system, these various factors need to be taken into account.

3.6 Conclusions

3.6.1 TFA vs. HS clustering analyses

The TFA and HS based reduced two-scale bridging approaches for heterogeneous composite materials were investigated in this chapter for a range of 2D microstructures. The main difference are the interaction functions, leading to the coupling between the sub-

domains: the TFA relies on eigenstrain influence functions, where the eigenstrains are evaluated purely from local constitutive relations. Consequently, it is assumed that the TFA provides reliable mechanical predictions for general composite materials. The HS approach makes use of the Green's polarization influence functions, where the polarization stresses are a measure of the local stress deviation from the virtual stress in a homogeneous reference medium, and therefore depend on the local constitutive relations and the homogenized behavior of the composite. The quality of the achieved results were compared with an emphasis on the critical case of stiff elastic inclusions inside a matrix with a very compliant inelastic behavior.

The use of the TFA leads to clearly overstiff inelastic homogenized responses in the range of low numbers of subdomains. Accurate results can be achieved with high numbers of subdomains, e.g. $K \geq 128$ for many of the tested material systems. The validity of the HS approach, relying on the stiffness of a homogeneous and isotropic reference medium, could be verified for general composites, in particular for cases of high stiffness contrasts between the material phases and strongly anisotropic microstructures. For many of the tested cases of microstructures and material systems, the HS method allows reliable homogenized responses already with only one subdomain per phase and a very fast convergence towards the full-field homogenization result in the range $K \geq 8$, achieving high peak stress accuracies with a total of only eight subdomains. The homogenized response when using the HS type analysis keeps becoming more compliant when the numbers of subdomains further increases, meaning that no convergence of the composite response under increasing numbers of subdomains can be recognized in several cases. No achieved convergence and overcompliant composite responses are found particularly for microstructures with increased complexity, as in the cases of high stiffness contrasts, structural anisotropies and high volume fractions of inclusions.

Consequently, the conclusion is drawn that the use of polarization field influences allows much more compliant responses, and a good convergence towards full-field results in most considered cases, than using eigenstrain field influences when piecewise uniform fields of variables are considered. Following Eqs. (2.18) and (2.22), the microscopic polarization field $\boldsymbol{\tau}(\boldsymbol{\chi})$ in elasto-plastic material phases has a similarly non-uniform character as the inelastic eigenstrain field $\boldsymbol{\varepsilon}^*(\boldsymbol{\chi})$. Therefore, the high differences in the convergence can not be explained by a better representation of the polarization field than of the eigenstrain field considering piecewise uniform fields. The reason for the difference in the results must rather be a consequence of the inherent characteristics of the eigenstrain and polarization fields. Eigenstrains occur only in phases that can deform inelastically, and with an elastic inclusion phase, the eigenstrain field is only existent in the matrix phase. It implies that the TFA can only converge towards the full-field solution under an increasing capture of the non-uniformity of the inelastic field. The requirement of an accurate capture of the inelastic fields gives the TFA a rather computational than analytical characteristic for cases of elastic inclusions in an elasto-plastic matrix. Polarization fields however, occur in both inelastic and elastic phases, meaning that influence contributions are provided by both elastic and inelastic phases. The homogenized stress response that is always in between the responses of the two material phases, and the polarization stresses from both material phases that occur as a consequence, lead to a much faster convergence towards the correct homogenized inelastic response. A reference stiffness that is assumed to have an isotropic character, closely represents the actual homogenized stiffness of a composite material with an isotropic microstructure. Consequently, the assumptions made for cases

of isotropic microstructures, and the difference of using the HS type approach with respect to the use of a generic PFA (Section 2.3.6) that relies on the actual homogenized stiffness of the composite, are rather low. The accurate results with low numbers of subdomains hint towards an intrinsically correctness of the PFA approach, with a low dependence of the homogenized responses on the number of subdomains.

For strongly anisotropic microstructures however, the HS approach is unable to deliver reliable homogenized responses in elastic and inelastic deformation. The assumption of an isotropic reference stiffness, representing the homogenized behavior of the composite, is much stronger in cases of actually anisotropic composite microstructures than for isotropic microstructures. As presented in the last paragraph of Section 3.5.5, the use of the HS approach for a strongly anisotropic structure with a high inclusion volume fraction leads in particular to high errors of the elastic response and the yield onset. It was demonstrated that the increasing number of subdomains for this kind of a highly anisotropic material does not allow a convergence of the homogenized response towards the reference FE result, implying that capabilities of the HS approach for general anisotropic structures is clearly limited. One way to approach this inability of the HS type analyses is the integration of certain correction factors. A constant scalar correction was proposed by Wulfinghoff, Cavaliere, and Reese (2018). However, as recognized in this work, the degree of inaccuracy of the HS approach depends on various material and structural parameters, e.g. the aspect ratio of the inclusions, the volume fraction of the inclusions, the stiffness contrast between the inclusion and the matrix phase, as well as on the number of subdomains used. The inaccuracy dependence on these various factors implies that the determination of effective correction factors needs to account for these factors.

A more general way to achieve reliable results for composite with anisotropic microstructures may be the extension of the from the definition of an isotropic reference medium (Section 2.3.7) towards a more general anisotropic definition of the reference medium. Since the HS type approach, considered as an PFA homogenization (Section 2.3.6) particularized for cases of isotropic composite microstructures, delivers very accurate results with low numbers of subdomains, a generalized PFA, relying on a reference stiffness that represents the homogenized response of an anisotropic composite structure more accurately, may provide high potentials for the homogenization of general composite microstructures.

3.6.2 Plasticity based spatial decompositions

The TFA approach using piecewise uniform fields is known to yield overstiff approximations for the inelastic mechanical behavior of composites, especially in cases of high localized plasticity when using reasonably low numbers of subdomains. The reason for computed overstiff composite predictions by the TFA homogenization is an insufficiently accurate distribution of the overall strain over the subdomains, resulting in overpredicted strain and stress accumulations in stiff or elastic phases during inelastic deformation of the composite. Not ideally determined eigenstrain-strain interaction tensors between subdomains, and therefore underestimated overall eigenfield influences were identified as a cause for incorrect strain distributions over the material phases (more detailed in Sections 3.3.2 and 3.5.6).

Formerly proposed two-scale approaches achieving a model order reduction by using piecewise uniform fields often use elastic strain distributions as the foundation for the spa-

tial decomposition, proven to result in improved mechanical predictions in comparison to the use of spatially regular subdomain decompositions (Liu, Bessa, and Liu, 2016; Wulfinghoff, Cavaliere, and Reese, 2018). In this work it was recognized, that the consideration of inelastic micromechanical deformation patterns provides an improved modeling using piecewise uniform field homogenization approaches. This new approach for the spatial decomposition provides a more physics based modeling respecting the real micromechanics due to an increased emphasis on the main features of the inelastic and therefore of the interaction field. Inelastic deformation patterns evolving due to plastic localization, often particularly in the form of plastic shear bands, are not detectable and therefore not respected by purely elastic pre-analyses. It is successfully shown that

- The accuracy of the strain localizations in both the inelastic matrix and the elastic inclusion phase are clearly improved using the TFA-P with respect to the TFA-E, as can be recognized in Figs. 3.10 and 3.27 for isotropic and anisotropic microstructures, respectively. Therefore,

- The predictions of the homogenized behavior and the convergence towards the full-field results are, using the TFA-P clearly more accurate with respect to the TFA-E.

The composite predictions for the strain-stress responses for the complex case of elastic inclusions in an elasto-plastic matrix can be improved by using the enhanced subdomain decomposition based on inelastic deformation fields.

Clear improvements of the TFA predictions and accurate modeling results using the enhanced spatial division are achieved for the very demanding cases of elastic inclusions in a perfectly plastic matrix phase for low to moderate volume fractions of inclusions v_{II}. The high TFA prediction quality is valid for heterogeneous composites materials with isotropic and anisotropic microstructures and material properties, as well as for different degrees of the phases elastic stiffness contrasts.

However, the error of the tangent behavior of composite materials increases with an increasing inclusion volume fraction as discussed in Section 3.5.6. The TFA predictions for the tangent behavior of composite materials with $v_{\mathrm{II}} = 50\%$ in this work are still overstiff for 512 subdomains defined using the inelasticity based spatial decomposition, although the error continues to decrease with an increasing number of subdomains, provided the mesh used during the offline stage is fine enough. Errors of the TFA are recognized to decrease as well when the size of the RVE is increasing.

The use of statistical field inhomogeneities is a first micromechanics based correction approach for the modeling of composite materials based on piecewise uniform fields. Although it is shown to provide an additional acceleration of the convergence of the achieved strain-stress responses by the TFA towards the reference full-field results, further work is required in order to optimize the use of in-subdomain field fluctuations for an efficient improvement of the inelastic response of composite materials. In order to take heterogeneities of inelastic fields more accurately into account, a new multi-step TFA homogenization scheme will be proposed in Section 5.

The offline stage in this work consists of two RVE deformation modes. More deformation modes can be included in the offline stage, allowing the enhanced inelasticity based TFA modeling of materials under arbitrary loading conditions. A higher number of offline deformation modes might lead to the requirement of higher numbers of subdomains in order to properly cover the various deformation patterns inside the RVE. Consequently, approaches for adapted subdomain decompositions achieved by either using pre-computed

load-specific sets of subdomains or performing re-clustering procedures during the online stage may be considered in the future.

Chapter 4

Two-step homogenization for woven composites

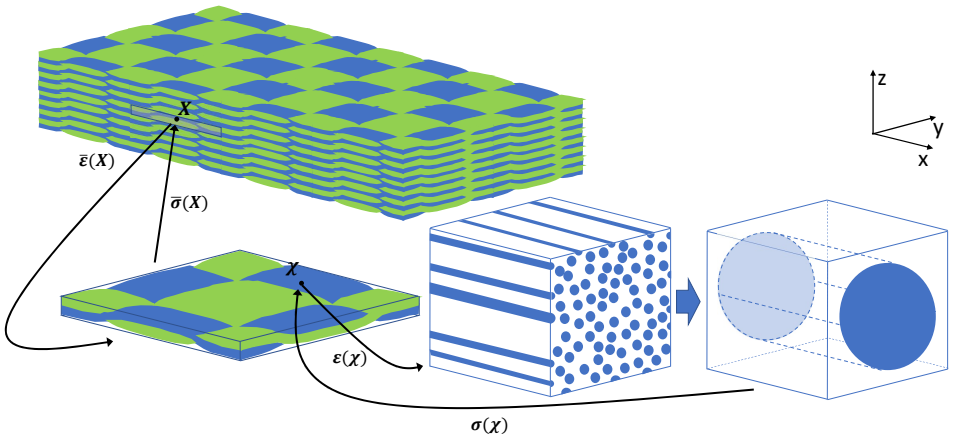

FIGURE 4.1: Schematic demonstration of a mechanical problem of a woven composite considering the associated scales. The deformation state at a certain location inside a structural woven composite $\overline{\boldsymbol{\varepsilon}}(\boldsymbol{X})$ states the boundary problem for the unit cell, representing the mesostructure. The microscopic material points of the yarns in the mesostructural cell are locally considered as a UD fiber composite material. Following from the local deformation at the yarns material points $\boldsymbol{\varepsilon}(\boldsymbol{\chi})$, the MFH is used for the computation of the homogenized response $\boldsymbol{\sigma}(\boldsymbol{\chi})$. The overall stress response of the woven unit cell $\overline{\boldsymbol{\sigma}}(\boldsymbol{X})$ follows from the consideration of the complete local field $\boldsymbol{\chi}$.

4.1 Introduction

This chapter focuses on the CAH of woven composite structures. A woven composite can be classified as a three-scale material, where the evaluation of the structural behavior is affected by mechanical processes on the mesoscopic and microscopic scales (Fig. 4.1). The woven composite on the mesoscale, represented by the mesoscale unit cell, consists of the yarns lying in the so-called ply-plane, surrounded by a matrix material. As presented previously in Section 3, the piecewise uniform homogenization approaches rely on the evaluation of constitutive equations in every subdomain that describe the response of the corresponding material. In the case of the woven composite however, the yarns are a composite material themselves, consisting of long fibers embedded in the same matrix

material. Consequently, the yarns can not be considered as a homogeneous material, but the homogenized behavior of the yarns microstructure needs to be computed simultaneously (Fig. 4.1). Therefore, the piecewise homogeneous constitutive relations are replaced by a homogenization procedure. The reduced three-scale bridging for the prediction of the macroscopic response of woven composites is thus accomplished by a two-step homogenization, exploiting the strengths of two different homogenization techniques for an efficient modeling:

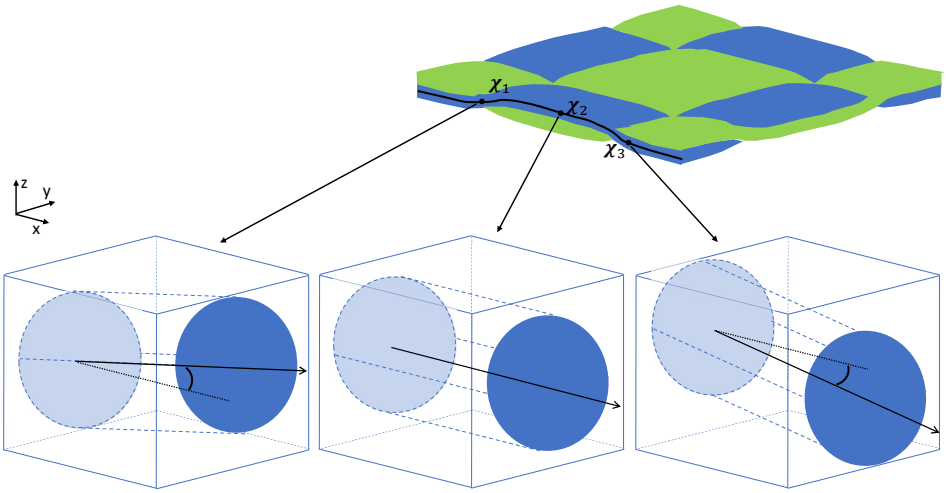

FIGURE 4.2: Depicted is the effect of the yarn inclinations, leading to locally different fiber orientations. The local different fiber orientations imply, as displayed, different orientations of the local equivalent inclusion for the MFH computation. The woven geometry used in this work is the one from the Section 6.2.1 of Wu et al. (2021).

- Piecewise uniform CAH approaches allow for the consideration of complex and anisotropic structures. Therefore, it is made use of the TFA (Sections 2.3.4 and 3.3) and the tangent HS formulation (Sections 2.3.7 and 3.4) in combination with an inelasticity-based subdomain decomposition for the mesoscopic to macroscopic homogenization of the woven RVE. With a subdomain decomposition that aims to accurately respect different inelastic patterns in a material, the number of possibly considered inelastic modes is limited. As the number of possible deformation modes in woven composite structures is rather low, modeling approaches based on a spatial decompositions into subdomains and uniform fields may be considered suitable modeling approaches. Following the good predictions for composites with both phases deforming inelastically (Section 3.5.3) and general anisotropic composite structures (Section 3.5.5), the TFA is expected to provide good captures of the homogenized behavior of the woven unit cell. As introduced previously, the HS approach, relying on a homogeneous reference medium that is isotropic, is adopted for the case of the strongly anisotropic woven structure. Considering the inadequate representation of the homogenized elastic response and yield point of a strongly anisotropic composite microstructure with elastic inclusions (see Table 3.6 and Fig. 3.28), the suitability of this approach is tested and assessed.

- The non-uniform anisotropic elastic and inelastic properties of the yarn materials due to locally varying fiber orientations (schematically depicted in Fig. 4.2) need to

be respected by the spatial division into subdomains in order to gather only material points with similar responses in the same subdomain and therefore, guarantee valid effective responses of the particular subdomain. For this sake, an adapted subdomain decomposition designed for the use of piecewise uniform fields is implemented for the CAH of three-scale composite materials, built by a mesostructure containing phases with possibly fully heterogeneous microstructures. It allows for piecewise uniform field approximations of composites with heterogeneous and anisotropic meso- and microstructures by respecting locally varying orientations of fibers or inclusions (Fig. 4.3). Several plastic fields were computed under typical loading conditions for the woven composite, providing subdomain refinements.

- In previous applications, CAH approaches as the TFA or the HS type method made use of the inelastic strains derived from the piecewise uniform materials constititutive relations. In Han et al. (2020), the mechanical response of woven composites was modeled by the SCCA approach, another CAH method based on piecewise uniform fields. The yarns were considered homogeneneously elastic during the online stage, with the yarns homogenized propertie. An RVE yield criterion was constructed a priori. In contrast to Han et al. (2020), in the present thesis, a MFH algorithm is used for the computation of the homogenized nonlinear behavior of the subdomains in the yarns during the online stage. While an a priori defined yield criterion may have limit the capabilities for modeling of complex history-dependent loading cases, the use of the MFH for the microscopic to mesoscopic scale bridging allows the consideration of arbitrary inelastic responses of the phases of the yarns microstructure and loading conditions. Using the aforementioned spatial decomposition, the composite yarn material can be treated as a piecewise uniform UD fiber composite per subdomain, allowing for the application of the MFH. In order to predict the homogenized behavior of the woven unit cell by the TFA, eigenstrains of the subdomains are to be determined. A new procedure is implemented here, where the eigenstrains of the subdomains are deduced from the homogenized response, computed by the MFH.

This chapter is structured as follows: Section 4.2 contains details of the homogenization from the mesoscopic to macroscopic scale of the woven unit cell. In Section 4.3, the microscopic to mesoscopic scale transition for the yarn material by the use of the MFH is outlined, presenting details on the microstructural setup, the adoption of the incremental-secant approach and its resolution. Subsequently, the Section 4.4 contains the developed clustering technique for the woven unit cell by taking into account the microstructural inhomogeneity of the yarn materials and evolved inelastic fields. Section 4.5 presents results from various numerical tests performed on the woven unit cell. Results of the TFA and HS homogenization approaches are displayed and compared to FE DNS, showing that complex non-proportional loading can be well represented by the two-step homogenization. The developed spatial decomposition is shown to hold for the representation of deformation fields in the woven unit cell even after extended loading histories. In Section 4.6, concluding remarks of this work and possible future contributions on this subject are pointed out.

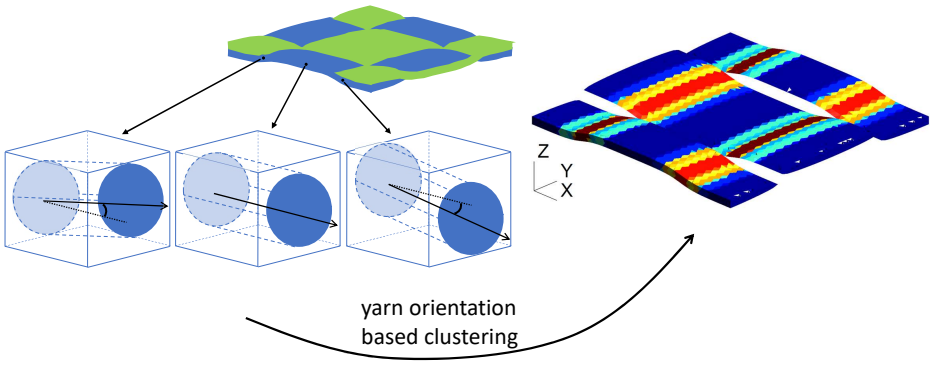

FIGURE 4.3: Displayed is the outcome of a clustering of the weft yarn in the woven unit cell purely based on the heterogeneous local yarn orientations. After the clustering, the subdomains represent the regions with different orientations of the yarn.

4.2 Macroscopic response of the woven composite: unit cell homogenization

4.2.1 Full-field homogenization

The woven composite can, as described, be considered as a three-scale material (Fig. 4.1). The homogenized response of the woven unit cell is referred to as the macroscopic response. The material points of the unit cell domain, $\boldsymbol{\chi}$, are referred to as the mesoscopic material points. Using a full-field homogenization technique for the solution of a BVP applied on a macroscopic material domain V, prescribing the homogenized strain

$$\overline{\boldsymbol{\varepsilon}} = \frac{1}{|V|}\int_V \boldsymbol{\varepsilon}(\boldsymbol{\chi})\mathrm{d}\boldsymbol{\chi} \tag{4.1}$$

of the domain V, the mesoscopic strain field $\boldsymbol{\varepsilon}(\boldsymbol{\chi})$ in the domain V is computed (Section 2.2). The homogenized stress response of the domain V is then computed as the average over the domain,

$$\overline{\boldsymbol{\sigma}} = \frac{1}{|V|}\int_V \boldsymbol{\sigma}(\boldsymbol{\chi})\mathrm{d}\boldsymbol{\chi}\,. \tag{4.2}$$

In this work, the yarns of the woven composite are considered to possess a heterogeneous, fibrous, microstructure, consisting of elastic fibers in a matrix material (Section 4.3.1), depicted in Fig. 4.1. The mesoscopic stress field $\boldsymbol{\sigma}(\boldsymbol{\chi})$ of the full-field solution in Eq. (4.2) is computed from a homogenization procedure of the microstructural composite at the mesoscopic material point $\boldsymbol{\chi}$ by means of the incremental-secant MFH (Section 4.3.2) by Wu et al. (2013a). Besides the mesoscopic stress field $\boldsymbol{\sigma}(\boldsymbol{\chi})$, the mesoscopic algorithmic tangent operators $\mathbb{C}^{\mathrm{alg}}(\boldsymbol{\chi})$ are to be determined from the incremental-secant MFH scheme in order to solve the BVP of the unit cell. The incremental-secant MFH, detailed in Section 2.4.2, is particularized to the present mesoscale of the woven composite in Section 4.3.2. Although this method is not a real full-field resolution in which the fibers would be

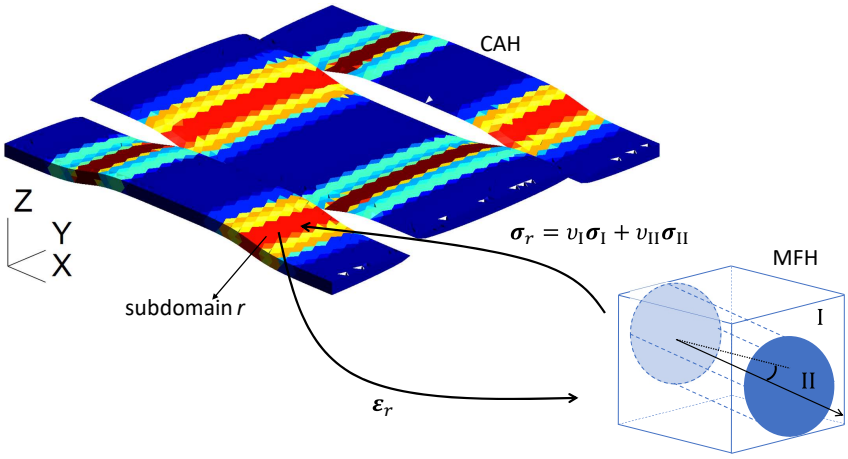

FIGURE 4.4: Schematic display of the CAH of the woven unit cell. The subdomains stress-strain responses follow from the homogenization of the underlying fibrous matrix-inclusion composite with the associated orientation of the fiber using the incremental-secant MFH scheme. The microstructural composite associated to the subdomain has the homogenized orientation of the local material points in the subdomain.

represented explicitly, it provides reference homogenized predictions, to which the CAH responses can be compared.

4.2.2 Clustering analysis based homogenization

The homogenized macroscopic mechanical response of the woven unit cell is analyzed by the means of CAH with a spatial decomposition of the mesoscopic unit cell domain using the TFA or the HS formulations (see Sections 3.3 and 3.4). For the construction of the reduced models, the unit cell is subdivided into several subdomains based on mesoscopic inelastic deformation fields computed under specific loading conditions during the offline stage. The subdomains represent the mesoscopic domain of the unit cell. The spatial decomposition into subdomains r based on inelastic strains, following Section 3.2.2, will be presented in Section 4.4.

The incremental TFA scale coupling relation (Eq. (2.49)), used here for the mesoscopic to macroscopic homogenization of the woven unit cell under a prescribed macroscopic strain increment $\Delta\overline{\boldsymbol{\varepsilon}}$, is recalled:

$$\Delta\boldsymbol{\varepsilon}_r = \mathbb{A}_r^{\mathrm{el}} : \Delta\overline{\boldsymbol{\varepsilon}} + \sum_{s=1}^{K} \mathbb{D}_{rs} : \Delta\boldsymbol{\varepsilon}_s^* \,. \tag{4.3}$$

The subdomains average elastic strain concentration tensors $\mathbb{A}_r^{\mathrm{el}}$ are computed as

$$\mathbb{A}_r^{\mathrm{el}} = \frac{1}{|V_r|} \int_{V_r} \mathbb{A}^{\mathrm{el}}(\boldsymbol{\chi}) \mathrm{d}\boldsymbol{\chi} \,, \tag{4.4}$$

where the estimation of the local field $\mathbb{A}^{\mathrm{el}}(\boldsymbol{\chi})$ was presented in Section 3.2.1. The determination of the interaction tensors $\mathbb{D}_{rs}$ between two subdomains r and s was explained

in Section 3.3.1. The eigenstrains $\boldsymbol{\varepsilon}_s^*$ of the mesoscopic subdomains during the solution stage of the TFA follow from the response of the underlying microstructural composite associated to the subdomain r (Section 4.3.1), computed by means of the incremental-secant MFH procedure (Section 4.3.2, with more details in Section 2.4.2). The scale-coupling between the subdomains of the unit cell and the microstructure by means of the MFH is schematically displayed in Fig. 4.4. The deduction of the eigenstrains from the homogenized stress response of the subdomain $\boldsymbol{\sigma}_r$, following the MFH scheme, will be explained in Section 4.3.2. The numerical solution of the TFA CAH scheme in Eq. (4.3) was outlined in Section 2.3.5 and remains unchanged.

The reduced incremental HS scale coupling relation (Eq. (2.97)) is written as:

$$\Delta\boldsymbol{\varepsilon}_r = \Delta\overline{\boldsymbol{\varepsilon}} + \sum_{s=1}^{K} \Gamma_{rs}^0 : \left(\frac{G^0}{\overline{G}^{\mathbf{alg}}} \Delta\boldsymbol{\sigma}_s - \mathbb{C}^{0,\mathrm{iso}} : \Delta\boldsymbol{\varepsilon}_s \right). \tag{4.5}$$

The HS formulation developed in this work relies on the definition of a reference medium with an isotropic algorithmic tangent stiffness, characterized only by the algorithmic shear modulus of the medium, $\overline{G}^{\mathbf{alg}}$. The computation of the algorithmic shear modulus of the reference medium, $\overline{G}^{\mathbf{alg}}$, was presented in Section 2.3.7. The mesoscopic subdomains stresses $\boldsymbol{\sigma}_s$ are, as the eigenstrains $\boldsymbol{\varepsilon}_s^*$ for the TFA, computed by means of the incremental-secant MFH procedure (Section 4.3.2, with more details in Section 2.4.2) of the underlying microstructural composite associated to the subdomain r (Section 4.3.1). The procedures for the determination of the stiffness operator of the elastic reference medium, $\mathbb{C}^{0,\mathrm{iso}}$, and the associated shear modulus G^0, as well as the computation of the Green's interaction tensors in the elastic reference medium, Γ_{rs}^0, between two subdomains s and r, are explained in the Sections 3.4.2 and 3.4.3, respectively. The numerical solution of the HS type analysis was presented in Section 2.3.8 and remains unchanged.

4.3 Mesoscopic constitutive relations: homogenization of the yarn material

The yarn material consists of 80% of longitudinal fibers in the yarn direction embedded in the matrix material. Accordingly, each mesoscopic material point $\boldsymbol{\chi}$ or each mesoscopic subdomain V_r located inside one of the yarns, is constituted by a two-phase composite medium (Fig. 4.4), consisting of an inclusion (fiber) phase (subscript II) embedded in a matrix (subscript I), with the phase volume ratios $v_{\mathrm{I}}(\boldsymbol{\chi})$ and $v_{\mathrm{II}}(\boldsymbol{\chi})$, or v_{I_r} and v_{II_r} for respectively full-field and CAH resolutions, where

$$v_{\mathrm{I}} + v_{\mathrm{II}} = 1\,. \tag{4.6}$$

The local volume ratios, $v_{\mathrm{II}} = 0.8$ and $v_{\mathrm{I}} = 0.2$, are assumed uniform in the yarn material. Homogenized responses at the mesoscopic material point $\boldsymbol{\chi}$, or of the subdomain r with uniform fields of variables, can be computed using Mean Field Homogenization (MFH) techniques (as detailed below in Section 4.3.2).

4.3.1 Microstructural definition of the yarn material

For the incremental-secant MFH approach (see Section 2.4.2) adopted in this work, the microscopic fibrous two-phase composite medium of the yarn material is locally treated as an equivalent two-phase medium of the composition Eq. (4.6) (Fig. 4.4), consisting of one equivalent inclusion (II) embedded in the matrix, or host, phase (I). The matrix (host) phase and the inclusion phase are represented by uniform fields of variables with average quantities. The strain localization of the incremental-secant MFH (Eqs. (2.155) and (2.156)) and therefore the homogenized response depends on the geometry information of the two-phase system. With an isotropic host phase, the local geometrical information are expressed by $g_{\mathrm{II}}(\boldsymbol{\chi})$, containing the aspect ratio and spatial orientation of the local equivalent inclusion at $\boldsymbol{\chi}$.

Here, the local equivalent elliptical inclusion represents unidirectional fibers, and so the ellipse aspect ratio is very large and considered uniform in the yarn material. The local orientation of the fibers however, varies according to the local yarn inclination (Fig. 4.2), and is characterized by the local euler angles $\theta(\boldsymbol{\chi}) = \big(\theta_1(\boldsymbol{\chi}), \theta_2(\boldsymbol{\chi}), \theta_3(\boldsymbol{\chi})\big)$, describing the orientation of the local rotated coordinate system with respect to the global coordinate system (if $\theta(\boldsymbol{\chi}) = (0°, 0°, 0°)$, rotated system equals global system). Before the rotation, the fibers align with the global z-axis $\vec{e}_z$. After the rotation, they align with the locally rotated z''-axis. With the fibers following the weft and warp yarns oriented in the global x- and y-axis directions, respectively, the first euler angle (rotation $Q_1\big(\theta_1(\boldsymbol{\chi})\big)$ around global z-axis) is given as

$$\theta_1(\boldsymbol{\chi}) = \begin{cases} 90° & , \boldsymbol{\chi} \in V_{\mathrm{Weft}} \\ 0° & , \boldsymbol{\chi} \in V_{\mathrm{Warp}}\,. \end{cases} \tag{4.7}$$

The second euler angle (rotation $Q_2\big(\theta_2(\boldsymbol{\chi})\big)$ around rotated x'-axis) represents the local vertical inclination of the yarn in which $\boldsymbol{\chi}$ is located, where $\theta_2(\boldsymbol{\chi}) = 90°$ means a perfectly horizontal alignment. The third euler angle $\theta_3(\boldsymbol{\chi})$ (rotation around rotated z''-axis) is of no importance for the local fiber orientation. In conclusion, the local fiber orientation may be expressed by

$$\vec{v}(\boldsymbol{\chi}) = Q_2\big(\theta_2(\boldsymbol{\chi})\big) \cdot Q_1\big(\theta_1(\boldsymbol{\chi})\big) \cdot \vec{e}_z = Q(\boldsymbol{\chi}) \cdot \vec{e}_z\,, \tag{4.8}$$

where $\vec{e}_z$ denotes the eigenvector in the z- direction of the global coordinate system and $Q(\boldsymbol{\chi}) = Q\big(\theta_1(\boldsymbol{\chi}), \theta_2(\boldsymbol{\chi})\big)$ is the total local rotation from the global z-axis towards the local fiber orientation at $\boldsymbol{\chi}$. Details on the rotations are given in Appendix E.

Considering the spatial decomposition into subdomains with uniform fields (Section 2.3.3) and uniform constitutive relations, the equivalent inclusion geometry g_{II_r} in the subdomain r is characterized by the homogenized euler angles $\theta_r = \big(\theta_{1_r}, \theta_{2_r}\big)$. The homogenized euler angles are computed as the circular mean following

$$\theta_r = \frac{1}{2}\arctan(A/B)\,, \tag{4.9}$$

where

$$A = \frac{1}{|V_r|}\int_{V_r} \sin\big(2\theta(\boldsymbol{\chi})\big)\mathrm{d}\boldsymbol{\chi} \tag{4.10}$$

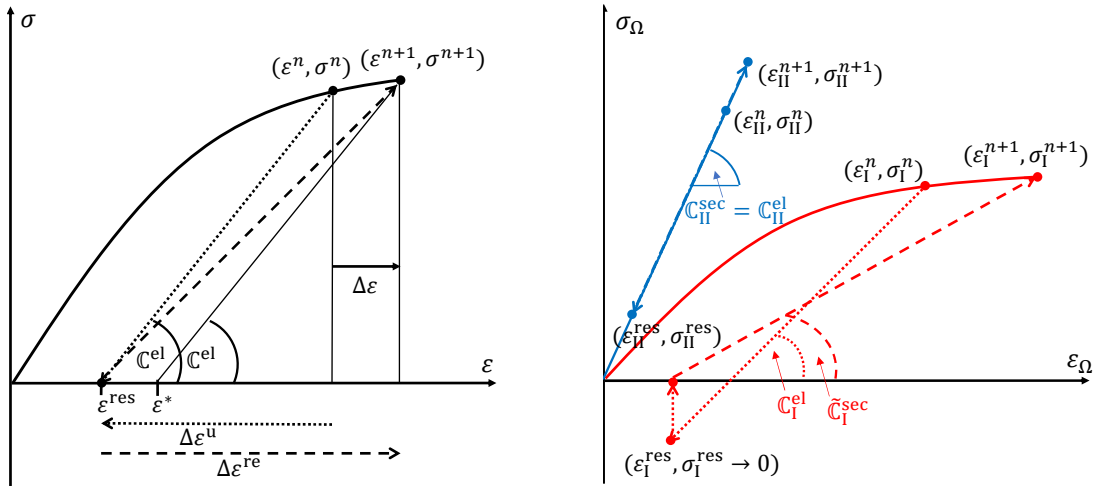

FIGURE 4.5: MFH procedure under an applied strain increment $\Delta\boldsymbol{\varepsilon}$ schematically for a two-phase composite, consisting of an elastic inclusion in an inelastic matrix: The (a) unloading-reloading procedure of the composite towards a zero-stress state (dotted) and to the new homogenized state (dashed), and (b) the unloading-reloading step translated to the two separate composite phases. The adopted zero-residual formulation for the matrix phase is demonstrated.

and

$$B = \frac{1}{|V_r|} \int_{V_r} \cos\big(2\theta(\boldsymbol{\chi})\big) \mathrm{d}\boldsymbol{\chi}\,, \tag{4.11}$$

where the factor two is required for the correct computation of the mean orientation. The Eqs. (4.9), (4.10) and (4.11) are applied for the homogenization of each component of θ_r. The homogenized fiber orientation of the subdomain r, required for the underlying microscopic homogenization of the equivalent two-phase composite using the MFH, is expressed as

$$\vec{v}_r = Q_2\big(\theta_{2_r}\big) \cdot Q_1\big(\theta_{1_r}\big) \cdot \vec{e}_z = Q(\theta_{1_r}, \theta_{2_r}) \cdot \vec{e}_z\,. \tag{4.12}$$

4.3.2 Incremental-secant MFH

As already mentioned in Section 4.2, each mesoscopic material point $\boldsymbol{\chi}$ in the full-field simulations and each subdomain V_r of the CAH models, located in the yarns of the woven structure, are constituted by a composite medium of the two phases $\Omega = \{\mathrm{I}, \mathrm{II}\}$, and their homogenized responses follow from the incremental-secant MFH scheme, detailed in Section 2.4.2 (remark on the difference of the used notations: in Section 2.4.3, the MFH is solved under the macroscopic strain $\bar{\boldsymbol{\varepsilon}}$). In the following equations, the material point denoted by $\boldsymbol{\chi}$ for the full-field simulations, and the subscript r referring to the subdomain of the CAH models, are omitted. The homogenized local incremental strains $\Delta\boldsymbol{\varepsilon}(\boldsymbol{\chi})$ and stresses $\boldsymbol{\sigma}(\boldsymbol{\chi})$ or subdomain incremental strain $\Delta\boldsymbol{\varepsilon}_r$ and stresses $\boldsymbol{\sigma}_r$ are expressed as

$$\Delta\boldsymbol{\varepsilon} = v_{\mathrm{I}} \Delta\boldsymbol{\varepsilon}_{\mathrm{I}} + v_{\mathrm{II}} \Delta\boldsymbol{\varepsilon}_{\mathrm{II}} \tag{4.13}$$

and

$$\boldsymbol{\sigma} = \upsilon_{\mathrm{I}}\boldsymbol{\sigma}_{\mathrm{I}} + \upsilon_{\mathrm{II}}\boldsymbol{\sigma}_{\mathrm{II}}\,. \tag{4.14}$$

It is noted for clarification, that the MFH is not applied on the homogenized unit cell strain $\Delta\overline{\boldsymbol{\varepsilon}}$. The strain $\Delta\overline{\boldsymbol{\varepsilon}}$ is processed by the CAH schemes on the mesoscopic unit cell level. The MFH is used for the computation of the local responses at $\boldsymbol{\chi}$ in the DNS, following the local microstructural configuration at $\boldsymbol{\chi}$, and the subdomains responses in the CAH, considering the subdomains homogenized microstructural configuration.

Each local material point in the yarns, or each subdomain located in the yarns, are composed by a microstructural composite that consists of an inclusion II with a certain orientation embedded in the matrix I. This equivalent composite represents the actual fibrous microstructure of the yarn materials. While the response of the inclusion follows from the residual incremental-secant method, the response of the matrix subdomains is governed by the zero-residual incremental-secant approach. Accordingly, the homogenized response of the two-phase composite follows from the incremental-secant reloading strain localization given by

$$\Delta\boldsymbol{\varepsilon}_{\mathrm{II}}^{\mathrm{re}} = \mathbb{B}_{\mathrm{II}}^{\mathrm{sec}} : \Delta\boldsymbol{\varepsilon}_{\mathrm{I}}^{\mathrm{re}} \tag{4.15a}$$

$$\mathbb{B}_{\mathrm{II}}^{\mathrm{sec}} = \{\mathbb{I} + \mathbb{S} : [(\tilde{\mathbb{C}}_{\mathrm{I}}^{\mathrm{sec}})^{-1} : \mathbb{C}_{\mathrm{II}}^{\mathrm{sec}} - \mathbb{I}]\}^{-1}\,, \tag{4.15b}$$

with the incremental-secant operator of the inclusion phase $\mathbb{C}_{\mathrm{II}}^{\mathrm{sec}}$ and the zero-residual incremental secant operator of the matrix $\tilde{\mathbb{C}}_{\mathrm{I}}^{\mathrm{sec}}$ (schematically displayed in Fig. 4.5). The Eshelby tensor $\mathbb{S}(g_{\mathrm{II}}, \tilde{\mathbb{C}}_{\mathrm{I}}^{\mathrm{sec}})$ in Eq. (4.15) is a function of the inclusion geometry g_{II} and the zero-residual incremental-secant operator $\tilde{\mathbb{C}}_{\mathrm{I}}^{\mathrm{sec}}$ of the host phase $\mathbb{C}_{\mathrm{I}}^{\mathrm{LCC}}$. With the volume fractions of the two phases and the inclusion aspect ratios (corresponding to a fiber) considered uniform in the yarns, the inclusion geometry is represented by the orientation of the fiber, locally at $\boldsymbol{\chi}$ by Eq. (4.8) for the full-field solution or homogenized over the subdomains according to Eq. (4.12) for the CAH (Fig. 4.4).

The homogenized eigenstrain, required to conduct the TFA CAH on the mesoscale level, results, as visible in Fig. 4.5a, in

$$\boldsymbol{\varepsilon}^{*} = \boldsymbol{\varepsilon} - (\mathbb{C}^{\mathrm{el}})^{-1} : \boldsymbol{\sigma}\,. \tag{4.16}$$

A comparison of Eqs. (2.149) and (4.16) shows that the homogenized residual strain at the following time step is equal to the homogenized eigenstrain at the current time step (Fig. 4.5a). Furthermore, the derivative $\partial\boldsymbol{\varepsilon}^{*}/\partial\boldsymbol{\varepsilon}$ is required for the resolution of the TFA algorithm (Section 2.3.5) on the mesoscale, while the algorithmic tangent $\mathbb{C}^{\mathrm{alg}}$ is required for the nonlinear resolutions of both the CAH algorithms (Sections 2.3.5 and 2.3.8) and the full-field solution (Section 4.2.1) for the computation of the homogenized unit cell response. The derivative of the eigenstrain is expressed as

$$\frac{\partial\boldsymbol{\varepsilon}^{*}}{\partial\boldsymbol{\varepsilon}} = \mathbb{I} - (\mathbb{C}^{\mathrm{el}})^{-1} : \mathbb{C}^{\mathrm{alg}}\,, \tag{4.17}$$

and the homogenized algorithmic tangent stiffness $\mathbb{C}^{\mathrm{alg}} = \partial\boldsymbol{\sigma}/\partial\boldsymbol{\varepsilon}$, following from Eq. (4.14), as

$$\mathbb{C}^{\mathrm{alg}} = \upsilon_{\mathrm{I}}\frac{\partial\boldsymbol{\sigma}_{\mathrm{I}}}{\partial\boldsymbol{\varepsilon}_{\mathrm{I}}}\frac{\partial\boldsymbol{\varepsilon}_{\mathrm{I}}}{\partial\boldsymbol{\varepsilon}} + \upsilon_{\mathrm{II}}\frac{\partial\boldsymbol{\sigma}_{\mathrm{II}}}{\partial\boldsymbol{\varepsilon}_{\mathrm{II}}}\frac{\partial\boldsymbol{\varepsilon}_{\mathrm{II}}}{\partial\boldsymbol{\varepsilon}} = \upsilon_{\mathrm{I}}\mathbb{C}_{\mathrm{I}}^{\mathrm{alg}}\frac{\partial\boldsymbol{\varepsilon}_{\mathrm{I}}}{\partial\boldsymbol{\varepsilon}} + \upsilon_{\mathrm{II}}\mathbb{C}_{\mathrm{II}}^{\mathrm{alg}}\frac{\partial\boldsymbol{\varepsilon}_{\mathrm{II}}}{\partial\boldsymbol{\varepsilon}}\,. \tag{4.18}$$

Its computation is outlined in Appendix B.4. The inclusion phase $\Omega = \mathrm{II}$ is represented by

elastic fibers, meaning that $\mathbb{C}_{\mathrm{II}}^{\mathrm{sec}} = \mathbb{C}_{\mathrm{II}}^{\mathrm{alg}} = \mathbb{C}_{\mathrm{II}}^{\mathrm{el}}$ and therefore $\boldsymbol{\sigma}_{\mathrm{II}} = \mathbb{C}_{\mathrm{II}}^{\mathrm{el}} : \boldsymbol{\varepsilon}_{\mathrm{II}}$, where $\mathbb{C}_{\mathrm{II}}^{\mathrm{el}}$ is the transverse-isotropic elastic stiffness of the fibers. The local nonlinear stress-strain response of the inelastic matrix phase $\Omega = \mathrm{I}$ follows from the incremental-secant J_2-plasticity model (see Section 2.5.3) with vanishing residuals, referred to as the zero-residual incremental-secant formalism. The solution of the incremental-secant MFH algorithm is explained in more detail in Section 2.4.3, where the formalism for the incremental-secant procedure of the matrix with residual stresses was considered (remark on the difference of the used notations: in Section 2.4.3, the MFH is solved under the macroscopic strain $\overline{\boldsymbol{\varepsilon}}$). The resolution, applied for the modeling of the woven composite with the zero-residual formalism for the matrix phase and with the notation used in this chapter, is summarized in Algorithm 9.

Algorithm 9: Numerical incremental-secant MFH procedure for the microstructural homogenization of the composite yarn materials, with the zero-residual formalism employed for the matrix response, at a glance: Newton-Raphson scheme at one load step for a given overall strain increment $\Delta\boldsymbol{\varepsilon}$. The solution scheme is presented in detail in Section 2.4.3 (remark on the difference of the used notations: in Section 2.4.3, the MFH is solved under the macroscopic strain $\overline{\boldsymbol{\varepsilon}}$).

compute residual state following Eqs. (2.163), (2.164) and (2.165).
Set matrix residual state to zero stress: $\boldsymbol{\sigma}_{\mathrm{I}}^{\mathrm{res}} = 0$
initialize: $\Delta\boldsymbol{\varepsilon}_{\mathrm{II}}^{\mathrm{re}} = \Delta\boldsymbol{\varepsilon}^{\mathrm{re}}$
iterative procedure:
repeat
  compute matrix reloading strain increment: $\Delta\boldsymbol{\varepsilon}_{\mathrm{I}}^{\mathrm{re}} = (\Delta\boldsymbol{\varepsilon}^{\mathrm{re}} - \upsilon_{\mathrm{II}}\Delta\boldsymbol{\varepsilon}_{\mathrm{II}}^{\mathrm{re}})/\upsilon_{\mathrm{I}}$
  call constitutive relations for both phases $\Omega = \mathrm{I}, \mathrm{II}$ to compute $\boldsymbol{\sigma}_{\Omega}$ and the stiffness tensors $\tilde{\mathbb{C}}_{\mathrm{I}}^{\mathrm{sec}}$ and $\mathbb{C}_{\mathrm{II}}^{\mathrm{sec}}$ (details in Section 2.5.3).
  evaluate the Eshelby tensor $\mathbb{S}(g_{\mathrm{II}}, \tilde{\mathbb{C}}_{\mathrm{I}}^{\mathrm{sec}})$
  compute stress residual $\boldsymbol{F}$ according Eq. (2.169).
  compute Jacobian matrix $\mathbb{J}$ according Eq. (2.172).
  solve $\delta\boldsymbol{\varepsilon}_{\mathrm{II}} = -\mathbb{J}^{-1} : \boldsymbol{F}$
  update $\Delta\boldsymbol{\varepsilon}_{\mathrm{II}}^{\mathrm{re}} = \Delta\boldsymbol{\varepsilon}_{\mathrm{II}}^{\mathrm{re}} - \delta\boldsymbol{\varepsilon}_{\mathrm{II}}$
until $|\boldsymbol{F}| < \mathrm{tol}$;
after convergence:
compute $\boldsymbol{\sigma}$ and $\mathbb{C}^{\mathrm{alg}}$, following Eq. (4.14) and Eq. (4.18), respectively.
For the TFA algorithm on the mesoscale level, the eigenstrain $\boldsymbol{\varepsilon}^*$ and its derivative $\partial\boldsymbol{\varepsilon}^*/\partial\boldsymbol{\varepsilon}$ are to be determined in addition using Eq. (4.16) and Eq. (4.17), respectively.

4.4 Clustering of the woven unit cell

The model order reduction step consists of a spatial division of the fully discretized RVE domain into several subdomains. An optimized subdomain decomposition is achieved using the k-means clustering technique. The k-means clustering partitions a number of local data points into subpartitions based on the similarity of the local data. The final partition is achieved by solving an optimization problem iteratively, minimizing the

deviations between all local data points and the subpartition mean values. In the context of mechanical fields, the k-means clustering divides the considered domain based on the similarity of the local mechanical behavior.

As shown by Spilker et al. (2022), respecting inelastic deformation patterns within a material allows an improved subdomain decomposition in comparison to the decomposition based on purely elastic deformation. In this work, the three inelastic deformation boundary modes

$$\overline{\boldsymbol{\varepsilon}}^{\mathrm{in}(1)} = E^{\mathrm{in}}(\vec{e}_x \otimes \vec{e}_x - \vec{e}_y \otimes \vec{e}_y) \tag{4.19a}$$

$$\overline{\boldsymbol{\varepsilon}}^{\mathrm{in}(2)} = E^{\mathrm{in}}(\vec{e}_y \otimes \vec{e}_y + \vec{e}_x \otimes \vec{e}_x) \tag{4.19b}$$

$$\overline{\boldsymbol{\varepsilon}}^{\mathrm{in}(3)} = E^{\mathrm{in}}(\vec{e}_x \otimes \vec{e}_y + \vec{e}_y \otimes \vec{e}_x)\,, \tag{4.19c}$$

with the overall deformation factor $E^{\mathrm{in}} = 3\%$ and the canonical unit vectors in a 3D space $\vec{e}_x$, $\vec{e}_y$, $\vec{e}_z$, were selected and applied on the woven composite RVE. The three chosen deformation modes inside the ply plane ($x-y$-plane) represent typical deformation conditions for the woven composite structure. The local eigenstrain fields $\boldsymbol{\varepsilon}^{*(l)}(\boldsymbol{\chi})$ emerging under each of the boundary conditions $l = 1, 2, 3$ are computed.

In this work, each yarn domain V_Y ($Y = \mathrm{Weft}, \mathrm{Warp}$) is spatially divided in two steps:

1. First, the necessary division based on the local fiber orientation is performed. The spatial decomposition that takes into account the local yarn, and thus fiber, orientation, is depicted in Fig. 4.3. Material points with very deviating fiber orientations gathered in the same subdomain would lead to not well representative subdomain fiber orientations and unreliable mechanical responses of the yarn material computed by the MFH algorithm. Each yarn domain V_Y is decomposed into K_Y^θ subdomains V_R, $R \in 1, ..., K_Y^\theta$. A sufficiently high K_Y^θ ensures that only local material points with similar fiber orientation are gathered in one subdomain and therefore reasonable averaged fiber orientations of the subdomain. For a general orientation-based subdivision, the function

$$J_Y^\theta[\theta(\boldsymbol{\chi})] = \sum_{R=1}^{K_Y^\theta} \sum_{i=1}^{N_R} |\vec{v}(\boldsymbol{\chi}_i) \times \vec{v}_R|^2, \quad \boldsymbol{\chi} \in V_Y, \quad \boldsymbol{\chi}_i \in V_R \subset V_Y, \quad R \in 1, ..., K_Y^\theta\,, \tag{4.20}$$

can be chosen to be minimized, where N_R is the number of local material points inside the subdomain R, $\vec{v}(\boldsymbol{\chi}_i)$ and $\vec{v}_R$ are the local and subdomain fiber orientations given by Eqs. (4.8) and (4.12). The operation " $\times$ " denotes the cross product between two vectors $\vec{a}$ and $\vec{b}$, with

$$|\vec{a} \times \vec{b}| = |a|\,|b|\,\sin(\Delta\theta)\,, \tag{4.21}$$

where $\Delta\theta$ is the angle between the two vectors in the plane they are located in. The cross product between the local fiber orientation $\vec{v}(\boldsymbol{\chi}_i)$ and the subdomain mean orientation $\vec{v}_R$ in above Eq. (4.20) represents the deviation of $\vec{v}(\boldsymbol{\chi}_i)$ from $\vec{v}_R$. In the case of the woven structure, the first euler rotation is uniform per yarn, meaning that all local fiber orientations in one yarn are distinguished only by the second euler angle $\theta_2(\boldsymbol{\chi})$. Since each yarn is subdivided separately, and considering Eq.

(4.21), the k-means clustering is applied to minimize the simplified function

$$J_Y^{\theta}[\theta(\boldsymbol{\chi})] = \sum_{R=1}^{K_Y^{\theta}} \sum_{i=1}^{N_R} \left(\sin(\theta_2(\boldsymbol{\chi}_i) - \theta_{2_R}) \right)^2, \quad \boldsymbol{\chi} \in V_Y, \quad \boldsymbol{\chi}_i \in V_R \subset V_Y, \quad R \in 1, ..., K_Y^{\theta}, \tag{4.22}$$

where the subdomain mean orientation θ_{2_R} follows Eq. (4.9).

2. As the second spatial division step, the subdomain decomposition is optimized by taking into account eigenstrain fields occurring under the applied inelastic boundary modes in Eq. (4.19) in the offline stage (the resulting inelastic fields are depicted in Fig. 4.6). Equivalently as described for the full-field homogenization in Section 4.2.1, the FE DNS of the offline stage were performed with the MFH for the homogenization of the yarns, providing the local responses $\boldsymbol{\sigma}(\boldsymbol{\chi})$ in the yarns on the mesoscale. Following the local stress response $\boldsymbol{\sigma}(\boldsymbol{\chi})$, the mesoscopic eigenstrain fields for the spatial decomposition were, according to Eq. (2.24), extracted as

$$\boldsymbol{\varepsilon}^*(\boldsymbol{\chi}) = \boldsymbol{\varepsilon}(\boldsymbol{\chi}) - \mathbb{C}^{\mathrm{el}}(\boldsymbol{\chi})^{-1} : \boldsymbol{\sigma}(\boldsymbol{\chi}) \,. \tag{4.23}$$

Each orientation-based subdomain V_R is divided into a number K_Y^{p} subdomains V_r, $r \in 1, ..., K_Y^{\mathrm{p}}$ based on the eigenstrain distributions. For the inelasticity based subdomain refinement, the eigenstrain fields $\boldsymbol{\varepsilon}^{*(l)}(\boldsymbol{\chi})$ under each of the boundary conditions $l = 1, 2, 3$ are normalized by the equivalent (scalar) per-phase averaged eigenstrain and arranged in local 6×1 vectors $\boldsymbol{q}^{(l)}(\boldsymbol{\chi})$. The normalized eigenstrain fields are then assembled in local 1×18 vectors

$$\boldsymbol{q}(\boldsymbol{\chi}) = \left(\boldsymbol{q}^{(1)^T}(\boldsymbol{\chi}) \,, \boldsymbol{q}^{(2)^T}(\boldsymbol{\chi}) \,, \boldsymbol{q}^{(3)^T}(\boldsymbol{\chi}) \right)^{\mathrm{T}} , \tag{4.24}$$

representing the entirety of the local eigenstrain fields. The k-means clustering technique is then applied on the eigenstrain field in each orientation-based subdomain R, minimizing the corresponding function

$$J_R^{\mathrm{p}}[\boldsymbol{q}(\boldsymbol{\chi})] = \sum_{r=1}^{K_Y^{\mathrm{p}}} \sum_{i=1}^{N_r} |\boldsymbol{q}(\boldsymbol{\chi}_i) - \boldsymbol{q}_r|^2, \quad \boldsymbol{\chi} \in V_R, \quad \boldsymbol{\chi}_i \in V_r \subset V_R \subset V_Y, \quad r \in 1, ..., K_Y^{\mathrm{p}}, \quad R \in 1, ..., K_Y^{\theta} \,, \tag{4.25}$$

where

$$|\boldsymbol{z}| = \sqrt{\boldsymbol{z} \cdot \boldsymbol{z}} \tag{4.26}$$

and the subdomain mean vectors $\boldsymbol{q}_r$ containing the inelastic field information are computed as

$$\boldsymbol{q}_r = \left(\boldsymbol{q}_1^{(1)} \,, \boldsymbol{q}_1^{(2)} \,, \boldsymbol{q}_1^{(3)} \right)^{\mathrm{T}} = \frac{1}{|V_r|} \int_{V_r} \boldsymbol{q}(\boldsymbol{\chi}) \mathrm{d}\boldsymbol{\chi} \,. \tag{4.27}$$

After both subdivision steps, the total number of subdomains per yarn is $K_Y = K_Y^{\mathrm{p}} \, K_Y^{\theta}$. It is noted that the isotropic pure matrix phase (subscript "I") of the woven unit cell is divided into a number K_{I} based on the local eigenstrain field distribution only. The total number of subdomains therefore $K = K_{\mathrm{I}} + K_{\mathrm{Warp}} + K_{\mathrm{Weft}}$.

4.5 Numerical applications

The presented combined scale bridging techniques of the CAH algorithms and the MFH (Sections 4.2.2 and 4.3.2) are used for the nonlinear microscale-mesoscale-macroscale analyses of a woven composite unit cell (Fig. 4.1). The microscale-mesoscale transition is depicted in Fig. 4.4. The unit cell consists of the yarns surrounded by the matrix material. The total yarn volume fraction of the unit cell is 64.56 %. The yarns consist of the same matrix material, reinforced by fibers with a volume fraction of 80 %, locally considered unidirectional (Fig. 4.2). The woven geometry used in this work is the one from the Section 6.2.1 of Wu et al. (2021). The mechanical properties of the isotropic elasto-plastic matrix material (index I) and of the transverse isotropic elastic fiber material (index II) are given in Table 4.1, where the longitudinal-transversal Poisson ratio of the elastic fibers is denoted as $\nu_{\mathrm{II}}^{\mathrm{LT}}$. The behavior of the matrix material is governed by the J2-plasticity law with the hardening stress R following

$$R = H_{\mathrm{I}} \left(1 - e^{-m_{\mathrm{I}} p}\right), \tag{4.28}$$

where p is the equivalent accumulated plastic strain (Eq. (2.186)). This section is divided into two parts: First, spatial subdivisions following the offline procedure described in Section 4.4 are displayed. Subsequently, elastic and inelastic responses of the woven composite unit cell during nonlinear analyses, computed by the CAH techniques based on TFA and HS (Section 4.2.2), are investigated. The results achieved by the two CAH approaches are compared to each other and the results following the FE DNS. To achieve the homogenized responses of the unit cell by full-field homogenization, the local microstructural responses are computed using the MFH (Section 4.2.1). The nonlinear reference DNS are performed using the same BC, outlined as follows in Section 4.5.1, as used throughout the offline stage.

4.5.1 Boundary conditions

Periodic boundary conditions (PBC) are typically applied for the modeling of materials RVEs or unit cells. However, fully applied PBC on all surfaces of the unit cell may provide mechanical responses that deviate strongly from experimental results on laminates of woven composites. It was shown that simulation results using modified PBC, where the surfaces with the ouf-of-plane normals (normals in z-direction) are kept flat without any distortion, deliver results that mirror the experimental results much more closely (Wu, Adam, and Noels, 2021). The modified PBC are referred to as mixed boundary conditions (MBC). The better results of using the MBC are explained by the fact that the use of flat upper and lower ply surfaces corresponds more accurately to the actual deformation modes of a woven composite laminate. The MBC are applied for all loading cases in the offline stage and during the nonlinear full-field homogenization analyses of the woven composite.

4.5.2 Offline stage

The goal of the inelastic simulations conducted in the offline stage is the production of inelastic fields that exhibit detailed inelastic deformation patterns. This allows an accurate capturing and representation of the essential features of inelastic deformation patterns by

TABLE 4.1: Material properties of the epoxy matrix phase and the carbon fibers. The material properties were adapted from Wu et al. (2015).

Matrix (M10.1 epoxy)		Fibre (UD300 HS(R) carbon fibre)	
Property	Value	Property	Value
Young's modulus E_{I} [GPa]	3.2	Young's modulus $E_{\mathrm{II}}^{\mathrm{L}}$ [GPa]	230
Poisson ratio ν_{I} [-]	0.3	Young's modulus $E_{\mathrm{II}}^{\mathrm{T}}$ [GPa]	40
Initial yield stress $\sigma_{\mathrm{I}}^{\mathrm{Y0}}$ [MPa]	30	Poisson ratio $\nu_{\mathrm{II}}^{\mathrm{TT}}$ [-]	0.2
Hardening modulus H_{I} [MPa] (offline)	130 (50)	Poisson ratio $\nu_{\mathrm{II}}^{\mathrm{LT}}$ [-]	0.256
Hardening exponent m_{I} [-]	300	shear modulus $G_{\mathrm{II}}^{\mathrm{LT}}$ [GPa]	24

the spatial subdivision procedure using the k-means clustering technique. Since lower hardening characteristics lead to more localized plasticity, the matrix hardening modulus in the offline stage DNS was reduced with respect to the real value, used during the actual nonlinear analyses. Two different subdomain decompositions were performed:

- Division of the matrix phase into $K_{\mathrm{I}} = 4$ subdomains. A division of each yarn into $K_Y = 8$ subdomains purely based on the local yarn orientation, i.e. the fiber orientation. The RVE is subdivided into a total of $K = 20$ subdomains.
- The same division of the matrix phase. A refinement of the eight subdomains per yarn into four subdomains each, based on inelastic deformation patterns. Therefore, each yarn consists of $K_Y = 32$ subdomains after both spatial decomposition steps. The total subdomain number amounts to $K = 68$.

As visible when analysing the inelastic fields within the weft yarn (Figs. 4.6a, 4.6c and 4.6e) and the warp yarn (Figs. 4.6b, 4.6d and 4.6f), the major inelastic deformation localizes where the yarns incline vertically, in patterns orthogonal to the yarns main direction. This implies that a spatial division based on the local yarn direction alone allows the capture of the main patterns of inelasticity, recognized in Figs. 4.6g and 4.6h. The account for inelastic strains occurring during the application of the selected boundary modes provides slight adoptions of the spatial division, refining the subdomains by additionally respecting particular inelastic patterns that can not be captured by the purely orientation based division. These additionally respected inelastic patterns are dominantly stretched out in the yarns main directions (Figs. 4.6i and 4.6j). In the subsequent results section, the CAH methods with the yarns subdivided based on the local orientation only are referred to as TFA-O and HS-O. The cases of a spatial division with an additional account of the inelastic deformation fields are referred to as TFA-OP and HS-OP.

4.5.3 Homogenized elastic behavior

The yarns of the woven composite are, due to the local variations of the yarn and fiber orientations and therefore of the elastic properties, elastically inhomogeneous materials. However, each yarn is considered as one material phase, and subdivided into a number of subdomains with uniform elastic properties. The first spatial subdivision step was performed in order to assemble regions of the yarns in the same subdomain that have

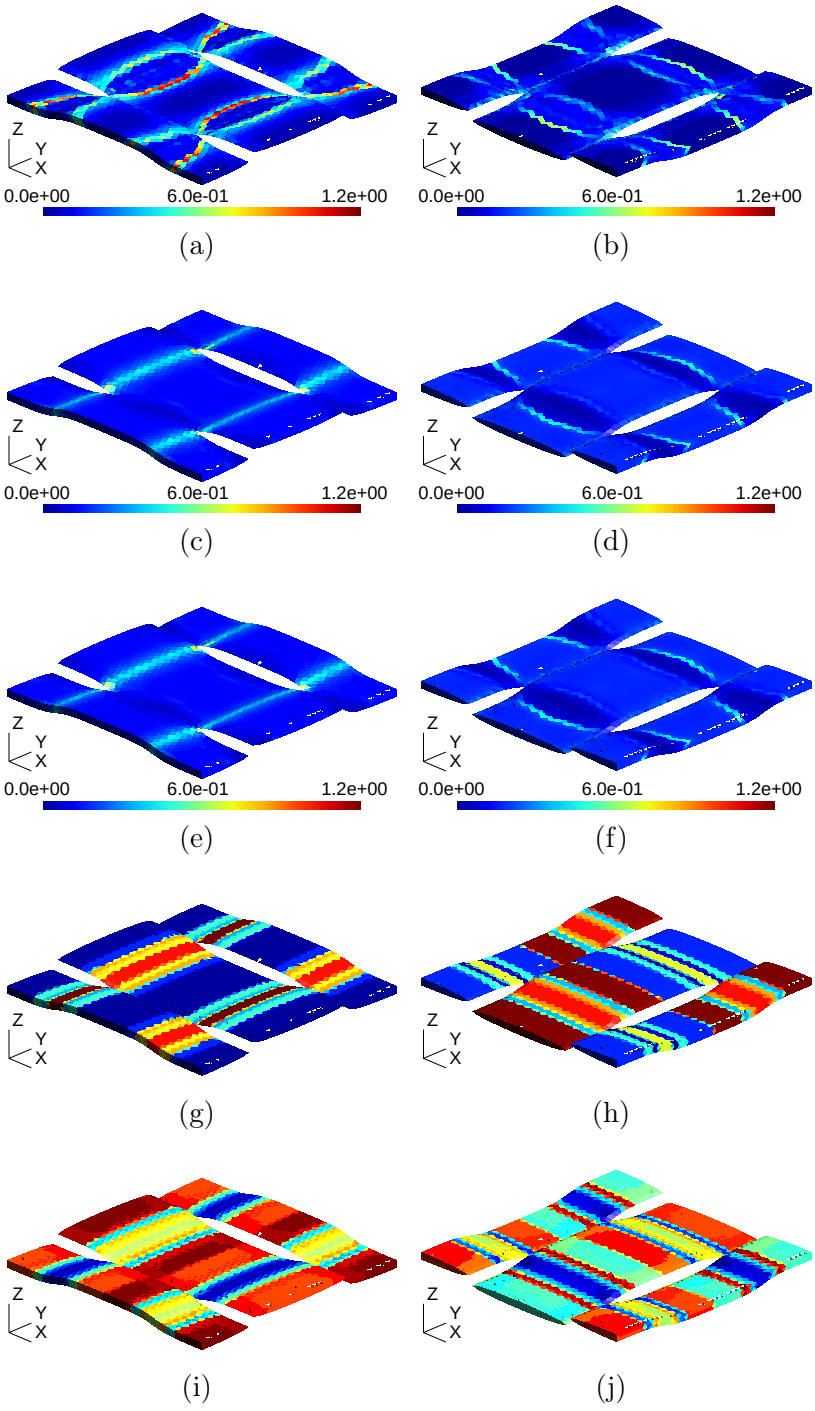

FIGURE 4.6: The (a,c,e,g) weft and (b,d,f,h) warp yarns of the woven composite mesostructure. Displayed are the inelastic deformation fields during the application of the three inelastic boundary modes in the offline stage, (a,b) isochoric deformation with tension in x-direction, (c,d) isochoric deformation with tension in y-direction, (e,f) pure shearing in the ply-plane, and the resulting subdomain decompositions based on (g,h) the local yarn orientation and (i,j) yarn orientation and inelastic strains.

equal or similar local fiber orientations. It is investigated if the homogenized elastic

behavior is well captured by the CAH methods with an underlying decomposition into subdomains with uniform variables. The elastic Young's modulus $\overline{E}_x^{\text{el}}$ and the elastic Poisson ratios in the ply plane $\overline{\nu}_{xy}^{\text{el}}$ and out of the ply plane $\overline{\nu}_{xz}^{\text{el}}$ can be identified as the instantaneous mechanical properties in the elastic regime (thus at low strains, denoted as "at $\overline{\varepsilon}_{xx} = 0$" under uniaxial tension $\overline{\sigma}_{xx}$) as

$$\overline{E}_x^{\text{el}} = \frac{\Delta\overline{\sigma}_{xx}}{\Delta\overline{\varepsilon}_{xx}} \quad \text{at } \overline{\varepsilon}_{xx} = 0 \tag{4.29}$$

and

$$\overline{\nu}_{xj}^{\text{el}} = -\frac{\Delta\overline{\varepsilon}_{jj}}{\Delta\overline{\varepsilon}_{xx}} \quad j = y, z \quad \text{at } \overline{\varepsilon}_{xx} = 0\,. \tag{4.30}$$

All elastic properties are predicted almost exactly by the TFA, with deviations below 0.1 % from the elastic properties computed using DNS Table 4.2. The HS method provides good agreements of the elastic properties as well, however the error level is higher than the one achieved by the TFA. In particular, estimations slightly too stiff are provided for the longitudinal Young's modulus $\overline{E}_x^{\text{el}}$.

TABLE 4.2: Elastic properties computed following Eqs. (4.29) and (4.30) using DNS and the TFA and HS algorithms.

method	DNS	TFA-O	TFA-OP	HS-O	HS-OP
$\overline{E}_x^{\text{el}}$ (GPa)	63.9	63.9	63.9	64.6	64.6
$\overline{\nu}_{xy}^{\text{el}}$ (-)	4.11e-2	4.12e-2	4.12e-2	4.10e-2	4.11e-2
$\overline{\nu}_{xz}^{\text{el}}$ (-)	4e-1	3.99e-1	3.99e-1	3.85e-1	3.85e-1

4.5.4 Nonlinear analyses

Inelastic loading conditions were applied on the woven composite unit cell, described by the following boundary conditions:

- overall axial cyclic loading up to 6% strain in x-axis orientation, see Fig. 4.7a, with free motion in the orthogonal orientations, corresponding to overall uniaxial tension boundary conditions

$$\begin{aligned} &\overline{\varepsilon}_{xx} = 0 \rightarrow 0.03 \rightarrow -0.03 \rightarrow 0.06 \rightarrow 0 \\ &\overline{\sigma}_{yy} = \overline{\sigma}_{zz} = 0 \end{aligned} \tag{4.31}$$

- overall pure shear strain cyclic loading up to 6%, see Fig. 4.7a, represented by the overall strain evolution $\overline{\boldsymbol{\varepsilon}}(t)$, $t = [0, T]$, $T = 1.0$ with $\overline{\varepsilon}_{zz} = \overline{\varepsilon}_{xz} = \overline{\varepsilon}_{yz} = 0$:

$$\begin{aligned} \begin{pmatrix} \overline{\boldsymbol{\varepsilon}}_{xx} & \overline{\boldsymbol{\varepsilon}}_{xy} \\ \overline{\boldsymbol{\varepsilon}}_{xy} & \overline{\boldsymbol{\varepsilon}}_{yy} \end{pmatrix}(0) = \begin{pmatrix} 0 & 0 \\ 0 & 0 \end{pmatrix} \rightarrow \overline{\boldsymbol{\varepsilon}}(T/4) = \begin{pmatrix} 0.03 & 0 \\ 0 & 0.03 \end{pmatrix} \rightarrow \overline{\boldsymbol{\varepsilon}}(T/2) = \begin{pmatrix} -0.03 & 0 \\ 0 & -0.03 \end{pmatrix} \\ \rightarrow \overline{\boldsymbol{\varepsilon}}(3T/4) = \begin{pmatrix} 0 & 0.06 \\ 0.06 & 0 \end{pmatrix} \rightarrow \overline{\boldsymbol{\varepsilon}}(T) = \begin{pmatrix} 0 & 0 \\ 0 & 0 \end{pmatrix}. \end{aligned} \tag{4.32}$$

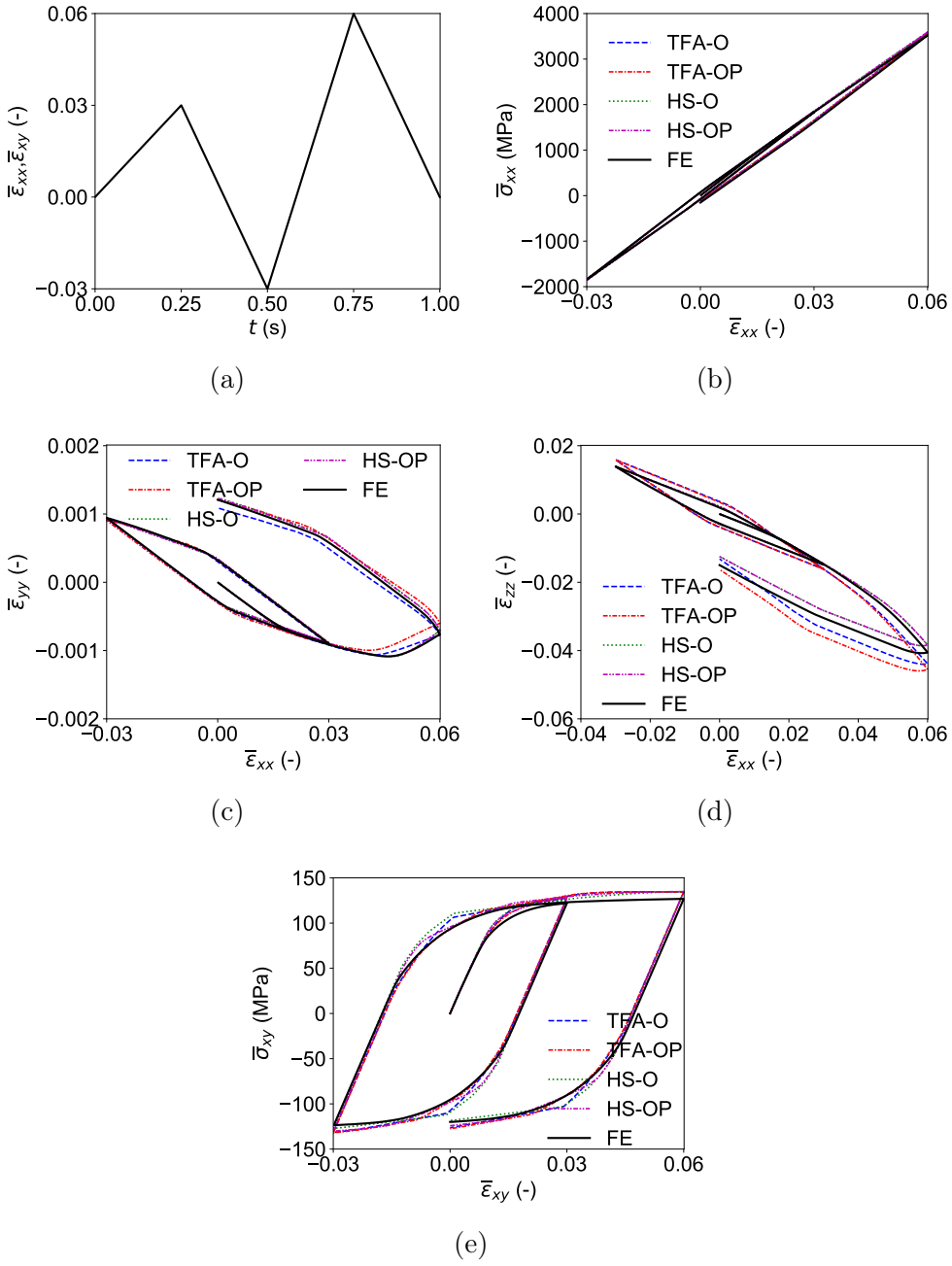

FIGURE 4.7: (a) Applied axial and shear deformation during the two separate uniaxial tension (Eq. (4.31)) and pure shear (Eq. (4.32)) tests. Uniaxial tension: evolution of the homogenized (b) axial stress and strain components perpendicular to the direction of tension (c) in plane and (d) out of plane. Pure-shear: evolution of the (e) homogenized shear stress.

- non-proportional loading, consisting of three different stages of uniaxial and shear deformation and a stage of simultaneous unloading towards the zero-strain state (Fig. 4.8a), represented by the overall strain evolution $\overline{\boldsymbol{\varepsilon}}(t)$, $t = [0, T]$, $T = 1.0$,

with $\overline{\varepsilon}_{zz} = \overline{\varepsilon}_{xz} = \overline{\varepsilon}_{yz} = 0$:

$$\begin{pmatrix} \overline{\boldsymbol{\varepsilon}}_{xx} & \overline{\boldsymbol{\varepsilon}}_{xy} \\ \overline{\boldsymbol{\varepsilon}}_{xy} & \overline{\boldsymbol{\varepsilon}}_{yy} \end{pmatrix}(0) = \begin{pmatrix} 0 & 0 \\ 0 & 0 \end{pmatrix} \rightarrow \overline{\boldsymbol{\varepsilon}}(T/4) = \begin{pmatrix} 0.04 & 0 \\ 0 & 0 \end{pmatrix} \rightarrow \overline{\boldsymbol{\varepsilon}}(T/2) = \begin{pmatrix} 0.04 & 0 \\ 0 & 0.04 \end{pmatrix} \rightarrow \overline{\boldsymbol{\varepsilon}}(3T/4) = \begin{pmatrix} 0.04 & 0.04 \\ 0.04 & 0.04 \end{pmatrix} \rightarrow \overline{\boldsymbol{\varepsilon}}(T) = \begin{pmatrix} 0 & 0 \\ 0 & 0 \end{pmatrix}. \tag{4.33}$$

- non-proportional loading, consisting of different loading stages consisting of simultaneous bi- and uniaxial and shear deformation (Fig. 4.9a), represented by the overall strain evolution $\overline{\boldsymbol{\varepsilon}}(t)$, with $\overline{\varepsilon}_{zz} = \overline{\varepsilon}_{xz} = \overline{\varepsilon}_{yz} = 0$:

$$\begin{pmatrix} \overline{\boldsymbol{\varepsilon}}_{xx} & \overline{\boldsymbol{\varepsilon}}_{xy} \\ \overline{\boldsymbol{\varepsilon}}_{xy} & \overline{\boldsymbol{\varepsilon}}_{yy} \end{pmatrix}(0) = \begin{pmatrix} 0 & 0 \\ 0 & 0 \end{pmatrix} \rightarrow \overline{\boldsymbol{\varepsilon}}(T/4) = \begin{pmatrix} 0.01 & 0.02 \\ 0.02 & -0.02 \end{pmatrix} \rightarrow \overline{\boldsymbol{\varepsilon}}(T/2) = \begin{pmatrix} 0.02 & 0 \\ 0 & -0.02 \end{pmatrix} \rightarrow \overline{\boldsymbol{\varepsilon}}(3T/4) = \begin{pmatrix} 0.03 & -0.02 \\ -0.02 & -0.04 \end{pmatrix} \rightarrow \overline{\boldsymbol{\varepsilon}}(T) = \begin{pmatrix} 0.04 & 0 \\ 0 & -0.04 \end{pmatrix}. \tag{4.34}$$

The predictions of the axial stress and the transverse strains in and out of the ply plane during the uniaxial tension test (Eq. (4.31)) and the shear stress response during the pure shear test (Eq. (4.32)) are presented in Fig. 4.7. The TFA allows a very high accuracy of the axial stress, while the HS approach leads to a slightly stiffer prediction (Fig. 4.7b). Considering the in-plane transverse strains, both TFA and HS methods deliver accurate results for the in-plane behavior (Fig. 4.7c). The HS approach shows a slightly underestimated transversal strains out-of-plane, while the TFA leads to slightly overestimated predictions of the out-of-plane deformation (Fig. 4.7d). It is noted that the HS type approach leads to less divergence from the DNS results under the progression of the loading cycles. In summary, both methods deliver accurate predictions of the in-plane deformation over both loading cycles. The out-of-plane deformation during the first loading cycle is well captured, while the methods lead to slightly overcompliant (TFA) and overstiff (HS) responses, with an increasing divergence from the DNS results under a progressive loading. Both methods perform very well and allow equivalently high accuracies of the shear stress evolution during the pure-shear test (Fig. 4.7e).

During the first non-proportional loading history given by Eq. (4.33), both the TFA and the HS approaches deliver high accuracies for the evolution of all stress components (Fig. 4.8). While the TFA perfectly covers both axial stresses during the complete loading history, the HS approach leads to very low stress overestimations. The TFA captures the shear stress during the shear deformation loading stage very accurately, while the HS approach overestimates the shear stress response. During the shear unloading stage, the TFA leads to an underestimation of the stress drop, while the HS approach allows a nearly perfectly matching final shear stress at the end of the applied loading. As recognized before, the TFA perfectly predicts both axial stress responses during the full non-proportional loading history given by Eq. (4.34) (Fig. 4.9). The HS approach leads to very light inaccuracies of the axial stresses. During the shear deformation, the TFA allwows a perfect capture of the shear stress during the shear loading and unloading down to zero shear deformation. During the further shearing with negative sign however, the

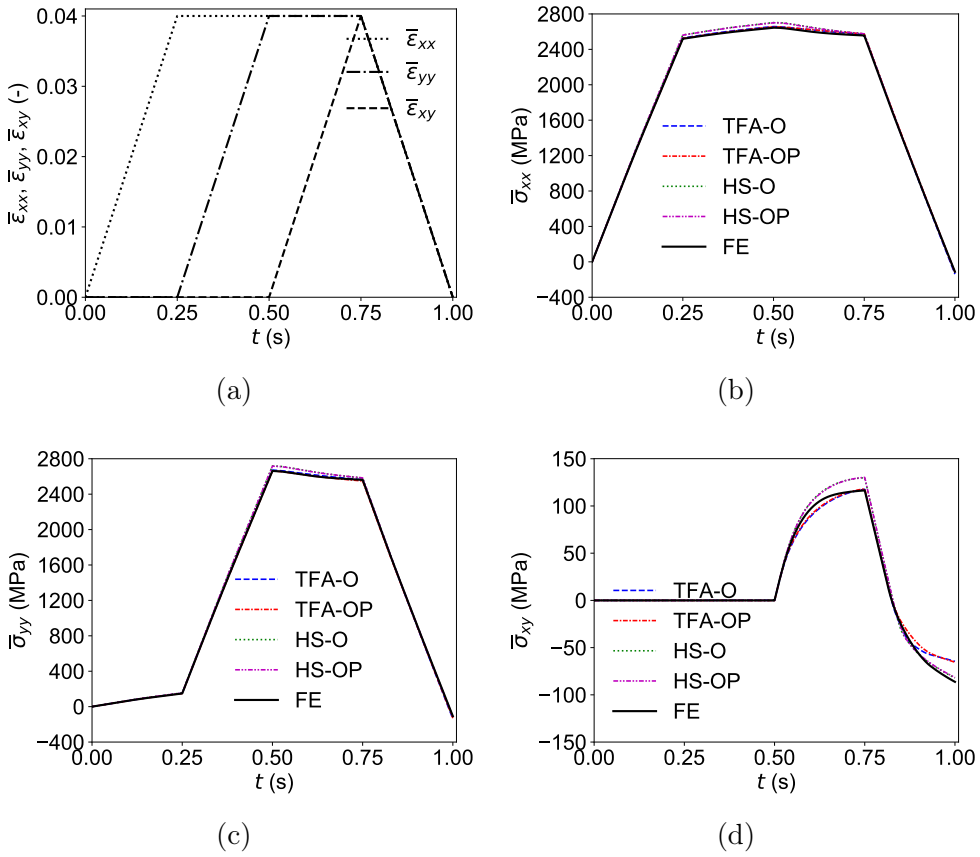

FIGURE 4.8: Applied loading history described by Eq. (4.33): evolution of the (a) applied strain path, normal stress responses in (b) x-direction and (c) y-direction and (d) in-ply plane shear stress response.

shear stress does not further drop as predicted by the full-field and HS approaches. Similarly, the shear stress increase predicted by the TFA during the following shear unloading towards a zero shear strain state is underestimated. Unlike the TFA, the HS approach allows very good agreements of the shear stress evolution during the full loading history.

As recognized, the CAH approaches allow to accurately represent the homogenized responses gathered by DNS. Nonetheless, it may be investigated to what degree the cluster decomposition based on the inelastic offline deformation modes (Eq. (4.19),Section 4.4) represents the actual deformation fields in the unit cell during more complex loading conditions. In order to evaluate the validity of the selected offline deformation modes for the non-proportional loading conditions applied in this section (Eqs. (4.33) and (4.33)), inelastic strain fields during and after the application of the two non-proportional deformation histories are inspected (Figs. 4.10 and 4.11). It can be recognized that the inelastic patterns in the yarns, even after the application of random loading paths, still correspond to the spatial division achieved by the subdomain decomposition based on the local yarn orientation and the plastic fields evolved during the selected static loading modes of the offline stage, displayed in Fig. 4.6.

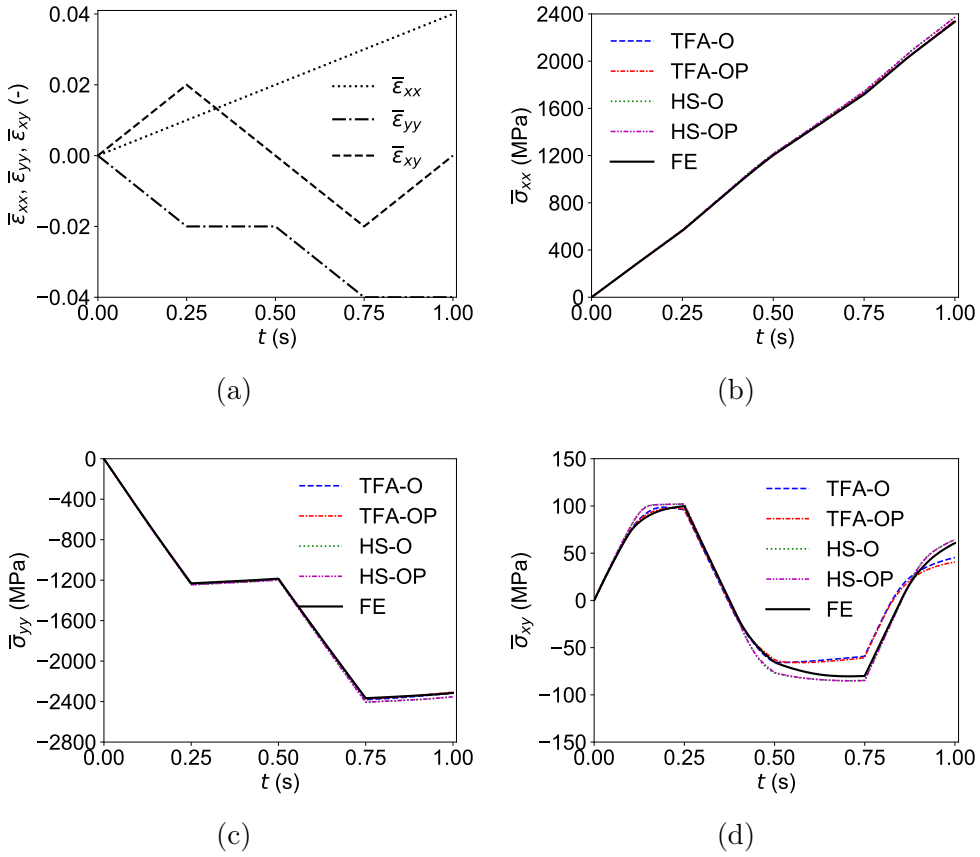

FIGURE 4.9: Applied loading history described by Eq. (4.34): evolution of the (a) applied strain path, normal stress responses in (b) x-direction and (c) y-direction and (d) in-ply plane shear stress response.

TABLE 4.3: CPU time speed-ups for the non-proportional loading program in Eq. (4.34) using the TFA and HS algorithms.

method	TFA-O (K=20)	TFA-OP (K=68)	HS-O (K=20)	HS-OP (K=68)
speed-up	12000	1200	11000	1000

4.5.5 Discussion

It is shown that the selected static offline deformation modes for the woven unit cell allow an inelasticity-based spatial division that supports inelastic fields emerging under proportional and random loading conditions. The spatial decomposition based on the local yarn inclination alone provides, using the TFA, exact results for the elastic properties of the woven unit cell (Table 4.2), proving that the variation of the elastic properties are well respected. Moreover, the yarn orientation based decomposition allows to capture many of the inelastic localization zones in the woven structure. The subdomain refinement based on inelastic fields leads to only small improvements of the mechanical predictions. The yield points are captured more accurately, particularly when using the TFA, but the stiffness response during inelastic loading is generally captured equally well without the inelasticity-based subdomain refinement.

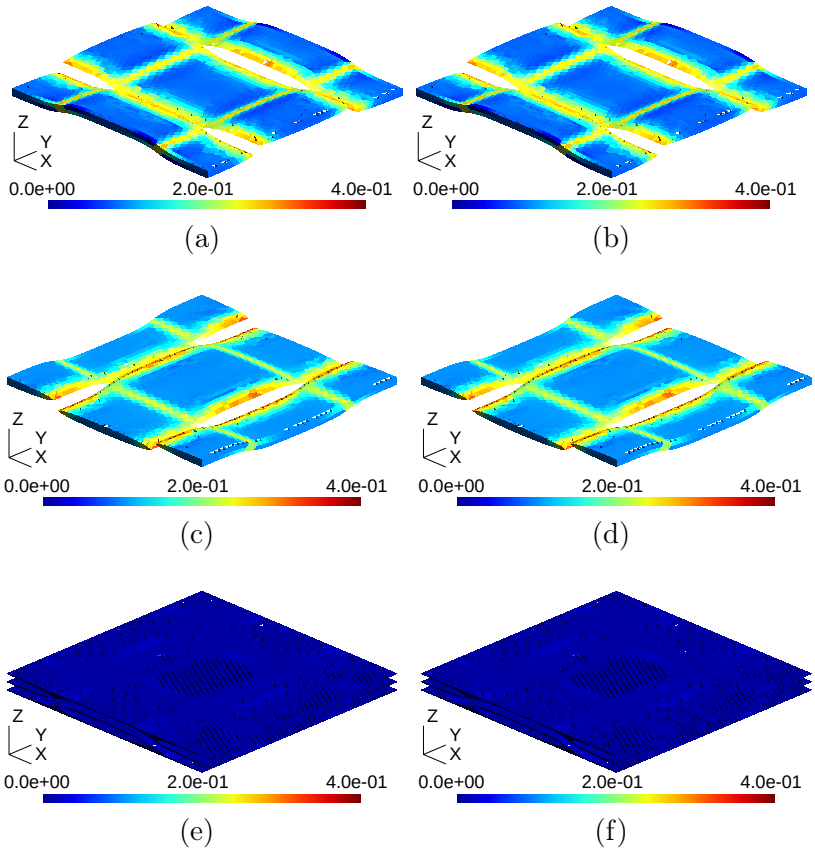

FIGURE 4.10: Equivalent plastic strain fields in the (a,b) weft yarn, (c,d) warp yarn and (e,f) matrix, (a,c,e) at $t = T/2$ and (b,d,f) at the end of the applied non-proportional loading history described by Eq. (4.33). It is noted that the displayed plastic strains in the yarns, consisting of elastic fibers in an elasto-plastic matrix, are result of the inelastic deforming matrix phase only.

Following the high accuracy of the representation of inelastic fields by the spatial division, the behaviors of the woven unit cell predicted by the two-step RH of inelastic loading show a very good agreement with the results achieved by DNS for all proportional and non-proportional inelastic loading histories. While the TFA provides slightly higher accuracies for axial stress responses, the HS approach allows better predictions for the transverse strains. Supported by well-covered inelastic localization zones during complex loading by the spatial decomposition, both approaches are well-capable to model the stress evolution during the applied non-proportional loading histories.

Comparing the computational efficiency of the CAH approaches with respect to the homogenization by DNS (Table 4.3), it becomes clear that high time savings are allowed. While the use of 20 subdomains allows a computation that is 10 thousand times faster, the use of 68 subdomains still allows an acceleration factor of 1 thousand. The time consumption by the TFA is lower than the one by the HS approach, as discussed at the end of Section 3.5.2.

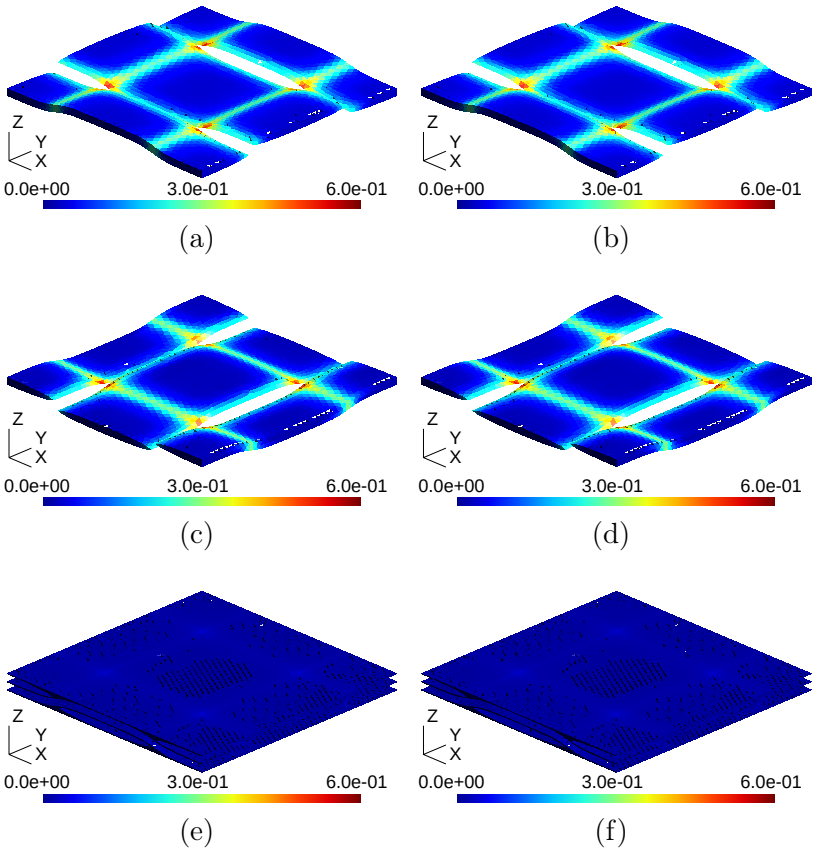

FIGURE 4.11: Equivalent plastic strain fields in the (a,b) weft yarn, (c,d) warp yarn and (e,f) matrix, (a,c,e) at $t = T/2$ and (b,d,f) at the end of the applied non-proportional loading history described by Eq. (4.34). It is noted that the displayed plastic strains in the yarns, consisting of elastic fibers in an elasto-plastic matrix, are result of the inelastic deforming matrix phase only.

4.6 Conclusions

Piecewise uniform field CAH schemes are used for the modeling of the macroscopic response of a woven composite unit cell. Each curved yarn is considered as one mesoscopic material phase, although the elastic and inelastic responses of the yarn materials are inhomogeneous due to the changing local yarn inclination, affecting the microstructural configuration. Therefore,

- a spatial decomposition into subdomains that takes into account the local orientation of the yarns (Fig. 4.3) is essential for an accurate modeling of the elastic and inelastic responses, and
- considering the mesoscopic to macroscopic homogenization step, a second homogenization step for the evaluation of the effective response of the mesoscopic yarns subdomains of the CAH is required because of the heterogeneous character of the yarns (Fig. 4.2).

A new spatial decomposition procedure is implemented, applicable for the mesoscopic model order reduction of three-scale materials that contain microstructures with hetero-

geneous fiber or inclusion orientations and therefore, heterogeneous stiffness fields. It is important to acknowledge that the clustering based on the local yarn orientations and inelastic fields leads to decompositions into subdomains that continue to represent the actual deformation fields in the woven unit cell even after non-proportional loading histories. It proves the suitability of the CAH approaches and the clustering procedures developed in this work for the use of complex histories of deformation. The CAH approaches were used in combination with the incremental-secant MFH scheme (Wu et al., 2013a), providing the homogenization of the matrix-fiber composite that constitutes the yarns microstructure (Fig. 4.4).

Two CAH approaches were tested for the modeling of a woven composite unit cell. The TFA, typically leading to clearly overstiff predictions of composites with high volume fractions of stiff elastic inclusions in an elasto-plastic matrix phase, but allowing accurate results if both phases deform inelastically, and the HS approach, relying on an homogeneous and isotropic reference material. The elastic and inelastic responses of the woven composite, predicted by the CAH, are in a good agreement with the responses modeled by DNS [1]. The high accuracies imply that the local yarn orientation is well represented by the spatial division and furthermore, that the two applied CAH approaches, TFA and HS analyses, are well suitable for the modeling of woven composites. The TFA benefits from the integration of the MFH for the yarn material, allowing the consideration of the yarn material as homogenized inelastic material phases. The high volume fraction of the stiff yarn material does not lead to inaccuracies using the TFA approach. The tangent HS approach is subject to only minor inaccuraries of the elastic response of the strongly anisotropic woven structure, although it relies on a virtual isotropic reference stiffness. In Section 3.5.5 it was recognized that the longitudinal deformation under uniaxial tension of a strongly anisotropic structure in plane-strain leads, using the HS approach, to a clearly overstiff elastic response and a poor representation of the yield point. This behavior could not be observed for the case of the woven unit cell under uniaxial tension in a three-dimensional strain setting, presented in the chapter.

The presented three-scale modeling for the reduced order modeling of the woven composite, using the extended spatial subdivision and a piecewise uniform CAH in combination with MFH for the homogenization on the different scales, allows very accurate predictions for the mechanical response of the woven unit cell. This is true even for complex non-proportional loading histories. One reason for the accurate results under extended loading histories is the integration of the MFH for the evaluation of the effective mesoscopic responses of of the yarns. The coupling of the CAH with the MFH allows the nonlinear modeling under arbitrary loading conditions without the requirement of a predefined yield criterion, as it was used by Han et al., 2020. The promising results suggest that accurate multiscale simulations for structural woven composites are possible. In future works, the modeling capability can be tested for cases of microscopic damage in the matrix and the yarns (Wu et al., 2013b; Wu, Maillard, and Noels, 2021; Wu et al., 2021). Furthermore, the two-step homogenization scheme can be tested for other types of three-scale materials, consisting of an either arranged or random mesostructure and a random microstructure. An example for a natural three-scale material is wood.

[1] This is not a full DNS of the meso and microstructures, since the fibrous microstructure is not explicitly represented (Section 4.2.1).

Chapter 5

Hierarchical Transformation Field Analysis

5.1 Introduction

As presented in Section 3.2, the TFA, even when relying on a subdomain division taking into account inelastic fields, leads to typically overstiff predictions for the composites responses. Large numbers of subdomains are required in order to achieve reasonable homogenized responses. As pointed out, the reason for the overstiff results are plastic field heterogeneities that can not be captured when considering uniform fields of variables in combination with reasonably low numbers of subdomains. In this chapter, the groundwork is laid for a hierarchical TFA, achieved from the separation of an RVE into subdomains on different scale levels and developed for

- The homogenization of generic two-scale composite materials, where the macroscopic response is affected by the underlying microstructure.
- The homogenization of microstructures that consist of only one homogeneous material phase, whose overall response depends solely on their geometrical characteristics. An example for this are porous materials.

This hierarchical TFA is introduced as an extension of the conventional TFA formulation for the one-step scale-bridging (Dvorak, 1992), presented in Section 2.3.4 and implemented in Section 3.3. The evaluation of constitutive equations for the subdomains of a classical TFA homogenization is replaced by subsequent TFA homogenization procedures on the lower scale levels. The proposed hierarchical TFA is here introduced for the case of a two-scale separation, where the TFA scheme on the higher scale levels states BVPs on the subdomains of the lower scale level, solved by the same TFA algorithm. This hierarchical TFA can, based on the two-scale formulation, be extended towards higher numbers of scale levels. This multi-step TFA is expected to provide reductions of the computational effort of the homogenization compared to classical TFA homogenization while considering the same degree of fidelity of the spatial division into uniform domains. The reduced effort for the homogenized solution is achieved by the decomposition of a large number of subdomains into a lower number of subdomains and several homogenization procedures inside the subdomains, corresponding to the decomposition of one large numerical system into smaller systems and subsystems. As a result, the resolution at each scale is faster, since less partitions are considered.

This chapter is structured as follows: The implementation of the two-step TFA homogenization scheme is presented in Section 5.2. This contains the theoretical foundation

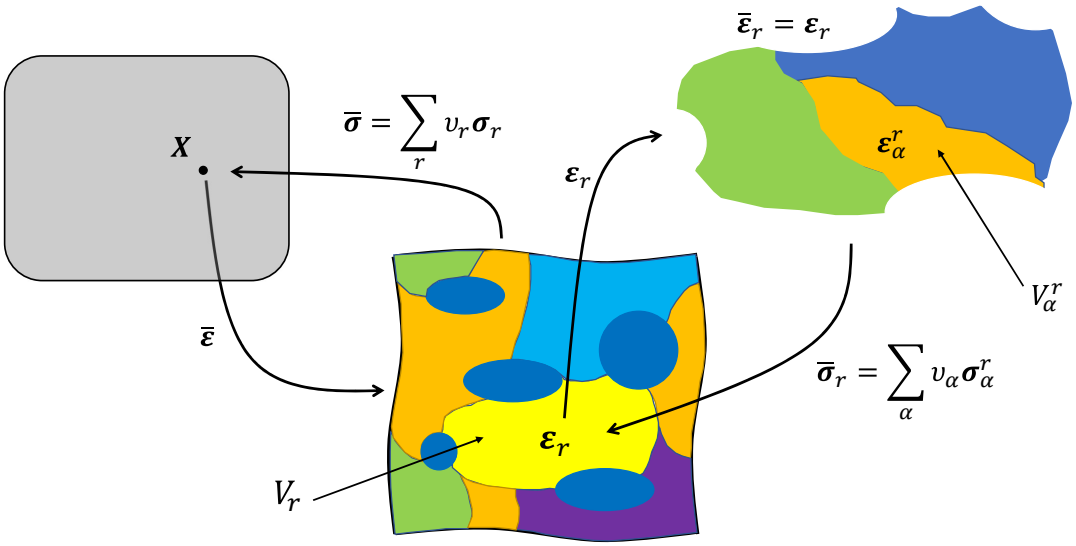

FIGURE 5.1: Schematic presentation of the two-step TFA: The spatial subdomain decomposition on the first scale level, with the stated BVP $\overline{\boldsymbol{\varepsilon}}$ and solution $\boldsymbol{\varepsilon}_r$ in the subdomain V_r. The subdomains V_α^r on the lower scale level being the result of the spatial division of the subdomain r, and the BVP stated through $\boldsymbol{\varepsilon}_r$.

of the upscaling and downscaling of variables, the determination of the concentration and interaction tensors on more than one scale level and the quantification of the reduction of the solution system. In Section 5.3, first results following numerical applications on a simple unit cell structure are given. Section 5.4 summarizes the (lack of) effectivity and the potential of the new approach.

5.2 Implementation of the TFA homogenization on two scales

5.2.1 Two-step homogenization formulation

The classical TFA is formulated as the two-scale coupling equation

$$\boldsymbol{\varepsilon}(\boldsymbol{\chi}) = \mathbb{A}^{\mathrm{el}}(\boldsymbol{\chi}) : \overline{\boldsymbol{\varepsilon}} + \mathbb{D}(\boldsymbol{\chi}, \boldsymbol{\chi}') : \boldsymbol{\varepsilon}^*(\boldsymbol{\chi}'), \quad \boldsymbol{\chi} \in V, \tag{5.1}$$

acting as a one-step micro to macroscale bridging relation, with the local microscopic strains $\boldsymbol{\varepsilon}(\boldsymbol{\chi})$ and $\boldsymbol{\varepsilon}^*(\boldsymbol{\chi})$ and the homogenized macroscopic strain $\overline{\boldsymbol{\varepsilon}} = 1/|V| \int_V \boldsymbol{\varepsilon}(\boldsymbol{\chi}) \mathrm{d}\boldsymbol{\chi}$. Assuming the existence of piecewise uniform fields of stress and deformation per several subdomains $V_r \in V$, the Eq. (5.1) can be written as

$$\boldsymbol{\varepsilon}_r = \mathbb{A}_r^{\mathrm{el}} : \overline{\boldsymbol{\varepsilon}} + \sum_{s=1}^{K} \mathbb{D}_{rs} : \boldsymbol{\varepsilon}_s^*, \tag{5.2}$$

which is the formulation of the conventional TFA approach. The homogenized strain, stress, and algorithmic tangent stiffness of the domain V are expressed as

$$\overline{\boldsymbol{\varepsilon}} = \sum_{r=1}^{K} v_r \boldsymbol{\varepsilon}_r \,, \tag{5.3}$$

$$\overline{\boldsymbol{\sigma}} = \sum_{r=1}^{K} v_r \boldsymbol{\sigma}_r \tag{5.4}$$

and

$$\overline{\mathbb{C}}^{\mathrm{alg}} = \sum_{r=1}^{K} v_r \frac{\partial \boldsymbol{\sigma}_r}{\partial \boldsymbol{\varepsilon}_r} \frac{\partial \boldsymbol{\varepsilon}_r}{\partial \overline{\boldsymbol{\varepsilon}}} = \sum_{r=1}^{K} v_r \mathbb{C}_r^{\mathrm{alg}} : \mathbb{A}_r^{\mathrm{in,TFA}} \,, \tag{5.5}$$

respectively, with details on the instantaneous strain concentration tensors $\mathbb{A}_r^{\mathrm{in,TFA}}$ in Section 2.3.4.

In the approach proposed in this chapter, the subdomains r are considered to contain non-uniform fields of variables. The subdomains r act, equivalently as the domain V, as host domains for a number of K_r sub-subdomains $V_\alpha^r \in V_r$ with uniform fields. Consequently, the strains and stresses in the subdomain V_r follow from a homogenization procedure on the lower scale level, formulated as

$$\boldsymbol{\varepsilon}_r = \overline{\boldsymbol{\varepsilon}}_r = \sum_{\alpha=1}^{K_r} v_\alpha^r \boldsymbol{\varepsilon}_\alpha^r, \tag{5.6}$$

and

$$\boldsymbol{\sigma}_r = \overline{\boldsymbol{\sigma}}_r = \sum_{\alpha=1}^{K_r} v_\alpha^r \boldsymbol{\sigma}_\alpha^r, \tag{5.7}$$

where $v_\alpha^r = |V_\alpha^r|/|V_r|$ and $\boldsymbol{\varepsilon}_\alpha^r$ and $\boldsymbol{\sigma}_\alpha^r$ are the strain and stress of the sub-subdomain V_α^r, being a subdomain of the domain V_r. The eigenstrains $\boldsymbol{\varepsilon}_r^*$ in V_r (Eq. (5.2)) are then given as

$$\boldsymbol{\varepsilon}_r^* = \boldsymbol{\varepsilon}_r - \left(\overline{\mathbb{C}}_r^{\mathrm{el}}\right)^{-1} : \boldsymbol{\sigma}_r \,, \tag{5.8}$$

with the homogenized elastic stiffness $\overline{\mathbb{C}}_r^{\mathrm{el}}$ of the subdomain r. The three Eqs. (5.6), (5.7) and (5.8) represent the upscaling formalism from the lower towards the higher scale level.

The strains in the sub-subdomains V_α^r on the lower scale level follow from the solution of a BVP stated by $\overline{\boldsymbol{\varepsilon}}_r$, solved by the TFA algorithm on the lower scale

$$\boldsymbol{\varepsilon}_\alpha^r = \mathbb{A}_\alpha^{\mathrm{el}^r} : \overline{\boldsymbol{\varepsilon}}_r + \sum_{\beta=1}^{K_r} \mathbb{D}_{\alpha\beta}^r : \boldsymbol{\varepsilon}_\beta^{*^r} \,, \tag{5.9}$$

where the eigenstrains $\boldsymbol{\varepsilon}_\beta^{*^r}$ follow from the constitutive relations of the subdomain β. The Eq. (5.9) characterizes the downscaling from a certain scale level towards the underlying subdomains on the lower scale level. The elastic strain concentration tensors $\mathbb{A}_\alpha^{\mathrm{el}^r}$ measure the strain $\boldsymbol{\varepsilon}_\alpha^r$ under an overall strain $\overline{\boldsymbol{\varepsilon}}_r$ during purely elastic behavior of the subdomain r as

$$\boldsymbol{\varepsilon}_\alpha^r = \mathbb{A}_\alpha^{\mathrm{el}^r} : \overline{\boldsymbol{\varepsilon}}_r \,. \tag{5.10}$$

The interaction tensors $\mathbb{D}^r_{\alpha\beta}$ measure the uniform reaction strain in a subdomain $V^r_\alpha \in V_r$ due to an eigenstrain in a subdomain $V^r_\beta \in V_r$ under an overall strain $\overline{\boldsymbol{\varepsilon}}_r = 0$ as

$$\boldsymbol{\varepsilon}^r_\alpha = \mathbb{D}^r_{\alpha\beta} : \boldsymbol{\varepsilon}^{*^r}_\beta \,, \quad \overline{\boldsymbol{\varepsilon}}_r = 0 \,. \tag{5.11}$$

The homogenized elastic stiffness of the subdomain r on the higher scale level is expressed as

$$\overline{\mathbb{C}}^{\mathrm{el}}_r = \sum_{\alpha=1}^{K_r} v^r_\alpha \, \mathbb{C}^{\mathrm{el}^r}_\alpha : \mathbb{A}^{\mathrm{el}^r}_\alpha \,. \tag{5.12}$$

5.2.2 Breakdown of the numerical solution

Following the scale decomposition presented in Section 5.2.1, the solution of the two-step homogenization is decomposed into one numerical system on the higher scale level and K subsystems on the lower scale level.

On the higher level, the assembled $K \times 1$ vector $[F]$ for the Newton-Raphson procedure contains the subdomain residuals

$$\boldsymbol{F}_r = \Delta\boldsymbol{\varepsilon}_r - \mathbb{A}^{\mathrm{el}}_r : \Delta\overline{\boldsymbol{\varepsilon}} - \sum_{s=1}^{K} \mathbb{D}_{rs} : \Delta\boldsymbol{\varepsilon}^*_s \,. \tag{5.13}$$

The $K \times K$ Jacobian system $\mathbb{J}$ is constituted by the single Jacobian matrices

$$\mathbb{J}_{rs} = \frac{\partial \boldsymbol{F}_r}{\partial \boldsymbol{\varepsilon}_s} = \delta_{rs}\mathbb{I} - \mathbb{D}_{rs} : \frac{\partial \boldsymbol{\varepsilon}^*_s}{\partial \boldsymbol{\varepsilon}_s}, \tag{5.14}$$

where, following Eq. (5.8), the derivatives of the eigenstrains by the strains are computed as

$$\frac{\partial \boldsymbol{\varepsilon}^*_r}{\partial \boldsymbol{\varepsilon}_r} = \mathbb{I} - \left(\overline{\mathbb{C}}^{\mathrm{el}}_r\right)^{-1} : \overline{\mathbb{C}}^{\mathrm{alg}}_r \tag{5.15}$$

and the homogenized algorithmic inelastic tangent stiffness $\overline{\mathbb{C}}^{\mathrm{alg}}_r$ follows from the homogenization process on the underlying decomposed domain.

On the lower scale level, each of the K subsystems is solved by a Newton-Raphson procedure with the $K_r \times 1$ residual vector $[\boldsymbol{F}]^r$ containing the residuals

$$\boldsymbol{F}^r_\alpha = \Delta\boldsymbol{\varepsilon}^r_\alpha - \mathbb{A}^{\mathrm{el}^r}_\alpha : \Delta\overline{\boldsymbol{\varepsilon}}_r - \sum_{\beta=1}^{K_r} \mathbb{D}^r_{\alpha\beta} : \Delta\boldsymbol{\varepsilon}^{*^r}_\beta \tag{5.16}$$

and the $K_r \times K_r$ Jacobian system $\mathbb{J}^r$ consisting of the entries

$$\mathbb{J}^r_{\alpha\beta} = \frac{\partial \boldsymbol{F}^r_\alpha}{\partial \boldsymbol{\varepsilon}^r_\beta} = \delta_{\alpha\beta}\mathbb{I} - \mathbb{D}^r_{\alpha\beta} : \frac{\partial \boldsymbol{\varepsilon}^{*^r}_\beta}{\partial \boldsymbol{\varepsilon}^r_\beta} \tag{5.17}$$

in order to iteratively correct the strains of the sub-subdomains $[\boldsymbol{\varepsilon}]^r = \boldsymbol{\varepsilon}^r_\alpha$. The homogenized algorithmic stiffness of the corresponding domain r on the upper level is given as

Algorithm 10: Numerical procedure of the hierarchical TFA with two scale levels at a glance: Newton-Raphson schemes on both scale levels at one load step for a prescribed macroscopic strain increment $\Delta\overline{\boldsymbol{\varepsilon}}$.

initialize: $\Delta\boldsymbol{\varepsilon}_r = \mathbb{A}_r^{\mathrm{el}} : \Delta\overline{\boldsymbol{\varepsilon}}$ $(r = 1, ..., K)$
for $r = 1, K$ **do**
  initialize: $\Delta\boldsymbol{\varepsilon}_\alpha^r = \mathbb{A}_\alpha^{\mathrm{el}^r} : \Delta\boldsymbol{\varepsilon}_r$ $(\alpha = 1, ..., K_r)$
end
iterative procedure on upper scale level:
repeat
  for $r = 1, K$ **do**
    initialize residual $\boldsymbol{F}_r = \Delta\boldsymbol{\varepsilon}_r - \mathbb{A}_r^{\mathrm{el}} : \Delta\overline{\boldsymbol{\varepsilon}}$
    iterative procedure on lower scale level:
    repeat
      for $\alpha = 1, K_r$ **do**
        call constitutive relations for subdomain α to compute $\boldsymbol{\sigma}_\alpha^r$, $\boldsymbol{\varepsilon}_\alpha^{*^r}$ and $\partial\boldsymbol{\varepsilon}_\alpha^{*^r}/\partial\boldsymbol{\varepsilon}_\alpha^r$, $\mathbb{C}_\alpha^{\mathrm{alg}^r}$ (details in Section 2.5)
      end
      for $\alpha = 1, K_r$ **do**
        initialize residual $\boldsymbol{F}_\alpha^r = \Delta\boldsymbol{\varepsilon}_\alpha^r - \mathbb{A}_\alpha^{\mathrm{el}^r} : \Delta\boldsymbol{\varepsilon}_r$
        for $\beta = 1, K_r$ **do**
          add eigenstrain interaction contribution to residual: $\boldsymbol{F}_\alpha^r = \boldsymbol{F}_\alpha^r - \sum_\beta \mathbb{D}_{\alpha\beta}^r : \Delta\boldsymbol{\varepsilon}_\beta^{*^r}$
          compute Jacobian matrix $\mathbb{J}_{\alpha\beta}^r = \delta_{\alpha\beta}\mathbb{I} - \mathbb{D}_{\alpha\beta}^r : (\partial\Delta\boldsymbol{\varepsilon}_\beta^{*^r}/\partial\boldsymbol{\varepsilon}_\beta^r)$
        end
      end
      solve $\delta[\boldsymbol{\varepsilon}]^r = \left(\{\mathbb{J}\}^r\right)^{-1} : [\boldsymbol{F}]^r$
      update $[\Delta\boldsymbol{\varepsilon}]^r = [\Delta\boldsymbol{\varepsilon}]^r - \delta[\boldsymbol{\varepsilon}]^r$
    until $|[\boldsymbol{F}]^r| < \mathrm{tol}$;
    after convergence:
    compute $\boldsymbol{\sigma}_r$, $\boldsymbol{\varepsilon}_r^*$, $\partial\Delta\boldsymbol{\varepsilon}_r^*/\partial\boldsymbol{\varepsilon}_r$ and $\mathbb{C}_r^{\mathrm{alg}}$ (Eqs. (5.7), (5.8), (5.15) and (5.18)).
    for $s = 1, K$ **do**
      add eigenstrain interaction contribution to residual: $\boldsymbol{F}_r = \boldsymbol{F}_r - \sum_s \mathbb{D}_{rs} : \Delta\boldsymbol{\varepsilon}_s^*$
      compute Jacobian matrix $\mathbb{J}_{rs} = \delta_{rs}\mathbb{I} - \mathbb{D}_{rs} : (\partial\Delta\boldsymbol{\varepsilon}_s^*/\partial\boldsymbol{\varepsilon}_s)$
    end
  end
  solve $\delta[\boldsymbol{\varepsilon}] = \{\mathbb{J}\}^{-1} : [\boldsymbol{F}]$
  update $[\Delta\boldsymbol{\varepsilon}] = [\Delta\boldsymbol{\varepsilon}] - \delta[\boldsymbol{\varepsilon}]$
until $|[\boldsymbol{F}]| < \mathrm{tol}$;
after convergence:
compute $\overline{\boldsymbol{\sigma}}$ and $\overline{\mathbb{C}}^{\mathrm{alg}}$, following Eq. (5.4) and Eq. (5.5), respectively.

$$\mathbb{C}_r^{\mathrm{alg}} = \overline{\mathbb{C}}_r^{\mathrm{alg}} = \sum_{\alpha=1}^{K_r} v_\alpha^r \mathbb{C}_\alpha^{\mathrm{alg}^r} : \left[\sum_{\beta=1}^{K_r} \left(\{\mathbb{J}\}^r\right)_{\alpha\beta}^{-1} : \mathbb{A}_\beta^{\mathrm{el}^r} \right]. \tag{5.18}$$

The derivatives $\partial\boldsymbol{\varepsilon}_\beta^{*r}/\partial\boldsymbol{\varepsilon}_\beta^r$ and the algorithmic tangent stiffness tensors $\mathbb{C}_\alpha^{\mathrm{alg}^r}$ follow from the constitutive relations of the subdomain α (see Section 2.5). The solution of the two-step TFA scheme, proposed and developed in this work and presented in this section, is summarized in Algorithm 10.

In the following, an example case is presented with a decomposition of an RVE domain V into $K = 16$ subdomains. Using the classical TFA formulation, the case $K = 16$ leads 16 integration points where the constitutive relation needs to be evaluated and a system (Eq. (5.14)) of the size $9 \cdot 16 \times 16 = 2304$ to be solved (where the factor 9 is valid for 2D computations). Using the hierarchical two-scale TFA approach, the 16 subdomains are distributed on two scales. Assuming the same number K_r of sub-subdomains in every of the K subdomains r, the total of 16 subdomains can be achieved with a division of the RVE into 4 subdomains and a subdivision of every subdomain into 4 sub-subdomains. While the number of integration points is still 16, the size of each system in Eqs. (5.14) and (5.17) results now in $9 \cdot 4 \times 4 = 144$, although several of the smallelr systems are to be solved iteratively. This demonstrates that the proposed system decoupling approach allows a computational reduction with respect to the conventional TFA homogenization, since the resolution of large systems can be circumvented by the consideration of more than one scale level.

5.2.3 Spatial decomposition on two scale-levels

In order to perform the two-scale TFA, the spatial division consists of two steps:

1. Division of the RVE domain into subdomains V_r, referred to as the subdomains on the higher scale level.

2. Each of the subdomains V_r on the higher scale level is considered as a host domain for the second division step into the sub-subdomains V_α^r on the lower scale level.

This spatial division can be further extended towards more scale levels by reiterations of the second step.

For the division of all microscopic points into the partitions, the k-means clustering procedure is performed, acting on the local inelastic strain accumulation vectors $\boldsymbol{q}(\boldsymbol{\chi})$ (Eq. (3.16)), containing the inelastic field information under the applied offline loading modes (Section 3.2.2). Equivalently, the domain can be divided into subdomains based on the elastic strain concentration tensors $\mathbb{A}^{\mathrm{el}}(\boldsymbol{\chi})$ (Section 3.2.1). Here, the spatial division on the first scale level (of the RVE domain) follows the minimization of the function

$$J[\boldsymbol{q}(\boldsymbol{\chi})] = \sum_{r=1}^{K_\Omega} \sum_{i=1}^{N_r} |\boldsymbol{q}(\boldsymbol{\chi}_i) - \boldsymbol{q}_r|^2, \quad \boldsymbol{\chi} \in V_\Omega, \quad \boldsymbol{\chi}_i \in V_r \subset V_\Omega, \quad r \in 1, ..., K_\Omega\,, \tag{5.19}$$

where Ω denotes the material phases in the RVE, K_Ω the number of subdomains in the specific phase and N_r is the number of points in one partition (subdomain) r, and $\boldsymbol{q}_r$ is the mean of all the points $i = 1, ..., N_r$ in the partition r, expressed as

$$\boldsymbol{q}_r = \frac{1}{|V_r|} \int_{V_r} \boldsymbol{q}(\boldsymbol{\chi}) \mathrm{d}\boldsymbol{\chi}\,. \tag{5.20}$$

The spatial division of the subdomains V_r, $r = 1, ..., K_\Omega$ into K_r^Ω sub-subdomains V_α^r on the lower scale level expresses as the minimization of the function

$$J_r[\boldsymbol{q}(\boldsymbol{\chi})] = \sum_{\alpha=1}^{K_r^\Omega} \sum_{i=1}^{N_\alpha} |\boldsymbol{q}(\boldsymbol{\chi}_i) - \boldsymbol{q}_\alpha|^2, \quad \boldsymbol{\chi} \in V_r, \quad \boldsymbol{\chi}_i \in V_\alpha^r \subset V_r \subset V_\Omega, \quad \alpha \in 1, ..., K_r^\Omega, \quad r \in 1, ..., K_\Omega \,, \tag{5.21}$$

where N_α denotes the number of local points in the partition (sub-subdomain) α and $\boldsymbol{q}_\alpha$ is the mean of all the points $i = 1, ..., N_\alpha$ in the partition α, expressed as

$$\boldsymbol{q}_\alpha = \frac{1}{|V_\alpha^r|} \int_{V_\alpha^r} \boldsymbol{q}(\boldsymbol{\chi}) \mathrm{d}\boldsymbol{\chi} \,. \tag{5.22}$$

The optimal decomposition of one material phase Ω into subdomains and sub-subdomains based on the entirety of the inelastic strain fields, $\boldsymbol{q}(\boldsymbol{\chi})$, is accomplished as follows:

1. First an arbitrary number of clusters K_Ω is chosen and inelastic strain accumulation vectors at random data points are defined as the $r = 1, ..., K_\Omega$ initial cluster mean values $\boldsymbol{q}_r$.

2. Iterative clustering procedure for the higher scale level starts

   2.1. Variances of all local inelastic strain accumulation vectors $\boldsymbol{q}(\boldsymbol{\chi})$ from the different cluster means

   $$||\boldsymbol{q}(\boldsymbol{\chi}) - \boldsymbol{q}_s||^2, \quad \boldsymbol{\chi} \in V_\Omega, \quad s \in 1, ..., K_\Omega \tag{5.23}$$

   are calculated. All corresponding local data points i are assigned to a set r, so that the variance between the local inelastic strain accumulation vector $\boldsymbol{q}(\boldsymbol{\chi}_i)$ and the assigned cluster mean $\boldsymbol{q}_r$ is minimal:

   $$||\boldsymbol{q}(\boldsymbol{\chi}_i) - \boldsymbol{q}_r||^2 \leq ||\boldsymbol{q}(\boldsymbol{\chi}_i) - \boldsymbol{q}_s||^2, \quad \boldsymbol{\chi}_i \in V_r \subset V_\Omega, \quad \forall s,\, r \in 1, ..., K_\Omega,\, s \neq r \,. \tag{5.24}$$

   2.2. Following, all inelastic strain accumulation vectors assigned to the cluster are used to determine the updated cluster means $\boldsymbol{q}_r$ using Eq. (5.20).

3. The iterative procedure on the higher scale level ends when convergence of the procedure is reached, indicated by a stationary assignment of the local data points to the sets. Subsequently, the iterative clustering procedure for the lower scale level can be performed.

4. For each subdomain $r = 1, ..., K_\Omega$:

   4.1. First an arbitrary number of clusters K_r^Ω is chosen and inelastic strain accumulation vectors at random data points are defined as the $\alpha = 1, ..., K_r^\Omega$ initial cluster mean values $\boldsymbol{q}_\alpha$.

   4.2. Iterative clustering procedure of the subdomain r for the decomposition on the lower scale level starts

4.2.1. Variances of all local vectors $\boldsymbol{q}(\boldsymbol{\chi})$, $\boldsymbol{\chi} \in V_r$ from the different cluster means

$$||\boldsymbol{q}(\boldsymbol{\chi}) - \boldsymbol{q}_\beta||^2, \quad \boldsymbol{\chi} \in V_r, \quad \beta \in 1, ..., K_r \tag{5.25}$$

are calculated. All corresponding local data points i are assigned to a set α, so that the variance between the local inelastic strain accumulation vector $\boldsymbol{q}(\boldsymbol{\chi}_i)$ and the assigned cluster mean $\boldsymbol{q}_\alpha$ is minimal:

$$\begin{aligned} ||\boldsymbol{q}(\boldsymbol{\chi}_i) - \boldsymbol{q}_\alpha||^2 \leq ||\boldsymbol{q}(\boldsymbol{\chi}_i) - \boldsymbol{q}_\beta||^2, \quad & \boldsymbol{\chi}_i \in V_\alpha^r \subset V_r \subset V_\Omega, \\ & \forall \beta,\, \alpha \in 1, ..., K_r^\Omega, \beta \neq \alpha \\ & r \in 1, ..., K_\Omega. \end{aligned} \tag{5.26}$$

4.2.2. Following, all inelastic strain accumulation vectors assigned to the cluster are used to determine the updated cluster means $\boldsymbol{q}_\alpha$ using Eq. (5.22).

The iterative procedure on the lower scale level in the subdomain r ends when convergence of the procedure is reached, indicated by a stationary assignment of the local data points to the sets α.

5. The domain V is divided on two scale levels into subdomains V_r and sub-subdomains V_r^α.

The spatial division of the RVE domain on the two scale levels is summarized in the Algorithm 11.

5.2.4 Determination of the elastic strain concentration tensors

The elastic strain concentration for the classical TFA homogenization are determined upon the application of six orthogonal BC on the RVE, fixating the homogenized strain of the RVE (Section 3.2.1). In the case of the hierarchical TFA with two scale levels, the elastic strain concentration tensors need to be determined on both scale levels. After the clustering of the RVE into subdomains V_r and sub-subdomains $V_\alpha^r \subset V_r$, the average elastic strain concentration tensors of the subdomains, with respect to the homogenized strain of the RVE $\overline{\boldsymbol{\varepsilon}}$ in elasticity, in

$$\boldsymbol{\varepsilon}_r = \mathbb{A}_r^{\mathrm{el}} : \overline{\boldsymbol{\varepsilon}} \tag{5.27}$$

on the higher scale level and in

$$\boldsymbol{\varepsilon}_\alpha^r = \mathbb{A}_\alpha^{\mathrm{el}} : \overline{\boldsymbol{\varepsilon}}\,, \tag{5.28}$$

on the lower scale level can be computed by

$$\mathbb{A}_r^{\mathrm{el}} = \frac{1}{|V_r|} \int_{V_r} \mathbb{A}^{\mathrm{el}}(\boldsymbol{\chi}) \mathrm{d}\boldsymbol{\chi} \tag{5.29}$$

and

$$\mathbb{A}_\alpha^{\mathrm{el}} = \frac{1}{|V_\alpha^r|} \int_{V_\alpha^r} \mathbb{A}^{\mathrm{el}}(\boldsymbol{\chi}) \mathrm{d}\boldsymbol{\chi}\,, \quad V_\alpha^r \in V_r\,, \tag{5.30}$$

respectively. Required for the two-step TFA scheme are the elastic strain concentration tensors on the lower scale level, however with respect to the elastic strain of the corre-

Algorithm 11: Overview of the spatial division based inelastic strain distributions and the computation of the strain concentration tensors of the subdomains and sub-subdomains. The superscript Ω for the numbers of subdomains on both scale levels, denoting the material phase, is here omitted for simplification of the notation. Details are given in the Section 3.2.

```
select elastic material properties for all phases Ω of the RVE domain
for i = 1, ..., 6 do
    perform DNS:
    apply ε̄^(i) (Eq. (3.4)) on RVE domain V
    compute ε(χ)
    compute i-th column of 𝔸^el(χ) (Eq. (3.3)) written in Voigt notation
end
set the actual, potentially inelastic material properties for the phases Ω
for l = 1, 2 do
    apply ε̄^in(l) (Eq. (3.10))
    compute ε^p(l)(χ) and store temporarily
    compute ε_Ω^p(l) and p_Ω^(l) (Eqs. (3.13) and (3.12))
    normalize: ε^p(l)(χ) → φ^(l)(χ) (Eq. (3.14))
    transform: φ^(l)(χ) → q^(l)(χ) (Eq. (3.15))
end
assemble q(χ) (Eq. (3.16))
perform spatial division on two scales:
perform spatial division based on q(χ) on the higher scale level into r = 1, ..., K
  subdomains V_r (Section 5.2.3, with more details in Section 3.2.1)
for r=1,...,K do
    perform spatial division based on q(χ), χ ∈ V_r on the lower scale level into
      α = 1, ..., K_r subdomains V_α^r (Section 5.2.3)
end
for r=1,...,K do
    compute 𝔸_r^el by averaging over V_r (Eq. (5.29))
    for α = 1, ..., K_r do
        compute 𝔸_α^el by averaging over V_α^r (Eq. (5.30))
        compute 𝔸_α^el^r (Eq. (5.33))
    end
end
```

sponding subdomain r, $\boldsymbol{\varepsilon}_r = \mathbb{A}_r^{\mathrm{el}} : \overline{\boldsymbol{\varepsilon}}$, as in the relation

$$\boldsymbol{\varepsilon}_\alpha^r = \mathbb{A}_\alpha^{\mathrm{el}^r} : \boldsymbol{\varepsilon}_r = \mathbb{A}_\alpha^{\mathrm{el}^r} : \mathbb{A}_r^{\mathrm{el}} : \overline{\boldsymbol{\varepsilon}}\,. \tag{5.31}$$

Therefore, upon the application of the different orthogonal boundary modes $\overline{\boldsymbol{\varepsilon}}$ on the RVE boundaries and computing the strain concentration tensors $\mathbb{A}_r^{\mathrm{el}}$ and $\mathbb{A}_\alpha^{\mathrm{el}}$ following Eqs. (5.29) and (5.30), respectively, and using the equivalence

$$\boldsymbol{\varepsilon}_\alpha^r = \mathbb{A}_\alpha^{\mathrm{el}} : \overline{\boldsymbol{\varepsilon}} = \mathbb{A}_\alpha^{\mathrm{el}^r} : \mathbb{A}_r^{\mathrm{el}} : \overline{\boldsymbol{\varepsilon}} \tag{5.32}$$

following the Eqs. (5.28) and (5.31), the expression

$$\mathbb{A}_{\alpha}^{\mathrm{el}^r} = \mathbb{A}_{\alpha}^{\mathrm{el}} : (\mathbb{A}_r^{\mathrm{el}})^{-1} \tag{5.33}$$

is achieved for the concentration tensors on the lower scale level with respect to the strain of the corresponding subdomain on the higher scale level. The determination of the strain concentration tensors $\mathbb{A}_r^{\mathrm{el}}$ and $\mathbb{A}_{\alpha}^{\mathrm{el}^r}$ is summarized in the Algorithm 11.

Algorithm 12: Overview of the computation of the eigenstrain-strain interaction tensors between subdomains V_r on the higher scale level and between subsubdomains V_{α}^r on the lower scale level.

```
select elastic material properties for all phases Ω of the RVE domain
perform the computation of the interaction tensors on the higher scale level:
for i = 1, ..., 6 do
    for s = 1, ..., K do
        perform DNS with ε̄ = 0:
        apply ε*^(i) (Eq. (3.24)) in the whole subdomain V_s
        compute ε(χ), ∀χ ∈ V
        for r = 1, ..., K do
            compute reaction strain ε_r (Eq. (5.39))
            compute i-th column of 𝔻_rs by consideration of Eq. (5.34) in Voigt
              notation
        end
    end
end
perform the computation of the interaction tensors on the lower scale level:
for i = 1, ..., 6 do
    for r = 1, ..., K do
        for β = 1, ..., K_r do
            perform DNS with ε̄ = 0:
            apply ε*^(i) (Eq. (3.24)) in the whole subdomain V_β^r
            compute ε(χ), ∀χ ∈ V_r
            compute ε̄_r (Eq. (5.39))
            for α = 1, ..., K_r do
                compute reaction strain ε_α^r (Eq. (5.38))
                compute i-th column of 𝔻_αβ^r by consideration of Eq. (5.37) in Voigt
                  notation
            end
        end
    end
end
```

5.2.5 Determination of the interaction tensors

The eigenstrain-strain interaction tensors $\mathbb{D}_{rs}$ express the effect of an eigenstrain $\boldsymbol{\varepsilon}_s^*$ of a subdomain s on the strain $\boldsymbol{\varepsilon}_r$ of a subdomain r under a vanishing overall strain $\overline{\boldsymbol{\varepsilon}} = 0$ as

$$\boldsymbol{\varepsilon}_r = \mathbb{D}_{rs} : \boldsymbol{\varepsilon}_s^* , \quad \text{at } \overline{\boldsymbol{\varepsilon}} = 0, \quad \forall r, s \in 1, ..., K_\Omega . \tag{5.34}$$

The computation of the interaction tensors $\mathbb{D}_{rs}$ follows the successive application of six orthogonal eigenstrain modes $\boldsymbol{\varepsilon}_s^*$ in V_s and the determination of the reaction strain averaged over subdomain V_r,

$$\boldsymbol{\varepsilon}_r = \overline{\boldsymbol{\varepsilon}}_r = \frac{1}{|V_r|} \int_{V_r} \boldsymbol{\varepsilon}(\boldsymbol{\chi}) \, \mathrm{d}\boldsymbol{\chi}, \tag{5.35}$$

and is presented in detail in Section 3.3.1.

Similarly, the interaction tensors $\mathbb{D}^r_{\alpha\beta}$ express the effect of an eigenstrain $\boldsymbol{\varepsilon}_\beta^*$ of a subdomain β on the strain $\boldsymbol{\varepsilon}_\alpha$ of a subdomain α, however under a vanishing strain of the corresponding subdomain on the higher scale level, $\overline{\boldsymbol{\varepsilon}}_r = 0$, as

$$\boldsymbol{\varepsilon}^r_\alpha = \mathbb{D}_{rs} : \boldsymbol{\varepsilon}^{*^r}_\beta , \quad \text{at } \overline{\boldsymbol{\varepsilon}}_r = 0 \quad \forall \alpha, \beta \in 1, ..., K_r . \tag{5.36}$$

The interaction tensors $\mathbb{D}^r_{\alpha\beta}$ follow from the successive application of the different eigenstrain modes $\boldsymbol{\varepsilon}^{*^r}_\beta$ in all subdomains $V^r_\beta \in V_r$ and the computation of the homogenized reaction strains $\boldsymbol{\varepsilon}^r_\alpha$ of every subdomain $V^r_\alpha \in V_r$. However, since no boundary conditions can be applied on the surface of a subdomain r, no overall strain $\overline{\boldsymbol{\varepsilon}}_r = 0$ of the corresponding subdomain on the upper scale level can be fixated. Therefore, the interaction tensors are determined with consideration of the relation

$$\boldsymbol{\varepsilon}^r_\alpha - \mathbb{A}^{\mathrm{el}^r}_\alpha : \overline{\boldsymbol{\varepsilon}}_r = \mathbb{D}^r_{\alpha\beta} : \boldsymbol{\varepsilon}^{*^r}_\beta , \quad \forall \alpha, \beta \in 1, ..., K_r . \tag{5.37}$$

For this reason, when the eigenstrain modes $\boldsymbol{\varepsilon}^{*^r}_\beta$ are applied, the averaged reaction strain in the other lower-level subdomains inside the same upper-level domain

$$\boldsymbol{\varepsilon}^r_\alpha = \frac{1}{|V^r_\alpha|} \int_{V^r_\alpha} \boldsymbol{\varepsilon}(\boldsymbol{\chi}) \, \mathrm{d}\boldsymbol{\chi} , \quad V^r_\alpha \in V_r \tag{5.38}$$

as well as the homogenized reaction strain

$$\overline{\boldsymbol{\varepsilon}}_r = \frac{1}{|V_r|} \int_{V_r} \boldsymbol{\varepsilon}(\boldsymbol{\chi}) \, \mathrm{d}\boldsymbol{\chi} \tag{5.39}$$

are computed. Upon computation of the homogenized reaction strains in Eqs. (5.38) and (5.39) and the known concentration tensors $\mathbb{A}^{\mathrm{el}^r}_\alpha$ (Eq. (5.33)), the interaction tensors $\mathbb{D}^r_{\alpha\beta}$ can be fully characterized. The determination of the interaction tensors $\mathbb{D}_{rs}$ and $\mathbb{D}^r_{\alpha\beta}$ is summarized in the Algorithm 12.

5.3 Numerical applications

In this section, computed homogenized responses following the conventional TFA approach and the hierarchical TFA with spatial divisions on two scale levels, referred to as TFA^2, are compared. The subsequent non-proportional prescribed loading was applied,

consisting of four different stages of biaxial isochoric and shear loading and unloading stages, represented by the overall strain evolution $\overline{\boldsymbol{\varepsilon}}(t)$, $t = [0, T]$, $T = 1.0$, with $\overline{\varepsilon}_{zz} = 0$:

$$\begin{aligned} \overline{\boldsymbol{\varepsilon}}(0) = \begin{pmatrix} 0 & 0 \\ 0 & 0 \end{pmatrix} \rightarrow \overline{\boldsymbol{\varepsilon}}(T/4) = \begin{pmatrix} 0.06 & 0 \\ 0 & -0.06 \end{pmatrix} \rightarrow \overline{\boldsymbol{\varepsilon}}(T/2) = \begin{pmatrix} 0.06 & 0.04 \\ 0.04 & -0.06 \end{pmatrix} \\ \rightarrow \overline{\boldsymbol{\varepsilon}}(3T/4) = \begin{pmatrix} 0 & 0.04 \\ 0.04 & 0 \end{pmatrix} \rightarrow \overline{\boldsymbol{\varepsilon}}(T) = \begin{pmatrix} 0 & 0 \\ 0 & 0 \end{pmatrix} . \end{aligned} \tag{5.40}$$

5.3.1 Unit cell with one centered stiff inclusion

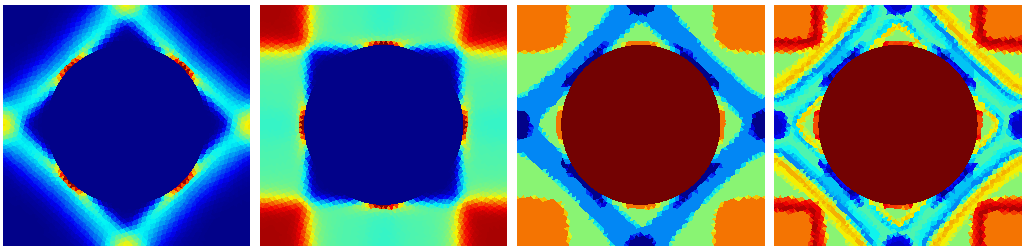

(a) (b) (c) (d)

FIGURE 5.2: Equivalent plastic strain fields under (a) biaxial isochoric (Eq. (3.10a)) and (b) pure shearing (Eq. (3.10b)) and the resulting spatial decomposition based on plastic strain distributions. Presented are the (c) division into four subdomains and the (d) division of the four subdomains into four sub-subdomains each for the application of the two-scale TFA.

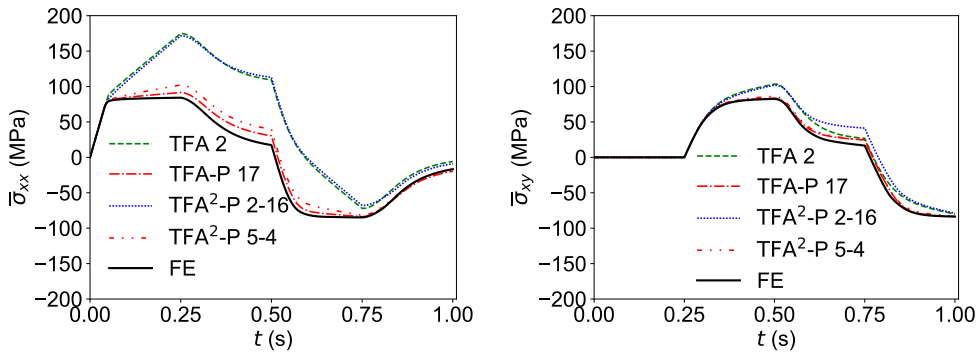

(a) (b)

FIGURE 5.3: Non-proportional loading: the computed homogenized (a) axial and (b) shear stress components predicted by the conventional TFA and the TFA on two scale levels compared to the FE full-field for the unit cell consisting of an elasto-plastic matrix with a spherical stiff centered inclusion.

Considered is a simple structure, consisting of a matrix material (Ω = I) with a centered stiff inclusion, occupying a fraction of 30 % of the unit cell domain (Fig. 5.2). The stiff inclusion (Ω = II) behaves elastic with the bulk modulus $\kappa_{\text{II}} = 20$ GPa and shear

modulus $\mu_{\mathrm{II}} = 6$ GPa and is represented by one subdomain. The response of the isotropic matrix material is controlled by the elastic bulk modulus $\kappa_{\mathrm{I}} = 10$ GPa and shear modulus $\mu_{\mathrm{I}} = 3$ GPa, and the inelastic response follows the hardening law

$$R = H_{\mathrm{I}}\, p^{m_{\mathrm{I}}} \tag{5.41}$$

with the initial yield strength $\sigma_{\mathrm{I}}^{\mathrm{Y0}} = 100$ MPa, the hardening modulus $H_{\mathrm{I}} = 50$ MPa and exponent $m_{\mathrm{I}} = 0.05$. The unit cell domain was decomposed into the subdomains in the following ways:

- Division of the matrix into $K_{\mathrm{I}} = 1$ and $K_{\mathrm{II}} = 1$ subdomains, referred to as TFA 2.
- Division of the matrix into $K_{\mathrm{I}} = 16$ and $K_{\mathrm{II}} = 1$ subdomains. This implies a division of the full unit cell domain into 17 subdomains and will be referred to as TFA-P 17.
- Division of the matrix phase into $K_{\mathrm{I}} = 1$ subdomain on the first scale level. Each matrix subdomain r is then divided into $K_r^{\mathrm{I}} = 16$ sub-subdomains. The inclusion phase is decomposed into $K_{\mathrm{II}} = 1$. This decomposition results in a division of the full unit cell domain into 17 subdomains and will be referred to as $\mathrm{TFA}^2 - P$ 2-16.
- Division of the matrix phase into $K_{\mathrm{I}} = 4$ subdomains on the first scale level (Fig. 5.4c). Each matrix subdomain r is then again divided into $K_r^{\mathrm{I}} = 4$ sub-subdomains (Fig. 5.4d). The inclusion phase is decomposed into $K_{\mathrm{II}} = 1$. This decomposition results in a division of the full unit cell domain into 17 subdomains and will be referred to as $\mathrm{TFA}^2 - P$ 5-4.

where the first spatial decomposition was used for the conventional TFA and the second and third decompositions were used for the TFA^2 approach. The matrix phase is decomposed based on the inelastic strain distributions, presented in Figs. 5.2a and 5.2b. The Figs. 5.2c and 5.2d depict the resulting subdomain decomposition into $K_{\mathrm{I}} = 4$ subdomains and into 16 subdomains on two scale levels with $K_{\mathrm{I}} = 4$ and a division of every matrix subdomain r by $K_r^{\mathrm{I}} = 4$. The elastic inclusion is always represented by one subdomain.

The homogenized response of the composite under the non-proportional loading path in Eq. (5.40) are presented in Fig. 5.3, where the annex "-P" for the TFA expresses the plasticity-based decomposition of the unit cell domain. While the TFA 2, with only one subdomain per material phase, results in clearly overstiff unit cell response, very accurate results are achieved using the conventional TFA with 16 subdomains representing the matrix phase (TFA-P 17). Using the two-step TFA with the same decomposition of the matrix phase ($\mathrm{TFA}^2 - P$ 2-16) shows a slightly improved capture of the yield point, however the inelastic stress-strain response is equally overstiff as using the conventional TFA 2. The TFA^2 5-4 however, delivers fairly accurate prediction of the unit cell response.

5.3.2 Porous unit cell with one center void

The TFA approaches are used for the computation of the response of the same structure, but where the stiff inclusion is replaced by a void in the same matrix material, occupying a fraction of 30 % of the unit cell domain (Fig. 5.4). The inelastic response of the matrix follows the hardening law in Eq. (5.41).

The structure is divided into 16 subdomains based on the plastic strain distributions (Section 3.2.2) under the two loading modes (Eq. (3.10)), applied on the boundaries of the

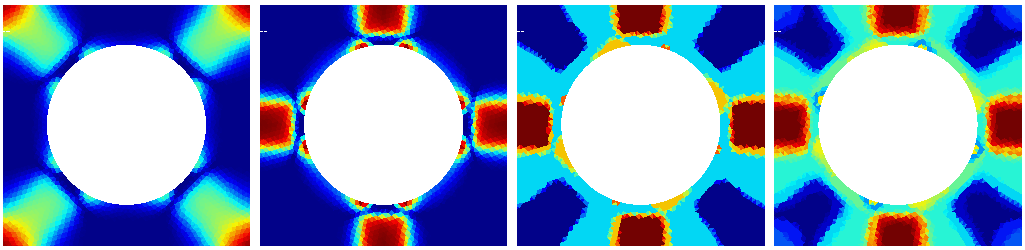

(a) (b) (c) (d)

FIGURE 5.4: Equivalent plastic strain fields under (a) biaxial isochoric (Eq. (3.10a)) and (b) pure shearing (Eq. (3.10b)) and the resulting spatial decomposition based on plastic strain distributions. Presented are the (c) division into four subdomains and the (d) division of the four subdomains into four sub-subdomains each for the application of the two-scale TFA.

structure containing the void. The occurring plastic strain fields under both loading modes are displayed in Figs. 5.4a and 5.4b. The determination of the elastic strain concentration tensors $\mathbb{A}_r^{\mathrm{el}}$ and $\mathbb{A}_\alpha^{\mathrm{el}^r}$ follows the application of the six orthogonal deformation modes on the structure (Section 3.2.1) containing the void and the computation of the occurring strains in the matrix phase. No strain concentration tensor of the void needs to be determined. The interaction tensors $\mathbb{D}_{rs}$ and $\mathbb{D}^r_{\alpha\beta}$ are computed through the application of the eigenstrain modes on the subdomains s on the first scale level (Section 3.3.1) and β on the second scale level. The interaction tensors are purely computed between the matrix subdomains, and no interactions between matrix subdomains and the void are required. The unit cell domain was decomposed into the subdomains in the following ways:

- Division of the matrix into $K_{\mathrm{I}} = 1$ subdomains, referred to as TFA 1.
- Division of the matrix into $K_{\mathrm{I}} = 16$ subdomains, referred to as TFA 16.
- Division of the matrix phase into $K_{\mathrm{I}} = 1$ subdomain on the first scale level. Each matrix subdomain r is then divided into $K_r^{\mathrm{I}} = 16$ sub-subdomains. This decomposition will be referred to as TFA^2 1-16.
- Division of the matrix phase into $K_{\mathrm{I}} = 4$ subdomains on the first scale level (Fig. 5.4c). Each matrix subdomain r is then again divided into $K_r^{\mathrm{I}} = 4$ sub-subdomains (Fig. 5.4d). This decomposition will be referred to as TFA^2 4-4.

where the first spatial decomposition was used for the conventional TFA and the second and third decompositions were used for the TFA^2 approach.

The homogenized response of the unit cell with the center void under the non-proportional loading path in Eq. (5.40) is presented in Fig. 5.5. It is noted that the strain $\overline{\boldsymbol{\varepsilon}}$ represents the deformation applied on the unit cell including the structure. Since besides the material, also the void accommodates deformation, the strain that accumulates in the matrix material, $\overline{\boldsymbol{\varepsilon}}_{\mathrm{I}}$, is not necessarily equal to the applied strain: $\overline{\boldsymbol{\varepsilon}}_{\mathrm{I}} \neq \overline{\boldsymbol{\varepsilon}}$. However, with a void that is stress-less, the homogenized stress of the unit cell equals the stress homogenized over the matrix material domain: $\overline{\boldsymbol{\sigma}} = \overline{\boldsymbol{\sigma}}_{\mathrm{I}}$. The results show equally good homogenized responses during the loading stages of the non-proportional loading

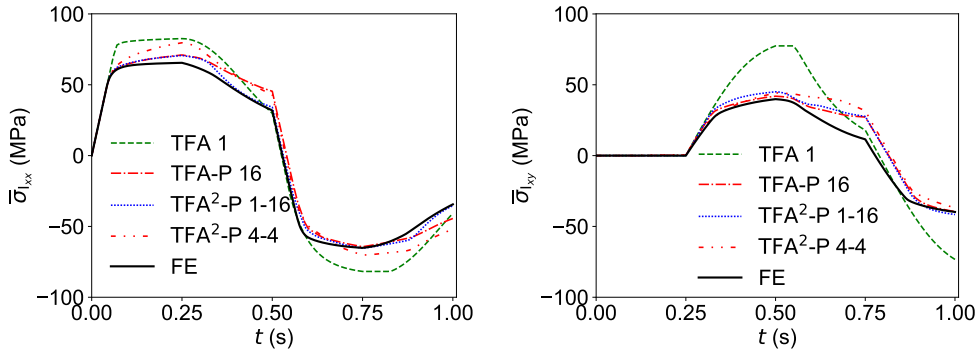

(a) (b)

FIGURE 5.5: Non-proportional loading: the computed (a) axial and (b) shear stress components in the matrix material predicted by the conventional TFA and the TFA on two scale levels compared to the FE full-field for the unit cell consisting of an elasto-plastic matrix with a spherical center void. It is noted that the matrix stress equals the homogenized unit cell stress: $\overline{\boldsymbol{\sigma}} = \overline{\boldsymbol{\sigma}}_{\mathrm{I}}$.

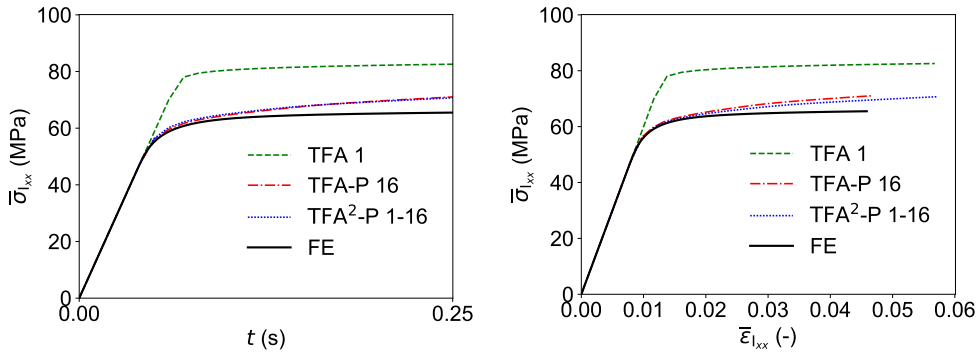

(a) (b)

FIGURE 5.6: First biaxial loading stage in the interval $t = [0,0.25]$ of the non-proportional loading history: the computed axial stress component in the direction of dilation in the matrix material, predicted by the conventional TFA and the TFA on two scale levels compared to the FE full-field for the unit cell consisting of an elasto-plastic matrix with a spherical center void. Displayed are the (a) stress evolution in time and the (b) stress-strain response. It is noted that the matrix stress equals the homogenized unit cell stress: $\overline{\boldsymbol{\sigma}} = \overline{\boldsymbol{\sigma}}_{\mathrm{I}}$.

path following the spatial division into $K = 16$ subdomains on the unit cell scale level and into $K = 1$ subdomain on the first scale level into $K_r = 16$ subdomains on the lower scale level (TFA^2 1-16). However, the division on the second scale levels leads to a much better prediction of the axial stress evolution in the stages $t = [0.25,0.5]$ and $t = [0.75,1.0]$. Inaccuracies of the TFA^2 1-16 are solely observed in the shear stress evolution in during the stage $t = [0.5,0.75]$. The TFA^2 4-4 leads to clearly worse captures of the homogenized inelastic responses.

The unit cell response during the first biaxial loading stage in the interval $t = [0,0.25]$

was investigated in more detail, displayed in Fig. 5.6, where the results following the same matrix phase division into 16 subdomains, on the first scale level for the conventional TFA (TFA-P 16, red dash-dotted curve) and on the second scale level for the two-step TFA (TFA^2-P 1-16, blue dotted), are compared to the case of only one subdomain representing the matrix phase (TFA 1, green dashed). Displayed are the homogenized stress evolution (Fig. 5.6a) and stress-strain response (Fig. 5.6b) of the matrix material. As was recognized above, the stress evolution predictions appear equally accurate using the conventional and the two-step TFA with the matrix division into 16 subdomains. Considering the computed stress-strain response however, it becomes clear that the accommodated strain in the matrix phase using the TFA^2-P 1-16 is clearly overestimated with respect to the conventional TFA-P 16, capturing the matrix strain accumulation of the full-field solution very accurately. More precisely, the matrix strain accumulation using the hierarchical TFA^2-P 1-16 equals the matrix strain predicted by the conventional TFA 1 with just one subdomain representing the matrix.

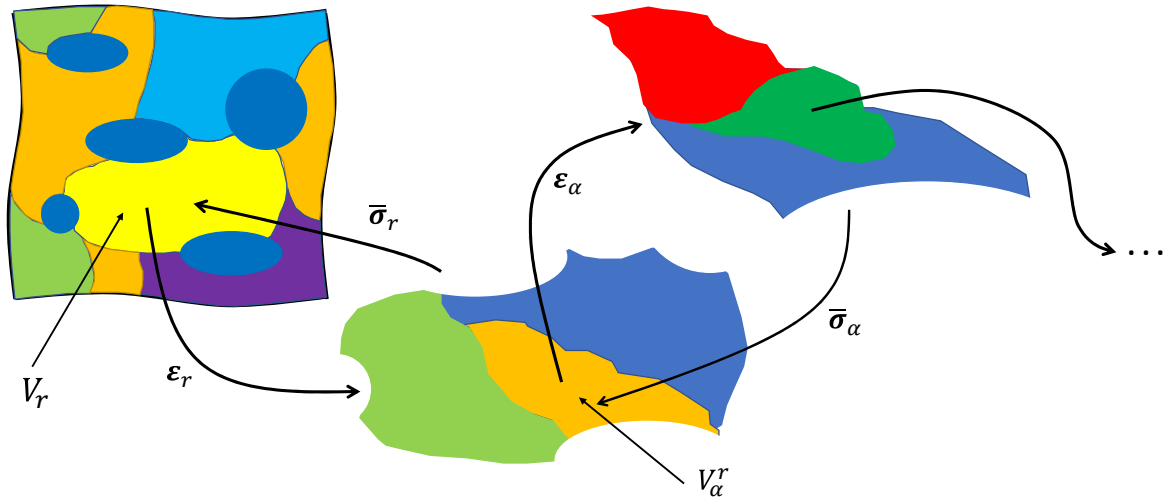

FIGURE 5.7: Schematic presentation of the extension from the two-step TFA towards a multi-step TFA.

5.4 Conclusions

In this section, a novel approach is proposed that aims for improved modeling results using the TFA with reduced computational efforts at the same time. The reduction of the computational effort is achieved by the separation of the BVP stated by the overall strain $\overline{\boldsymbol{\varepsilon}}$ into a BVP on the RVE scale level and several BVPs on all the subdomains of the RVE.

First considered is the case of the centered stiff elastic inclusion in the elasto-plastic matrix material. In the case of the composite unit cell with the center inclusion, the division of the subdomains on the higher scale level into sub-subdomains on the lower scale level does have little effect. The TFA^2 2-16 does not provide any improvements of the inelastic stress response with respect to the conventional TFA with one subdomain per phase only and much worse results than the conventional TFA with a matrix phase

divided into 16 subdomains. The inelastic response of the unit cell is controlled by the TFA procedure on the upper scale level, and therefore by the sum

$$\sum_{s=1}^{K} \mathbb{D}_{rs} : \Delta\boldsymbol{\varepsilon}_s^* \,, \tag{5.42}$$

representing the inelastic interaction effects of the subdomains. Translated to the case of a matrix material with one elastic inclusion, and the matrix represented by one subdomain $r = 1$, this can be expressed as

$$\sum_{s=1}^{K} \mathbb{D}_{r1} : \Delta\boldsymbol{\varepsilon}_1^* \,. \tag{5.43}$$

Using the conventional TFA, the eigenstrain of the matrix subdomains, $\boldsymbol{\varepsilon}_1^*$, follows directly from the subdomains inelastic constitutive relations. Using the two-step TFA^2 method, the eigenstrain $\boldsymbol{\varepsilon}_1^*$ follows from the subdomain stress $\overline{\boldsymbol{\sigma}}_1$ as

$$\boldsymbol{\varepsilon}_1^* = \boldsymbol{\varepsilon}_1 - (\overline{\mathbb{C}}_1^{\mathrm{el}})^{-1} : \overline{\boldsymbol{\sigma}}_1 \,, \tag{5.44}$$

and therefore from a homogenization procedure from the lower scale level

$$\overline{\boldsymbol{\sigma}}_1 = \sum_{\alpha=1}^{K_r} v_\alpha^1 \boldsymbol{\sigma}_\alpha^1 \,. \tag{5.45}$$

The equal responses provided by the conventional TFA with one subdomain and the two-step TFA^2 2-16, where the matrix is divided into one subdomain on the upper scale level and this subdomain is subdivided into 16 subdomains on the lower scale level means that the eigenstrain of the matrix on the upper scale level, $\Delta\boldsymbol{\varepsilon}_1^*$, is equal in both cases following directly from the matrix constitutive relations or following from the homogenization procedure on the lower scale level, although higher eigenstrains of the matrix were expected due to the refined spatial division. With eigenstrains following from the homogenization procedure on the lower scale level being equal to the ones following from the constitutive relations of the subdomains on the upper scale level, the TFA homogenization procedure on the lower scale level has no effect on the predicted response of the unit cell.

The predicted stress responses of the unit cell with a centered void are clearly better than the ones of the unit cell with the inclusion. While the stress response during the first biaxial loading stage is equally well using the TFA-P 16 or the TFA^2-P 1-16, the subsequent stress decrease is modeled even better by the TFA^2-P 1-16 than by the TFA-P 16. Furthermore, the modeled responses during the full applied loading path are clearly improved using the TFA^2-P 1-16, where the matrix is represented by one subdomain on the upper scale level and this subdomain is subdivided into 16 subdomains, with respect to the conventional TFA with only one matrix subdomain. This improvement was not recognized for the case of the unit cell with the center inclusion. However, considering the full-field result of the first biaxial loading stage (Fig. 5.6b), it is visible that the strain accumulation in the material is predicted much more accurately using the TFA-P 16 than using the TFA^2-P 1-16. With the strain accumulation predicted by the TFA^2-P 1-16, where the matrix subdomain is refined into 16 subdomains on the lower scale level, that equals the prediction provided by the conventional TFA with only one matrix subdomain,

it is recognized that the strain accumulation in the material is purely governed by the TFA on the upper scale level. The TFA procedure on the lower scale level does seem to have no effect on the strain accumulation of the subdomains on the upper scale level, although it was expected to provide improved strain accumulations as well as stress-strain responses. A strain distribution that is purely controlled by the TFA on the upper scale level, without an effect of the TFA procedure on the lower scale level, delivers an explanation of the visible ineffectivity of the hierarchical TFA homogenization procedure with respect to the conventional TFA.

Following the achieved results, even though improved predicted responses of the porous unit cell were provided by the TFA^2, it must be admitted that the spatial division on more than one scale level does not yet allow for the desired improvements of the results. Once the occurring issues can be tackled and solved, the two-scale TFA^2 formulation can be extended towards a multi-step TFA^N, with N denoting the number of scale levels. This would allow for the efficient modeling with very high numbers of subdomains, particularly important if more deformation modes are used in the offline stage. For the extension of the present approach (Fig. 5.7), the same downscaling as described in Sections 5.2.3, 5.2.4 and 5.2.5 can be implemented for the a priori computation of concentration and interaction tensors on more scale levels. The scale level transitioning between two hierarchical scale levels for the upscaling of homogenized quantities in the solution stage is described in Section 5.2.1. Furthermore, if the choice of another formulation for the homogenization appears convenient on a certain scale level or for all scale levels, the hierarchical approach can be employed for different CAH^N formulations.

Chapter 6

General conclusions

This work investigates the performance of approaches for the reduced homogenization (RH) of the mechanics of composite materials and proposes strategies for the improvement of their accuracy and efficiency. The particular kind of RH approaches are referred to as clustering analyses, basing on the spatial domain decomposition by means of statistical clustering techniques and the assumption of piecewise uniform fields of variables. The capabilities of the two clustering analysis approaches based on the TFA (Dvorak, 1992) and HS (Liu, Bessa, and Liu, 2016; Wulfinghoff, Cavaliere, and Reese, 2018) algorithms are evaluated extensively for various 2D structures and material systems.

While the HS analysis allows to provide accurate results for isotropic structures with very coarse spatial subdomain divisions, the TFA leads to typically far overstiff composite responses when the inclusion phase behaves purely elastic. The high errors in cases of high volume fractions of stiff elastic inclusions embedded in an elasto-plastic matrix emerge as a result of inelastic fields that are not captured sufficiently enough. The TFA can only converge towards the reference results gathered by DNS if the actual inelastic deformation fields during the inelastic loading conditions are captured accurately. Using an elasticity-based domain decomposition for the modeling of materials with nonlinear responses, meaning that the deformation patterns may strongly diverge from the elastic deformation patterns, leads to insufficient captures of the inelastic fields by the subdomains, resulting in underestimated interaction effects and finally overstiff composite responses. The requirement of an accurate capture of the inelastic deformation patterns for good predictions of the composite responses imply a rather computational character of the TFA used as an RH approach.

Clear improvements of the TFA approach were accomplished by the enhanced integration of the actual inelastic physics of the RVE problems by accounting for inelastic deformation patterns and localization effects through an inelasticity-based clustering. The offline stage can, theoretically, be extended to arbitrary numbers of various inelastic modes, proportional as well as non-proportional, in order to account for general loading conditions in the online stage. However, the issue emerging simultaneously is, that the identification of well-defined subdomains becomes more difficult when using strategies as the k-means clustering for high-dimensional quantities. Feeding the clustering algorithm with many inelastic deformation fields, possibly diverging strongly from each other, may lead to reduced emphasis on the single inelastic patterns and therefore to more stiff predictions by the TFA as the consequence. The TFA can be used for general microstructures, independently of anisotropies. However, unacceptable errors still occur if the inclusions deform purely elastic and the inclusion volume fraction is high. Besides the enhanced spatial division, allowing for improved TFA results, a correction is proposed in this work that bases on a quantification of the non-uniformity of inelastic fields in the subdomains.

It was recognized that the HS approach (Section 2.3.7), implemented as an PFA algorithm (Section 2.3.6) particularized and simplified for the modeling of composites with isotropic microstructures, allows much more accurate responses for isotropic materials with elastic inclusions in a matrix with low hardening characteristics than the TFA. The reason for this is, that the TFA accuracy is purely controlled by the fidelity of capture of the strongly heterogeneous inelastic fields. The consideration of a reference stiffness operator in the HS (PFA) algorithm that represents the homogenized response of the composite, leading to the resulting polarization stresses of the subdomains, allows accurate results with very low numbers of subdomains, typically only one subdomain per material phase. This result implies that the analytical solution of the HS approach is nearly independent of the fidelity of the spatial decomposition, and therefore of number of subdomains used. The fast convergence is governed by the existence of polarization stresses in both inelastic and elastic phases, and thus, contributions from both material phases. The justification of the HS approach could, based on the achieved results in this work, be approved for microstructures with an homogenized behavior that is close to isotropic. In cases of isotropic or quasi-isotropic microstructures, the actual homogenized stiffness of the composite is close to isotropic, making the imposed isotropic reference stiffness a rather weak assumption. Therefore it can be concluded that the use of the HS type approach, relying on an isotropic reference stiffness, is a sensible choice for the modeling of isotropic microstructures.

For strongly anisotropic microstructures however, the HS approach is unable to deliver reliable homogenized responses in elastic and inelastic deformation. The use of the HS approach for a strongly anisotropic microstructure, implying strong assumptions for the reference medium that aims to represent the homogenized response of the composite, with a high inclusion volume fraction leads to high errors of the elastic response, the yield onset and the inelastic response of the composite. It was demonstrated that the increasing number of subdomains for this kind of a highly anisotropic material does not allow a convergence of the homogenized response towards the reference FE result, implying that capabilities of the HS approach for general anisotropic structures is clearly limited. Following

- the very accurate homogenized responses of the HS type approach, relying on an isotropic reference stiffness, for the modeling of composites with isotropic microstructures, and
- the rather weak assumption of using an isotropic reference stiffness for the modeling of composites with isotropic microstructures

imply that the avoidance of the strong assumptions of an isotropic reference stiffness for the modeling of composites with anisotropic microstructures may allow clearly improved predicted responses. Consequently, the implementation of a generalized PFA, relying on a generalized anisotropic reference stiffness instead of an isotropic one, may be considered in the future for a more accurate modeling of general composite microstructures.

Following the achieved results, both TFA and HS reduced homogenization approaches were applied to a woven composite structure. With the three-scale character of the woven composite, the RH methods were applied for the modeling based on piecewise uniform fields of the woven mesostructure. Besides the woven mesostructure, the microstructure of the yarns is to be respected as well. The microstructure based spatial division of the yarns and the representation of the actual microstructure of the yarns by the approx-

imation of piecewise uniform unidirectional fiber composites allow the use of the MFH of the microstructure in combination with the RH approaches on the mesoscale level. The resulting computation of the predictions of the woven composite material consists therefore of a two-step homogenization procedure. While good predictions using the TFA could be expected after the accurate results of composites with two inelastic phases and anisotropic microstructures, the applicability of the HS, relying on the assumption of an isotropic reference medium, was to be validated for the strongly anisotropic woven structure. Both the TFA and HS approaches could successfully be confirmed as appropriate algorithms for the woven composite material, with high prediction accuracies achieved for the response of the woven unit cell under complex loading conditions.

Finally, after the extensive investigation on a range of various 2D structures and the testing for woven composite materials, it is concluded that the HS approach provides high prediction accuracies for isotropic and anisotropic structures, if the degree of the structural and material anisotropy does not exceed a certain level. Consequently, the generalized PFA, not relying on an isotropic reference medium may be considered in the future to achieve reliable predictions for strongly anisotropic materials. The TFA allows for reliable predictions for general composite materials and material systems. The weakest point of the TFA, with (possibly far) overstiff homogenized predictions, are structures consisting of an elevated volume fraction of an elastic inclusion phase in an elasto-plastic matrix. The reason for the poor results were found to be insufficient captures of the non-uniformity of highly localized inelastic fields. For this sake, a novel multi-step homogenization approach based on the TFA formulation was introduced in this work, tackling the issue of poor captures of the inelastic fields by a hierarchical domain decomposition. At the same time, the system to be solved is decoupled by means of a consideration of more than one scale level. This strategy targets for the reduction of computational efforts when using fine spatial decompositions, in turn allowing for the use of more accurate captures of the heterogeneous inelastic fields by the subdomains. The new TFA strategy was employed in this work for two scale levels and requires, as is clearly visible considering the achieved results, further research. The case of a composite with an elastic stiff inclusion in particular seems to show that the spatial decomposition on the second scale level is ineffective. If the reasons for this behavior can be identified and the clustering on the second scale level leads to positive effects on the homogenized responses, the hierarchical TFA approach may unlock new potentials for the modeling of inelastic composites. An extension to higher numbers of scales would further reduce the numerical solution and the computational requirements.

Appendix A

Uniaxial TFA and PFA in the one-dimensional element

Details on the TFA and PFA algorithms used for the investigation of the one-dimensional bar, consisting of two subdomains, are presented. The determination of the interaction factors allows, following Sections 2.3.4 and 2.3.6, to characterize the instantaneous strain concentration tensors.

TFA Considered is the case of a vanishing overall strain $\overline{\varepsilon} = 0$ and an existing eigenstrain in the subdomain 1, ε_1^*, in elasticity. From $\overline{\varepsilon} = v_1\,\varepsilon_1 + v_2\,\varepsilon_2 = 0$ follow

$$\varepsilon_1 = -(v_2/v_1)\,\varepsilon_2 \tag{A.1a}$$
$$\varepsilon_2 = -(v_1/v_2)\,\varepsilon_1\,, \tag{A.1b}$$

and from $\sigma_1 = E_1^{\mathrm{el}}\,(\varepsilon_1 - \varepsilon_1^*) = E_2^{\mathrm{el}}\,\varepsilon_2 = \sigma_2$ follow

$$\varepsilon_1 = (E_2^{\mathrm{el}}/E_1^{\mathrm{el}})\,\varepsilon_2 + \varepsilon_1^* \tag{A.2a}$$
$$\varepsilon_2 = (E_1^{\mathrm{el}}/E_2^{\mathrm{el}})\,(\varepsilon_1 - \varepsilon_1^*)\,. \tag{A.2b}$$

Inserting Eq. (A.2b) into Eq. (A.1a) leads to

$$\varepsilon_1 = \frac{v_2\,E_1^{\mathrm{el}}}{v_1\,E_2^{\mathrm{el}} + v_2\,E_1^{\mathrm{el}}}\,\varepsilon_1^* \tag{A.3}$$

and therefore to the interaction factor

$$D_{11} = \frac{v_2\,E_1^{\mathrm{el}}}{v_1\,E_2^{\mathrm{el}} + v_2\,E_1^{\mathrm{el}}}\,. \tag{A.4}$$

Inserting Eq. (A.2a) into Eq. (A.1b) results in

$$\varepsilon_2 = -\frac{v_1\,E_1^{\mathrm{el}}}{v_1\,E_2^{\mathrm{el}} + v_2\,E_1^{\mathrm{el}}}\,\varepsilon_1^* \tag{A.5}$$

and

$$D_{21} = -\frac{v_1\,E_1^{\mathrm{el}}}{v_1\,E_2^{\mathrm{el}} + v_2\,E_1^{\mathrm{el}}}\,. \tag{A.6}$$

Equivalently, an eigenstrain ε_2^* under the overall strain $\overline{\varepsilon} = 0$ results in

$$D_{22} = \frac{\upsilon_1 E_2^{\mathrm{el}}}{\upsilon_1 E_2^{\mathrm{el}} + \upsilon_2 E_1^{\mathrm{el}}} \tag{A.7}$$

and

$$D_{12} = -\frac{\upsilon_2 E_2^{\mathrm{el}}}{\upsilon_1 E_2^{\mathrm{el}} + \upsilon_2 E_1^{\mathrm{el}}} \,. \tag{A.8}$$

PFA In a homogeneous bar with $E_1 = E_2 = \overline{E}$, with an eigenstress σ_1^* under vanishing overall strain $\overline{\varepsilon} = 0$, it follows from $\sigma_1 = \overline{E}\,\varepsilon_1 + \sigma_1^* = \overline{E}\,\varepsilon_2 = \sigma_2$ that

$$\varepsilon_1 = \varepsilon_2 - \sigma_1^*/\overline{E} \tag{A.9a}$$

$$\varepsilon_2 = \varepsilon_1 + \sigma_1^*/\overline{E} \,. \tag{A.9b}$$

Inserting Eq. (A.9b) into Eq. (A.1a) yields

$$\varepsilon_1 = -\upsilon_2 \frac{\sigma_1^*}{\overline{E}} \tag{A.10}$$

and therefore

$$\Gamma_{11} = -\frac{\upsilon_2}{\overline{E}} \,. \tag{A.11}$$

Inserting Eq. (A.9a) into Eq. (A.1b) results in

$$\varepsilon_2 = \upsilon_1 \frac{\sigma_1^*}{\overline{E}} \tag{A.12}$$

and

$$\Gamma_{21} = \frac{\upsilon_1}{\overline{E}} \,. \tag{A.13}$$

Equivalently, the remaining Green's influence factors result in

$$\Gamma_{22} = -\frac{\upsilon_1}{\overline{E}} \tag{A.14}$$

and

$$\Gamma_{12} = \frac{\upsilon_2}{\overline{E}} \,. \tag{A.15}$$

Appendix B

Mean-Field Homogenization

B.1 Homogenized LCC operators

Using the Mori-Tanaka MFH formulation, the homogenized LCC stiffness can be computed from the corresponding phases LCC stiffnesses $\mathbb{C}_\omega^{\mathrm{LCC}}, \omega = \mathrm{I}, \mathrm{II}$ and the strain concentration tensor $\mathbb{B}_{\mathrm{II}}$ (Eq. (2.140)). The homogenized LCC operator reads

$$\overline{\mathbb{C}}^{\mathrm{LCC}} = \left[v_{\mathrm{II}} \mathbb{C}_{\mathrm{II}}^{\mathrm{LCC}} : \mathbb{B}_{\mathrm{II}} + v_{\mathrm{I}} \mathbb{C}_{\mathrm{I}}^{\mathrm{LCC}} \right] : \left[v_{\mathrm{II}} \mathbb{B}_{\mathrm{II}} + v_{\mathrm{I}} \mathbb{I} \right]^{-1}, \tag{B.1}$$

so that, e.g., the homogenized elastic operator in Eqs. (2.148) and (4.16) and Fig. 2.4a reads

$$\overline{\mathbb{C}}^{\mathrm{el}} = \left[v_{\mathrm{II}} \mathbb{C}_{\mathrm{II}}^{\mathrm{el}} : \mathbb{B}_{\mathrm{II}}^{\mathrm{el}} + v_{\mathrm{I}} \mathbb{C}_{\mathrm{I}}^{\mathrm{el}} \right] : \left[v_{\mathrm{II}} \mathbb{B}_{\mathrm{II}}^{\mathrm{el}} + v_{\mathrm{I}} \mathbb{I} \right]^{-1} \tag{B.2}$$

and the homogenized secant operator

$$\overline{\mathbb{C}}^{\mathrm{sec}} = \left[v_{\mathrm{II}} \mathbb{C}_{\mathrm{II}}^{\mathrm{sec}} : \mathbb{B}_{\mathrm{II}}^{\mathrm{sec}} + v_{\mathrm{I}} \mathbb{C}_{\mathrm{I}}^{\mathrm{sec}} \right] : \left[v_{\mathrm{II}} \mathbb{B}_{\mathrm{II}}^{\mathrm{sec}} + v_{\mathrm{I}} \mathbb{I} \right]^{-1}. \tag{B.3}$$

B.2 Residual vector

The resolution of the incremental-secant MFH formulation (Section 2.4.3) results in

$$\Delta \overline{\boldsymbol{\varepsilon}}^{\mathrm{re}} = v_{\mathrm{I}} \Delta \boldsymbol{\varepsilon}_{\mathrm{I}}^{\mathrm{re}} + v_{\mathrm{II}} \Delta \boldsymbol{\varepsilon}_{\mathrm{II}}^{\mathrm{re}}. \tag{B.4}$$

Multiplying this relation by $\mathbb{B}_{\mathrm{II}}^{-1}$ and using the expression in Eq. (2.156), this leads to

$$\begin{aligned} &\left(v_1 \left\{ \mathbb{I} + \mathbb{S} : [(\tilde{\mathbb{C}}_{\mathrm{I}}^{\mathrm{sec}})^{-1} : \mathbb{C}_{\mathrm{II}}^{\mathrm{sec}} - \mathbb{I}] \right\} + v_2 \, \mathbb{I} \right) : \Delta \boldsymbol{\varepsilon}_{\mathrm{II}}^{\mathrm{re}} \\ &= \Delta \boldsymbol{\varepsilon}_{\mathrm{II}}^{\mathrm{re}} + v_1 \left\{ \mathbb{S} : [(\tilde{\mathbb{C}}_{\mathrm{I}}^{\mathrm{sec}})^{-1} : \mathbb{C}_{\mathrm{II}}^{\mathrm{sec}} - \mathbb{I}] \right\} : \Delta \boldsymbol{\varepsilon}_{\mathrm{II}}^{\mathrm{re}} = \Delta \overline{\boldsymbol{\varepsilon}}^{\mathrm{re}}. \end{aligned} \tag{B.5}$$

After several reformulation steps, the following relation

$$\mathbb{C}_{\mathrm{II}}^{\mathrm{sec}} : \Delta \boldsymbol{\varepsilon}_{\mathrm{II}}^{\mathrm{re}} = \tilde{\mathbb{C}}_{\mathrm{I}}^{\mathrm{sec}} : \left[\Delta \boldsymbol{\varepsilon}_{\mathrm{II}}^{\mathrm{re}} - \frac{1}{v_{\mathrm{I}}} \mathbb{S}^{-1} : (\Delta \boldsymbol{\varepsilon}_{\mathrm{II}}^{\mathrm{re}} - \Delta \overline{\boldsymbol{\varepsilon}}^{\mathrm{re}}) \right] \tag{B.6}$$

can be obtained, leading to the expression of the stress residual $\boldsymbol{F}$ in Eq. (2.167), here reiterated:

$$\boldsymbol{F} = \mathbb{C}_{\mathrm{I}}^{\mathrm{sec}} : \left[\Delta \boldsymbol{\varepsilon}_{\mathrm{II}}^{\mathrm{re}} - \frac{1}{v_{\mathrm{I}}} \mathbb{S}^{-1} : (\Delta \boldsymbol{\varepsilon}_{\mathrm{II}}^{\mathrm{re}} - \Delta \overline{\boldsymbol{\varepsilon}}^{\mathrm{re}}) \right] - \mathbb{C}_{\mathrm{II}}^{\mathrm{sec}} : \Delta \boldsymbol{\varepsilon}_{\mathrm{II}}^{\mathrm{re}}. \tag{B.7}$$

B.3 Computation of the Jacobian matrix

The resolution of the MFH scheme (Section 2.4.3), with the linearization of the residual $\boldsymbol{F}$ (Eq. (2.167)), is expressed as

$$\boldsymbol{F} \to \boldsymbol{F} + \delta\boldsymbol{F} = 0\,, \tag{B.8}$$

where

$$\delta\boldsymbol{F} = \frac{\partial \boldsymbol{F}}{\partial \Delta\boldsymbol{\varepsilon}_{\mathrm{I}}^{\mathrm{re}}}\delta\Delta\boldsymbol{\varepsilon}_{\mathrm{I}}^{\mathrm{re}} + \frac{\partial \boldsymbol{F}}{\partial \Delta\boldsymbol{\varepsilon}_{\mathrm{II}}^{\mathrm{re}}}\delta\Delta\boldsymbol{\varepsilon}_{\mathrm{II}}^{\mathrm{re}} + \frac{\partial \boldsymbol{F}}{\partial \Delta\overline{\boldsymbol{\varepsilon}}^{\mathrm{re}}}\delta\Delta\overline{\boldsymbol{\varepsilon}}^{\mathrm{re}}\,. \tag{B.9}$$

With a constant overall strain increment $\Delta\overline{\boldsymbol{\varepsilon}}^{\mathrm{re}}$, and therefore the constant relation $\Delta\overline{\boldsymbol{\varepsilon}}^{\mathrm{re}} = \upsilon_{\mathrm{I}}\Delta\boldsymbol{\varepsilon}_{\mathrm{I}}^{\mathrm{re}} + \upsilon_{\mathrm{II}}\Delta\boldsymbol{\varepsilon}_{\mathrm{II}}^{\mathrm{re}}$, the variational term can be expressed as

$$\delta\boldsymbol{F} = \mathbb{J}\delta\Delta\boldsymbol{\varepsilon}_{\mathrm{II}}^{\mathrm{re}}\,, \tag{B.10}$$

with the Jacobian (Eq. (2.172))

$$\mathbb{J} = \frac{d\boldsymbol{F}}{d\Delta\boldsymbol{\varepsilon}_{\mathrm{II}}^{\mathrm{re}}} = \frac{\partial \boldsymbol{F}}{\partial \Delta\boldsymbol{\varepsilon}_{\mathrm{II}}^{\mathrm{re}}} + \frac{\partial \boldsymbol{F}}{\partial \Delta\boldsymbol{\varepsilon}_{\mathrm{I}}^{\mathrm{re}}}\frac{\partial \Delta\boldsymbol{\varepsilon}_{\mathrm{I}}^{\mathrm{re}}}{\partial \Delta\boldsymbol{\varepsilon}_{\mathrm{II}}^{\mathrm{re}}}\,, \tag{B.11}$$

whose full expression (with $\partial\square/\partial\Delta\boldsymbol{\varepsilon}_{\Omega}^{\mathrm{re}} = \partial\square/\partial\boldsymbol{\varepsilon}_{\Omega}$) amounts in

$$\begin{aligned}\mathbb{J} = {}& \tilde{\mathbb{C}}_{\mathrm{I}}^{\mathrm{sec}} : [\mathbb{I} - \mathbb{S}^{-1}] - \mathbb{C}_{\mathrm{II}}^{\mathrm{sec}} - \frac{\partial \mathbb{C}_{\mathrm{II}}^{\mathrm{sec}}}{\partial \boldsymbol{\varepsilon}_{\mathrm{II}}} : \Delta\boldsymbol{\varepsilon}_{\mathrm{II}}^{\mathrm{re}} - \\ & \frac{\upsilon_{\mathrm{II}}}{\upsilon_{\mathrm{I}}}\frac{\partial \tilde{\mathbb{C}}_{\mathrm{I}}^{\mathrm{sec}}}{\partial \boldsymbol{\varepsilon}_{\mathrm{I}}} : \left[\Delta\boldsymbol{\varepsilon}_{\mathrm{II}}^{\mathrm{re}} - \mathbb{S}^{-1}\frac{\Delta\boldsymbol{\varepsilon}_{\mathrm{II}}^{\mathrm{re}} - \Delta\overline{\boldsymbol{\varepsilon}}^{\mathrm{re}}}{\upsilon_{\mathrm{I}}}\right] - \\ & \frac{\upsilon_{\mathrm{II}}}{\upsilon_{\mathrm{I}}^2}\tilde{\mathbb{C}}_{\mathrm{I}}^{\mathrm{sec}} \otimes (\Delta\boldsymbol{\varepsilon}_{\mathrm{II}}^{\mathrm{re}} - \Delta\overline{\boldsymbol{\varepsilon}}^{\mathrm{re}}) :: (\mathbb{S}^{-1} \otimes \mathbb{S}^{-1}) :: \frac{\partial \mathbb{S}}{\partial \boldsymbol{\varepsilon}_{\mathrm{I}}} - \\ & \frac{\upsilon_{\mathrm{II}}}{\upsilon_{\mathrm{I}}}\tilde{\mathbb{C}}_{\mathrm{I}}^{\mathrm{sec}} : \mathbb{S}^{-1}\,.\end{aligned} \tag{B.12}$$

B.4 Homogenized tangent

The homogenized algorithmic tangent stiffness (Eq. (2.159)) is computed as

$$\overline{\mathbb{C}}^{\mathrm{alg}} = \frac{\partial \overline{\boldsymbol{\sigma}}}{\partial \overline{\boldsymbol{\varepsilon}}} = \upsilon_{\mathrm{I}}\frac{\partial \boldsymbol{\sigma}_{\mathrm{I}}}{\partial \boldsymbol{\varepsilon}_{\mathrm{I}}}\frac{\partial \boldsymbol{\varepsilon}_{\mathrm{I}}}{\partial \overline{\boldsymbol{\varepsilon}}} + \upsilon_{\mathrm{II}}\frac{\partial \boldsymbol{\sigma}_{\mathrm{II}}}{\partial \boldsymbol{\varepsilon}_{\mathrm{II}}}\frac{\partial \boldsymbol{\varepsilon}_{\mathrm{II}}}{\partial \overline{\boldsymbol{\varepsilon}}}\,. \tag{B.13}$$

Here, the inclusion phase behaves elastic, meaning that $\partial\boldsymbol{\sigma}_{\mathrm{II}}/\partial\boldsymbol{\varepsilon}_{\mathrm{II}} = \mathbb{C}_{\mathrm{II}}^{\mathrm{el}}$. The derivatives of the matrix phase stresses by the phase strains, $\partial\boldsymbol{\sigma}_{\mathrm{I}}/\partial\boldsymbol{\varepsilon}_{\mathrm{I}}$, follow from the computation of the stresses in Eqs. (2.154b) and (2.158), resulting in

$$\frac{\partial \boldsymbol{\sigma}_{\mathrm{I}}}{\partial \boldsymbol{\varepsilon}_{\mathrm{I}}} = \mathbb{C}_{\mathrm{I}}^{\mathrm{sec}} + \frac{\partial \mathbb{C}_{\mathrm{I}}^{\mathrm{sec}}}{\partial \boldsymbol{\varepsilon}_{\mathrm{I}}} : \Delta\boldsymbol{\varepsilon}_{\mathrm{I}}^{\mathrm{re}}\,. \tag{B.14}$$

The computation of the derivative of the matrix incremental-secant operator $\mathbb{C}_{\mathrm{I}}^{\mathrm{sec}}$ in Eq. (B.14), $\partial\mathbb{C}_{\mathrm{I}}^{\mathrm{sec}}/\partial\boldsymbol{\varepsilon}_{\mathrm{I}}$, is presented in Appendix C.2.

In case of the zero-residual formalism for the matrix, the stress derivative $\partial\boldsymbol{\sigma}_\mathrm{I}/\partial\boldsymbol{\varepsilon}_\mathrm{I}$ follows from Eq. (2.161) and results in

$$\frac{\partial\boldsymbol{\sigma}_\mathrm{I}}{\partial\boldsymbol{\varepsilon}_\mathrm{I}} = \tilde{\mathbb{C}}_\mathrm{I}^\mathrm{sec} + \frac{\partial\tilde{\mathbb{C}}_\mathrm{I}^\mathrm{sec}}{\partial\boldsymbol{\varepsilon}_\mathrm{I}} : \Delta\boldsymbol{\varepsilon}_\mathrm{I}^\mathrm{re} \,. \tag{B.15}$$

The computation of the derivative of the matrix zero-residual incremental-secant operator $\tilde{\mathbb{C}}_\mathrm{I}^\mathrm{sec}$ in Eq. (B.14), $\partial\tilde{\mathbb{C}}_\mathrm{I}^\mathrm{sec}/\partial\boldsymbol{\varepsilon}_\mathrm{I}$, is presented in Appendix C.2.

The derivatives $\partial\boldsymbol{\varepsilon}_\mathrm{I}/\partial\overline{\boldsymbol{\varepsilon}}$ and $\partial\boldsymbol{\varepsilon}_\mathrm{II}/\partial\overline{\boldsymbol{\varepsilon}}$ follow after the MFH solution in Eq. (B.8) with Eq. (B.10) as

$$\frac{\partial\boldsymbol{\varepsilon}_\mathrm{II}}{\partial\overline{\boldsymbol{\varepsilon}}} = -\mathbb{J}^{-1} : \frac{\partial\boldsymbol{F}}{\partial\overline{\boldsymbol{\varepsilon}}} \tag{B.16}$$

and

$$\frac{\partial\boldsymbol{\varepsilon}_\mathrm{I}}{\partial\overline{\boldsymbol{\varepsilon}}} = \frac{1}{v_\mathrm{I}}\big(\mathbb{I} - v_\mathrm{II}\frac{\partial\boldsymbol{\varepsilon}_\mathrm{II}}{\partial\overline{\boldsymbol{\varepsilon}}}\big) \,. \tag{B.17}$$

Appendix C

Derivatives of the incremental stress-strain response using the J_2-plasticity model

C.1 Algorithmic tangent operator

In the following, the derivative of the incremental stress-strain response computed by the J_2-plasticity model are given. The stress tensor is computed as

$$\boldsymbol{\sigma} = \boldsymbol{\sigma}^{\mathrm{tr}} - 2G^{\mathrm{el}}\Delta\boldsymbol{\varepsilon}^{\mathrm{p}} = \boldsymbol{\sigma}^{\mathrm{tr}} - 2G^{\mathrm{el}}\Delta p\boldsymbol{N}. \tag{C.1}$$

Derivatives with respect to the strain (it is noted that $\partial\square/\partial\Delta\boldsymbol{\varepsilon} = \partial\square/\partial\boldsymbol{\varepsilon}$) follow from the derivatives

$$\frac{\partial\boldsymbol{\sigma}^{\mathrm{tr}}}{\partial\boldsymbol{\varepsilon}} = \mathbb{C}^{\mathrm{el}}, \tag{C.2}$$

$$\frac{\partial\Delta p}{\partial\boldsymbol{\varepsilon}} = \frac{2G^{\mathrm{el}}}{h}\boldsymbol{N}, \tag{C.3}$$

and

$$\frac{\partial\boldsymbol{N}}{\partial\boldsymbol{\varepsilon}} = \frac{\partial\boldsymbol{N}}{\partial\boldsymbol{\sigma}^{\mathrm{tr}}} : \frac{\partial\boldsymbol{\sigma}^{\mathrm{tr}}}{\partial\boldsymbol{\varepsilon}} = \frac{1}{\sigma^{\mathrm{tr,eq}}}\left(\frac{3}{2}\mathbb{I}^{\mathrm{dev}} - \boldsymbol{N}\otimes\boldsymbol{N}\right) : \mathbb{C}^{\mathrm{el}} = \frac{2G^{\mathrm{el}}}{\sigma^{\mathrm{tr,eq}}}\left(\frac{3}{2}\mathbb{I}^{\mathrm{dev}} - \boldsymbol{N}\otimes\boldsymbol{N}\right), \tag{C.4}$$

where

$$h = 3G^{\mathrm{el}} + dR/dp. \tag{C.5}$$

These relations result in the expression of the plastic strain derivative in Eq. (2.196),

$$\frac{\partial\Delta\boldsymbol{\varepsilon}^{\mathrm{p}}}{\partial\boldsymbol{\varepsilon}} = \frac{2G^{\mathrm{el}}}{h}\boldsymbol{N}\otimes\boldsymbol{N} + 2G^{\mathrm{el}}\frac{\Delta p}{\sigma^{\mathrm{tr,eq}}}\left(\frac{3}{2}\mathbb{I}^{\mathrm{dev}} - \boldsymbol{N}\otimes\boldsymbol{N}\right), \tag{C.6}$$

and into the expression of the algorithmic tangent in Eq. (2.197),

$$\mathbb{C}^{\mathrm{alg}} = \mathbb{C}^{\mathrm{el}} - 2G^{\mathrm{el}}\frac{\partial\Delta\boldsymbol{\varepsilon}^{\mathrm{p}}}{\partial\boldsymbol{\varepsilon}} = \mathbb{C}^{\mathrm{el}} - \frac{(2G^{\mathrm{el}})^2}{h}\boldsymbol{N}\otimes\boldsymbol{N} - (2G^{\mathrm{el}})^2\frac{\Delta p}{\sigma^{\mathrm{tr,eq}}}\left(\frac{3}{2}\mathbb{I}^{\mathrm{dev}} - \boldsymbol{N}\otimes\boldsymbol{N}\right). \tag{C.7}$$

C.2 Derivative of the incremental-secant operator by the strain

In this work, the inclusion phase behaves elastic, such that $\mathbb{C}_{\mathrm{II}}^{\mathrm{sec}} = \mathbb{C}_{\mathrm{II}}^{\mathrm{el}} = \text{const}$. In the following, the derivatives of the matrix incremental-secant operators with residual stresses, $\mathbb{C}_{\mathrm{I}}^{\mathrm{sec}}$, and without the residual stresses, $\tilde{\mathbb{C}}_{\mathrm{I}}^{\mathrm{sec}}$, are given. The matrix subscript I will be omitted. The derivative of the matrix incremental secant operator $\mathbb{C}^{\mathrm{sec}}$ following Eq. (2.204) with a pressure-independent plasticity, is given as

$$\frac{\partial \mathbb{C}^{\mathrm{sec}}}{\partial \boldsymbol{\varepsilon}} = 2\,\mathbb{I}^{\mathrm{dev}} \otimes \frac{\partial G^{\mathrm{sec}}}{\partial \boldsymbol{\varepsilon}}\,. \tag{C.8}$$

Consequently, the derivative of the incremental secant shear modulus

$$G^{\mathrm{sec}} = \frac{\Delta\sigma^{\mathrm{re,eq}}}{3\,\Delta\varepsilon^{\mathrm{re,eq}}} \tag{C.9}$$

is to be computed. With

$$\frac{\partial \Delta\sigma^{\mathrm{re,eq}}}{\partial \boldsymbol{\varepsilon}} = \frac{3}{2}\frac{\mathrm{dev}(\Delta\boldsymbol{\sigma}^{\mathrm{re}})}{\Delta\sigma^{\mathrm{re,eq}}} : \mathbb{C}^{\mathrm{alg}} = \frac{\mathrm{dev}(\Delta\boldsymbol{\sigma}^{\mathrm{re}})}{2\,G^{\mathrm{sec}}\Delta\varepsilon^{\mathrm{re,eq}}} : \mathbb{C}^{\mathrm{alg}} \tag{C.10}$$

and

$$\frac{\partial \Delta\varepsilon^{\mathrm{re,eq}}}{\partial \boldsymbol{\varepsilon}} = \frac{2}{3}\frac{\mathrm{dev}(\Delta\boldsymbol{\varepsilon}^{\mathrm{re}})}{\Delta\varepsilon^{\mathrm{re,eq}}}\,, \tag{C.11}$$

the derivative of the incremental secant shear modulus results in

$$\frac{\partial G^{\mathrm{sec}}}{\partial \boldsymbol{\varepsilon}} = \frac{1}{6\,G^{\mathrm{sec}}\,(\Delta\varepsilon^{\mathrm{re,eq}})^2}\,\mathrm{dev}(\Delta\boldsymbol{\sigma}^{\mathrm{re}}) : \mathbb{C}^{\mathrm{alg}} - \frac{2}{3}G^{\mathrm{sec}}\frac{\mathrm{dev}(\Delta\boldsymbol{\varepsilon}^{\mathrm{re}})}{(\Delta\varepsilon^{\mathrm{re,eq}})^2}\,, \tag{C.12}$$

with the algorithmic tangent

$$\mathbb{C}^{\mathrm{alg}} = \mathbb{C}^{\mathrm{el}} - 2G^{\mathrm{el}}\,\frac{\partial \Delta\boldsymbol{\varepsilon}^{\mathrm{p}}}{\partial \boldsymbol{\varepsilon}}\,, \tag{C.13}$$

where

$$\frac{\partial \Delta\boldsymbol{\varepsilon}^{\mathrm{p}}}{\partial \boldsymbol{\varepsilon}} = \boldsymbol{N}^{\mathrm{sec}} \otimes \frac{\partial \Delta p}{\partial \boldsymbol{\varepsilon}} + \Delta p\,\frac{\partial \boldsymbol{N}^{\mathrm{sec}}}{\partial \boldsymbol{\varepsilon}}\,. \tag{C.14}$$

The derivative of the plastic flow direction results in

$$\frac{\partial \boldsymbol{N}^{\mathrm{sec}}}{\partial \boldsymbol{\varepsilon}} = \frac{2G^{\mathrm{el}}}{\Delta\sigma^{\mathrm{re,tr,eq}}}\left(\frac{3}{2}\mathbb{I}^{\mathrm{dev}} - \boldsymbol{N}^{\mathrm{sec}} \otimes \boldsymbol{N}^{\mathrm{sec}}\right). \tag{C.15}$$

The derivative of the plastic strain increment in the incremental-secant formulation follows from the derivative of the current yield stress

$$\begin{aligned}\frac{\partial \sigma^{\mathrm{eq}}}{\partial \boldsymbol{\varepsilon}} &= \frac{dR_{\mathrm{I}}}{dp}\,\frac{\partial p}{\partial \boldsymbol{\sigma}}\,\frac{\partial \boldsymbol{\sigma}}{\partial \boldsymbol{\varepsilon}_{\mathrm{I}}} \\ &= \boldsymbol{N} : \left[\mathbb{C}^{\mathrm{el}} - \mathbb{C}^{\mathrm{el}} : \left(\boldsymbol{N}^{\mathrm{sec}} \otimes \frac{\partial \Delta p}{\partial \boldsymbol{\varepsilon}} + \Delta p\,\frac{\partial \boldsymbol{N}^{\mathrm{sec}}}{\partial \boldsymbol{\varepsilon}}\right)\right]\end{aligned} \tag{C.16}$$

which can be reformulated to finally obtain

$$\frac{\partial \Delta p}{\partial \boldsymbol{\varepsilon}} = \frac{2G^{\mathrm{el}}}{h^{\mathrm{sec}}}\,\boldsymbol{N} - \frac{2G^{\mathrm{el}}\Delta p}{h^{\mathrm{sec}}}\,\boldsymbol{N} : \frac{\partial \boldsymbol{N}^{\mathrm{sec}}}{\partial \boldsymbol{\varepsilon}}\,, \tag{C.17}$$

where

$$h^{\mathrm{sec}} = 2G^{\mathrm{el}}\,\boldsymbol{N}_{\mathrm{I}}^{\mathrm{sec}} : \boldsymbol{N} + \frac{dR}{dp}\,. \tag{C.18}$$

The derivative of the plastic strain increment $\partial \Delta p / \partial \boldsymbol{\varepsilon}$ of the incremental-secant formulation was developed by Cagegi (2022).

Similarly, the derivative of the zero-residual incremental-secant operator $\tilde{\mathbb{C}}^{\mathrm{sec}}$ follows as

$$\frac{\partial \tilde{\mathbb{C}}^{\mathrm{sec}}}{\partial \boldsymbol{\varepsilon}} = 2\,\mathbb{I}^{\mathrm{dev}} \otimes \frac{\partial \tilde{G}^{\mathrm{sec}}}{\partial \boldsymbol{\varepsilon}}\,, \tag{C.19}$$

where

$$\frac{\partial \tilde{G}^{\mathrm{sec}}}{\partial \boldsymbol{\varepsilon}} = \frac{1}{6\,G_{\mathrm{I}}^{\mathrm{sec}}\,(\Delta \varepsilon^{\mathrm{re,eq}})^2}\,\mathrm{dev}(\boldsymbol{\sigma}) : \mathbb{C}^{\mathrm{alg}} - \frac{2}{3} G^{\mathrm{sec}} \frac{\mathrm{dev}(\Delta \boldsymbol{\varepsilon}^{\mathrm{re}})}{(\Delta \varepsilon^{\mathrm{re,eq}})^2} \tag{C.20}$$

and $\mathbb{C}^{\mathrm{alg}}$ given by Eq. (C.7) with

$$h = 3\,G^{\mathrm{el}} + \frac{dR}{dp}\,. \tag{C.21}$$

Appendix D

Convergence study of the overall deformation factor $\boldsymbol{E}^{\mathrm{BC,in}}$ for the inelastic deformation modes

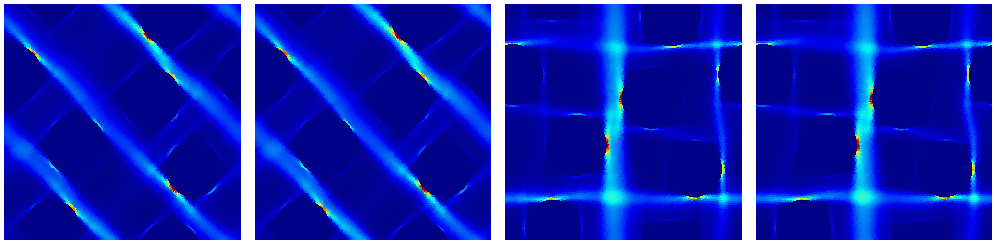

(a) (b) (c) (d)

FIGURE D.1: Equivalent plastic field patterns inside the RVE with $v_{\mathrm{II}} = 30$ % of circular stiff elastic inclusions in an elasto-plastic matrix under the two deformation modes (a, b) $l = 1$ and (c, d) $l = 2$ (Eq. (3.10)) with the deformation factors (a, c) $E^{\mathrm{in}} = 2\%$ and (b, d) $E^{\mathrm{in}} = 8\%$.

In this section, the justification of the overall deformation factor for the inelastic offline deformation modes $E^{\mathrm{in}} = 2\%$ is presented by means of a convergence study using the RVE with $v_{\mathrm{II}} = 30$ % of circular stiff elastic inclusions in an elasto-plastic matrix. The k-means clustering method is based on the differences of local quantities, and is therefore sensitive to spatial distributions rather than the particular magnitudes of the local quantity. In order to achieve a clustering into subdomains that does not change if the overall deformation increases, it is important that the final spatial plastic field configurations are achieved under the offline deformation modes. Thus, the overall deformation factor for the inelastic offline simulations was selected with the goal to be just high enough to achieve the final spatial plastic patterns in the composite RVEs with the material properties given in Section 3.5.1.

According to Fig. D.1, the achieved plastic patterns under both deformation modes in Eq. (3.10) with the overall deformation factors $E^{\mathrm{in}} = 2\%$ and $E^{\mathrm{in}} = 8\%$ are identical, implying that final plastic field patterns are established under the selected deformation factor $E^{\mathrm{in}} = 2\%$. We note that the clustering is achieved by considering the plastic strain tensor components and not the equivalent plastic strain scalar, but for readability Fig. D.1 displays a scalar value. Additionally, the achieved TFA results for the uniaxial tension and the pure-shear tests in Eqs. (3.62) and (3.63) using the subdomain decomposition

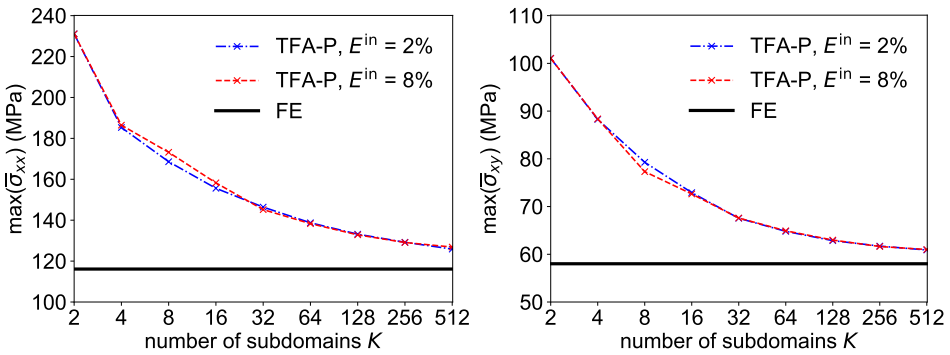

FIGURE D.2: The convergence of the (a) peak normal stress under uniaxial tension (Eq. (3.62)) and of the (b) peak shear stress under pure shear deformation (Eq. (3.63)) depending on the number of subdomains for the RVE with $v_{\mathrm{II}} = 30$ % of circular stiff elastic inclusions in an elasto-plastic matrix. Compared are the use of the TFA-P using subdomains computed with the offline deformation factors $E^{\mathrm{in}} = 2\%$ and $E^{\mathrm{in}} = 8\%$.

based on the two offline deformation factors are compared in Fig. D.2. It is visible that the deviations between the two results are negligible. Based on this, it can be concluded that the RVE deformation of 2 % in combination with the mentioned material properties is sufficient to achieve the final plastic field patterns in the offline stage.

Appendix E

Local yarn and fiber orientation in the woven composite

The yarn and fiber orientation at $\boldsymbol{\chi}$ is expressed as

$$\vec{v}(\boldsymbol{\chi}) = Q_2\big(\theta_2(\boldsymbol{\chi})\big) \cdot Q_1\big(\theta_1(\boldsymbol{\chi})\big) \cdot \vec{e}_z \,. \tag{E.1}$$

The first euler angle $\theta_1(\boldsymbol{\chi})$ represents a rotation of the global coordinate system around the z-axis, meaning

$$Q_1\big(\theta_1(\boldsymbol{\chi})\big) = \begin{bmatrix} \cos(\theta_1) & -\sin(\theta_1) & 0 \\ \sin(\theta_1) & \cos(\theta_1) & 0 \\ 0 & 0 & 1 \end{bmatrix} . \tag{E.2}$$

The second euler represents a rotation of the once rotated coordinate system around the x'-axis. Inside the rotated system, the second euler angle is therefore expressed as

$$Q_2\big(\theta_2(\boldsymbol{\chi})\big) = \begin{bmatrix} 1 & 0 & 0 \\ 0 & \cos(\theta_2) & -\sin(\theta_2) \\ 0 & \sin(\theta_2) & \cos(\theta_2) \end{bmatrix} . \tag{E.3}$$

The total local rotation matrix in Eq. (4.8) is given as

$$\begin{aligned} Q(\boldsymbol{\chi}) &= Q_2\big(\theta_2(\boldsymbol{\chi})\big) \cdot Q_1\big(\theta_1(\boldsymbol{\chi})\big) \\ &= \begin{bmatrix} \cos(\theta_1) & -\sin(\theta_1)\,\cos(\theta_2) & \sin(\theta_1)\,\sin(\theta_2) \\ 0 & \cos(\theta_1)\,\cos(\theta_2) & -\cos(\theta_1)\,\sin(\theta_2) \\ 0 & \sin(\theta_2) & \cos(\theta_2) \end{bmatrix} . \end{aligned} \tag{E.4}$$

Bibliography

Aboudi, Jacob, Steven M. Arnold, and Brett A. Bednarcyk (2013). "Chapter 3 - Fundamentals of the Mechanics of Multiphase Materials". In: *Micromechanics of Composite Materials*. Ed. by Jacob Aboudi, Steven M. Arnold, and Brett A. Bednarcyk. Oxford: Butterworth-Heinemann, pp. 87–145. ISBN: 978-0-12-397035-0. DOI: https://doi.org/10.1016/B978-0-12-397035-0.00003-3. URL: https://www.sciencedirect.com/science/article/pii/B9780123970350000033.

Benveniste, Y. (1987). "A new approach to the application of Mori-Tanaka's theory in composite materials". In: *Mechanics of Materials* 6.2, pp. 147–157. ISSN: 0167-6636. DOI: 10.1016/0167-6636(87)90005-6. URL: https://www.sciencedirect.com/science/article/pii/0167663687900056.

Berveiller, M. and A. Zaoui (1978). "An extension of the self-consistent scheme to plastically-flowing polycrystals". In: *Journal of the Mechanics and Physics of Solids* 26.5, pp. 325–344. ISSN: 0022-5096. DOI: 10.1016/0022-5096(78)90003-0. URL: https://www.sciencedirect.com/science/article/pii/0022509678900030.

Budiansky, B. (1965). "On the elastic moduli of some heterogeneous materials". In: *Journal of the Mechanics and Physics of Solids* 13.4, pp. 223–227. ISSN: 0022-5096. DOI: 10.1016/0022-5096(65)90011-6. URL: https://www.sciencedirect.com/science/article/pii/0022509665900116.

Cagegi, M. Pérez (2022). "Integration scheme of a continuous formulation based on incremental-secant homogenization". MA thesis. Université de Liège. URL: https://matheo.uliege.be/handle/2268.2/13855.

Castrogiovanni, Alfredo et al. (2021). "TFA and HS based homogenization techniques for nonlinear composites". In: *International Journal of Solids and Structures* 225, p. 111050. ISSN: 0020-7683. DOI: https://doi.org/10.1016/j.ijsolstr.2021.111050. URL: https://www.sciencedirect.com/science/article/pii/S0020768321001347.

Cavaliere, Fabiola, Stefanie Reese, and Stephan Wulfinghoff (2020). "Efficient two–scale simulations of engineering structures using the Hashin–Shtrikman type finite element method". In: *Computational Mechanics* 65, pp. 159 –175. DOI: 10.1007/s00466-019-01758-4. URL: https://www.springerprofessional.de/en/efficient-two-scale-simulations-of-engineering-structures-using-/17118994.

Chaboche, J.L., P. Kanouté, and A. Roos (2005). "On the capabilities of mean-field approaches for the description of plasticity in metal matrix composites". In: *International Journal of Plasticity* 21.7, pp. 1409–1434. ISSN: 0749-6419. DOI: https://doi.org/10.1016/j.ijplas.2004.07.001. URL: https://www.sciencedirect.com/science/article/pii/S0749641904001433.

Chaboche, J.L. et al. (2001). "Towards a micromechanics based inelastic and damage modeling of composites". In: *International Journal of Plasticity* 17.4, pp. 411–439. ISSN: 0749-6419. DOI: https://doi.org/10.1016/S0749-6419(00)00056-5. URL: https://www.sciencedirect.com/science/article/pii/S0749641900000565.

Charalambakis, Nicolas (2010). "Homogenization Techniques and Micromechanics. A Survey and Perspectives". In: *Applied Mechanics Reviews* 63.3. ISSN: 0003-6900. DOI: 10.1115/1.4001911. eprint: https://asmedigitalcollection.asme.org/appliedmechanicsreviews/article-pdf/63/3/030803/5442740/030803_1.pdf. URL: https://doi.org/10.1115/1.4001911.

Covezzi, F. et al. (2016). "Complementary formulation of the TFA for the elasto-plastic analysis of composites". In: *Composite Structures* 156. 70th Anniversary of Professor J. N. Reddy, pp. 93–100. ISSN: 0263-8223. DOI: https://doi.org/10.1016/j.compstruct.2016.01.094. URL: https://www.sciencedirect.com/science/article/pii/S0263822316001173.

Cózar, I.R. et al. (2022). "A three-dimensional plastic-damage model for polymer composite materials". In: *Composites Part A: Applied Science and Manufacturing* 163, p. 107198. ISSN: 1359-835X. DOI: https://doi.org/10.1016/j.compositesa.2022.107198. URL: https://www.sciencedirect.com/science/article/pii/S1359835X22003797.

Doghri, I. and C. Friebel (2005). "Effective elasto-plastic properties of inclusion-reinforced composites. Study of shape, orientation and cyclic response". In: *Mechanics of Materials* 37.1, pp. 45–68. ISSN: 0167-6636. DOI: https://doi.org/10.1016/j.mechmat.2003.12.007. URL: https://www.sciencedirect.com/science/article/pii/S016766360400002X.

Doghri, I. and A. Ouaar (2003). "Homogenization of two-phase elasto-plastic composite materials and structures: Study of tangent operators, cyclic plasticity and numerical algorithms". In: *International Journal of Solids and Structures* 40.7, pp. 1681 – 1712. ISSN: 0020-7683. DOI: 10.1016/S0020-7683(03)00013-1. URL: http://www.sciencedirect.com/science/article/pii/S0020768303000131.

Doghri, I. et al. (2011). "A second-moment incremental formulation for the mean-field homogenization of elasto-plastic composites". In: *International Journal of Plasticity* 27.3, pp. 352–371. ISSN: 0749-6419. DOI: 10.1016/j.ijplas.2010.06.004. URL: https://www.sciencedirect.com/science/article/pii/S0749641910000835.

Dvorak, G, Y Bahei-El-Din, and A Wafa (1994). "Implementation of the transformation field analysis for inelastic composite materials". In: *Computational Mechanics* 14, pp. 201–228. DOI: 10.1007/BF00370073. URL: https://link.springer.com/article/10.1007%2FBF00370073.

Dvorak, George J. (1990). "On uniform fields in heterogeneous media". In: *Proceedings of the Royal Society of London. Series A: Mathematical and Physical Sciences* 431.1881, pp. 89–110. DOI: 10.1098/rspa.1990.0120. eprint: https://royalsocietypublishing.org/doi/pdf/10.1098/rspa.1990.0120. URL: https://royalsocietypublishing.org/doi/10.1098/rspa.1990.0120.

— (1992). "On transformation strains and uniform fields in multiphase elastic media". In: *Proceedings of the Royal Society of London. Series A: Mathematical and Physical Sciences* 437.1900, pp. 291–310. DOI: 10.1098/rspa.1992.0062. eprint: https://royalsocietypublishing.org/doi/pdf/10.1098/rspa.1992.0062. URL: https://royalsocietypublishing.org/doi/10.1098/rspa.1992.0062.

— (2013). *Micromechanics of Composite Materials*. Solid Mechanics and Its Applications. Springer, Dordrecht. ISBN: 978-94-007-9781-9. DOI: 10.1007/978-94-007-4101-0. URL: https://link.springer.com/book/10.1007/978-94-007-4101-0.

Eshelby, John D. (1957). "The determination of the elastic field of an ellipsoidal inclusion, and related problems". In: *Proceedings of the Royal Society of London. Series A: Mathematical and Physical Sciences* 241.1226, pp. 376–396. DOI: 10.1098/rspa.1957.0133. eprint: https://royalsocietypublishing.org/doi/pdf/10.1098/rspa.1957.0133. URL: https://royalsocietypublishing.org/doi/10.1098/rspa.1957.0133.

Feyel, Frédéric (1999). "Multiscale FE2 elastoviscoplastic analysis of composite structures". In: *Computational Materials Science* 16.1, pp. 344–354. ISSN: 0927-0256. DOI: 10.1016/S0927-0256(99)00077-4. URL: https://www.sciencedirect.com/science/article/pii/S0927025699000774.

Fritzen, Felix and Matthias Leuschner (2013). "Reduced basis hybrid computational homogenization based on a mixed incremental formulation". In: *Computer Methods in Applied Mechanics and Engineering* 260, pp. 143–154. ISSN: 0045-7825. DOI: 10.1016/j.cma.2013.03.007. URL: https://www.sciencedirect.com/science/article/pii/S0045782513000583.

Gajek, Sebastian, Matti Schneider, and Thomas Böhlke (2020). "On the micromechanics of deep material networks". In: *Journal of the Mechanics and Physics of Solids* 142, p. 103984. ISSN: 0022-5096. DOI: 10.1016/j.jmps.2020.103984.

Geers, M.G.D., V.G. Kouznetsova, and W.A.M. Brekelmans (2010). "Multi-scale computational homogenization: Trends and challenges". In: *Journal of Computational and Applied Mathematics* 234.7. Fourth International Conference on Advanced COmputational Methods in ENgineering (ACOMEN 2008), pp. 2175–2182. ISSN: 0377-0427. DOI: https://doi.org/10.1016/j.cam.2009.08.077. URL: https://www.sciencedirect.com/science/article/pii/S0377042709005536.

Geers, Marc G. D. et al. (2017). "Homogenization Methods and Multiscale Modeling: Nonlinear Problems". In: *Encyclopedia of Computational Mechanics Second Edition*. Ed. by Erwin Stein, René de Borst, and Thomas Hughes. Wiley, pp. 1–34. ISBN: 9781119176817. DOI: 10.1002/9781119176817.ecm2107. eprint: https://onlinelibrary.wiley.com/doi/pdf/10.1002/9781119176817.ecm2107. URL: https://onlinelibrary.wiley.com/doi/abs/10.1002/9781119176817.ecm2107.

Gorji, Maysam B. et al. (2020). "On the potential of recurrent neural networks for modeling path dependent plasticity". In: *Journal of the Mechanics and Physics of Solids* 143, p. 103972. ISSN: 0022-5096. DOI: https://doi.org/10.1016/j.jmps.2020.103972. URL: https://www.sciencedirect.com/science/article/pii/S0022509620302076.

Han, Xinxing et al. (2020). "Efficient multiscale modeling for woven composites based on self-consistent clustering analysis". In: *Computer Methods in Applied Mechanics and Engineering* 364, p. 112929. ISSN: 0045-7825. DOI: https://doi.org/10.1016/j.cma.2020.112929. URL: https://www.sciencedirect.com/science/article/pii/S0045782520301122.

Hashin, Z. and S. Shtrikman (1962). "On some variational principles in anisotropic and nonhomogeneous elasticity". In: *Journal of the Mechanics and Physics of Solids* 10.4, pp. 335–342. ISSN: 0022-5096. DOI: 10.1016/0022-5096(62)90004-2. URL: https://www.sciencedirect.com/science/article/pii/0022509662900042.

— (1963). "A variational approach to the theory of the elastic behaviour of multiphase materials". In: *Journal of the Mechanics and Physics of Solids* 11.2, pp. 127–140. ISSN: 0022-5096. DOI: 10.1016/0022-5096(63)90060-7. URL: ttps://www.sciencedirect.com/science/article/pii/0022509663900607.

Hernández, J.A. et al. (2014). "High-performance model reduction techniques in computational multiscale homogenization". In: *Computer Methods in Applied Mechanics and Engineering* 276, pp. 149–189. ISSN: 0045-7825. DOI: 10.1016/j.cma.2014.03.011. URL: https://www.sciencedirect.com/science/article/pii/S0045782514000978.

Hill, Rodney J. (1963). "Elastic properties of reinforced solids: some theoretical principles". In: *Journal of the Mechanics and Physics of Solids* 11.5, pp. 357–372. DOI: 10.1016/0022-5096(63)90036-X. URL: https://www.sciencedirect.com/science/article/abs/pii/002250966390036X#!.

— (1965a). "A self-consistent mechanics of composite materials". In: *Journal of the Mechanics and Physics of Solids* 13.4, pp. 213–222. DOI: 10.1016/0022-5096(65)90010-4. URL: https://www.sciencedirect.com/science/article/pii/0022509665900104.

— (1965b). "Continuum micro-mechanics of elastoplastic polycrystals". In: *Journal of the Mechanics and Physics of Solids* 13.2, pp. 89–101. DOI: 10.1016/0022-5096(65)90023-2. URL: https://www.sciencedirect.com/science/article/pii/0022509665900232.

Kanouté, P., D.P. Boso, and J.L. et al. Chaboche (2009). "Multiscale Methods for Composites: A Review". In: *Archives of Computational Methods in Engineering* 16, pp. 31–75. DOI: 10.1007/s11831-008-9028-8. URL: https://link.springer.com/article/10.1007%2Fs11831-008-9028-8#citeas.

Kouznetsova, V., W. Brekelmans, and F. Baaijens (2001). "An approach to micro-macro modeling of heterogeneous materials". In: *Computational Mechanics* 27.1, pp. 37–48. ISSN: 0927-0256. DOI: 10.1007/s004660000212. URL: https://link.springer.com/article/10.1007/s004660000212.

Kröner, E. (1977). "Bounds for effective elastic moduli of disordered materials". In: *Journal of the Mechanics and Physics of Solids* 25.2, pp. 137–155. ISSN: 0022-5096. DOI: https://doi.org/10.1016/0022-5096(77)90009-6. URL: https://www.sciencedirect.com/science/article/pii/0022509677900096.

— (1978). "Self-consistent scheme and graded disorder in polycrystal elasticity". In: *Journal of Physics F: Metal Physics* 8, pp. 2261–2267.

Kröner, Ekkehart (1958). "Berechnung der elastischen Konstanten des Vielkristalls aus den Konstanten des Einkristalls". In: *Zeitschrift für Physik* 151, 504–518. DOI: 10.1007/BF01337948. URL: https://link.springer.com/article/10.1007/BF01337948.

Le, B. A., J. Yvonnet, and Q.-C. He (2015). "Computational homogenization of nonlinear elastic materials using neural networks". In: *International Journal for Numerical Methods in Engineering* 104.12, pp. 1061–1084. DOI: https://doi.org/10.1002/nme.4953. eprint: https://onlinelibrary.wiley.com/doi/pdf/10.1002/nme.4953. URL: https://onlinelibrary.wiley.com/doi/abs/10.1002/nme.4953.

Lippmann, B. A. and Julian Schwinger (1950). "Variational Principles for Scattering Processes. I". In: *Phys. Rev.* 79, pp. 469–480. DOI: 10.1103/PhysRev.79.469. URL: https://link.aps.org/doi/10.1103/PhysRev.79.469.

Liu, Zeliang, M.A. Bessa, and Wing Kam Liu (2016). "Self-consistent clustering analysis: An efficient multi-scale scheme for inelastic heterogeneous materials". In: *Computer Methods in Applied Mechanics and Engineering* 306, pp. 319 –341. ISSN: 0045-7825. DOI: 10.1016/j.cma.2016.04.004. URL: http://www.sciencedirect.com/science/article/pii/S0045782516301499.

Liu, Zeliang, Mark Fleming, and Wing Kam Liu (2018). "Microstructural material database for self-consistent clustering analysis of elastoplastic strain softening materials". In: *Computer Methods in Applied Mechanics and Engineering* 330, pp. 547 –577. ISSN: 0045-7825. DOI: 10.1016/j.cma.2017.11.005. URL: http://www.sciencedirect.com/science/article/pii/S0045782517307107.

Liu, Zeliang and C.T. Wu (2019). "Exploring the 3D architectures of deep material network in data-driven multiscale mechanics". In: *Journal of the Mechanics and Physics of Solids* 127, pp. 20 –46. ISSN: 0022-5096. DOI: 10.1016/j.jmps.2019.03.004.

Liu, Zeliang, C.T. Wu, and M. Koishi (2019). "A deep material network for multiscale topology learning and accelerated nonlinear modeling of heterogeneous materials". In: *Computer Methods in Applied Mechanics and Engineering* 345, pp. 1138 –1168. ISSN: 0045-7825. DOI: 10.1016/j.cma.2018.09.020.

Lopez-Pamies, O. and P. Ponte Castañeda (2004). "Second-Order Homogenization Estimates Incorporating Field Fluctuations in Finite Elasticity". In: *Mathematics and Mechanics of Solids* 9.3, pp. 243–270. DOI: 10.1177/1081286504038467.

Lopez-Pamies, Oscar, Taha Goudarzi, and Kostas Danas (2013). "The nonlinear elastic response of suspensions of rigid inclusions in rubber: II—A simple explicit approximation for finite-concentration suspensions". In: *Journal of the Mechanics and Physics of Solids* 61.1, pp. 19–37. ISSN: 0022-5096. DOI: 10.1016/j.jmps.2012.08.013. URL: https://www.sciencedirect.com/science/article/pii/S0022509612001925.

MacQueen, James B. (1967). "Some methods for classification and analysis of multivariate observations". In:

Masson, R. and A. Zaoui (1999). "Self-consistent estimates for the rate-dependent elastoplastic behaviour of polycrystalline materials". In: *Journal of the Mechanics and Physics of Solids* 47.7, pp. 1543–1568. ISSN: 0022-5096. DOI: 10.1016/S0022-5096(98)00106-9. URL: https://www.sciencedirect.com/science/article/pii/S0022509698001069.

McLaughlin, R. (1977). "A study of the differential scheme for composite materials". In: *International Journal of Engineering Science* 15.4, pp. 237–244. ISSN: 0020-7225. DOI: 10.1016/0020-7225(77)90058-1. URL: https://www.sciencedirect.com/science/article/pii/0020722577900581.

Michel, J.C. and P. Suquet (2003). "Nonuniform transformation field analysis". In: *International Journal of Solids and Structures* 40.25. Special issue in Honor of George J. Dvorak, pp. 6937 –6955. ISSN: 0020-7683. DOI: 10.1016/S0020-7683(03)00346-9. URL: http://www.sciencedirect.com/science/article/pii/S0020768303003469.

Michel, Jean-Claude and Pierre Suquet (2004). "Computational analysis of nonlinear composite structures using the Nonuniform Transformation Field Analysis". In: *Computer Methods in Applied Mechanics and Engineering* 193, pp. 5477–5502. URL: https://hal.archives-ouvertes.fr/hal-00088245.

— (2009). "Nonuniform transformation field analysis: a reduced model for multiscale nonlinear problems in solid mechanics". In: *Multiscale Modelling in Solid Mechanics - Computational Approaches*. Ed. by U. Galvanetto and F. Aliabadi. Imperial College Press. ISBN: 978-1-84816-307-2. Imperial College Press, London., pp. 159–206. URL: https://hal.archives-ouvertes.fr/hal-00367772.

— (2016). "A model-reduction approach in micromechanics of materials preserving the variational structure of constitutive relations". In: *Journal of the Mechanics and Physics of Solids* 90, pp. 254 –285. ISSN: 0022-5096. DOI: 10.1016/j.jmps.

2016.02.005. URL: http://www.sciencedirect.com/science/article/pii/S0022509616300928.

Moakher, Maher and Andrew N. Norris (2006). "The Closest Elastic Tensor of Arbitrary Symmetry to an Elasticity Tensor of Lower Symmetry". In: *Journal of Elasticity* 85.3, 215–263. ISSN: 1573-2681. DOI: 10.1007/s10659-006-9082-0. URL: http://dx.doi.org/10.1007/s10659-006-9082-0.

Molinari, A., G.R. Canova, and S. Ahzi (1987). "A self consistent approach of the large deformation polycrystal viscoplasticity". In: *Acta Metallurgica* 35.12, pp. 2983–2994. ISSN: 0001-6160. DOI: 10.1016/0001-6160(87)90297-5. URL: https://www.sciencedirect.com/science/article/pii/0001616087902975.

Mori, T and K Tanaka (1973). "Average stress in matrix and average elastic energy of materials with misfitting inclusions". In: *Acta Metallurgica* 21.5, pp. 571–574. DOI: 10.1016/0001-6160(73)90064-3. URL: https://www.sciencedirect.com/science/article/pii/0001616073900643.

Moulinec, H. and P. Suquet (1998). "A numerical method for computing the overall response of nonlinear composites with complex microstructure". In: *Computer Methods in Applied Mechanics and Engineering* 157.1, pp. 69–94. ISSN: 0045-7825. DOI: 10.1016/S0045-7825(97)00218-1. URL: https://www.sciencedirect.com/science/article/pii/S0045782597002181.

Moulinec, H. and Pierre Suquet (1994). "A fast numerical method for computing the linear and nonlinear mechanical properties of composites". In: *Comptes rendus de l'Académie des sciences. Série II. Mécanique, physique, chimie, astronomie.* URL: https://hal.archives-ouvertes.fr/hal-03019226.

Mozaffar, M. et al. (2019). "Deep learning predicts path-dependent plasticity". In: *Proceedings of the National Academy of Sciences* 116.52, pp. 26414–26420. DOI: 10.1073/pnas.1911815116. eprint: https://www.pnas.org/doi/pdf/10.1073/pnas.1911815116. URL: https://www.pnas.org/doi/abs/10.1073/pnas.1911815116.

Nguyen, Van-Dung and Ludovic Noels (2022a). "Interaction-based material network: a general framework for (porous) microstructured materials". In: *Computer Methods in Applied Mechanics and Engineering* 389, p. 114300. DOI: http://dx.doi.org/10.1016/j.cma.2021.114300.

— (2022b). "Micromechanics-based material networks revisited from the interaction viewpoint; robust and efficient implementation for multi-phase composites". In: *European Journal of Mechanics - A/Solids* 91, p. 104384. ISSN: 0997-7538. DOI: https://doi.org/10.1016/j.euromechsol.2021.104384.

Nguyen, Van-Dung, Ling Wu, and Ludovic Noels (2017). "Unified treatment of microscopic boundary conditions and efficient algorithms for estimating tangent operators of the homogenized behavior in the computational homogenization method". In: *Computational Mechanics* 59.3, pp. 483–505. ISSN: 1432-0924. DOI: 10.1007/s00466-016-1358-z. URL: https://doi.org/10.1007/s00466-016-1358-z.

Norris, A.N. (1985). "A differential scheme for the effective moduli of composites". In: *Mechanics of Materials* 4.1, pp. 1–16. ISSN: 0167-6636. DOI: 10.1016/0167-6636(85)90002-X. URL: https://www.sciencedirect.com/science/article/pii/016766368590002X.

Ostoja-Starzewski, M. et al. (2007). "Comparisons of the size of the representative volume element in elastic, plastic, thermoelastic, and permeable random microstructures".

English (US). In: *International Journal for Multiscale Computational Engineering* 5.2, pp. 73–82. ISSN: 1543-1649. DOI: 10.1615/IntJMultCompEng.v5.i2.10.

Peric, D. et al. (2010). "On micro-to-macro transitions for multi-scale analysis of non-linear heterogeneous materials: unified variational basis and finite element implementation". In: *International Journal for Numerical Methods in Engineering* 87, pp. 149 –170. ISSN: 1097-0207. URL: http://dx.doi.org/10.1002/nme.3014.

Ponte Castañeda, P. (1991). "The effective mechanical properties of nonlinear isotropic composites". In: *Journal of the Mechanics and Physics of Solids* 39.1, pp. 45–71. ISSN: 0022-5096. DOI: 10.1016/0022-5096(91)90030-R. URL: https://www.sciencedirect.com/science/article/pii/002250969190030R.

— (1992). "New variational principles in plasticity and their application to composite materials". In: *Journal of the Mechanics and Physics of Solids* 40.8, pp. 1757–1788. ISSN: 0022-5096. DOI: 10.1016/0022-5096(92)90050-C. URL: https://www.sciencedirect.com/science/article/pii/002250969290050C.

— (1996). "Exact second-order estimates for the effective mechanical properties of nonlinear composite materials". In: *Journal of the Mechanics and Physics of Solids* 44.6, pp. 827–862. ISSN: 0022-5096. DOI: 10.1016/0022-5096(96)00015-4. URL: https://www.sciencedirect.com/science/article/pii/0022509696000154.

— (2002a). "Second-order homogenization estimates for nonlinear composites incorporating field fluctuations: I—theory". In: *Journal of the Mechanics and Physics of Solids* 50.4, pp. 737–757. ISSN: 0022-5096. DOI: 10.1016/S0022-5096(01)00099-0. URL: https://www.sciencedirect.com/science/article/pii/S0022509601000990.

— (2002b). "Second-order homogenization estimates for nonlinear composites incorporating field fluctuations: II—applications". In: *Journal of the Mechanics and Physics of Solids* 50.4, pp. 759–782. ISSN: 0022-5096. DOI: https://doi.org/10.1016/S0022-5096(01)00098-9. URL: https://www.sciencedirect.com/science/article/pii/S0022509601000989.

Reuss, A (1929). "Berechnung der Fließgrenze von Mischkristallen auf Grund der Plastizitätsbedingung für Einkristalle". In: *Z. angew. Math. Mech.* 9, pp. 49–58.

Ri, Jun-Hyok, Hyon-Sik Hong, and Sung-Gyu Ri (2021). "Cluster based nonuniform transformation field analysis: An efficient homogenization for inelastic heterogeneous materials". In: *International Journal for Numerical Methods in Engineering* 122.17, pp. 4458–4485. DOI: https://doi.org/10.1002/nme.6696. eprint: https://onlinelibrary.wiley.com/doi/pdf/10.1002/nme.6696. URL: https://onlinelibrary.wiley.com/doi/abs/10.1002/nme.6696.

Ryckelynck, D. (2009). "Hyper-reduction of mechanical models involving internal variables". In: *International Journal for Numerical Methods in Engineering* 77.1, pp. 75–89. DOI: 10.1002/nme.2406. eprint: https://onlinelibrary.wiley.com/doi/pdf/10.1002/nme.2406. URL: https://onlinelibrary.wiley.com/doi/abs/10.1002/nme.2406.

Saeb, S., P. Steinmann, and A. Javili (2016). "Aspects of Computational Homogenization at Finite Deformations: A Unifying Review From Reuss' to Voigt's Bound". In: *Applied Mechanics Reviews* 68.5. DOI: 10.1115/1.4034024. URL: https://asmedigitalcollection.asme.org/appliedmechanicsreviews/article-abstract/68/5/050801/443653/Aspects-of-Computational-Homogenization-at-Finite?redirectedFrom=fulltext.

Schröder, Jörg, Matthias Labusch, and Marc-André Keip (2016). "Algorithmic two-scale transition for magneto-electro-mechanically coupled problems: FE2-scheme: Localization and homogenization". In: *Computer Methods in Applied Mechanics and Engineering* 32, pp. 253–280. ISSN: 0045-7825. DOI: http://dx.doi.org/10.1016/j.cma.2015.10.005. URL: http://www.sciencedirect.com/science/article/pii/S0045782515003242.

Sepe, Valentina, Sonia Marfia, and Elio Sacco (2013). "A nonuniform TFA homogenization technique based on piecewise interpolation functions of the inelastic field". In: *International Journal of Solids and Structures* 50.5, pp. 725–742. ISSN: 0020-7683. DOI: 10.1016/j.ijsolstr.2012.11.005. URL: https://www.sciencedirect.com/science/article/pii/S0020768312004684.

Spilker, Kevin et al. (2022). "Piecewise-uniform homogenization of heterogeneous composites using a spatial decomposition based on inelastic micromechanics". In: *Composite Structures* 295, p. 115836. ISSN: 0263-8223. DOI: https://doi.org/10.1016/j.compstruct.2022.115836. URL: https://www.sciencedirect.com/science/article/pii/S0263822322006018.

Suquet, P. M. (2001). "SECTION 10.3 - Nonlinear Composites: Secant Methods and Variational Bounds". In: *Handbook of Materials Behavior Models*. Ed. by JEAN LEMAITRE. Burlington: Academic Press, pp. 968–983. ISBN: 978-0-12-443341-0. DOI: 10.1016/B978-012443341-0/50099-5. URL: https://www.sciencedirect.com/science/article/pii/B9780124433410500995.

Talbot, D. R. S. and J. R. Willis (1985). "Variational Principles for Inhomogeneous Nonlinear Media". In: *IMA Journal of Applied Mathematics* 35.1, pp. 39–54. ISSN: 0272-4960. DOI: 10.1093/imamat/35.1.39. eprint: https://academic.oup.com/imamat/article-pdf/35/1/39/2037184/35-1-39.pdf. URL: https://doi.org/10.1093/imamat/35.1.39.

Voigt, W (1889). "Ueber die Beziehung zwischen den beiden Elasticitätsconstanten isotroper Körper". In: *Annalen der Physik* 274.12, pp. 573–587.

Willis, J.R. (1977). "Bounds and self-consistent estimates for the overall properties of anisotropic composites". In: *Journal of the Mechanics and Physics of Solids* 25.3, pp. 185–202. ISSN: 0022-5096. DOI: 10.1016/0022-5096(77)90022-9. URL: https://www.sciencedirect.com/science/article/pii/0022509677900229.

Wu, L. et al. (2013a). "A combined incremental-secant mean-field homogenization scheme with per-phase residual strains for elasto-plastic composites". In: *International Journal of Plasticity* 51, pp. 80 –102. ISSN: 0749-6419. DOI: 10.1016/j.ijplas.2013.06.006. URL: http://www.sciencedirect.com/science/article/pii/S0749641913001174.

— (2013b). "An implicit-gradient-enhanced incremental-secant mean-field homogenization scheme for elasto-plastic composites with damage". In: *International Journal of Solids and Structures* 50.24, pp. 3843–3860. ISSN: 0020-7683. DOI: https://doi.org/10.1016/j.ijsolstr.2013.07.022. URL: https://www.sciencedirect.com/science/article/pii/S0020768313003028.

Wu, L. et al. (2015). "A study of composite laminates failure using an anisotropic gradient-enhanced damage mean-field homogenization model". In: *Composite Structures* 126, pp. 246–264. ISSN: 0263-8223. DOI: https://doi.org/10.1016/j.compstruct.2015.02.070. URL: https://www.sciencedirect.com/science/article/pii/S0263822315001580.

Wu, L. et al. (2017). "An incremental-secant mean-field homogenization method with second statistical moments for elasto-visco-plastic composite materials". In: *Mechanics of Materials* 114, pp. 180–200. ISSN: 0167-6636. DOI: 10.1016/j.mechmat.2017.08.006. URL: https://www.sciencedirect.com/science/article/pii/S0167663617300698.

Wu, Ling, Laurent Adam, and Ludovic Noels (2021). "Micro-mechanics and data-driven based reduced order models for multi-scale analyses of woven composites". In: *Composite Structures* 270, p. 114058. ISSN: 0263-8223. DOI: https://doi.org/10.1016/j.compstruct.2021.114058. URL: https://www.sciencedirect.com/science/article/pii/S0263822321005183.

Wu, Ling, Etienne Maillard, and Ludovic Noels (2021). "Tensile failure model of carbon fibre in unidirectionally reinforced epoxy composites with mean-field homogenisation". In: *Composite Structures* 273, p. 114270. ISSN: 0263-8223. DOI: https://doi.org/10.1016/j.compstruct.2021.114270. URL: https://www.sciencedirect.com/science/article/pii/S0263822321007327.

Wu, Ling et al. (2020). "A recurrent neural network-accelerated multi-scale model for elasto-plastic heterogeneous materials subjected to random cyclic and non-proportional loading paths". In: *Computer Methods in Applied Mechanics and Engineering* 369, p. 113234. ISSN: 0045-7825. DOI: https://doi.org/10.1016/j.cma.2020.113234. URL: https://www.sciencedirect.com/science/article/pii/S0045782520304199.

Wu, Ling et al. (2021). "Per-phase spatial correlated damage models of UD fibre reinforced composites using mean-field homogenisation; applications to notched laminate failure and yarn failure of plain woven composites". In: *Computers & Structures* 257, p. 106650. ISSN: 0045-7949. DOI: https://doi.org/10.1016/j.compstruc.2021.106650. URL: https://www.sciencedirect.com/science/article/pii/S0045794921001723.

Wulfinghoff, Stephan, Fabiola Cavaliere, and Stefanie Reese (2018). "Model order reduction of nonlinear homogenization problems using a Hashin–Shtrikman type finite element method". In: *Computer Methods in Applied Mechanics and Engineering* 330, pp. 149 –179. ISSN: 0045-7825. DOI: 10.1016/j.cma.2017.10.019. URL: http://www.sciencedirect.com/science/article/pii/S0045782517306904.

Yvonnet, J. (2019). *Computational Homogenization of Heterogeneous Materials with Finite Elements*. Solid Mechanics and Its Applications. Springer, Cham. ISBN: 9783030183820. DOI: 10.1007/978-3-030-18383-7. URL: https://link.springer.com/book/10.1007/978-3-030-18383-7.

Zhuang, Fujian et al. (2019a). "Mesoscale modelling of damage in half-hole pin bearing composite laminate specimens". In: *Composite Structures* 214, pp. 191–213. ISSN: 0263-8223. DOI: https://doi.org/10.1016/j.compstruct.2019.01.062. URL: https://www.sciencedirect.com/science/article/pii/S0263822318340236.

Zhuang, Fujian et al. (2019b). "Mesoscale modelling of damage in single- and double-shear composite bolted joints". In: *Composite Structures* 226, p. 111210. ISSN: 0263-8223. DOI: https://doi.org/10.1016/j.compstruct.2019.111210. URL: https://www.sciencedirect.com/science/article/pii/S0263822319305884.

Zimmerman, Robert W. (1991). "Elastic moduli of a solid containing spherical inclusions". In: *Mechanics of Materials* 12.1, pp. 17–24. ISSN: 0167-6636. DOI: 10.1016/0167-

6636(91)90049-6. URL: https://www.sciencedirect.com/science/article/pii/0167663691900496.